Disorder and Defects in Functional Molecular Frameworks

Matthew J. Cliffe
Merton College



A thesis submitted for the degree of
Doctor of Philosophy

Department of Chemistry
University of Oxford

Hilary 2015

Abstract

This Thesis explores the role of structural defects and disorder and their relationship to experimental data, with a particular emphasis on molecular framework materials. The question of how we can build atomistic models of amorphous materials from experimental data without needing to make system-specific assumptions is addressed. The role of 'structural invariance', *i.e.* the limited range of distinct local atomic environments within a material, as a restraint within reverse Monte Carlo refinement (RMC) is investigated. The operation of these invariance restraints operate is shown to be system-dependent and the challenges associated with effective refinement, *e.g.* configurational 'jamming', are also investigated. A generalisation to the 'structural simplicity', *i.e.* the simplest model, holding all else constant, is most likely to be correct. Three new metrics of structural simplicity are proposed: two intrinsically three-dimensional measures of local geometric invariance and one measure of local symmetry. These metrics are shown to robustly quantify the configurational quality. The ability of these metrics to act as effective restraints for the RMC refinement of amorphous materials is demonstrated by the construction of the first data-driven tetrahedral models of amorphous silicon. The role of defects and disorder within metal–organic frameworks (MOFs) is investigated through the canonical MOF UiO-66(Hf). Through a combination of techniques, including X-ray diffuse scattering, anomalous diffraction, total scattering and electron diffraction measurements, the existence of correlated metal-cluster absences in UiO-66(Hf) is demonstrated. Furthermore the ability to synthetically tune both the interactions and concentration of defects is shown. The thermomechanical properties of defective UiO-66(Hf) are also examined. UiO-66(Hf) is shown to rapidly densify by up to 5% ($\Delta V/V$) on ligand elimination. The resultant densified phase exhibits colossal ($\geq 100\,\mathrm{MK}^{-1}$) volumetric negative thermal expansion (NTE); the largest reported value for any MOF. Finally, the capability to tune the physical properties of MOFs through defect incorporation is demonstrated through the defect-dependence of both the densification and the NTE.

Declaration

This Thesis is the result of my own original work, and where it draws on the work of others this is acknowledged at the appropriate points in the text. This dissertation has not been submitted in whole or in part for a degree at this or any other institution.

Matthew Cliffe

Acknowledgements

First, I would like to thank my supervisor Prof. Andrew Goodwin, who has been a truly inspiring mentor.

I would also like to thank all my colleagues for all their contributions to the work presented in this Thesis. In particular I would like to acknowledge Dr Milen Gateshki (PANalytical) for collecting X-ray total scattering data on C_{60}; Dr Albert Bartók-Partay for providing me with access to the SOAP library and for generous support in its use; Dr Heribert Wilhelm, Dr Annette Kleppe, Dr Phil Chater and Dr Matt Tucker (I15, Diamond Light Source) for their help in designing and carrying out the anomalous diffraction measurements on defective UiO-66(Hf); Prof. Xiaodong Zou and Dr Wei Wan (University of Stockholm) for carrying out the electron diffraction measurements on UiO-66(Hf); Dr François-Xavier Coudert (Chimie ParisTech–CNRS) for carrying out extensive quantum mechanical calculations on UiO-66(Hf) and Dr Claire Murray (Diamond Light Source) and Joshua Hill for their help carrying out the variable temperature PXRD experiments on defective UiO-66(Hf) at I11.

Some portions of Thesis draw on published papers based on work carried out during my doctoral research. The co-authors of these papers will therefore—through their suggestions and contributions to the content, structure and phrasing—have also directly contributed to the content, structure and phrasing of this Thesis.

I would also like to thank the Goodwin Group—for too many individual moments to mention—but suffice to say I am grateful that I had the opportunity to be part of such a supportive and entertaining group of scientists.

Finally I would like to thank my sisters Helen, Frances and my parents for their constant grounded support.

Contents

1 Introduction **1**

1.1 Disordered materials 1

1.2 Average and local structure 2

1.3 Theory of diffraction 5

1.4 Types of disorder 9

1.5 Making models of disordered materials 21

1.6 INVERT 32

1.7 Metal–organic frameworks 36

1.8 Aims and structure of the Thesis 50

2 Scattering theory **52**

2.1 Theory of diffraction experiments 52

3 Parametrising the INVERT approach **63**

3.1 Implementation 64

3.2 Fitting process 68

3.3 Solution spaces 72

3.4 Outlook and conclusions 77

4 Structural simplicity in disordered materials **80**

4.1 Introduction 81

4.2 Descriptors of local geometry and symmetry 83

4.3 Case-study: *a*-Si 89

4.4 Refinement 94

4.5 Conclusions 100

5 Correlated defect nano-regions in a MOF **102**

5.1 Results . . . 104

5.2 Discussion . . . 112

5.3 Methods . . . 114

6 Defect-controlled MOF mechanics **127**

6.1 Results and discussion . . . 129

6.2 Concluding remarks . . . 136

6.3 Methods . . . 137

7 Conclusion **140**

Bibliography **145**

Appendix A **163**

A1 Experimental . . . 163

Appendix B **178**

B1 Synthesis . . . 178

B2 Structure solution of the α phase . . . 178

Appendix C **179**

C1 PASCal: a principal axis strain calculator for thermal expansion and compressibility determination . . . 182

C2 Negative area compressibility in silver(I) tricyanomethanide . . . 193

C3 Flexibility transition and guest-driven reconstruction in a ferroelastic metal–organic framework . . . 197

Publications arising from the Thesis

The published articles arising from this Thesis detailed below, along with the location within the Thesis of the work on which they are based.

- Chapter 3

  Nanostructure determination from the pair distribution function: a parametric study of the INVERT approach. **M. J. Cliffe** and A. L. Goodwin, *J. Phys.: Condens. Matter*, 2013, **25**, 454218.

- Chapter 4

  Quantification of local geometry and local symmetry in models of disordered materials. **M. J. Cliffe** and A. L. Goodwin, *Phys. Status Solidi B*, 2013, **250**, 949–956.

- Chapter 5

  Correlated defect nanoregions in a metal–organic framework. **M. J. Cliffe**, W. Wan, X. Zou, P. A. Chater, A. K. Kleppe, M. G. Tucker, H. Wilhelm, N. P. Funnell, F.-X. Coudert and A. L. Goodwin, *Nat. Commun.*, 2014, **5**, 4176.

- Chapter 6

  Defect-dependent colossal negative thermal expansion in UiO-66(Hf) metal-organic framework. **M. J. Cliffe**, J. A. Hill, C. A. Murray, F.-X. Coudert, A. L. Goodwin, *Phys. Chem. Chem. Phys.*, 2015, **17**, 11586–11592.

- Appendix C

  PASCal: a principal axis strain calculator for thermal expansion and compressibility determination. **M. J. Cliffe** and A. L. Goodwin, *J. Appl. Cryst.*, 2012, **45**, 1321–1329.

  Negative area compressibility in silver (I) tricyanomethanide S. A. Hodgson, J. Adamson, S. J. Hunt, **M. J. Cliffe**, A. B. Cairns, A. L. Thompson, M. G. Tucker, N. P. Funnell and A. L. Goodwin, *Chem. Commun.*, 2014, **50**, 5264–5266.

  Flexibility transition and guest-driven reconstruction in a ferroelastic metal–organic framework. S. J. Hunt, **M. J. Cliffe**, J. A. Hill, A. B. Cairns, N. P. Funnell and A. L. Goodwin, *CrystEngComm*, 2015, **17**, 361–369 .

List of Figures

1.1 Illustration of average *vs.* local structure 4
1.2 Scattering diagram 6
1.3 Types of framework disorder 10
1.4 Compositional disorder in Cu_3Au and the binary oxide TiO 11
1.5 Positional disorder in cristobalite 14
1.6 Positional disorder in $BaTiO_3$ 15
1.7 Charge, spin and water ices 16
1.8 Amorphous materials 20
1.9 Illustration of the limitations of PDFs 26
1.10 Models of amorphous materials 27
1.11 Comparison of various models of *a*-Si 30
1.12 NMR spectra of *c*-Si and *a*-Si 31
1.13 RMC refinement of C_{60} 34
1.14 Data-driven model of SiO_2 35
1.15 Illustration of the modular, open and soft nature 36
1.16 Modularity of the IRMOF and MOF-74 families 38
1.17 Properties of nonstochiometric IRMOFs 39
1.18 Postsynthetic modification and postsynthetic exchange in MOFs 40
1.19 Influence of ligand vacancies on MOF properties 42
1.20 Examples of open MOFs, including NU-110E and dimethylammonium manganese formate 45
1.21 MOF softness illustrated by MIL-53(Cr) and silver methylimidazolate . . . 46
1.22 Two examples of amorphous MOFs, $Zn(Im)_2$ and $[Zn(HPO_4)(H_2PO_4)_2$ . . 48

3.1 Schematic representation of the PDF refinement landscape 64
3.2 Three possible methods for fitting the PDF 66
3.3 Evolution of fit-to-data and variance contributions to χ^2 during RMC refinement 69
3.4 Evolution of density variance and root mean squared displacement per accepted move during RMC refinement of *a*-Si. 71
3.5 Trajectory length distributions for RMC refinement of *a*-Si 72
3.6 Representations of the solution spaces for refinements of C_{60}, *a*-Si, and *a*-SiO_2 73
3.7 The effect of data quality of the INVERT+RMC refined models of C_{60} . . 77
3.8 Illustrations of molecular geometries and PDFs associated with local minima in the INVERT-weighted configuration space for S_{12} 78

4.1 Graphical representations of the spherical harmonics 84
4.2 Values of the orientationally-invariant descriptors Q_l determined for a range of common high-symmetry local environments. 85
4.3 Values of the symmetry descriptor S for a number of SiO_2 polymorphs. . . 89
4.4 Values of Q_l determined for six Si configurations with different neighbour weightings 90
4.5 Values of $\mathrm{Var}(Q_l)$ determined for six Si configurations using different weighting functions 91
4.6 Benchmarking of four metrics of structural invariance using a range of configurations of *a*-Si 92
4.7 A configuration of *a*-Si produced using INVERT+RMC coloured by metrics of local invariance 93
4.8 Angle distributions for models of *a*-Si 98
4.9 Electronic density of states for models of *a*-Si 99
4.10 Comparison of WWW and K configurations 100

5.1 Structural description of UiO-66(Hf) 103
5.2 PXRD patterns of nano-**reo** and **fcu** UiO-66(Hf) 104
5.3 Chemical control of defect nano-region concentration and domain size . . . 105

5.4 TEM characterisation of nano-**reo** UiO-66(Hf) 106
5.5 Low angle-regions of the PXRD patterns of nano-**reo** UiO-66(Hf) after chemical treatment 107
5.6 Calculation of PXRD patterns for ligand absence models for UiO-66(Hf) . 108
5.7 Experimental characterisation of correlated defect inclusion 109
5.8 Modelling of the experimentally observed diffuse scattering 110
5.9 Structural description of defect nano-regions in UiO-66(Hf) 111
5.10 PXRD patterns of attempted PSM of UiO-66(Hf) 116
5.11 Pawley fits of UiO-66(Hf) 118
5.12 Predicted variation of the anomalous components of the Hf form factor and the variation of diffracted intensity with beam exposure 120
5.13 Experimental X-ray total scattering functions 122
5.14 TGA traces for samples of UiO-66(Hf) 125
5.15 N_2 adsorption measurements on UiO-66(Hf) 126

6.1 The cluster coordination environments in non-defective **fcu** and defective **reo** UiO-66(Hf). 128
6.2 Variation in defect concentration with H_2bdc concentration for UiO-66(Hf) 129
6.3 Thermomechanical behaviour of defective UiO-66(Hf) 131
6.4 Structural changes on ligand-elimination in UiO-66(Hf) 132
6.5 Defect dependence of the thermomechanical properties of UiO-66(Hf) . . . 133
6.6 Defect dependence of TGA traces for UiO-66(Hf) 138

A1.1 Synchrotron PXRD diffraction measurements of the variation in lattice parameter for defective UiO-66(Hf) 166
A1.2 Rietveld fits for each sample at 200 °C 169
B1.3 PXRD patterns of hafnium formate 179
B2.4 Representation of hafnium formate viewed along the a direction 180
B2.5 Representation of hafnium formate viewed along the b direction 181

List of Tables

4.1 Summary of the key fit metrics for a variety of *a*-Si 97

4.2 Summary of the calculated energy per Si for a variety of configurations . . 98

5.1 Experimentally observed peak intensities for nano-**reo** UiO-66(Hf) at 55 and 65.340 keV. 121

A1.1 Summary of crystallographic details for nano-**reo** UiO-66(Hf) obtained by PDFGui refinement against X-ray total scattering data. 163

A1.2 Summary of crystallographic details for **fcu** UiO-66(Hf) obtained by PDFGui refinement against X-ray total scattering data. 164

A1.3 Summary of the variation in thermomechanical properties with defect concentration presented in Fig. 6.5 165

A1.4 Lattice parameters for the initial variable temperature measurements presented in Fig. 6.5(a,b) 167

A1.5 Lattice parameters for the variable temperature measurements presented in Fig. 6.5(c,d) 168

A1.6 Refined parameters for the Rietveld fits shown in Fig. A1.2. 170

A1.7 Atomic coordinates for the model of α hafnium formate derived from X-ray powder diffraction data. 171

A1.8 Atomic coordinates for the optimised structure of **reo** UiO-66(Hf). 172

A1.9 Atomic coordinates for the optimised structure of **reo** UiO-66(Hf) after ligand elimination. 173

A1.10 Atomic coordinates for the optimised structure of **fcu** UiO-66(Hf). 174

A1.11 Atomic coordinates for the optimised structure of **reo** UiO-66(Zr). 175

A1.12 Atomic coordinates for the optimised structure of **fcu** UiO-66(Zr). 176

A1.13 Calculated mechanical properties for UiO-66(Hf) 177
A1.14 Calculated mechanical properties for UiO-66(Zr) 177

Abbreviations

BET	Brunauer–Emmett–Teller
CRN	continuous random network
DMF	N,N-dimethylformamide
EXAFS	Extended X-ray Absorption Fine Structure
fcc	face-centered cubic
H_2bdc	terephthalic acid (1,4-benzenedicarboxylic acid)
INVERT	invariant environment refinement technique
MOF	metal–organic framework
NTE	negative thermal expansion
PDF	pair distribution function
PSM	post-synthetic modification
PSE	post-synthetic exchange
PXRD	powder X-ray diffraction
RMC	reverse Monte Carlo
SC-SC	single crystal to single crystal
TEM	transmission electron microscopy
TGA	thermogravimetric analysis
VT	variable temperature
WWW	Wooten–Winer–Weaire

Chapter 1

Introduction

1.1 Disordered materials

The fundamental concept of solid-state science is the crystal—a long-range ordered periodic array of atoms. The periodicity of crystals has two important consequences. First, periodicity, *via* the formalism of reciprocal space, determines many properties of crystals, including the electronic band structures and the vibrational density of states. Second, periodicity allows for the determination of the positions of atoms within the material—the structure—*via* diffraction experiments. Despite the centrality of periodicity to the structures and properties of solids, perfectly periodic materials occupy only a small fraction of possible chemical space. Those materials that lack complete periodic order are known as 'disordered' materials. Disordered materials range from ordered crystals containing a structural feature that lacks long-range order, through to amorphous materials with no periodic order at all. They are a ubiquitous part of our world, playing an important role in technological materials, both ancient, such as silicate glasses [1] and concrete [2]; and modern, such as ferroelectrics [3] or phase-change chalocogenide glasses [4]; and the natural environment, such as amorphous phases utilised in biomineralisation [5] and the amorphous sulfates recently discovered on Mars [6].

Disorder is not just an incidental feature of these materials and so can have important consequences for their properties. The presence of disorder implies a large number of (near) degenerate states. In many disordered materials, therefore, a small external stimulus can produce dramatic changes in state, which can be harnessed to produce useful function. This is as true for amorphous biominerals—for which their lack of crystallinity facilitates the formation of complex nanostructures with curved surfaces [7]—as for the fast-ion conductors used in solid oxide fuel cells—where the large number of low-energy sites provide a pathway for rapid ionic diffusion [8].

Disordered materials, especially those which contain correlations within the disorder, can also exist in unique states with non-periodic structural order. One of the most strik-

ing examples of correlated disorder is the magnetism of the "spin ice" pyrochlores, *e.g.* $Ho_2Ti_2O_7$. The combination of the magnetic interactions and the geometry of the lattice frustrates the periodic ordering of the spin ices, but does not prevent the formation of strong local order. These correlations thus lead to a range of surprising emergent phenomena, including magnetic excitations that behave as magnetic monopoles [9]. Correlated disordered states, along with other materials with aperiodic structural order, such as 'chaotic crystals' [10] or, 'turbulent crystals' [11] therefore force us to re-examine our fundamental ideas about structure [12].

The fact that disordered materials very often show significant local order not reflected in the long-range order is also responsible for the challenges that are still faced in its study: it is difficult to experimentally characterise and synthetically control. Experimental structure determination is hard as the information about the structure within the disorder is not present in the sharp Bragg peaks, but in the broad structured-diffuse scattering, complicating both measurement and analysis. Modelling disordered materials is difficult as both periodic average structure based models, able to account for long range order, and isolated cluster models, able to account for the short-range order, incompletely describe the properties of disordered materials. Our methods for synthetically controlling disorder are also currently limited, in part due to the complexity of possible disordered structures. The combination of function, relevance to important theoretical questions and unresolved challenges in both characterisation and control of structure mean that disordered materials remain one of the most exciting areas of solid-state science.

1.2 Average and local structure

The structure of a perfect crystal can be described entirely by specifying its repeat unit, *i.e.* its unit cell. For a disordered crystal this is no longer true—the disordered component is by definition aperiodic. It is therefore useful to draw a distinction between the *average* and the *local* structure. The local structure is the structure that one would see with an idealised microscope: it is the short-range arrangement of atoms. The average structure of a material is formally the periodic average over space of the material: $\langle\rho(\mathbf{r})\rangle$, where $\rho(\mathbf{r})$ is the scatterer density. As the periodic component of the structure, the average structure is fully described by a periodic unit cell, just as for a perfect crystal. Amorphous

materials, as they lack all periodicity, do not have average structures, beyond the density and composition. The total crystal structure can therefore be written as a sum of a periodic component (the convolution of the periodic lattice with the average structure) and a non-periodic component $\Delta\rho(\mathbf{r})$ (which, by definition, has a total density of zero):

$$\rho(\mathbf{r}) = \sum_{U,V,W} \delta(\mathbf{r} - (U\mathbf{a} + V\mathbf{b} + W\mathbf{c})) * \langle\rho(\mathbf{r})\rangle + \Delta\rho(\mathbf{r}), \tag{1.1}$$

where $\mathbf{a}, \mathbf{b}, \mathbf{c}$ are the lattice basis vectors (*i.e.* the edges of the unit cell) and U, V, W integers. The average structure is the only structure directly accessible by the Bragg scattering of conventional diffraction techniques (discussed further in Section 1.3).

The distinction between average and local structure, and its connection to the diffraction data, can be illustrated with a simple example of disorder: a two-dimensional square lattice, over which equal numbers of two types of atoms, A and B, are distributed. This model is a chemical realisation of the magnetic Ising model widely used in solid state physics [13]. If A and B are distributed completely randomly, then every site will have a 50% chance of being occupied by A or B. In this case the material will have an average structure consisting of the smallest possible unit cell, containing one atomic site, with occupancy of 0.5 A and 0.5 B [Fig. 1.1(a,d)]. For this random case, the knowledge that a particular site is occupied by A gives no information about whether any other site is occupied by A or B. At the opposite extreme of randomness is the case where the positions of A and B are completely ordered. One of the simplest orderings is a chequerboard pattern, where A and B occupy alternate sites [Fig. 1.1(b)]. This ordered material has an average structure with a unit cell twice the size of the random material containing two sites, one occupied solely by A and the other by B [Fig. 1.1(e)]. For this ordered model, the knowledge of the occupancy of any given site thus allows us to determine the identity of every other atom in the material: it has long-range order. But what about intermediate cases, where A and B tend to alternate, but this order is not long-range—*i.e.* where the probability that a given site adjacent to A contains B is greater than half, but still less than 1.0 [Fig. 1.1(c)]? In this case the average structure is the same as the random case: a unit cell containing a single site which has and occupancy of 0.5 A and 0.5 B [Fig. 1.1(f)]. Examination of the configuration shows that this model, although random, clearly has a

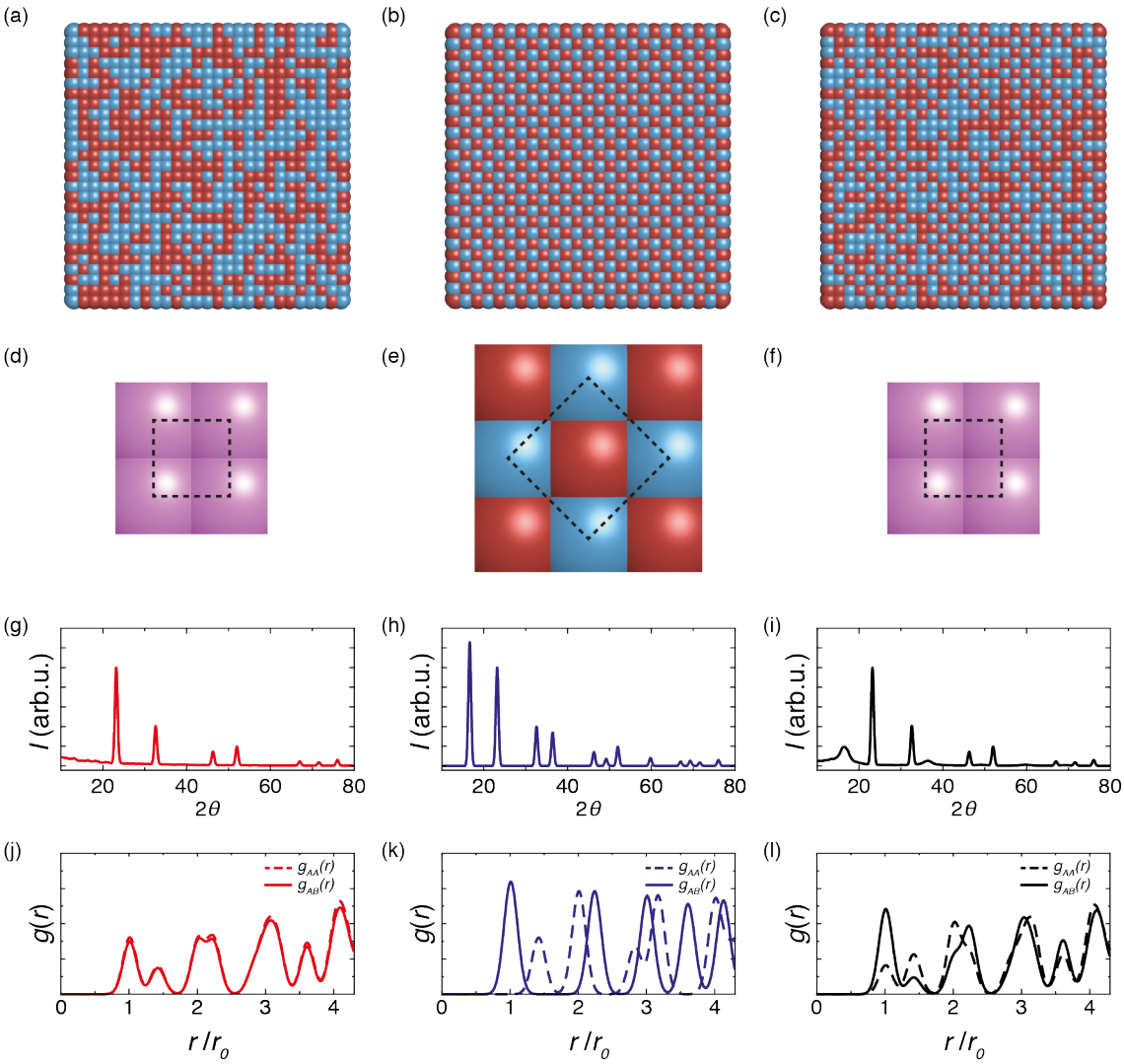

Figure 1.1: An illustration of disorder, order and correlated in a simple model of a compositionally disordered square lattice. Configurations with: (a) random distribution of atoms, *i.e.* the probability of a given neighbouring atom being dissimilar $P(A_i|B_{i+1}) = 0.5$, (b) chequerboard ordering, $P(A_i|B_{i+1}) = 1.0$, and (c) correlated disorder $P(A_i|B_{i+1}) = 0.8$. (d-f)The average structures of the three models. Powder diffraction patterns of the three models show identical Bragg scattering (g-i), except the ordered configuration has additional superlattice reflections. The configuration with correlated disorder shows broad structured diffuse scattering. (j-l) Pair correlation functions for each of the models clearly show their differences.

distinct local structure: it shows correlated disorder.

The most straightforward method of quantifying this local structure would be to determine the average number of atoms B at a distance r from each atom A. This is the

one-dimensional pair distribution function (PDF) $g_{AB}(r)$,

$$g_{AB}(r)\mathrm{d}r = \frac{1}{N_j N_k} \sum_{j \in A} \sum_{k \in B} \delta(r - r_{jk}). \tag{1.2}$$

$g_{AB}(r)$, together with the corresponding functions g_{BA}, g_{AA} and g_{AB}, allows us to describe the local ordering within this material*. In this example the differences between the three models are visible in the PDFs, and these difference are particularly clear at shorter distances [Figs. 1.1(j-l)].

The pair correlation functions can describe the short-range order, but how can we detect short-range order experimentally? If we measured the powder diffraction patterns for these three materials [Figs. 1.1(g-i)], we would see that all three models show identical Bragg peaks at the positions corresponding to that of the smaller disordered unit cell, because all three models appear equivalent when projected onto the disordered unit cell. For the ordered model, there are additional Bragg peaks resulting from the long-range ordering of the A and B atoms [Fig. 1.1(h)]. As the correlated disordered model shares the same average structure as the random model, its diffraction pattern has no such additional sharp Bragg peaks [Fig. 1.1(i)]. However, its diffraction pattern does contain additional broad features, the structured diffuse scattering resulting from the short-range order. By measuring this diffuse scattering in addition to the sharp Bragg peaks we can therefore gather information about local structure.

1.3 Theory of diffraction

To understand why diffraction is ideally suited to the determination of local structure, I will give a brief introduction to scattering theory. This is not intended to be a complete and rigorous description of scattering theory, and is drawn in large part from Refs. 14, 15. In particular, I will demonstrate that the measured diffraction data are simply the Fourier transform of the interatomic vectors and that the distinction between average and local structure is exactly paralleled by the Bragg and diffuse scattering. Our starting point is to take a simple system of two atoms, with positions $\mathbf{r}_a$ and $\mathbf{r}_b$, that interact with a parallel

*For this model the overall probability of any given site being occupied by A or B is equal and so the pair correlations are symmetric to the interchange of A and B. Thus $g_{AA} \equiv g_{BB}$ and $g_{AB} \equiv g_{BA}$.

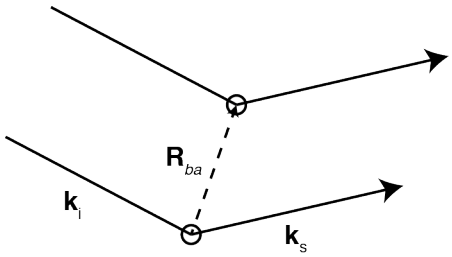

Figure 1.2: An incident parallel beam with wavevector $\mathbf{k}_\mathrm{i}$ scattering off two identical particles, separated by the vector $\mathbf{R}_{ba}$ to produce a wave with wavevector $\mathbf{k}_\mathrm{s}$.

beam of incident radiation [Fig. 1.2].

The incident beam of radiation can be described by the following wave equation

$$\psi_\mathrm{i}(\mathbf{x}) = A\exp(\mathrm{i}\,\mathbf{x}\cdot\mathbf{k}_\mathrm{i}), \tag{1.3}$$

where $\mathbf{k}_\mathrm{i}$ is its wavevector, and A its amplitude. If this wave is (elastically) scattered by a pair of (identical) particles, it will emerge as a pair of waves, each with wavevector $\mathbf{k}_\mathrm{s}$. As the second particle is separated from the first by the vector $\mathbf{r}_b - \mathbf{r}_a = \mathbf{R}_{ba}$, its wave will have travelled an extra distance l:

$$l = \frac{\mathbf{k}_\mathrm{i}\cdot\mathbf{R}_{ba}}{|\mathbf{k}_\mathrm{i}|} + \frac{\mathbf{k}_\mathrm{s}\cdot-\mathbf{R}_{ba}}{|\mathbf{k}_\mathrm{s}|} = \frac{(\mathbf{k}_\mathrm{i}-\mathbf{k}_\mathrm{s})\cdot\mathbf{R}_{ba}}{k}, \tag{1.4}$$

as $|\mathbf{k}_\mathrm{i}| = |\mathbf{k}_\mathrm{s}| = k$. Defining the scattering vector $\mathbf{Q} = \mathbf{k}_\mathrm{i} - \mathbf{k}_\mathrm{s}$, and noting that the relationship between the phase difference ϕ and path difference l is

$$\phi = \frac{2\pi l}{\lambda} = kl, \tag{1.5}$$

allows for the determination of the phase difference between the two scattered waves

$$\phi = \mathbf{Q}\cdot\mathbf{R}_{ba}. \tag{1.6}$$

The scattered wave as a function of scattering vector, the structure factor, $F(\mathbf{Q})$, is the coherent sum of the two scattered waves* :

$$F(\mathbf{Q}) \;=\; A\left[1 + \exp(\mathrm{i}\mathbf{Q}\cdot\mathbf{R}_{ba})\right]. \tag{1.7}$$

This can be extended to arbitrarily many particles:

$$F(\mathbf{Q}) \;=\; \sum_j \exp(\mathrm{i}\mathbf{Q}\cdot\mathbf{r}_j), \tag{1.8}$$

recognising that moving the origin is equivalent to a phase shift, and normalising by the intensity of the incident radiation. Recasting this equation as follows:

$$F(\mathbf{Q}) \;=\; \sum_j \exp(\mathrm{i}\mathbf{Q}\cdot\mathbf{r}_j) \;=\; \int \exp(\mathrm{i}\mathbf{Q}\cdot\mathbf{r})\rho(\mathbf{r})d\mathbf{r} \;=\; \mathcal{FT}[\rho(\mathbf{r})], \tag{1.9}$$

where $\rho(\mathbf{r}) = \sum_i \delta(\mathbf{r}-\mathbf{r}_i)$ is the density of scatterers, makes it clear that the scattered wave is the Fourier transform of the positions of the particles. Thus in theory a reverse Fourier transform of the scattered radiation will give $\rho(\mathbf{r})$ and hence the positions of the atoms. However, diffraction experiments only measure the amplitude of $F(\mathbf{Q})$, $I(\mathbf{Q})$:

$$I(\mathbf{Q}) = |F(\mathbf{Q})|^2 \;=\; \left|\sum_j \exp(\mathrm{i}\mathbf{Q}\cdot\mathbf{r}_j)\right|^2 \;=\; \sum_{j,k} \exp[\mathrm{i}\mathbf{Q}\cdot(\mathbf{r}_j-\mathbf{r}_k)]; \tag{1.10}$$

i.e. they are only sensitive to the vectors between atoms, rather than their absolute positions. The relationship between the PDFs and the scattered intensity can be seen by expressing $I(\mathbf{Q})$ as a Fourier transform and making use of the convolution theorem:

$$I(\mathbf{Q}) \;=\; |\mathcal{FT}[\rho(\mathbf{r})]|^2 \;=\; \mathcal{FT}[\rho(\mathbf{r})] \times \mathcal{FT}[\rho(-\mathbf{r})] \;=\; \mathcal{FT}[G(\mathbf{r})]; \tag{1.11}$$

*There is an unfortunate ambiguity in diffraction terminology. The structure factor, $F(\mathbf{Q})$ is used to refer to both the complex wave, and its squared modulus, $|F(\mathbf{Q})|^2$. This ambiguity is amplified as $F(\mathbf{Q})$ is used to refer to both meanings of structure factor. In this thesis I will be using the structure factor, $F(\mathbf{Q})$, to refer to the complex function, and the intensity, $I(\mathbf{Q})$, to refer to its squared modulus. This is in accordance with crystallographic but not total scattering conventions, which are in any case diverse [16, 17].

where $G(\mathbf{r}) = \rho(\mathbf{r}) * \rho(-\mathbf{r})$ is the three dimensional PDF (that is, the Patterson map).*

The distinction between average and local structure raised above can also be seen in the measured diffraction data and is best demonstrated by again taking advantage of the convolution theorem. A perfect crystal is the convolution of the lattice and the contents of the unit cell.

$$\rho_{\text{cryst}}(\mathbf{r}) = \sum_{U,V,W} \delta(\mathbf{r} - (U\mathbf{a} + V\mathbf{b} + W\mathbf{c})) * \rho_{\text{cell}}(\mathbf{r}), \tag{1.12}$$

where $\rho_{\text{cryst}}(\mathbf{r})$ is the density of scatterers within the entire crystal, $\mathbf{a}$,$\mathbf{b}$ and $\mathbf{c}$ are the basis vectors of the lattice (*i.e.* the unit cell axes) and $\rho_{\text{cell}}(\mathbf{r})$ the scatterer density within a unit cell. By the convolution theorem, therefore, the Fourier transform of the crystal structure (*i.e.* the scattered radiation) is:

$$\mathcal{FT}[\rho_{\text{cryst}(\mathbf{r})}] = \mathcal{FT}\left[\sum_{U,V,W} \delta(\mathbf{r} - (U\mathbf{a} + V\mathbf{b} + W\mathbf{c}))\right] \times \mathcal{FT}[\rho_{\text{cell}}(\mathbf{r})], \tag{1.13}$$

The Fourier transform of the lattice is simply the reciprocal lattice and so can be expressed as:

$$F(\mathbf{Q}) = \sum_{h,k,l} \delta(\mathbf{Q} - (h\mathbf{a}^* + k\mathbf{b}^* + l\mathbf{c}^*))] \times \sum_{j \in \text{cell}} \exp(\mathrm{i}\mathbf{Q} \cdot \mathbf{r}_j), \tag{1.14}$$

which reduces to

$$F(\mathbf{Q}_{h,k,l}) = \sum_{j} \exp(\mathrm{i}\mathbf{Q}_{h,k,l} \cdot \mathbf{r}_j) \tag{1.15}$$

where $\mathbf{Q}_{h,k,l}$ is a reciprocal lattice vector. A disordered crystal is no longer perfectly periodic so in addition to the periodic average structure a non-periodic deviation, $\Delta\rho(\mathbf{r})$, needs to be included:

$$\rho_{\text{cryst}}(\mathbf{r}) = \Delta\rho(\mathbf{r}) + \sum_{U,V,W} \delta(\mathbf{r} - (U\mathbf{a} + V\mathbf{b} + W\mathbf{c})) * \langle\rho(\mathbf{r})\rangle. \tag{1.16}$$

*The definition of $G(\mathbf{r})$ varies widely in the total scattering community, as there are a variety of possible choices of normalisations. This issue is discussed further in Chapter 2.

The observed scattering is therefore:

$$I(\mathbf{Q}) \;=\; |F(\mathbf{Q})|^2 \;=\; \left| \int \Delta\rho(\mathbf{r}) \mathrm{exp}(\mathrm{i}\mathbf{Q}\cdot\mathbf{r})\, \mathrm{d}\mathbf{r} + F(\mathbf{Q}_{h,k,l})_{\mathrm{av}} \right|^2 , \tag{1.17}$$

where $F(\mathbf{Q}_{h,k,l})_{\mathrm{av}}$ is the Bragg scattering from the average structure (*i.e.* the Fourier transform of the lattice with $\langle\rho(\mathbf{r})\rangle$). This expression can be expanded as follows

$$\begin{aligned} I(\mathbf{Q}) \;=\; \left| \int \Delta\rho(\mathbf{r}) \mathrm{exp}(\mathrm{i}\mathbf{Q}\cdot\mathbf{r})\, \mathrm{d}\mathbf{r} \right|^2 + |F(\mathbf{Q}_{h,k,l})_{\mathrm{av}}|^2 \\ + 2 \left| \int \Delta\rho(\mathbf{r}) \mathrm{exp}(\mathrm{i}\mathbf{Q}\cdot\mathbf{r})\, \mathrm{d}\mathbf{r} \times F(\mathbf{Q}_{h,k,l})_{\mathrm{av}} \right|^2 . \end{aligned} \tag{1.18}$$

Thus, noting that by definition $\Delta\rho(\mathbf{r})$ is non periodic and $\int \Delta\rho(\mathbf{r})\mathrm{d}\mathbf{r} \;=\; 0$, one can simplify 1.18 to the following expression

$$\begin{aligned} I(\mathbf{Q}) \;&=\; \left| \int \Delta\rho(\mathbf{r}) \mathrm{exp}(\mathrm{i}\mathbf{Q}\cdot\mathbf{r})\, \mathrm{d}\mathbf{r} \right|^2 + |F(\mathbf{Q}_{h,k,l})_{\mathrm{av}}|^2 , \\ &=\; \int \Delta\rho(\mathbf{r}_j)\Delta\rho(\mathbf{r}_k) \mathrm{exp}(\mathrm{i}\mathbf{Q}\cdot(\mathbf{r}_j - \mathbf{r}_k))\, \mathrm{d}\mathbf{r}_j \mathrm{d}\mathbf{r}_k + |F(\mathbf{Q}_{h,k,l})_{\mathrm{av}}|^2 , \\ &=\; \mathcal{FT}[\Delta\rho(\mathbf{r}) * \Delta\rho(-\mathbf{r})] + |F(\mathbf{Q}_{h,k,l})_{\mathrm{av}}|^2 . \end{aligned} \tag{1.19}$$

This makes clear that the diffraction data can be split into the sum of the Fourier transform of the difference pair distribution function, the diffuse scattering, and the Fourier transform of the periodic average structure, the Bragg peaks. The two together form what is called the 'total scattering'. In the above formalism I have discussed scattering in a very general fashion. I continue this discussion, elaborating in particular the experimental aspects of diffraction, in Chapter 2.

1.4 Types of disorder

But what kinds of disorder are possible? In this Section I will outline some broad categories of disorder, with a particular emphasis on how disorder manifests itself in framework materials. Framework materials are distinguished by having two or three dimensional connectivity through strong (*i.e.* primarily covalent) bonds. Their structures can therefore be represented as 'nets' consisting of 'nodes' joined by 'linkers' [18, 19]. Disorder in framework materials can classified under three headings: (i) compositional disorder, where a

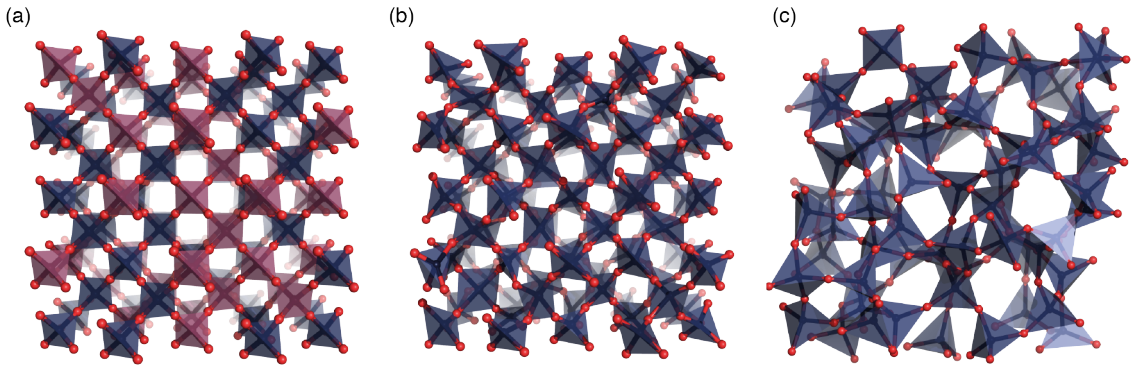

Figure 1.3: The types of framework disorder illustrated by cartoons of an SiO_2 tetrahedral network: (a) compositional disorder, (b) positional disorder and (c) topological disorder.

given average structure framework site is occupied by more than one species [Fig. 1.3(a)]; (ii) positional disorder, where framework units are displaced from their average structure position [Fig. 1.3(b)]; or topological disorder, where the framework topology itself is aperiodic and lacks long-range order, and so the material is amorphous [Fig. 1.3(c)].

1.4.1 Compositional disorder

A material has compositional disorder wherever a number of different species occupy the same average structure site and as a result, one very common cause of compositional disorder is nonstoichiometry. Even very small amounts of compositional disorder can introduce functional properties, such as the parts-per-million doping of hole or electron donors into silicon to produce the p- and n-type semiconductors that form the basis of modern electronics [20]. At higher dopant concentrations the interactions between the different components can no longer be neglected, and so non-stoichiometric materials are therefore a rich source of correlated structural disorder.

Nonstochiometry is not the only source of compositional disorder; as illustrated by the example from Section 1.2, which exhibits a range of compositional disorder despite their fixed AB stochiometry. The square AB lattice thus resembles a two-dimensional version of some of the earliest examples of correlated compositional disorder found in real materials, the binary alloys, of which Cu_3Au is a prototypical example [21, 22]. At very high temperatures the structure of Cu_3Au consists of a statistical distribution of Cu and Au atoms across a face-centered cubic (fcc) lattice [Fig. 1.4(a)]. Its average structure unit

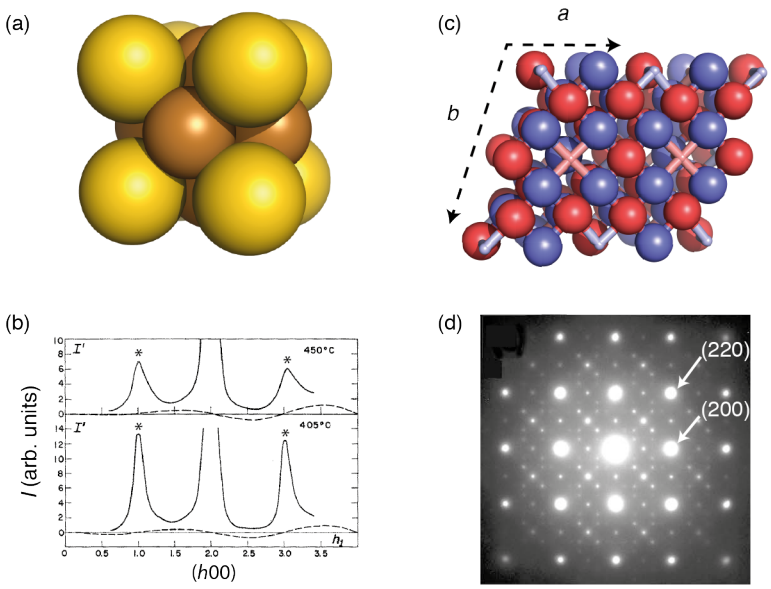

Figure 1.4: (a) Crystal structure of ordered Cu_3Au. Colour scheme: Cu, brown; Au, gold. (b) X-ray diffuse scattering just above the phase transition to the disordered cubic phase of Cu_3Au. Structured diffusing scattering around (100) and (300) positions (marked by *) is indicative of the correlated disorder within the material. Figure adapted from Ref. 23. (c) Crystal structure of ordered TiO. Colour scheme: Ti, blue, O, red, with vacancies shown as small light spheres. (d) An electron diffraction pattern of low-temperature monoclinic TiO (the crystal is heavily twinned). The bright diffraction peaks result from the small face-centered rock-salt unit cell, and the many weaker diffraction peaks result from the ordering of the vacancies. Figure adapted from Ref. 26.

cell therefore contains a single site, occupied by 0.75 Cu and 0.25 Au. On slow cooling Cu_3Au undergoes a phase transition to an ordered lower-symmetry, primitive structure, where the corner site of the face-centered unit cell is now fully occupied by Au and the other three sites are fully occupied by Cu. At intermediate temperatures the preference for Cu-Au contacts persists, and so despite the lack of long-range order, short-range structural correlations persist. These short-range correlations can be detected in the diffraction pattern as structured diffuse scattering [Fig. 1.4(b)] [22, 23]. Short-range order within alloys can have very important consequences for their properties, from the shape memory effect in $Ni_{50-x}Ti_{50+x}$ [24] to hydrogen storage in $LaNi_5$ [25].

Compositional disorder is just as common in oxide framework materials, as judicious cation doping allows for tuning of electron count, magnetism and strain [27]. The interactions of these compositional defects are implicated in a wide range of phenomena, from superconductivity [28] to colossal magnetoresistance [29, 30].

Vacancies

Instead of substituting a framework component for an equivalent component, compositional disorder can be introduced by removing components, thereby producing vacancies. Vacancies are ubiquitous, occurring even in very simple ionic structures such as the rock-salt M^{II} metal monoxides, especially those of the early transition metals, V, Ti and Nb [31]. These compounds, as well as being surprisingly nonstochiometric, *e.g.* "TiO" is stable from $Ti_{0.8}O$ to $TiO_{0.7}$ ($\equiv Ti_{1.4}O$), can incorporate large numbers of Schottky vacancies, *i.e.* missing oxide anion and metal cation pairs [31]. The vacancy distribution in the defect rock salt oxides is by no means necessarily random; and in fact they can form a large variety of correlated vacancy phases. The simplest is perhaps stoichiometric NbO, which forms an ordered structure analogous to that of Cu_3Au—both the Nb and O fcc sublattices have $\frac{1}{4}$ of their sites vacant, with the vacancies ordered along the $\langle 100 \rangle$ directions, just as for Au in Cu_3Au. The other defect rock salt materials form a much wider variety of complex phases, for example $Ti_{\frac{5}{6}}O_{\frac{5}{6}}$ forms phases ranging from a disordered high-temperature high-symmetry cubic phase to a low-symmetry, monoclinic, ordered phase [Fig. 1.4(c,d)]. In these metallic defective metal oxides the presence of vacancy ordering is a result of metal ion clustering due to *d*-orbital overlap. The correlation of defects controls therefore not just the distribution of atoms within these oxides, but also their volumes—the defective phases have smaller unit cells than the non-defective [32]—and their electronic conductivity [33]. Defect clustering due to metal-metal interactions are also important in nonmetallic defective oxides, *e.g.* the magnetism of $Fe_{1-x}O$ [34].

Vacancies can also be formed to compensate for aliovalent doping, as is found in the family of cation-stabilised defect zirconia phases [8]. The high temperature cubic fluorite structure adopted by pure ZrO_2 can be stabilised via doping with di- or trivalent cations, and the very high oxide defect concentrations that can be achieved cause this stabilised zirconia family to have amongst the highest solid oxide anion conductivities [8]. The most widely-used solid oxide conductor from this family is yttria–stabilised zirconia (YSZ, $Y_xZr_{1-x}O_{2-\frac{x}{2}}$), where the replacement of a Zr^{4+} ion with a Y^{3+} ion introduces half an O^{2-} vacancy. The movements of the oxide anions through YSZ are not independent of each other, and so the mechanism of ionic conductivity depends crucially on defect

interactions—in fact the maximum in O^{2-} diffusivity (at around $x = 0.18$) occurs due to the limitations imposed by defect trapping [35]. As a consequence, understanding the role of disorder is crucial to disentangling the properties of these low-barrier ionic-conductors [36].

Dynamic disorder

The defining characteristic of oxide ion conductors is that the vacancies/oxide ions move—that is, their disorder is dynamic, not static. The timescale over which disorder occurs is thus also crucial information for understanding disordered materials. In most materials compositional disorder can be thought of as essentially static, as diffusion through the material is for most materials very slow (*e.g.* the diffusion coefficient, D, of Cl^- in NaCl at 520 °C is $1.9 \times 10^{-12}\,cm^2\,s^{-1}$ [37]). This is approximation is clearly false for ionic conductors—in fact the motion can become so extensive that it can be considered liquid-like [8, 38], for example for Ag^+ in α-AgI at 250 °C $D = 2 \times 10^{-5}\,cm^2\,s^{-1}$ [39, 40], which compares to $D = 2.30 \times 10^{-5}\,cm^2\,s^{-1}$ for water at 25 °C [41]. Just as spatial information is encoded in the diffraction data as the variation in intensity with the scattering vector, $\mathbf{Q}$, so information about timescale is included in the modulation of intensity with the energy of the scattered radiation. As routine diffraction experiments, for both neutrons and X-rays, implicitly integrate over the energy range of scattered radiation, this information about timescales becomes obscured. It is possible in favourable circumstances to reconstruct this information from the energy integrated diffraction data [42], but techniques such as NMR [43], quasielastic neutron [39, 44, 45], inelastic neutron [45, 46] and inelastic X-ray [47, 48] spectroscopy provide much more direct access to this dynamical information.

1.4.2 Positional disorder

Positional disorder occurs in every real material, as the ordinary thermally-activated vibrational motion of atoms moves them away from their average sites. In most cases, this disorder can be treated as the result of uncorrelated harmonic motion around the average site and so can be accounted for by the formalism of atomic displacement parameters (ADPs) [15]. In framework materials the motion of atoms is strongly coupled by the bonds between them. The average picture of positional disorder provided by the ADPs

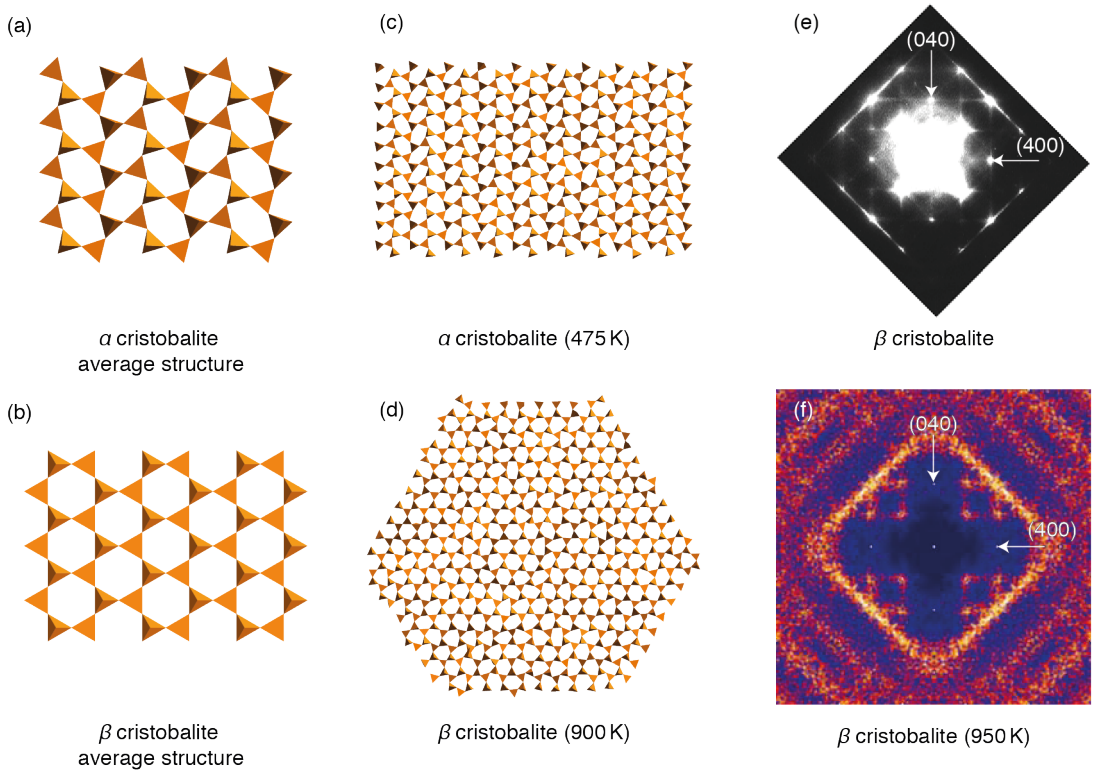

Figure 1.5: Cristobalite undergoes a phase transition at around 590 K between a low-temperature α phase and a high temperature β phase. (a) Average structure of α cristobalite, showing the bent Si–O–Si bond angles. (b) Average structure of β cristobalite, showing an apparent Si–O–Si bond angle of 180 ° [49]. (c) A model of α cristobalite refined using RMC against neutron total scattering data measured at 490 K. (d) A model of β cristobalite refined using RMC against neutron total scattering data measured at 900 K. From this model it is apparent that the true Si–O–Si bond angles remain bent, as in the low-temperature phase. (e) Electron diffraction data of the (001) plane of β cristobalite. Pronounced diffuse scattering is visible, indicating the presence of correlated disorder. (f) Calculated electron diffraction data based on RMC models of β cristobalite are in good agreement with the experimental diffuse scattering measurements. Figure adapted from [50].

may therefore only provide a partial picture of the behaviour of the framework.

The correlated harmonic vibrations of a crystal are the phonons, and these collective excitations are at the heart of many physical phenomena, from soft mode driven phase transitions [51] to negative thermal expansion [52]. One family of materials where phonons, and dynamic disorder in general, play an important role are the polymorphs of silica (SiO_2) [Fig. 1.5]. At high temperatures the silica polymorphs adopt high symmetry structures (known as 'β' phases), for example β-cristobalite is cubic [53] and β-quartz hexagonal [54], but on cooling, these materials undergo what appear to be displacive phase transitions to lower symmetry 'α' phases. In the average structure of the β phases, the Si—O—Si

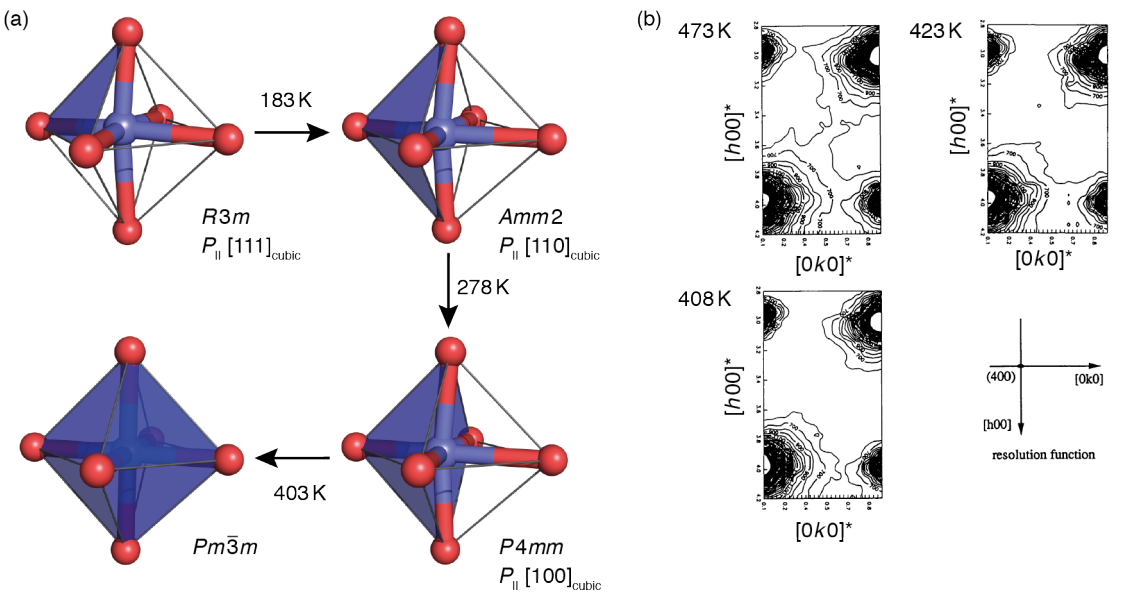

Figure 1.6: (a) The TiO_6 coordination octahedron for each of the four phases of $BaTiO_3$. The faces towards which the Ti^{4+} cation is displaced in each phase are highlighted in blue [56, 57]. (b) X-ray single crystal diffuse scattering measurement of high temperature cubic $BaTiO_3$, in the (300) plane, highlighting the existence of correlated disorder even in the cubic paraelectric phase of $BaTiO_3$. Figure adapted from Ref. 58.

bonds are linear and the Si—O bond length is shorter than found the α phases [50, 55]. The diffraction patterns of the β phases show pronounced diffuse scattering, implying the presence of correlated disorder in these systems [Fig. 1.5(e,f)]. Total scattering analysis of these data was able to show that the local structures of the β phases are less symmetric than implied by the average structure and for the β phases, just as in the α phases, the Si—O bond length expands on heating and the Si—O—Si bond angle remains bent. The apparent high symmetry of the β phases thus results from averaging over many different dynamically fluctuating O positions [50, 55].

Correlated positional disorder is also responsible for the function of many important technological materials, including the very widely used ferroelectric $BaTiO_3$ [51]. In the low-temperature, $R3m$, phase of $BaTiO_3$, the Ti atoms are displaced away from the centre of their oxygen coordination octahedra towards the faces in the $[111]_{\text{cubic}}$ direction [Fig. 1.6(a)] [57]. As the displacements are all in the same direction, the crystal develops a net electrical polarisation, which can be switched by applying a suitably strong electric field, *i.e.* it is a ferroelectric. On heating, $BaTiO_3$ undergoes three main phase transitions:

first, from the low-temperature $R3m$ phase, to an orthorhombic phase ($Amm2$) where the Ti atom appears to displace towards the edge of the octahedron, in the $[110]_{\text{cubic}}$ direction; then to a $P4mm$ tetragonal phase where Ti displaces along the $[100]_{\text{cubic}}$ towards corner of the octahedron; before finally transitioning to the cubic $Pm\bar{3}m$ aristotype structure, where the Ti rests in the centre of the octahedron [59, 60] [Fig. 1.6(a)]. Just as in quartz and cristobalite, these phase transitions appear from an average structure perspective to be displacive transitions, but again, the presence of pronounced diffuse scattering indicates the picture is more complex [Fig. 1.6(b)]. Refinement of the local structure revealed that the displacement of the Ti atom along the $[111]_{\text{cubic}}$ direction seen in the lowest temperature ($R3m$) phase persists throughout. The series of phase transitions can then be thought of as disordering of the Ti displacement over one ($R3m$), two ($Amm2$), four ($P4mm$) or eight ($Pm\bar{3}m$) directions [57, 60] [Fig. 1.6(a)].

Positional disorder can also give rise to more exotic correlated states that rely on the absence of long-range order. One example of this would be the so-called 'charge ices',

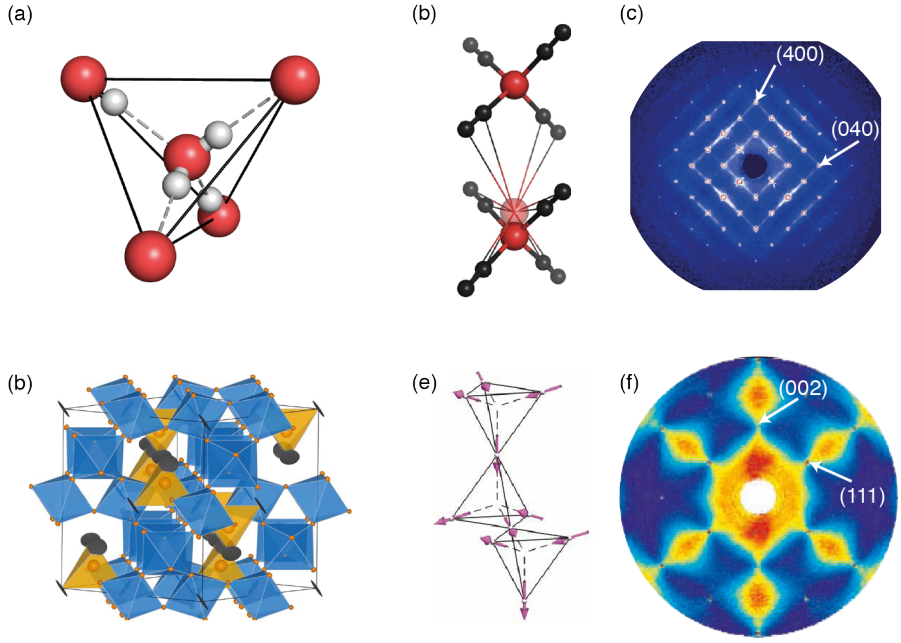

Figure 1.7: The 2-in 2-out ice rules derived for hydrogen bonding in water ice (a) [61] provide for a remarkable variety of correlated states through solid state science, from the charge ices (b) $Cd(CN)_2$ [62] and (d) $Bi_2Ti_2O_7$ [63] to the magnetic spin ice (e) $Ho_2Ti_2O_7$ [9]. The strong correlations throughout the system in turn lead to pronounced diffuse scattering, as seen for $Cd(CN)_2$ in the $(hk0)$ plane of single crystal XRD data and for $Ho_2Ti_2O_7$ in the $(hh0)$ plane of polarised single crystal neutron diffraction data. Panels (b,c) adapted from Ref. 62, (d) taken from Ref. 63 and (e,f) from Ref. 64.

for example $Cd(CN)_2$ [62] and $Bi_2Ti_2O_7$ [63] [Fig. 1.7]. In these materials the displacements of the Cd/Bi atoms away from their high-symmetry average sites are both locally anisotropic and very highly correlated. In fact, considering just the Cd/Bi sublattices, the displacements map directly onto the 2-in 2-out 'ice rules' that regulate the H atom positions in ordinary water Ice Ih [61] and the orientation of the magnetic moment in the spin ices, $Ho_2Ti_2O_7$ and $Dy_2Ti_2O_7$ [9].

Coupling positional and compositional disorder

Although in the above sections I have discussed positional and compositional disorder as separate phenomena, they are very often intimately connected. Compositional disorder can lead to point defects which, in turn, can be the source of local fields, including strain, coulombic, dipolar and magnetic fields. These local fields can couple with the lattice to produce structural relaxation also hence induce positional disorder. The coupling between positional and compositional disorder can thus generate collective states that produce functional properties. For example, in the relaxor ferroelectric PMN ($PbMg_{\frac{1}{3}}Nb_{\frac{2}{3}}O_3$) the local strains produced by the compositional disorder stabilise the presence of the polar nanoregions [65]. It is the rapid switching of these nanoscale ferroelectric regions that gives rise to the giant electrostriction of PMN. In this way, manipulation of the composition of frameworks can also provide control over the nanoscale displacements within a system.

Orientational disorder

In some frameworks it is natural to think of the constituent elements as units larger than single atoms, such as SiO_4 tetrahedra in silicates. In these materials the positional degrees of freedom can be split into distortions of the unit, *e.g.* for SiO_4 bending or stretching of the tetrahedron, and rigid motion of the unit itself [66]. The degrees of freedom for these rigid units now includes rotations as well as simple translations and so their orientations become important. Orientational disorder is the logical extension of positional disorder to materials containing 'rigid' units.

The positional disorder in β cristobalite and β quartz described in Section 1.4.2 can thus also be thought of as examples of correlated orientational disorder of SiO_4 tetrahedra. In addition to the disorder of correlated cation polyhedra, a second common class of

frameworks which display orientational disorder are those with porosity. In porous frameworks, the typically weak interactions between guest and framework leave confined guests free to rotate. They therefore exhibit a wide variety of disordered behaviour [67, 68].

Orientational disorder is also very common in salts with molecular anions, *e.g.* SO_4^{2-}, NO_2^- or CO_3^{2-}, indeed, the high-temperature phases of many of salts show complete anion disorder [69–71]. The disorder can be coupled to the properties of the material, including the mechanical properties [72] or the ionic conductivity [73], *e.g.* the mixed metal alkali metal sulfates, $LiMSO_4$ (M = alkali metal), where the large high temperature Li^+ conductivity has been linked to the orientational disorder of the sulfate anion through a 'paddlewheel mechanism' [69, 73, 74]. The coupling between the orientations of molecules in these salts can be relatively strong, and so the order/disorder phase transitions tend to occur at correspondingly higher temperatures than the equivalent transitions in magnetic systems. This means exploration of many unusual phases that are usually studied through magnetism can become more tractable; for example $K_2Ba(NO_2)_4$ is an analogue of the frustrated 2D Ising kagome antiferromagnet [71] and $K(CN)_{1-x}Br_x$ is a quadrupolar glass on the fcc lattice [75, 76].

Molecular materials can show a very wide variety of orientational disorder, up to an including crystalising in structures without any orientational order. These so-called 'plastic crystals', usually formed from relatively isotropic molecules, despite lacking all orientational order still possess well-defined long-range translational order [77, 78]. But what happens where the material possesses neither long-range translational nor long-range orientational order?

1.4.3 Topological disorder

Materials which entirely lack long-range order (whether translational or orientational) are amorphous. Amorphous materials, as a category of exclusion rather than inclusion, have very few commonalities in their chemistries. Some of the most important classes of amorphous materials are: organics, including pharmaceuticals [79] and semiconductors [80]; ionic materials, common in the natural world as both biogenic [5, 7], terrestrial [81] and extraterrestrial minerals [6]; metallic glasses [82, 83] and framework materials, usually comprised of p-block elements, of which the most important groups are the oxide glasses

[84], chalcogenide glasses [85] and amorphous tetrahedral semiconductors [86].

One feature common to all amorphous materials is that they are metastable, kinetic phases*. The synthesis of amorphous materials is therefore constrained by the need to prepare them more rapidly than the time needed to form the thermodynamic crystalline phase. Some of the most important methods are vapour deposition processes, used for the synthesis of *e.g.* *a*-Si; rapid precipitation from solution, *e.g.* amorphous salts [89] and perhaps the most prototypical, rapid cooling from the melt. The range of amorphous materials that can be prepared is therefore limited both by the speed with which these processes can be carried out and their 'glass-forming ability', that is, how slowly the thermodynamic crystalline phases form. Extension of this range can be correspondingly carried out either by enhancing the glass-forming ability, for example through producing complex multicomponent mixtures to frustrate crystallisation [82], or by developing more sophisticated routes to produce faster cooling rates [Fig. 1.8(a,b)] [83].

The earliest uses of amorphous materials, and indeed the most widespread current uses, arise from the ease of forming homogenous objects with a wide variety of shapes [Fig. 1.8(c)]. Nature has also taken advantage of this [Fig. 1.8(d)], for example, amorphous calcium carbonate is used as an intermediate in the formation of complexly-structured shells [5]. The homogeneity possible in amorphous materials is responsible for the utility of silicate glass as a transparent material, as by eliminating the boundaries that scatter light, large bulk transparent objects can be formed, *e.g.* windows or long, low loss optical fibres [92]. Grain boundaries are also a critical factor in the mechanical properties of materials, and so by engineering their absence in metallic glasses, remarkable strengths and toughnesses can be obtained [93, 94]. The importance of homogeneity of surface coverage is also paramount for (opto)electronic thin film applications [95].

The lack of long-range order in amorphous materials has implications for the properties of the materials themselves: unlike crystalline Si, which possesses an indirect band gap, *a*-Si has a direct band gap, drastically increasing its optical absorption, thus permitting much thinner Si films to be used in solar cells [96]. This absence of long-range order tends to increase the electrical resistivity of a material, through Anderson localisation of

*Recent theoretical work has predicted a number of hypothetical phases that may be amorphous at their thermodynamic minimum [87, 88].

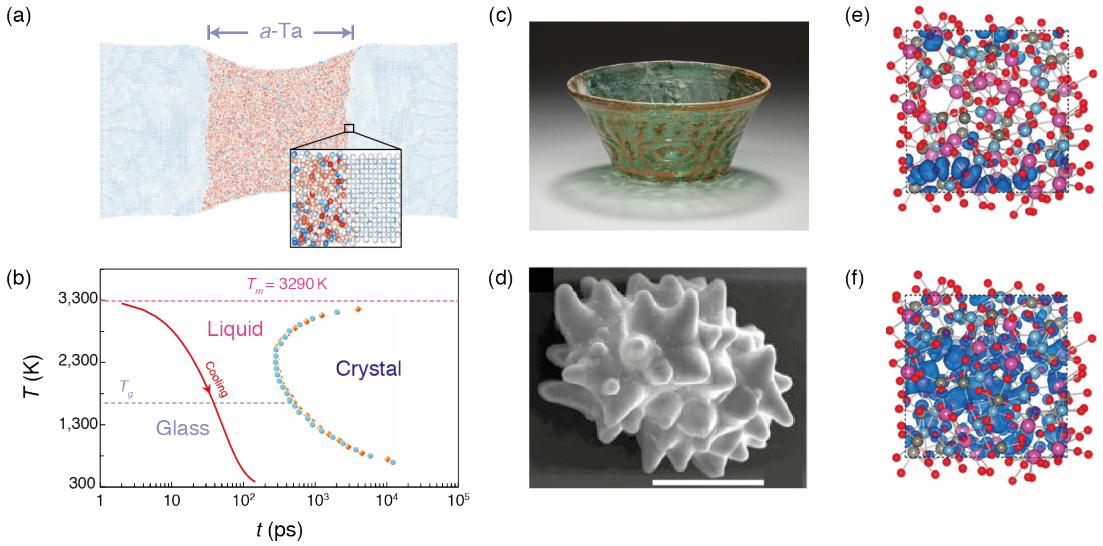

Figure 1.8: (a) A section of the molecular dynamics model of a nanowire of amorphous Ta 30 nm in length. The atoms are coloured by the degree of bond-orientational order, with blue indicating more order and red indicating less. The inset highlights the structure of the interface between *a*- and bcc-Ta. (b) A time–temperature–transformation diagram derived from isothermal MD simulations, showing the approximate formation conditions of *a*-Ta. The crystallisation conditions are estimated by the crystal growth rates of the {100} (cyan circles) and {110} (orange squares) planes. The red solid line indicates the temperature evolution of the narrow nanowire section, showing the rapid cooling rate of 10^{-14} Ks^{-1}. (c) A mould-blown glass bowl, probably 11th Century Iranian, in the Nasli M. Heeramaneck Collection at the Los Angeles County Museum of Art. (d) A scanning electromicrograph of a cystolith from the leaves of *Ficus microcarpa* (Chinese Banyan), constructed from stabilised *a*-$CaCO_3$. (e,f) Band-decomposed charge density isosurfaces of the band edge states in amorphous $InAlZnO_4$. (e) The valence band maximum (VBM, highest occupied state) and (f) the conduction band minimum (CBM, lowest unoccupied state). Despite the structural disorder the CBM shows extensive delocalisation, responsible for the high conductivity of this material. The origins of the panels are as follows: (a,b) from Ref. 83, (c) from Ref. 90, (d) from Ref. 7, (e,f) from Ref. 91.

conduction band electrons [97], leading to the widespread use of metallic glasses in low loss electrical transformers [98].

The relationship between disorder and responsiveness also holds for amorphous materials. This is perhaps best exemplified by the chalcogenide glasses. These materials show a wide variety of photoresponsive behaviour, from photoconductivity in *a*-Se [99], later exploited in photocopying [100]; to the reversible photoinduced amorphous-crystalline transitions in GST ($Sb_2Te_3(GeTe)_x$) and related glasses used to store data in CDs and DVDs [85]. These amorphous-crystal transitions can also be triggered by electrical stimuli, and this ability to alter electrical conductivity through electrical pulses has been exploited for use in non-volatile RAM memory [4]. Disorder can also confer superior properties to that of the related crystalline phases; for example, the transparent conducting oxide

$InGaZnO_4$ shows enhanced conductivity over the related crystalline phases, with electron mobilities $>10\,cm^2\,V^{-1}\,s^{-1}$ [101, 102] [Fig. 1.8(e,f)]. The role that disorder plays in many of these properties is still not fully understood [91, 102].

1.5 Making models of disordered materials

One of the outstanding challenges in studying disordered materials is the difficulty of deriving meaningful atomistic models of their structures, whether experimentally- or computationally-driven. Because of the lack of perfect periodic long-range order in disordered materials, modelling their structures requires constructing atomistic configurations of sufficient size to account for the length scale of the disorder. As correlations can occur over nanometres, this imposes significant additional computational costs on quantum mechanical calculations. Much theoretical modelling of disordered materials therefore makes use of simplified potentials that attempt to capture the dominant interactions within a system while minimising computational expense. This lack of long-range order in the disorder also means many of the powerful tools of conventional crystallography are of restricted utility. Despite this, diffraction data, due to their direct relationship to the PDFs, are still our most reliable experimental guide for producing atomistic models. The technical difficulties of reliable collection of and quantitative fitting to three-dimensional total scattering data have meant that the overwhelming majority of studies have up to this point focussed on fitting one-dimensional powder data. As amorphous materials are isotropic, their diffraction data are unavoidably one-dimensional.

Methods for producing atomistic models of disordered materials can be broadly classified into the so-called "small box" and "big box" approaches. These approaches are distinguished primarily by the size of the model used: small box models typically consist of only a few unit cells, whereas big box models are ordinarily hundreds or thousands of unit cells in size.

1.5.1 Small box modelling

Small box modelling aims to capture the local structure of the disordered material in a small, periodic model. The small size of the resultant model means that fitting to the experimental data using a rapid least-squares "Rietveld-like" algorithm is computationally

tractable. Any small periodic model that reflects the local structure of a material containing correlated disorder, will of course not accurately reflect its average structure. Small box models are therefore ordinarily only fitted to real-space experimental data (*i.e.* to the PDF), as the discrepancies will be more prominent at higher r, and so can be minimised by restricting the range over which the data are fitted.

The small box approach has been most prominently implemented in the PDFGui suite of programs [103], and has been successfully applied to a wide range of problems, especially to correlated disorder in functional oxides [57, 104, 105]. Small box models struggle to deal with situations where the interactions between long-range and short-range order are important—for example systems with anisotropic correlation lengths [106]. A further limitation is the need to choose a particular local structural model before beginning the refinement. This utility of these models is also limited for amorphous materials, where the assumption that local structure can be modelled by a periodic model cannot be safely made.

1.5.2 Big box modelling

In contrast, "big box" approaches try to unify the local and average structures, by using a "supercell" larger than the correlation length of the disorder in the material. This larger supercell can thus account for the local distortions while also conforming to the average structure. The methods for generating big box models can be broadly split into two paradigms: interaction-driven, *e.g.* direct Monte Carlo, and data-driven, *e.g.* reverse Monte Carlo (RMC).

Direct Monte Carlo

The primary approach for generating realistic atomistic configurations with interaction based modelling are direct Monte Carlo simulations, either using 'bespoke' software or through packages such as DISCUS [107]. First model of the interactions in the material and an initial set of coupling parameters are chosen, then the simulation is minimised. The calculated diffraction data from the minimised model are then compared to the experimental data, and from this a new and improved set of parameters chosen. By iterating this process, a set of parameters that reproduce the experimentally observed diffraction data

can be obtained. This directly yields information about the driving forces determining disorder in the system and has been successfully used to understand the correlated disorder in materials as diverse as molecular organics [108], relaxor ferroelectrics [65] and spin ices [109]. The direct Monte Carlo approach is currently the most widely-used method for the analysis of three-dimensional diffraction data, as it minimises the still substantial computational expense of calculating the large three-dimensional diffraction data set. The major disadvantage of this approach is that assumptions need to made about the interaction model and potentials within a system.

Reverse Monte Carlo

In many cases, especially for new materials, the interactions within a material are unknown, however. In these situations, a fruitful approach is to instead fit the model directly to the data—the RMC approach [110, 111]. RMC is conceptually simple: whereas direct Monte Carlo aims to minimise the energy of a model, RMC aims to minimise the discrepancy between the calculated and experimental data. This is done by carrying out a series of small moves, ordinarily thousands of proposed moves per atom, and accepting or rejecting them according to the Metropolis criterion [110, 111]. This stochastic element means that RMC refinement therefore produces the most disordered possible model consistent with the experimental data. As there is no need to include information about either the expected structural features or interactions, RMC allows us to verify (or falsify) our assumptions about the structure of a material. Equally, the presence of disorder in an RMC configuration is not evidence of that disorder existing in a real material. The potential for entropic ordering (or order-by-disorder) should also be borne in mind [112]. This data-driven paradigm is therefore very attractive from a theoretical viewpoint.

A further advantage of the RMC approach is its flexibility. Although RMC has historically been mainly applied to fitting total scattering diffraction data, due to the ease of calculating the PDFs, it can be extended to include any experimental data that are computationally accessible, for example EXAFS [113]. The refinement can also be augmented by the inclusion of restraints, either purely structural (*e.g.* coordination constraints or distance windows) or those based on interatomic potentials [111, 114]. Additionally, although its name implies the use of the Monte Carlo algorithm, any global optimisation

algorithm could in theory be employed to fit the configuration to data, provided it is able to generate the correct equilibrium distribution. This algorithmic flexibility also extends to the types of move: there is no *a priori* reason to prefer one kind of move to another, provided it obeys the balance condition [115].

Empirical potential structure refinement

A conceptually different approach for producing 'big box' models consistent with total scattering data emerges from the relationship between the pairwise correlations and the pairwise potentials [116]. Empirical Potential Structure Refinement (EPSR) is an approach that relies on pairwise interatomic potentials to constrain the range of structural solutions. It does this in a conceptually novel way, however, as instead of simply applying potentials to an RMC refinement (*e.g.* as implemented in RMCProfile), the potentials are themselves refined against the diffraction data, with the moves consisting of molecular dynamics type adjustments of all the atom positions and velocities. The use of potentials provides three principal advantages for EPSR over the ordinary RMC approach: firstly and most straightforwardly, the use of potentials introduces chemical information into the refinement; secondly, the potentials are differentiable and so EPSR can make use of molecular-dynamics-like whole configurational moves, allowing for faster convergence; and finally, as every atom of a given type will have the same potential, the EPSR algorithm has less of a tendency towards the overly disordered configurations generated by RMC. The choice of potential will therefore to a large extent determine the outcome of the refinement in a non-trivial fashion, meaning interpretation of the resultant configuration is significantly more complex than for an RMC configuration.

1.5.3 Limits of pair distribution functions

As derived in Section 1.3, the diffraction data are simply the Fourier transform of the pair correlations, and so do not contain direct information about higher order correlation functions. Considered in the context of crystallography, this may seem counterintuitive, as a crystal structure of a material determines not only its pair correlations but also the higher order correlation functions, and the crystal structure can be determined using diffraction data alone. That this seems counterintuitive at all derives from the success of crystallog-

raphy in converting pair-correlation information into atomistic models—that is, in solving the phase problem [15]. Nevertheless, even for fully ordered materials, non-trivially equivalent structures exist which would produce identical diffraction data, so-called 'homometric' structures [117]. The rarity of these homometric structures is due to the powerful constraints that long-range periodic order places on diffraction data. When these constraints are relaxed the number of homometric structures can dramatically increase, and the amount of structural information about higher-order correlation functions that can be determined through direct fitting of the diffraction data correspondingly decreases.

The most extreme example of this underdetermination of structure occurs where there are no pair correlations at all; as in the random model described in Section 1.2 and shown in Figs. 1.1(a) and 1.9(a) [118]. It is possible to introduce strong third-order correlations into this model without altering the PDFs at all [Fig. 1.9(b,d)]. Thus, even though the model is no longer random, the diffuse scattering is still unstructured. This information about higher order structural correlation would therefore be completely missed by an analysis that only used diffraction data. For disordered crystals, the presence of translational periodicity can provide a sufficient constraint on the potential models such that some information about the higher order correlations can be deduced from diffraction data. For materials without long-range order, this problem can be much more severe, even pathological.

1.5.4 Making models of amorphous materials

Determining the structures of amorphous materials has been recognised as a challenge for almost as long as X-ray diffraction has existed [119, 120]. Initial speculation on the structures of amorphous materials (and liquids) relied heavily on comparison with the relevant crystalline phases [121, 122]. In particular, these comparisons imply that the structure of amorphous materials can be represented by the crystalline structure with a finite correlation length or domain size [81]. These models can prove very useful for understanding the general structural features of amorphous materials [81], but often the derived domain size is on the order of the length of a single unit cell. In this case much of the structure is determine by the surfaces of the domains, which will form a substantial fraction of the material. These questions become particularly acute for amorphous frameworks materials,

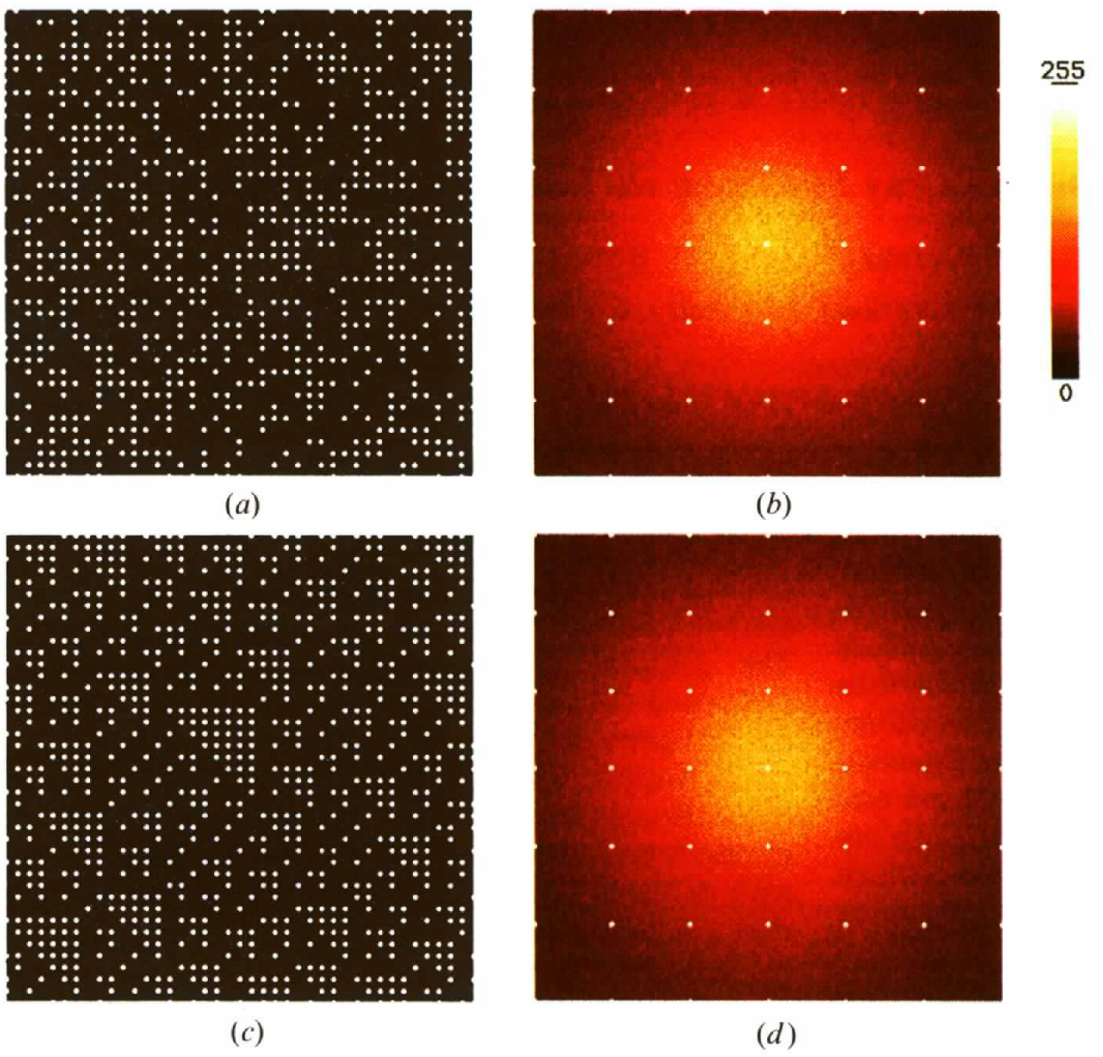

Figure 1.9: An extension of the square lattice model shown in Fig. 1.1 to include three body correlations. Neither (a) nor (c) have significant two-body correlations, and so the calculated single crystal diffraction data contain no structured diffuse scattering (b,d). The second configuration, (c), does have large three-body correlations, visible in the configuration itself but not the calculated single crystal diffraction data (d), demonstrating that for materials with no pair correlations, the higher order correlations are completely underdetermined by diffraction data. Figure taken from Ref. 118.

of which the archetypes are amorphous SiO_2 and Si, which are experimentally known to have very low concentrations of coordinative defects [123, 124].

The first convincing alternative to the nanocrystallite model was articulated by Zachariasen [125]* who suggested that amorphous frameworks need not consist of an agglomeration of tiny crystallites, but could instead by represented as a continuous random net-

*Rosenhain also, independently devised an analogous model of amorphous materials, but this was not recognised at the time [126].

work (CRN) [Fig. 1.10(a)]. The question of whether this hypothetical CRN model could properly account for the structures of amorphous frameworks was first answered through directly building physical models. These models extended earlier work on random sphere packing [127] and comprised rigid units assembled into a network in as random a fashion as the experimenter could manage [Fig. 1.10(b)] [128, 129]. The laborious nature of this approach and the limitations associated with the physical properties of the system (the stiffness of the units and gravity both influence the resulting experimental model) and the worries about experimenter bias meant that this approach has now been almost completely replaced by computer modelling*.

Computer modelling of amorphous materials began as a tool to relax the configurations generated through physical modelling to minimise artefacts due to the physical nature of the model [129], but computers very rapidly became modelling tools in their own right. The need to use large model sizes (hundreds of atoms at the minimum) has meant that it is only recently that models of amorphous materials generated through *ab-initio* methods have been possible, and these have focussed on amorphous materials that can be produced exceptionally rapidly [4, 91]. Even with the use of reasonable empirical potentials (*e.g.* the Stillinger-Weber [132] or Tersoff [133] potentials) producing equilibrated structures of amorphous frameworks has proved a tricky challenge. The Wooten-Winer-Weaire (WWW) algorithm, also known as the *sillium* method, has been a phenomenally successful approach, generating configurations of *a*-Si that are widely regarded as the benchmark of

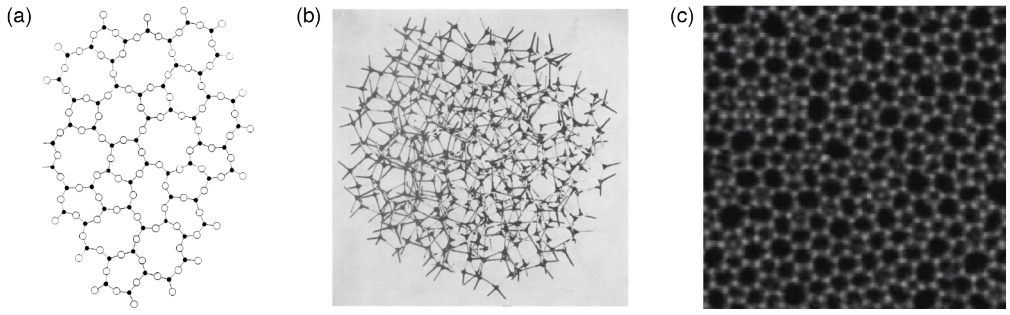

Figure 1.10: (a) The original Zachariasen sketch of a 2D CRN. (b) A photograph of a physical model of *a*-Si. (c) STM image of a silica bilayer, showing a close resemblance to the Zachariasen hypothetical CRN. The bright spots are the Si atoms. Figure adapted from Refs. 125, 128, 131, respectively.

*A recent ingenious study using M&Ms as a physical model for studying the random packing of ellipsoids is an interesting exception [130].

quality [134–137]. The crucial step in this algorithm is use of an explicit bonding list with a bond-switching move in the Monte Carlo minimisation, which ensures that the correct 4-fold coordination is maintained throughout. The signature success of the WWW model is the ease of generating large (up to 10000 atom) configurations in concordance with experimental evidence, including crucially both structural (*i.e.* total scattering) evidence and the electronic properties, in particular an electronic density of states containing a 'clean' band gap [136].

The high quality of the WWW model means that it has been used as a foundation on which to build realistic models of other tetrahedral CRNs, including SiO_2 and amorphous MOFs [138, 139]. This approach, of using one CRN as a base to generate sensible models of other CRNs has been generalised into a class of 'connectivity transformations' that can be used to convert a CRN of a given connectivity and local geometry into a variety of CRNs with different topologies [140]. Although connectivity transformations can produce a wide variety of local geometries , they can also introduce unwanted constraints into the higher order correlation functions, for example, restricting the possible ring statistic distributions.

The methods of model building described above require either the assumption of explicit geometry—as is the case for physical model building—or some knowledge of the interactions within a material. In many cases, especially for new materials, these assumptions cannot be safely made. This is highlighted by *a*-Si: the liquid state has a very different structure to the amorphous state [141, 142], and thus most widely used potentials used to model the liquid and crystalline states of Si produce models of the amorphous state which are much too liquid–like [143]. The capability to derive realistic structural models of amorphous materials from experimental diffraction data is therefore extremely desirable. The RMC approach, as a data-driven approach that does not rely on an average structural model offers a promising pathway to this goal.

RMC and amorphous materials

The RMC method originated as a technique to model structures of non-crystalline materials [110]. RMC has had some notable successes, particularly for systems that can be described by pair potentials, such as liquid noble gases [110] or metallic glasses [144], but

despite these successes, it became clear that simply fitting a random atomistic starting model to total scattering data is not appropriate for more complex materials [145]. This failure comes about not only because the pair distribution function does not directly contain information on higher-order correlation functions [Section 1.3] [118, 146], but also because RMC tends to generate the most disordered configuration consistent with the data, minimising still further the importance of the higher order correlation functions.

This deficiency was demonstrated most dramatically for the case of *a*-Si—the simplest amorphous material for which higher order correlation functions play a very important structural role. Naïvely applying the RMC method to fit a model to total scattering data, without including any other information or constraints, produces models that are deeply physically unrealistic: both inconsistent with other experimental measurements and also containing features that are extremely high in energy [145, 147] [Fig. 1.11]. Comparison of the bond angle distribution for RMC and WWW models of amorphous silicon demonstrates where naïve RMC fails: the bond angle distribution contains a much broader peak at the tetrahedral angle than the WWW model, and there is an additional peak centred at 60° [Fig. 1.11(c)]. This peak corresponds to the formation of Si_3 triangles, features essentially unknown in neutral Si chemistry. The model also has an unfeasibly wide range of coordination environments, as demonstrated by extreme breadth of the coordination number distribution, which even contains zero- and nine-coordinate silicon atoms.

If we are to use RMC to generate data-driven models of amorphous materials, then this failure of RMC needs to be addressed. Responses have come in a number of forms:

First, one can eliminate features known to be unchemical (*e.g.* Si_3 triangles, unphysical coordination numbers), by introducing constraints that penalise their presence in the configuration [147, 149]. Additional care is needed for the analysis of the resultant configurations, as many structural features are present simply because they have been included as prior constraints.

Second, one can attempt to create more realistic models by including information about the chemical energetics. The need to carry out a very large number of moves to produce a refined RMC configuration has confined the use of quantum chemical calculations in conjunction with RMC to methods where RMC-refined configurations are computationally

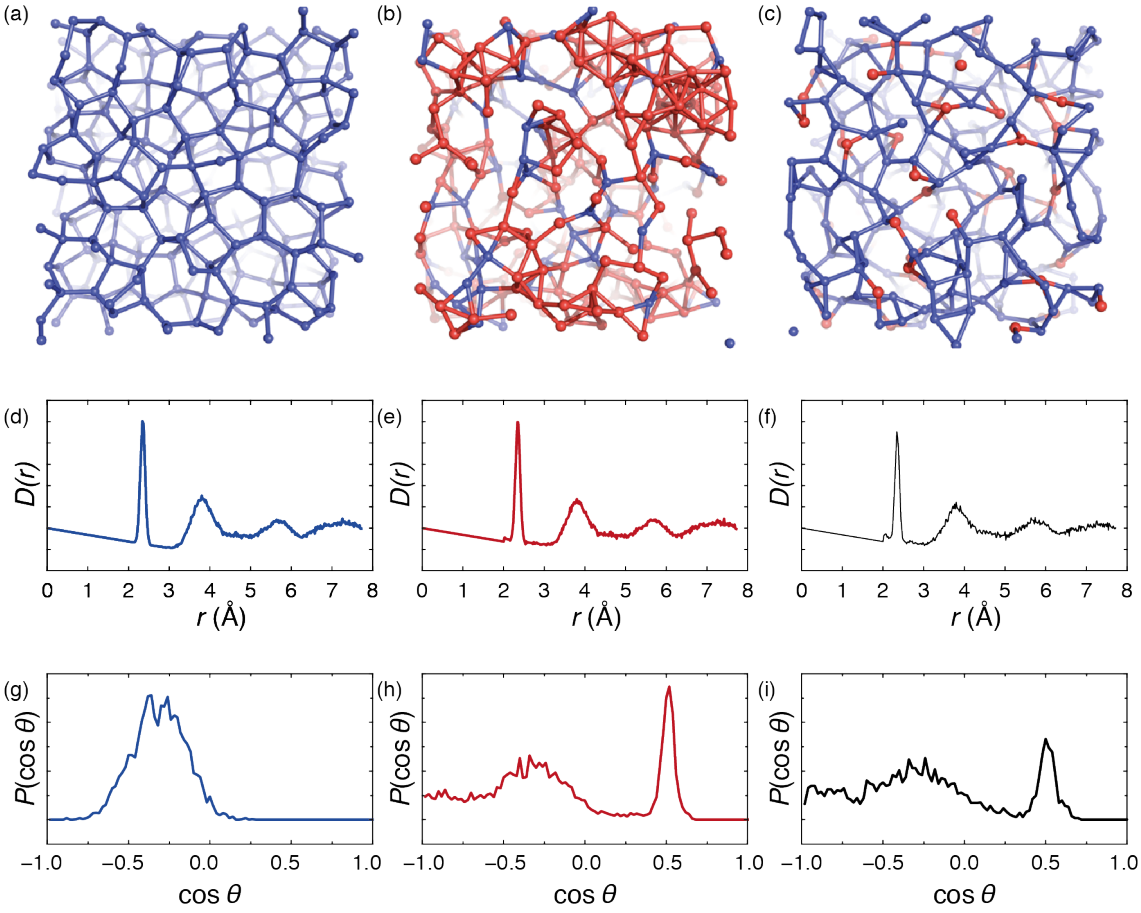

Figure 1.11: (a-c) Sections through three different models of *a*-Si with near equivalent pair distribution functions: (a) a high quality model generated using the WWW method [134], (b) a model generated by RMC refinement against PDF data, (c) a model generated RMC refinement against PDF data making use of in addition the INVERT PDF similarity constraint [148]. Four coordinate atoms are coloured blue, other coordination numbers are shown in red. (d-f) All three models show near equivalent PDFs despite their divergent structures. (g-i) The bond-angle distributions for the three models highlight the structural differences. (g) The WWW model shows a single peak centred at the tetrahedral angle, $\cos(\theta) = -\frac{1}{3}$. (h) For the RMC only model, the tetrahedral peak is much broader, and there is in addition a sharp peak at $\cos(\theta) = 0.5$ corresponding to the formation of Si_3 triangles. (i) The INVERT similarity constraint reduces the intensity of the peak at $\cos(\theta) = 0.5$ [148].

relaxed (or vice-versa) [150]. The use of simple, classical potentials has been successfully integrated into the RMC algorithm for amorphous tetrahedral semiconductors [114]. Parametrising these potentials still necessitates making assumptions about the chemical environments of the atoms in the configuration, and in many practical forms the potentials used resemble those where the local geometry has been assumed [132, 133].

Finally, one could include more data! Spectroscopic techniques in particular, can be very sensitive to the local geometry of atoms and therefore would provide important in-

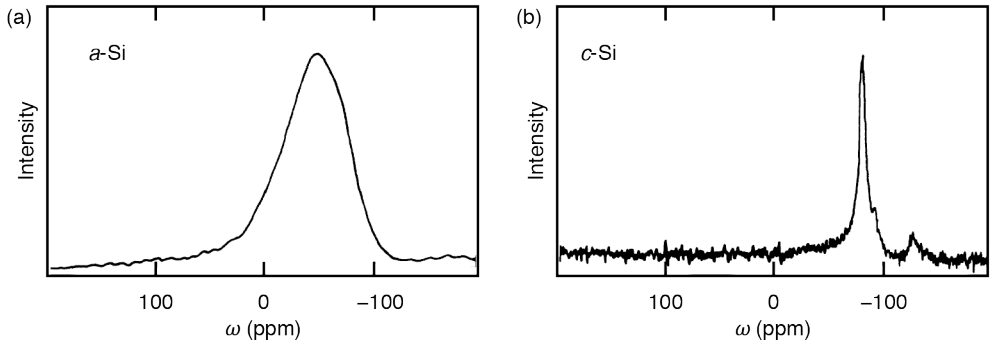

Figure 1.12: (a) Magic–angle spinning (MAS) solid state ^{29}Si NMR of *a*-Si. A single peak indicates there is a single Si environment. (b) On annealing at 640 °C *a*-Si crystallises to form *c*-Si.

formation complementary to that available through total scattering. This approach is obviously attractive but there has been only limited success so far in integrating spectroscopic information into RMC refinements. In the case of NMR, for example, the calculation of NMR spectra from a configuration ordinarily requires quantum chemical calculations, which are sufficiently computationally expensive to make their inclusion in RMC type algorithms impractical. Similar limitations are also present for vibrational spectroscopies (infrared, Raman, inelastic neutron), or indeed comparison against the electronic density of states. One spectroscopic technique that has been successfully integrated into RMC is EXAFS [151]. EXAFS, as an element specific probe of local structure provides useful additional data for RMC refinement, however, as the primary information that one can glean from EXAFS are the local PDFs, this unfortunately means that it very often provides insufficient additional information to completely overcome the difficulties encountered with RMC.

An alternative technique able to provide extremely direct information on structure is microscopy. Recently there have been some astonishing successes using scanning probe microscopies, with the imaging, for the first time, of an atomic two-dimensional CRN [131, 152]. These silica bilayer glasses bear a remarkable resemblance to the first sketches of a 2D CRN drawn up by Zachariasen [Fig. 1.10(a,c)] [125]. Atomic resolution microscopy is still currently limited to two dimensional materials and surfaces, and so unsuitable for determining bulk structure.

A persistent difficulty, as described above, is that the computational expense of calculating experimentally measurable data from atomistic configurations is sufficient to prevent the practical use of that experimental data within the RMC refinement. There is a need therefore to be able to make use of the information that can be gained from these techniques without the cost of these calculations. Where the problem is already well-constrained, it can be possible to devise approximate parametrisations able to near-quantitatively account for the experimental data [153]. As interpolations, these will naturally only have a relatively narrow range of applicability, and so would be challenging to implement for very disordered materials. An alternative approach is to use the information gained from these techniques to devise constraints. Perhaps the most straightforward information that can be extracted from NMR spectra is the number and distribution of atomic environments in a material. For example, in amorphous silicon, NMR evidence informs us that there is only a single atomic environment [154] [Fig. 1.12]. This is a powerful constraint on structure: examination of the naïve RMC configuration described above immediately reveals that its diversity of atomic environments rules it out as a realistic model of *a*-Si.

1.6 INVERT

In previous work [148], I have shown that it is possible to use this idea—namely, that there should be only a relatively limited range of environments in a material—to create general constraints that are able to produce significantly-improved models of amorphous and nanostructured materials, without making any *a-priori* assumptions about the geometries of the material. If two atoms are in the same environment, they should have the same local data, therefore, by minimising the variance across the configuration between different data sets then it ought to be possible to produce configurations with only a single atomic environment. This work is described briefly below, and drawn from Ref. 148.

In this initial work, we made use of perhaps the simplest metric of local environment, the atomistic pair distribution $g_i(r)$. Whereas in ordinary RMC refinement, one would minimise a cost function χ^2 of the form

$$\chi^2 = \sum_r [\langle g(r) \rangle - G_{\mathrm{expt}}(r)]^2, \tag{1.20}$$

where $\langle g(r) \rangle$ is the average atomistic pair distribution for the configuration, what we proposed was the alternative cost function

$$\chi^2 = \frac{1}{N} \sum_j \sum_r [g_j(r) - G_{\text{expt}}(r)]^2. \tag{1.21}$$

Note that in this reformulation one obtains $\chi^2 = 0$ if and only if the model PDF matches $G_{\text{expt}}(r)$ and each individual $g_j(r)$ has the same form. It is straightforward to show that the new penalty function χ^2 of (1.21) is in fact equal to that of (1.20) plus a variance term $\chi^2_{\text{Var}} = \langle g(r)^2 \rangle - \langle g(r) \rangle^2$. What the spectroscopic result suggests is to add to a conventional PDF refinement a term that penalises variance in local coordination environments; for this reason we termed our approach an INVariant Environment Refinement Technique (INVERT).

In practice, the individual $g_j(r)$ for a static atomistic model consist of a series of delta functions, and in order to obtain a well-behaved variance term, it is necessary to adopt a modified formulation such as:

$$\chi^2_{\text{Var}} = \frac{1}{N} \sum_j \sum_i \frac{\left[d_j(i) - \langle d(i) \rangle\right]^2}{\langle d(i) \rangle^2}, \tag{1.22}$$

where $d_j(i)$ measures the distance from atom j to its i-th neighbour, and $\langle d(i) \rangle$ is the average such distance over all atoms j. The term in the denominator of Eq. (1.22) appears in order to account for the fact that the number of neighbours at a distance d scales with d^2. The extension to multiple atom types and/or atom environments is straightforward. A separate variance term is included for each different pair of atom types (A and B, say); the form of each individual term is the same as in Eq. (1.22) except that the $d_j(i)$ will refer to i-th neighbour of type B around the j-th atom of type A, and so on.

At this point it is important to emphasise that no assumptions have been made regarding the actual distribution of neighbours around each atom—only that this distribution should be similar for equivalent atoms. Moreover, we are able to constrain the partial PDF functions for multi-component systems despite the experimental PDF data representing a sum over these separate contributions. This approach also has the advantage of being

computationally straightforward, allowing for lengthy RMC refinements.

We chose C_{60} as a simple first case study, not least because the task of determining its well-known icosahedral structure from the experimental PDF [Fig. 1.13(a)] was highlighted as a benchmark challenge in nanostructure determination [155]. As straightforward as the task might seem, conventional RMC refinement from a random starting configuration [Fig. 1.13(b)] fails entirely, giving a set of small clusters that contains only a few of the real set of interatomic separations [Fig. 1.13(c)]. The same result is obtained even if idealised PDF data are used.

The INVERT modification exploits the experimental NMR result that C_{60} contains a single C environment [156]. Clearly the RMC configuration in Fig. 1.13(c) violates this property, and so would now give rise to a large χ^2_{Var} term that will help drive refinement forward. Indeed, INVERT+RMC refinement from the same random starting configuration gives the correct solution for idealised data [Fig. 1.13(d)] and a near-perfect solution for the experimental neutron PDF data of Ref. 157—enjoys similar success.

As discussed in Section 1.5.4, the paradigmatic "stumbling block" for RMC has always

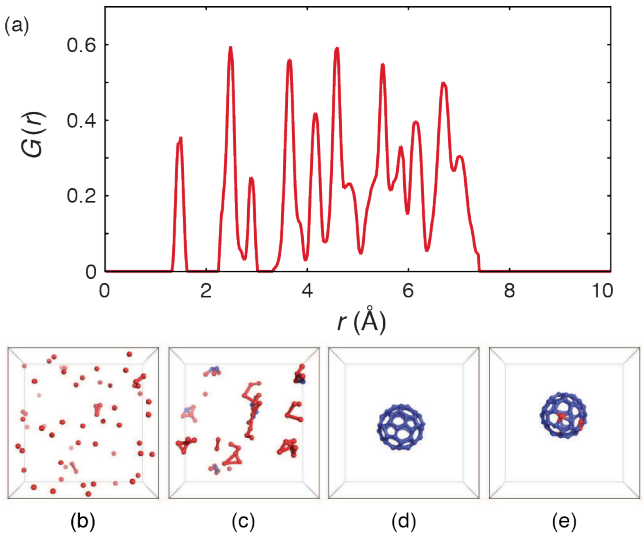

Figure 1.13: RMC refinement of the experimental PDF of C_{60}: (a) the neutron PDF, corrected to remove inter-molecular correlations as described in Ref. 155; (b) a random starting configuration of 60 carbon atoms; (c) a typical configuration produced by conventional RMC refinement of either idealised or experimental PDF data; and those produced by INVERT+RMC using (d) idealised, and (e) experimental PDF data. In panels (b)–(e), atoms with three nearest neighbours are coloured blue and others are coloured red.

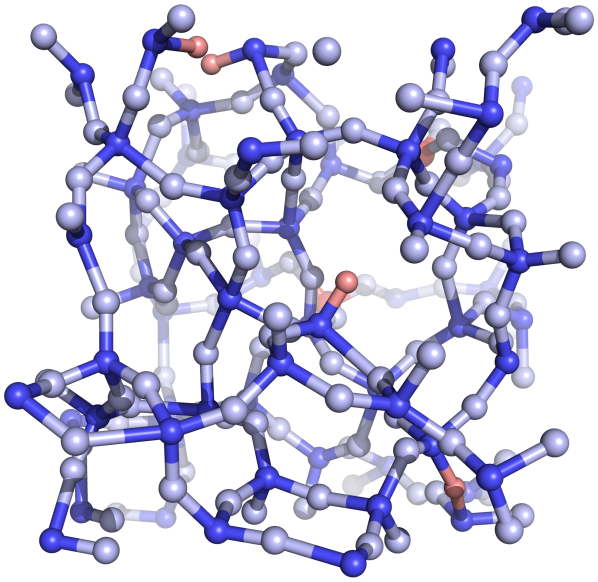

Figure 1.14: A slice of the information-driven CRN model of a-SiO_2 obtained using INVERT+RMC refinement as described in the text. Si and O atoms shown in dark and light colours, respectively; atoms in shades of blue have the expected coordination numbers of 4 (Si) and 2 (O), while the few in shades of red have incorrect coordination numbers.

been *a*-Si [137]. The failures of the configurations generated by naïve RMC refinements of *a*-Si can also be thought of in the light of the variation in atomic environments: crudely speaking, a pair of atoms of coordination numbers three and five will contribute to the average PDF indistinguishably from two four-fold coordinated atoms, and yet the former state is statistically more likely during a sequence of random moves.

Similar results are obtained for amorphous SiO_2, which is a conceptual extension in that it contains two distinct atom environments: that of the Si atoms and that of the O atoms. Experimental neutron PDF data were taken from Ref. 138, and starting configurations generated from a random distribution of 64 Si atoms and 128 O atoms in a periodic cubic box of side 14.37 Å. RMC refinement both with and without the INVERT modification gave excellent fits to the PDF, but the INVERT+RMC model had a much higher percentage of fourfold Si coordination (97% *vs.* 59% for the RMC-only configuration). Indeed, we believe the INVERT+RMC configuration to be the first information-based CRN model of *a*-SiO_2 [Fig. 1.14].

First, a conventional RMC refinement was performed using $G(r)$ "data" generated from

the trusted WWW model of [Fig. 1.11(d-f)].The starting configuration was a random collection of 512 Si atoms in a cubic box of side 21.7 Å. Refinement gave a highly-disordered configuration that displayed all the hallmarks of previously-described problematic RMC studies [147]: only 27 % of Si atoms are four-fold coordinated, there are substantial density variations, and large numbers of unphysical Si_3 "triangles" [Fig. 1.11(b,h)]. In contrast, a parallel INVERT+RMC refinement achieved an almost perfect coordination distribution (95 % four-fold). The improvement extended even to the higher-order correlations: in particular, the number of Si_3 triangles is halved [Fig. 1.11(i)] and the density distribution is much more even. Inspection of the configuration itself [Fig. 1.11(c)] now reveals obvious similarities to the trusted WWW model [Fig. 1.11(a)]. The PDF itself is relatively insensitive to this fundamental improvement in local structure modelling [Fig. 1.11(d-f)]. Nevertheless these INVERT models cannot be thought of as completely representative models of amorphous silicon, as they still bear the hallmarks of the randomness introduced by RMC (particularly visible in the bond angle distribution). It is therefore necessary to explore and extend this INVERT approach if we are to produce data-driven models of amorphous and nanostructured materials.

1.7 Metal–organic frameworks

Much of this thesis will focus on understanding and controlling disorder in the particular class of materials known as metal–organic frameworks (MOFs). MOFs are framework materials where the nodes are metal ions or clusters, and the linkers organic ligands.

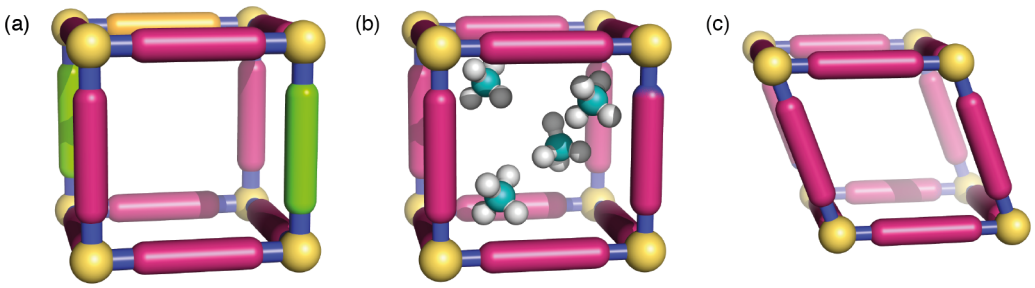

Figure 1.15: A schematic illustration of the modular, open and soft nature of MOFs. (a) In a modular material it is possible to exchange one component for another while maintaining its structure. (b) MOFs can be very highly porous, and hence serve as a host for guest molecules. (c) Many MOFs are soft—small external stimuli can cause large changes in their structures and properties.

Although many MOFs have structures that can be considered directly analogous to those of traditional framework materials, for example the zeolitic imidazolate frameworks (ZIFs) and zeolites [158] or the metal ammonium formates and oxide perovskites [159, 160], the incorporation organic ligands means that the chemistry of MOFs has a number distinctive features. Three of the most important ways in which MOFs differ from conventional frameworks are their tendency to be more modular, more open and softer [Fig. 1.15]. In the following sections I explore each of these aspects of MOF chemistry in turn, making particular reference to the corresponding propensity for disorder [161].

1.7.1 Modularity

For a framework to be modular, it must be possible to exchange one component of the framework (whether node or linker) for another without significantly perturbing the overall framework structure. Modularity is thus an integral part of framework chemistry as it allows framework properties to be rationally tuned. The modularity of conventional frameworks is demonstrated by the impressive range of possible cation substitution [164]. In contrast, the range of anion substitution chemistry in conventional frameworks is comparatively restricted, despite recent advances in using topochemical reactions [165, 166]. MOFs not only show the full range of cation substitution seen in oxides [167, 168], but also have a very extensive ligand substitution chemistry [162, 163].

The enhanced modularity of MOFs stems in large part from the molecular nature of the linker: one atom no longer has to connect two (or more) different structural units, and so varying the central element of the ligand has a much reduced impact on the geometry and strength of its binding. Thus, a very large number of MOFs with the same topology but with different connecting ligands, that is, MOFs that are 'isoreticular' to each other can be synthesised [162]. The prototypical family of isoreticular MOFs are IRMOFs, which are constructed from basic zinc acetate $Zn_4O(O_2C)_6$ clusters connected by linear linkers, typically dicarboxylates into a primitive cubic (**pcu**) net [171]. The original IRMOF is MOF-5 (IRMOF-1) [171], synthesised using 1,4-benzenedicarboxylic acid (H_2bdc), but dozens more IRMOFs have since been synthesised [Fig. 1.16(a)], with enhanced gas sorption capacities [162, 172] or catalytic activity [173]. This flexibility is not unique to the IRMOFs, as many other MOF families have a similar diversity of poten-

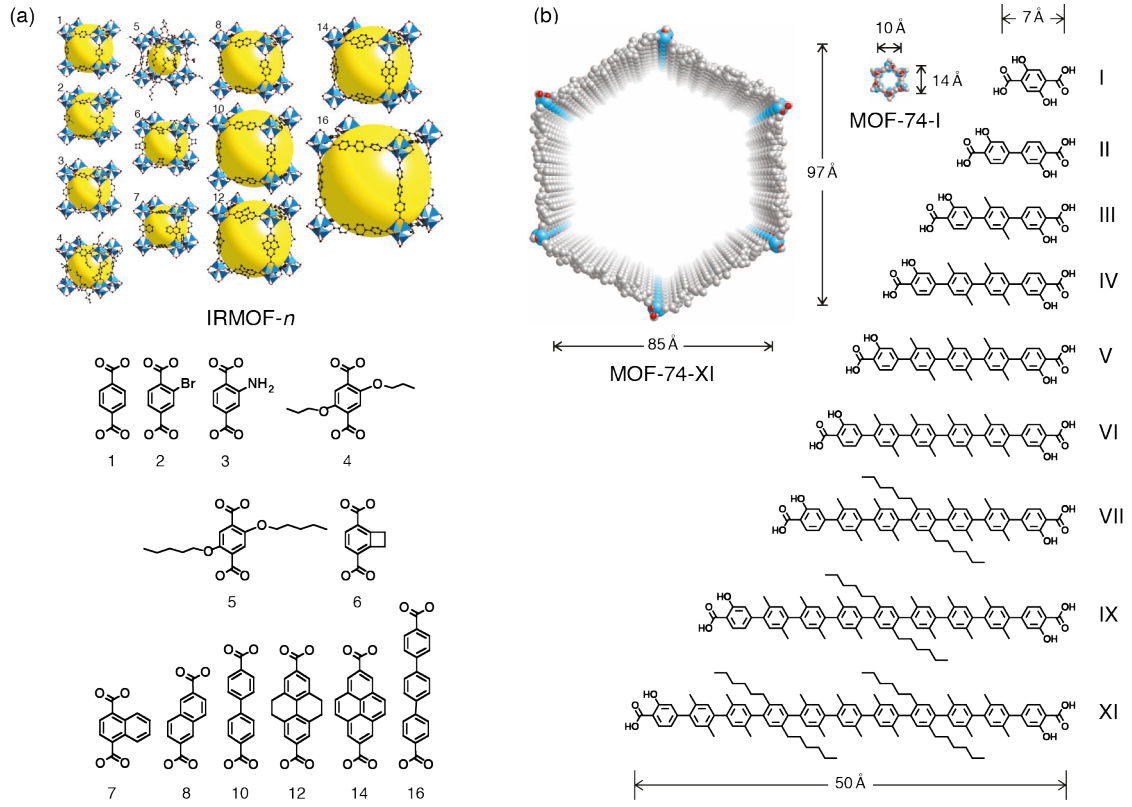

Figure 1.16: The modularity of MOFs is demonstrated by the ease of forming isoreticular families, *i.e.* MOFs with identical topology, but with varied ligand or metal clusters. (a) Single crystal structures of IRMOF-n (Zn_4OL_3, where L is a linear dicarboxylate ligand). Colour scheme is as follows: Zn (blue polyhedra), O (red spheres), C (black spheres), Br (green spheres in IRMOF-2), amino-groups (blue spheres in IRMOF-3). The large yellow spheres represent the largest van der Waals spheres that would fit in the cavities without touching the frameworks. All hydrogen atoms have been omitted, and only one orientation of disordered atoms is shown for clarity. Panel adapted from Ref. 162. (b) The structures of MOF-74-XI and MOF-74-I, along with the series of intermediate length ligands in the MOF-74-n family. MOF-74-XI has the largest pores of any crystal. Colour scheme as follows: Mg (blue), O (red), C (grey), H(white). Panel adapted from Ref. 163

tial ligands, for example the UiO-66 family ($Zr_6O_4(OH)_4(bdc)_6$, face-centered cubic **fcu** topology) [174–176], or the MOF-74/CPO-27/M_2dobdc family (M = divalent metal, dobdc = 4,6-dioxido-1,3-benzenedicarboxylate), which consists of metal oxide chains linked by linear linkers into a honeycomb structure [Fig. 1.16(b)] [163, 177].

This ability to substitute in a wide variety of ligands and metals while maintaining essentially the same framework connectivity has also been exploited to make materials with complex stoichiometries and thus show compositional disorder. This has been extended to its logical limit by so-called 'multivariate' MOFs, where large numbers of different metals (up to ten) [178] or ligands (up to nine) [Fig. 1.17(a)] [172] are incorporated into the

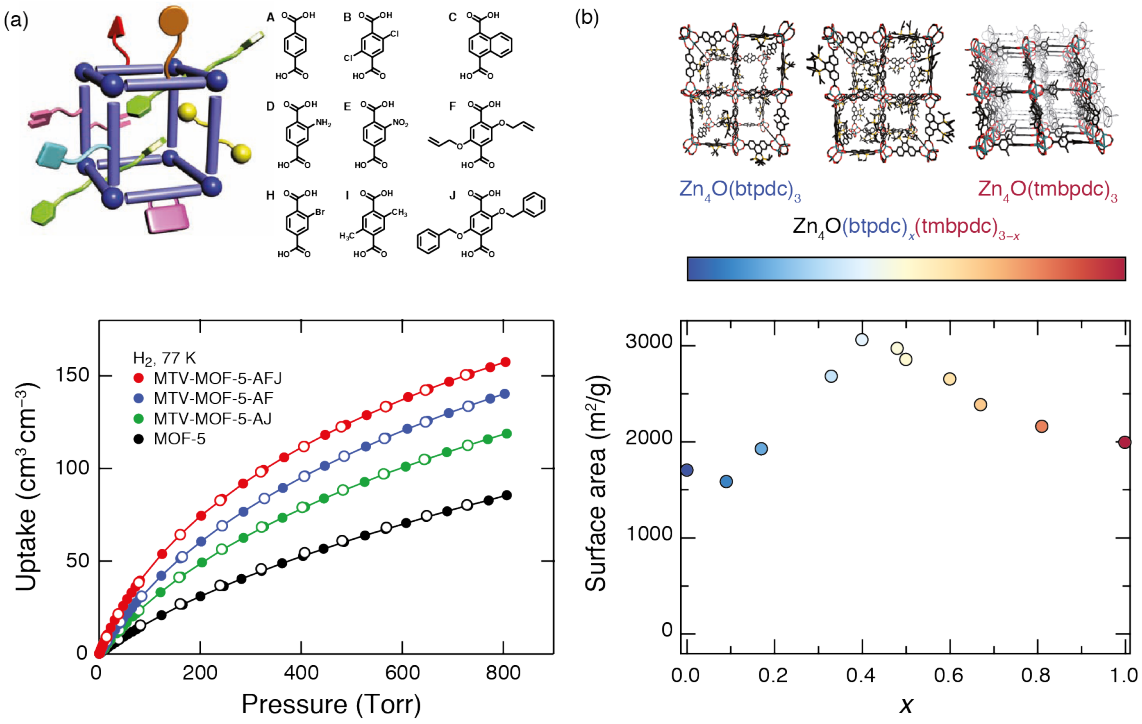

Figure 1.17: (a) The IRMOF series of MOFs have the widest range of ligand substitution chemistry reported for MOFs, with up to 9 distinct ligands included in a single crystal [top]. Through synthesis of these mixed-ligand IRMOFs it has proved possible to significantly enhance the H_2 uptake in this material, shown by the adsorption isotherms [bottom]. (b) Doping in non-stochiometric quantities of a bulky ligand, 9,10-bi(triisopropylsilyloxy)phenanthrene-2,7-dicarboxylate (btp!dc) into the IRMOF [ZnO_4(tmbpdc)$_3$] (tmbdpc = 3,3',5,5'-tetramethyl-4,4'-biphenyldicarboxylate) suppressed framework interpenetration, increasing the surface area above that for either end-member phase [169]. Figure adapted from Ref. 170.

same crystal. Non-stochiometry in MOFs has also been productively used to tune their properties, with examples ranging from introducing new spin-crossover phases and transitions [179] to creating ratiometric oxygen sensors [180]. While very often the resultant properties can simply be thought of a linear combination of the two end-member phases [170], it is also possible to introduce cooperative effects, leading to for example, increased internal surface area [Fig. 1.17(b)] [169].

Postsynthetic reactions

A further source of compositional complexity are postsynthetic reactions, which naturally produce non-stochiometric materials not carried out to completion. These postsynthetic reactions are analogous to what might be termed "chimie douce" in oxide materials [184]

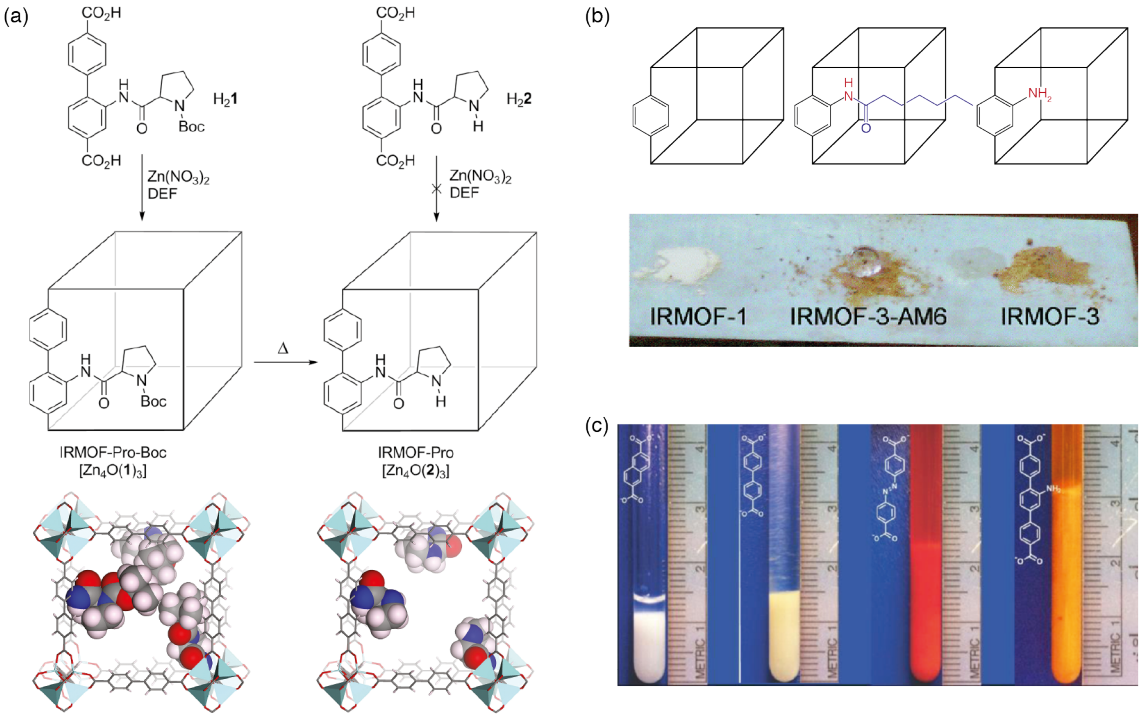

Figure 1.18: (a) The basic amine moiety of the proline functionalised ligand prevents the formation of IRMOF-Pro directly. Protecting the amine with the thermolabile tert-butyloxycarbonyl (Boc) protecting group therefore allows IRMOF-Pro-Boc to form. The SC-SC thermal deprotection yields the desired IRMOF-Pro. Colour scheme as follows: Zn shown as teal polyhedra, C in dark grey, H in pink, O in red and N in dark blue. The pendant functional groups are shown as spheres. (b) IRMOF-1 and -3 are hydrophilic and water sensitive. Selective PSM of the exterior of IRMOF-3 with bulky hexanoic anhydride yields a superhydrophobic and water stable MOF that retains its porosity. (c) bio-MOF-101 can be transformed into the more porous bio-MOF-100 by ligand PSE in a SC-SC fashion. Sequential ligand PSE yields the synthetically inaccessible bio-MOF-102 and bio-MOF-103, increasing the size of the original bio-MOF-101 crystals by more than a factor of 2. Origin of panels as follows: (a) from Ref. 181, (b) from Ref. 182, (c) from Ref. 183.

but, in comparison, can occur under much less onerous conditions, ordinarily requiring much lower temperatures (*i.e.* $< 100°C$) and milder reagents (*e.g.* organic acid anhydrides or dilute solutions of ligand) [185, 186], and often can be carried out in a single-crystal to single-crystal (SC-SC) process. Post–synthetic reactions in MOFs fall into two categories: postsynthetic modification (PSM), where reactions are carried out on the framework, typically through organic chemistry transformation, drawing inspiration in part from post translation modification techniques used for tagging proteins [185, 187]; and postsynthetic exchange (PSE) reactions, where the metal or ligand building blocks of the framework are substituted [186, 188]. These two sets of techniques have been applied to a wide range of MOFs and are of great utility as they allow the synthetic chemist to circumvent the

restrictions that are imposed by conventional solvothermal synthesis.

As a result PSM has been particularly useful for the synthesis of catalytically active materials, where the intrinsic reactivity of the catalytic centre often inhibits the formation of the desired framework [181, 189, 190] [Fig. 1.18(a)]. PSM has also been used to introduce functional groups capable of sensing [191], enhancing the increase both the capacity and selectivity of carbon dioxide uptake [192], or even introduce biologically active moieties [193]. The chemical versatility of this technique has also led to a number of ingenious uses, including synthesising MOFs using ligands with bulky, but thermo- or photo-labile, functional groups to ensure that a non-interpenetrated framework forms, before removing the group to release the latent porosity [181, 194]. By using instead bulky reagents the MOF surface can be selectively functionalised to be superhydrophobic, protecting water-sensitive MOFs while retaining their porosity [Fig. 1.18(b)] [182].

The successes of PSM were a vivid demonstration of the reactivity of the MOF framework itself and so naturally led to the demonstration that the building units themselves could be interchanged [188, 195]. In addition to broadening the range of possible ligands, PSE also allows for exchange of framework metal cations, *e.g.* Mn-doped ZIF-8 [196], thus introducing magnetism to a diamagnetic framework, or Ti-doped UiO-66 [188], dramatically improving the adsorption properties of the MOF, by both gravimetric and volumetric measures. One of the most surprising features of PSE is that it is possible to not only use ligands that could be incorporated with no strain but also much larger ligands. This was demonstrated very effectively in the bio-MOF family, where it is possible to expand a MOF crystal by at least factor of two through sequential PSE reactions [197] [Fig. 1.18(c)]. PSE reactions have also been extended to so-called 'tandem PSE' [196], where both metal and ligand are exchanged, making those MOFs crystalline exemplars of the philosophical Ship of Theseus paradox.* The reversibility of these PSE reactions has also led to their investigation as dynamic combinatorial systems [200].

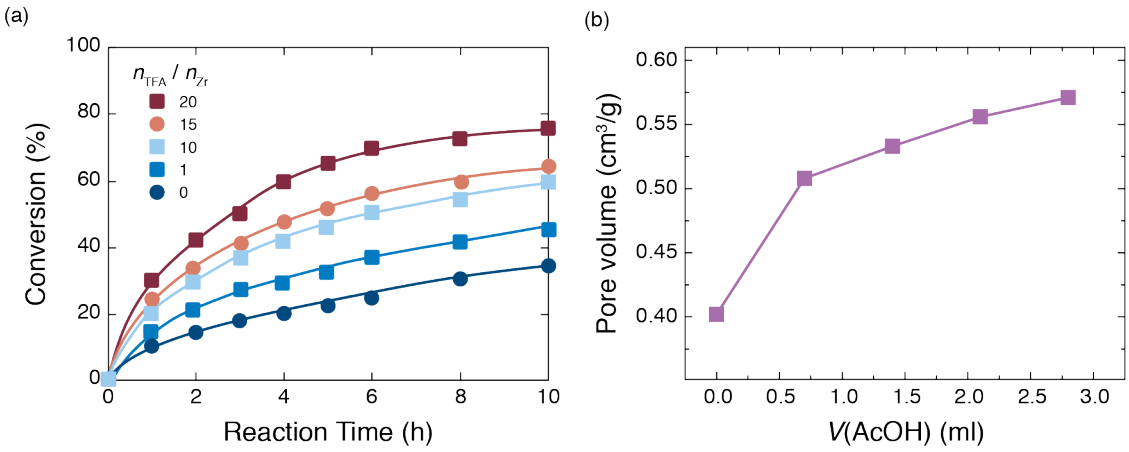

Figure 1.19: (a) The activity of UiO-66(Zr) can be enhanced by a factor of 2.2 by introducing ligand vacancies through the use of trifluoroacetic acid (TFA) as a modulator. Figure adapted from Ref. 201 (b) Introducing ligand vacancies using acetic acid (AcOH) modulation substantially increases (40%) the micropore volume (NLDFT method) [202].

Vacancies

In frameworks with sufficiently high connectivity (*i.e.* those that are over-constrained), it is possible not only to exchange ligands, but also to remove them entirely, introducing vacancies. Vacancy chemistry is well established in conventional materials [Section 1.4.1] but it is only very recently its importance has been recognised in MOFs. It is now possible to create MOFs containing ligand absence defects in a number of MOF families [161, 203–207], particularly in those based on $M_2(O_2C)_4$ paddlewheels [208–211] and the UiO-66 $M_6O_4(OH)_4$ clusters [201, 202, 212]. However, these studies of defect-containing MOFs have so far relied on a relatively restricted range of approaches: 'ligand–fragment coassembly' [205, 208], mesoscale texturing *via* surfactant inclusion [131, 203], and labile asymmetric ligands [206]. The potential utility of these defects has been demonstrated by their ability to enhance both the catalytic activity, through the generation of active metal sites [Fig. 1.19(a)] [201], and the porosity [Fig. 1.19(b)] [202, 205, 208].

*This paradox, first recorded in a story recounted by Plutarch, concerns whether a ship in which all its planks of wood have been replaced by new planks remains the same ship [198]. Alternative equivalent more modern formulations are the "Trigger's Broom" or "Sugababes" paradoxes [199].

Correlation in non-stochiometry

Non-stochiometry in MOFs, whether created through PSM, PSE or during synthesis, can introduce complexity not only in composition but also through compositional inhomogeneity. This has been most productively harnessed in the creation of mesostructured MOFs [213–215] of which the most widely investigated class is core-shell MOFs, that is, materials where the exterior and interior of the MOF crystal have distinct stoichiometries [215]. One application of these core-shell MOFs that has been extensively explored is the role of the shell as a 'gatekeeper' for the crystal porosity, whether to modulate the sorption properties or to use it as a hydrophobic coating to protect moisture-sensitive MOFs [183]. In contrast to the widespread use of mesoscale structuring, there are only isolated reports of nanoscale control of order and disorder [216] and even fewer of the creation of nanoscale correlations [217]. This nanoscale control is necessary if MOFs are to show the same diversity of functional correlated states as conventional materials.

1.7.2 Openness

The strong directional bonding found in many frameworks permits the formation of non-close packed open structures, of which the very porous zeolites are perhaps the best example [218]. In MOFs, the single atom linkers of conventional frameworks are replaced by much longer molecules and so a MOF will have a much more open structure than an oxide with the same topology (*c.f.* ZIFs and zeolites). This openness has meant that host-guest chemistry has been at the heart of MOF chemistry from its genesis [219–221]. The potential openness of MOF structures enabled by the use of long, rigid organic linkers is demonstrated by their potential for extreme porosity: for example, the current record internal surface area for a solid is held by NU-110E ($7140\,m^2g^{-1}$) [Fig. 1.20(a)] [222]*.

The huge surface areas and internal free volumes have led to intensive investigation for gas storage applications [162, 224–226], but many of the most promising applications derive from the combination of this porosity with chemical tunability rather than sheer pore volume alone. Three of the most important applications are gas separation [227], catalysis [228] and as bioactive materials [229]. Gas separation has received extensive

*The largest predicted surface area for a MOF is currently $14\,937\,m^2\,g^{-1}$ [223].

investigation [227, 230], with CO_2 separation of particular importance due to its environmental relevance [231]. The utility of MOFs as gas separation materials does not arise from their geometrical pore structure alone but also depends crucially upon their specific chemistries, with features such as open metal sites shown to be of particular importance [232]. MOFs, as their porous structures allow for the infiltration of both reagent and substrate, can potentially combine many of the advantages of heterogenous catalysis (ease of recyclability, stability) with those of homogenous catalysis (well-defined active sites, high active site concentration and hence specific activity) [228]. Their activity can be the result of catalytically active linkers [233, 234], encapsulated molecular or nanoparticle catalysts [235–237] or even intrinsic to the chemistry of the MOF metal clusters, for example open metal sites [238–241]. The open structures of MOFs has been further harnessed to deliver biologically active molecules, including as drug delivery hosts providing controllable pharmokinetics [242] or as easily storable sources of biologically important gases, both as devices to provide localised stimuli for cell biology [243] and as treatments in themselves [244].

Guests molecules can themselves be a source of useful properties. As guests are, by definition, not covalently bonded to the framework, they are typically very disordered. Despite this, in favourable circumstances, particularly where the MOF has small and low symmetry pores and at high guest occupancies, it is possible to use the MOF as a crystalline template to order guests for crystallographic analysis [246]. Nevertheless, this is the exception, and most guests (particularly solvents) tend to be liquid-like (as the effect of confinement tends to suppress ordering [247]). MOFs with cationic or anionic frameworks by contrast, interact much more strongly with their guests and so display a much wider range orderings, including (anti)ferroelectricity [248]. This is demonstrated by the AMX_3 ammonium metal formates (and the related azides) [Fig. 1.20(b)] [159, 160, 249, 250]. These materials adopt structures related to that of the ABO_3 oxides, with the majority crystallising with the perovskite structure. Just like their ceramic analogues, these formates show correlated disorder that results in functional properties. In the case of the ammonium metal formates, it is the orientational disorder of the ammonium cations occupying the "pores" of the anionic metal-formate framework that is of interest. The coupling of rotational disorder to the lattice through hydrogen bonding means that

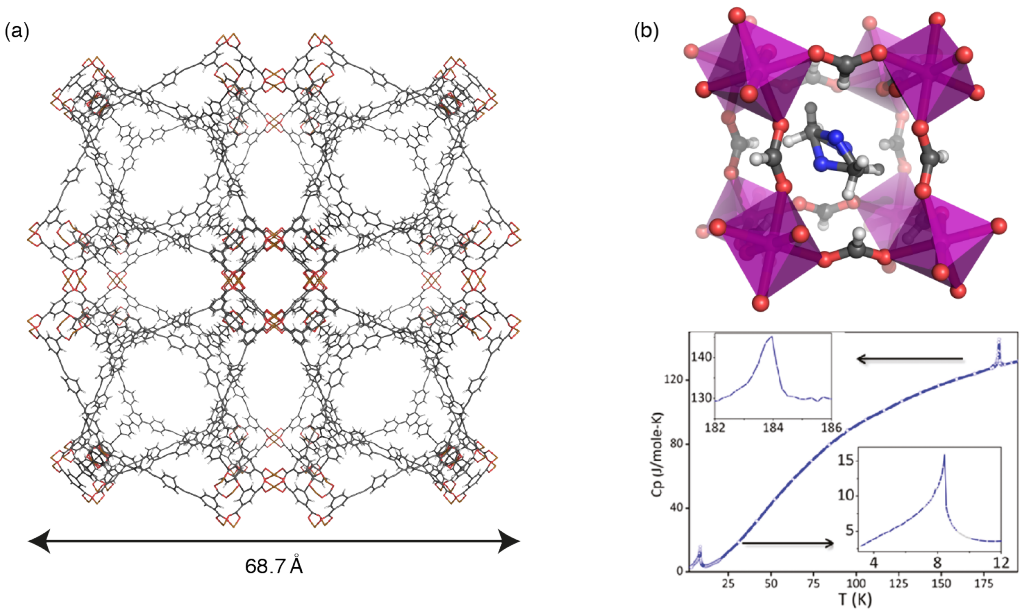

Figure 1.20: (a) Unit cell of NU-110E, the crystal with the current record internal surface area [222]. (b) The ferromagnetic and antiferroelectric MOF perovskite, dimethylammonium manganese formate $(Me_2NH_2)Mn(HCOO)_3$. Top: a section of the crystal structure showing a single ReO_3 type cavity, containing a single Me_2NH_2 cation, with the N disordered over three sites. Mn is shown in purple, O in red, C in black and H in white. Bottom: heat capacity measurements showing both the weak ferromagnetic (8 K) and antiferroelectric (184 K) orderings. Figure adapted from Ref. 245.

these formates show (anti)ferroelectric ordering at low temperatures [245]. As the dipolar ordering occurs through the 'A' site of the perovskite it is possible to use magnetic 'B' sites to produce materials that show simultaneous magnetic and electric order, *i.e.* are multiferroic [245]. However, as the electric and magnetic orderings result from two different mechanisms they possess relatively small magnetoelectric couplings [245]. This family of materials is perhaps the best example of how orientational disorder, due to ligand and guest motion, can be harnessed to produce new functional properties.

The separation of metal centres necessary for high porosity also tends to weaken the interactions between them. This poses a challenge for chemists if we want to be able to replicate the range of electronic and magnetic properties seen in conventional oxide ceramics. One promising approach is to use molecular ligands that can effectively delocalise charge. This has already led to the synthesis of MOFs with high electronic conductivities (up to $50\,S\,cm^{-1}$) [251–254] and dense molecular frameworks with above room temperature magnetic ordering [255]. Theoretical calculations also suggest that careful ligand design

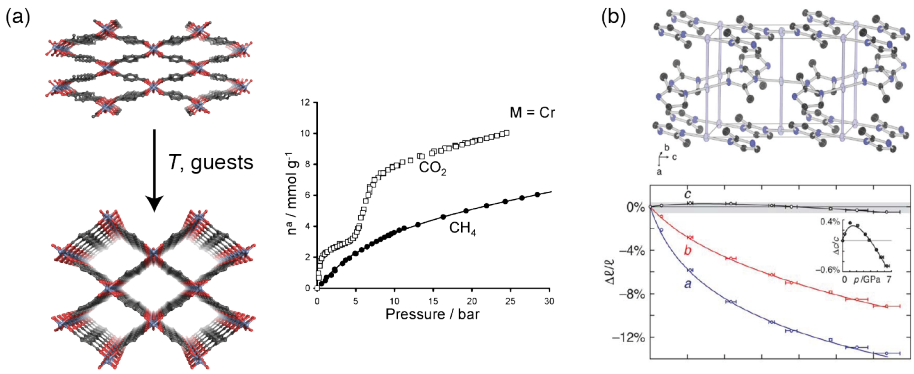

Figure 1.21: (a) MIL-53(Cr) was the first example of a MOF to show a 'breathing' transition. On heating, or on adsorbing a suitable guest (*e.g.* CO_2, DMF), the low-temperature form (top) undergoes a first-order phase transition to the high-temperature form (bottom) and its volume increases by approximately 40%. This transition allows for enhanced selectivity for CO_2 adsorption over other possible adsorbate gases (right). (b) Silver methylimidazolate (Ag mIm) (top) has anomalous mechanical properties, and is one of the first MOFs to exhibit NLC (bottom). Origin of panels: (a) from Ref. 262, (b) Ref. 263.

could allow even porous carboxylate MOFs to show magnetism well above the boiling point of nitrogen [256]. The challenges caused by longer length-scales and lower energy scales also present an opportunity for MOF chemists: MOFs can show a wide-range of guest-dependent behaviour, from altering the ordering temperature [257], to switching the spin-crossover state [258] or swapping the sign of magnetic coupling [230]; moreover the use of long linkers allows the design of three-dimensionally connected materials that exhibit low-dimensional magnetic behaviour [259, 260]. The propensity of MOFs to show responsive behaviour is not restricted to their magnetic properties, and can be seen throughout their optical, electrical and especially, mechanical properties. MOFs have thus been called "soft porous crystals" [261].

1.7.3 Soft crystals

The potential for responsive behaviour in MOFs is by now well-established, and the paradigmatic demonstration of the flexibility in MOFs is the 'breathing' of MIL-53, a M^{III} terephthalate MOF with a wine-rack topology [Fig. 1.21(a)] [264]. On heating, adsorption of CO_2 or uptake of a variety of solvents, MIL-53 undergoes a phase transition to a much larger, open structure ($\Delta V/V = 40\%$) [262, 264]. This transition dramatically increases its guest capacity, and so the chemical specificity of the breathing transition translates

into a specificity of its sorption properties. MIL-53 is not the only MOF to show this kind of transition, with a number of other MOFs that exhibit even larger breathing transitions, including the MIL-88 family ($\Delta V/V = 270\%$) [265] and the **xmz** topology family ($\Delta V/V = 105\%$) [266], both built from $M^{III}O(O_2C)_6$ clusters. Guest responsive behaviour is not limited to breathing, with other examples including the gating of interpenetrated MOFs (materials where the MOF consists of two or more networks topologically intertwined) [267] and guest responsive ligand rotations such as those in ZIF-8 [268]. The guest-induced transitions that occur in these materials all preserve the framework connectivity, but there are a number of puzzling reconstructive transitions where the entire framework connectivity can be transformed, often in a SC-SC fashion: *e.g.* the reversible interpenetration/deinterpenetration of MOF-257 on DMF re/decoordination, in which the crystal size changes by factor of two [269].

The flexibility of MOFs can also be seen through their anomalous mechanical and thermomechanical properties. These include very large negative thermal expansion, both anisotropic, as result of topologies that couple a rapid expansion in one direction to a contraction in others [270, 271], and isotropic, where the negative thermal expansion often arises because of the intrinsic ligand flexibility [272–274]. Even more unusually, a number of MOFs also exhibit negative linear compressibility (NLC) [183, 263, 275], an extremely rare property [276] [Fig. 1.21(b)]. The modular perspective is also valuable for rationalising the anomalous mechanical properties of MOFs, although it is important to note that the mechanical and structural building units need not, and often do not, coincide [263]. A further manifestation of the softness of MOFs is in their propensity to readily amorphise. The topologically disordered phases that result are now of increasing interest to materials chemists [277].

1.7.4 Topologically disordered MOFs

Amorphous MOFs can be formed via a wide variety of processes, including heating [139], compression [279] and grinding [280] but the most common route by which amorphous MOFs are formed is desolvation [281–284]. This susceptibility of MOFs to collapse on desolvation was a challenge faced, and largely solved, by early MOF chemists [285]. Perhaps more surprisingly, many of these desolvated amorphous phases can be reversibly

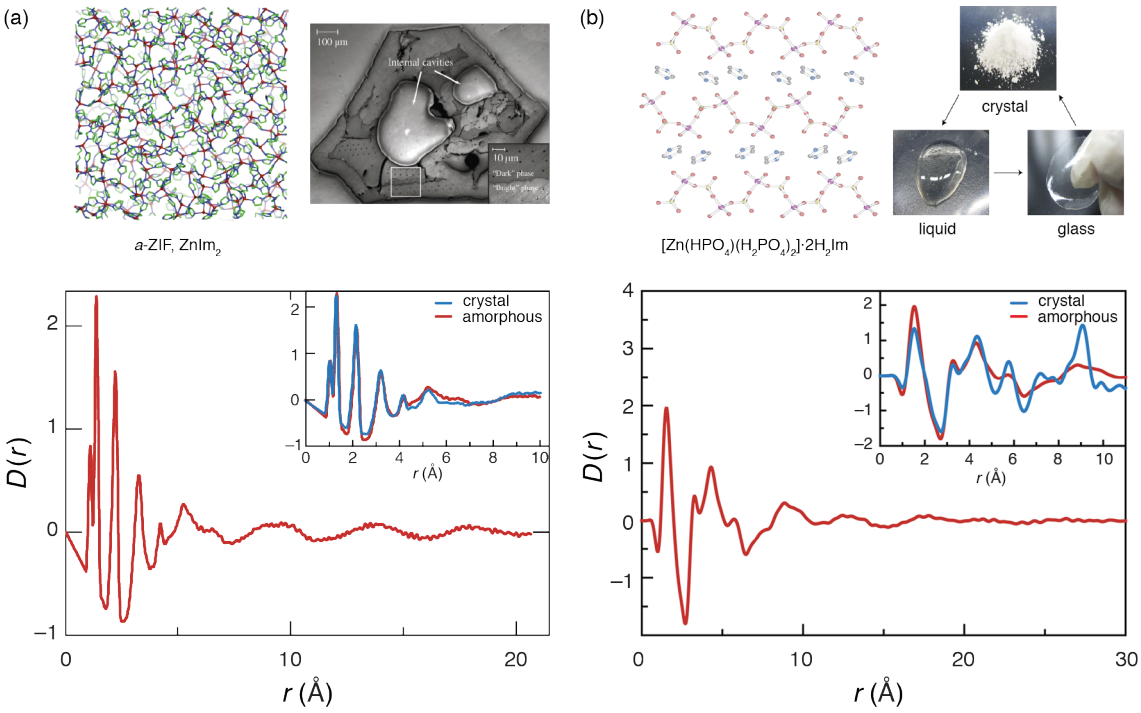

Figure 1.22: Two examples of amorphous MOFs: (a) the best characterised example of an amorphous MOF, *a*-ZIF and (b) the first example of MOF glass $[Zn(HPO_4)(H_2PO_4)_2]\cdot H_2Im$. (a) [Top left] A model of *a*-ZIF, derived by RMC refinement of total scattering data from a decorated model of SiO_2. [Top right] TEM imaging of the phase transition from crystalline ZIF-4 to *a*-ZIF reveals curved internal surfaces characteristic of amorphous materials. [Bottom] Experimental PDF data reveals the lack of long-range order in *a*-ZIF, and the close similarity in the local structure between the crystalline ZIF-4 and amorphous phases. (b) [Top left] the crystal structure of $[Zn(HPO_4)(H_2PO_4)_2]\cdot H_2Im$. [Top right] $[Zn(HPO_4)(H_2PO_4)_2]\cdot H_2Im$ melts to stable liquid, which on rapid cooling, transforms into a glassy phase, which recrystallises upon annealing. [Bottom] The experimental $D(r)$ shows no long-range order in the glassy phase. Comparison of the PDF data for the crystalline and amorphous phases reveals that although the short-range order is similar, there are significant differences beyond approximately 4 Å. Figure adapted from Refs. 139, 278.

transformed through solvent exposure back to crystalline materials [281–283]. These transitions have thus been investigated for their potential as selective solvent sensors [282].

The amorphous ZIF frameworks, as SiO_2 analogues, represent the best-characterised family of amorphous MOFs. On heating, ZIF-4 (zinc imidazolate, $ZnIm_2$) goes through two phase transitions: first, from a porous phase with the CAG topology to an amorphous phase; and second, from the amorphous phase to a dense crystalline phase with the **zni** topology framework [Fig. 1.22(a)] [139]. As this phase is bounded by two crystalline phases of identical stoichiometry, it must share the same stoichiometry. X-ray total scattering measurements confirm that the *a*-ZIF phase maintains the same local coordination as

found in the two crystalline ZIF phases but RMC modelling demonstrates that its structure is not consistent with distorted forms of either of its neighbouring crystalline phases. It is instead consistent with a 'decorated' model of SiO_2 glass [139]. Amorphous ZIFs can also be formed by the application of pressure and through prolonged ball-milling [286, 287]. The ability to make MOF glasses (*i.e.* amorphous MOFs formed by rapid cooling of a melt) has been shown to be feasible in the zinc imidazole phosphate family of dense proton conducting MOFs, which melt at relatively modest temperatures [Fig. 1.22(b)] [278].

1.7.5 Characterising disorder in MOFs

The difficulties in characterising disorder are one of the principal reasons for the relatively limited exploitation of disorder as a design motif. In many of the above studies, the major methods used to confirm compositional disorder are techniques only sensitive to the bulk composition: for example, NMR and mass spectrometry on solutions of 'digested' MOF and combustion analysis. Spectroscopic measurement, including EXAFS [288], NMR [289] and IR/Raman [211] have proved very powerful probes of local structure as well as bulk composition. These techniques have also been combined with microscopy of various kinds, in order to map out the distribution of composition on a mesoscale [213, 214]. This still leaves a significant gap in our understanding of the structure of these materials, lying between the very local structure available from spectroscopy and the microstructure visible in microscopy.

It is in this gap where diffraction—and total scattering techniques in particular—can be most useful. However, the modelling of disorder in these materials can often be challenging, and as disorder manifests itself ordinarily in weak, broad features in the diffraction pattern, it has very often been neglected altogether. This is a particular problem in the MOF literature, as, unlike in, *e.g.* oxide chemistry, the focus of the work is very often not on the quantitative analysis of diffraction data. Consequently, powder diffraction data are often incompletely analysed, even for papers published in the most prestigious journals [163]. While these omissions do not throw doubt onto the general identity of the synthesised materials, the nature of disorder means relatively subtle changes in the diffraction pattern can be indicative of large-scale structural changes. As a result, the scope of disorder in MOFs is likely to be much broader than is currently appreciated.

1.8 Aims and structure of the Thesis

In this introduction I have explored the many ways that disorder can manifest itself in materials, and shown how disordered materials are both ubiquitous and useful. Understanding the origin of the properties of a material relies fundamentally on being able to produce an atomistic model of its structure. Despite the importance these models, the tools we have at present to produce them are still very limited. There is a need therefore to develop more powerful methods for characterising disordered materials. Correlated disorder can give rise to states that would be forbidden in perfect crystals, and hence produce unique emergent properties. We currently only have very limited control over correlated disorder, however, and so our investigations are inherently restricted to a narrow range of cases.

MOFs are a compelling class of materials that have potential applications across many areas. Their diversity of structure also encompasses a wide variety of forms of structural disorder and defects. Their predictable structures, and in particular their modular construction, make it therefore possible to anticipate and exert chemical control over those defects and disordered structure through routes that would be very difficult for other materials. In this thesis I aim, therefore, to demonstrate that disorder can be used a functional motif in its own right, and that MOFs provide ideal platform for this. This thesis contains two related programmes: first, I aim to show that pair distribution function data can provide significantly more structural information on disordered frameworks than currently believed, using *a*-Si as an exemplar; second, I show that correlated disorder does exist in MOFs, that we can characterise and chemically control it and thus disorder can be used to tune the physical properties.

Detailed description of the methods employed in each Chapter are included at the end of the relevant Chapter. Since diffraction data forms the basis for all of the work described in this Thesis, I begin, in Chapter 2 by describing in more detail the relevant theory of diffraction, with a particular focus on the practical aspects of diffraction experiments.

Chapter 3 contains a detailed investigation of the concept of structural invariance as implemented in the INVERT algorithm introduced in Section 1.6, demonstrating where

its application is likely to be successful and also highlighting some of the challenges facing its use. This Chapter consists primarily of work published as Ref. 290.

Chapter 4 extends the concept of structural invariance to the more general idea of 'structural simplicity' and outlines how simplicity might be used to design quantitative metrics for assessing the quality of structural models of amorphous materials. It continues by demonstrating that these measures of structural simplicity are able to drive refinements of amorphous materials towards more realistic configurations. This Chapter consists primarily of work published in Ref. 291.

Having demonstrated how we can use diffraction data to begin to unravel structure for even the most disordered materials, in the final two chapters I shift to discussing disorder and dynamics in MOF materials. In Chapter 5, I introduce UiO-66(Hf), one of the canonical MOFs, and demonstrate that it is possible to controllably introduce correlated defects into a MOF. I further go on to uncover the nature of these correlated defects, showing that it contains metal cluster, as well as ligand, absences. This Chapter consists primarily of work published in Ref. 292.

In Chapter 6 I explore the relationship between these defects and the thermomechanical properties of UiO-66(Hf). I demonstrate that the defects can be used to control the thermomechanical mechanical properties of UiO-66(Hf) and further show that it exhibits both very large thermal densification and also the largest known isotropic NTE in a MOF. This Chapter consists primarily of work published in Ref. 293.

I conclude, in Chapter 7 by summarising the main findings of this thesis and discussing some aspects of the future possibilities for disorder in MOFs.

Chapter 2

Scattering theory

In Section 1.3, I introduced the fundamentals of diffraction theory in a general sense. The practical measurement and interpretation of diffraction data requires a little more elaboration of this theory.

2.1 Theory of diffraction experiments

Powder average

In many cases three dimensional scattering data are not available due to the lack of suitable single crystals, whether because of the intrinsic limitations of the system in question, *e.g.* if it is amorphous or a device *in operando*, or simply that single crystals are not synthetically accessible. In these cases, only the orientationally (powder) averaged diffraction data $I(Q)$ are available

$$I(Q) = \int\int I(\mathbf{Q})\ Q^2 \sin\theta\, \mathrm{d}\theta \mathrm{d}\phi. \tag{2.1}$$

$I(Q)$ is thus the Fourier transform of the one dimension pair correlation function:

$$I(Q) = \int\int\int G(\mathbf{r}) \exp(i\mathbf{Q}\cdot\mathbf{r})\ Q^2 \sin\theta \mathrm{d}\theta \mathrm{d}\phi \mathrm{d}r = \int 4\pi r^2 G(r) \exp(iQ\cdot r) \mathrm{d}r \tag{2.2}$$

where, $G(r) = \frac{1}{4\pi r^2}\int\int G(\mathbf{r})\ r^2 \sin\theta \mathrm{d}\theta \mathrm{d}\phi$. The loss of 3D information is partially compensated for by the higher real-space resolution obtained through the greater experimental accessibility of high Q diffraction data for polycrystalline samples (discussed in Section 2.1.2).

Multi component systems

The formalism developed in Section 1.3 considered the structure as either a series of identical point delta-functions or as a continuous density function. To describe real, multi-element materials it is convenient to augment the identical point delta-functions

by convolving with the atomic scatterer density $w_a(\mathbf{r})$,

$$\rho((r)) = \sum_a \sum_i w_a(\mathbf{r})_i * \delta(\mathbf{r} - \mathbf{r}_j), \tag{2.3}$$

where a is the atom type. The scattering is thus just

$$F(\mathbf{Q}) = \sum_a \mathcal{FT}^{-1}[w_a(\mathbf{r})] \sum_j \exp(i\mathbf{Q} \cdot \mathbf{r}_j). \tag{2.4}$$

The Fourier transform of $w_a(\mathbf{r})$ is known as the 'form factor' for X-rays, and the 'scattering length' for neutrons. Neutrons are (for diamagnetic systems) only scattered by the nuclei. The atoms can be treated to a very good approximation as points and the differing strengths of the interactions can therefore be described by a single scalar value, the neutron scattering length, b_i. The interaction between a nucleus and a neutron depends on the nuclear physics of a system, and so is isotope-specific and has a complex dependence on the nuclear structure. As X-rays are scattered instead by the diffuse electron density, the point scatterer approximation is inapplicable and so the Q dependence cannot be neglected. The form factor $f(Q)$ will of course vary from element to element. As a result, for both X-rays and neutrons, each individual pair correlation $g_{a,b}(\mathbf{r})$ will make a different contribution to the measured scattering. The general expression for the observed scattering is thus for neutrons

$$I(\mathbf{Q}) = \sum_{a,b} c_a c_b b_a b_b \sum_{j \in a, k \in b} \exp[i\mathbf{Q} \cdot (\mathbf{r}_j - \mathbf{r}_k)], \tag{2.5}$$

and for X-rays

$$I(\mathbf{Q}) = \sum_{a,b} \sum_{j \in a, k \in b} c_a c_b f_a(Q) f_b(Q) \exp[i\mathbf{Q} \cdot (\mathbf{r}_j - \mathbf{r}_k)], \tag{2.6}$$

where c_a is the concentration of species a. For neutrons, the reverse Fourier transform is trivially a weighted sum of the individual pair correlation functions, $g_{ab}(\mathbf{r})$:

$$G(\mathbf{r}) = \mathcal{FT}^{-1}[I(\mathbf{Q})] = \sum_{a,b} c_a c_b b_a b_b \, g_{ab}(\mathbf{r}). \tag{2.7}$$

The inverse Fourier transform is more complex for X-rays, as each element's form factor will have a different dependence upon Q. By assuming an average Q-dependence (*i.e.* $f_a(Q) \approx f_a(0)\langle f_i(Q)\rangle_i$, known as the Morningstar-Warren approximation [294]), an approximate relationship between the atomic pair correlation functions and the Fourier transform of the diffraction data can be found that is robust enough to allow for real-space fitting of the X-ray data in most circumstances.

Atomic displacement parameters

The above description of a structure as a convolution of delta functions with atomic density functions can be extended to account for the harmonic thermal motion of atoms. If the motion is isotropic and harmonic, the broadening due to thermal motion can be represented by a three-dimensional Gaussian function, with a width determined by the mean squared atomic displacement, $\langle u_i^2 \rangle$. By convolving the thermal motion with the atomic positions and taking the Fourier transform, the following expression for the neutron structure factor can be derived:

$$F(\mathbf{Q}) = \sum_a c_a b_a \sum_{j \in a} \exp[i\mathbf{Q} \cdot \mathbf{r}_j] \exp\left[\frac{1}{2} |\mathbf{Q}|^2 \langle u_j^2 \rangle\right]. \tag{2.8}$$

This expression can be easily extended to account for X-ray form factor and anisotropic harmonic motion [15], and the mean squared atomic displacements are the ADPs. As discussed in the introduction, energy-integrated diffraction experiments do not distinguish between static and dynamic disorder—thus the atomic displacement parameters include contributions from both static and dynamic disorder.

Normalisations

Thus far I have not dealt with the issue of normalisation of total scattering data in much detail. Unfortunately, as there is no consensus within the total scattering community of the choice of normalisation it is necessary to briefly discuss the relationship between the functions I have made use of in Chapter 1, $I(Q)$ and $G(r)$, and the most widely used normalisations. The two most widely used normalisations of total scattering data are

$F_{\mathrm{Keen}}(Q)$ and $S_{\mathrm{Keen}}(Q)$, or for neutron data,

$$F_{\mathrm{Keen}}(Q) = I(Q) - \sum_{a,b} c_a c_b b_a b_b, \tag{2.9}$$

$$S_{\mathrm{Keen}}(Q) = F_{\mathrm{Keen}}(Q) \Big/ \sum_{a,b} c_a c_b b_a b_b \ . \tag{2.10}$$

For pair distribution function data,

$$G_{\mathrm{Keen}}(r) = G(r) - \sum_{a,b} c_a c_b b_a b_b = \mathcal{FT}[F_{\mathrm{Keen}}(Q)], \tag{2.11}$$

$$D_{\mathrm{Keen}}(r) = 4\pi r \rho \, G_{\mathrm{Keen}}(r), \tag{2.12}$$

$$G_{\mathrm{PDFGui}}(r) = D(r) \Big/ \sum_{a,b} c_a c_b b_a b_b \ , \tag{2.13}$$

where ρ is the atomic number density. Analogous relationships can established for X-ray data. These functions differ from $I(Q)$ and $G(r)$ in that the self-scattering has been subtracted, *i.e.* the contribution to the scattering due to correlations with $r = 0$ has been removed. For compatability with the literature I have made use of the Keen definitions in my presentation of the experimental results in this thesis. Further discussion of these issues and even further normalisations can be found in Refs. 16, 295, 296.

2.1.1 Measurement of powder diffraction data

In general, most diffractometers utilise radiation of single wavelength (the two most important exceptions being time-of-flight neutron and energy dispersive X-ray diffractometers) and for these it is possible to express the diffraction data as a function of the scattering angle 2θ. The ordinary operation of most diffractometers, whether constant wavelength neutrons, synchrotron or laboratory source X-rays therefore consists of measuring intensity as a function of scattering angle. This can be done by moving detectors, as is done for most ordinary laboratory sources, or by measuring the entirety of the scattering angle range at once, for example using image plates or position sensitive detectors, at synchrotrons.

There are a number of factors that influence the measured intensities beyond those relating to the sample, which need to be accounted for to obtain quantitative structural information. The most important factors are: the Lorentz correction, polarisation of the

radiation, preferred orientation, absorption and radiation damage. I will briefly deal with these in turn.

Lorentz correction

This correction is necessary because diffraction experiments do not necessarily uniformly sample reciprocal space. For example, a 1D detector, or a point detector moved through a single scattering angle will only measure a portion of the Debye-Scherrer cone, and this fraction will decrease linearly with increasing Q. The Lorentz correction is a Q-dependent function which depends only on instrumental geometry [297].

Polarisation

A second correction that needs to be applied for X-rays is due to polarisation. The amplitude with which X-rays are scatted is proportional to the sine of the angle between the direction of the electric vector of the incident radiation and the direction of scattering [297]. The extent of beam polarisation therefore makes an important difference to the measured intensities. Ordinary laboratory diffractometers produce unpolarised X-ray radiation, synchrotron radiation is nearly perfectly polarised and monochromated laboratory sources have an intermediate degree of polarisation. For the standard, Bragg-Brentano, geometry of diffractometers, this leads to a correction of the form:

$$\frac{1 + \cos^2(2\theta_{\mathrm{M}}) \cos^2(2\theta)}{1 + \cos^2(2\theta_{\mathrm{M}})}, \tag{2.14}$$

where $2\theta_{\mathrm{M}}$ is the monochromator angle, and specifies the degree of beam polarisation: $2\theta_{\mathrm{M}} = 0$ for an unpolarised beam and $2\theta_{\mathrm{M}} = 90^\circ$ for a polarised beam. As both the Lorentz and polarisation contributions are entirely dictated by the instrument, they are very often treated together, but their physical origins are unrelated.

Preferred orientation

In the above discussion, I have assumed the sample consists of a 'perfect powder' consisting of micro crystals that are uniformly randomly oriented. If the crystals have very anisotropic morphologies, the powder can consist of partially aligned crystals. This is referred to as preferred orientation, and leads to systematic variations in the intensity of

reflections that are either over- or under-represented by the crystal alignments. Careful sample preparation to avoid preferred orientation is the best solution to this problem, although corrections during refinement are feasible [298].

Absorption

Another factor that can alter intensities is absorption. This affects both X-rays and neutron alike. For X-rays, absorption is most important for heavier elements, and particularly where the energy of the radiation approaches that of an absorption edge. Neutron absorption coefficients are, like the scattering length, highly dependent on the specific isotope, but unlike the scattering length, which varies over a single order of magnitude, neutron absorption cross-sections can vary by over 5 orders of magnitude, rendering some isotopes effectively impossible to measure (*e.g.* ^{157}Gd). For less severe cases, absorption corrections can be ameliorated through careful choice of experimental geometry and post-measurement data corrections.

Radiation damage

A final factor that must be considered, and of particular importance for synchrotron X-ray studies due to their high brilliance, is radiation damage. This is of particular concern for samples containing more fragile moieties and as such has been extensively considered by protein crystallographers [299]. As damage occurs in a chemically specific manner, it can be very difficult to correct for, and so must be minimised by careful experimental design.

2.1.2 Total scattering

Measurement of total scattering data

There are two principal factors that are much more important for total scattering measurements than ordinary Bragg diffraction measurements: the measured Q-range and the accurate measurement of low intensity data.

Q_{max} determines the real-space resolution of the experiment and so the level of structural detail in the PDF. As the maximum value of $2\theta = \pi$, the largest possible Q_{max} for an experiment using radiation of wavelength λ is $Q_{\mathrm{max}} = \frac{4\pi}{\lambda}$. The shorter the wavelength,

the higher the possible real-space resolution. This is particularly important because the 'default' radiation, Cu Kα X-rays ($\lambda = 1.54\,$Å), gives a $Q_{\max} = 8.15\,\text{Å}^{-1}$ which is inadequate to resolve atoms. The highest resolution data are available from central facilities, with high energy beam lines at synchrotrons (*e.g.* 11-ID-B at the Advanced Photon Source, $\lambda_{\min} = 0.143$ Å; XPDF at Diamond Light Source, $\lambda_{\min} = 0.16\,$Å) and the higher energy neutrons available at spallation sources (*e.g.* the Polaris diffractometer at ISIS has an effective $Q_{\max} > 50\,\text{Å}^{-1}$). Laboratory diffractometers equipped with high energy X-ray sources (*e.g.* Mo Kα $\lambda = 0.71\,$Å and Ag Kα $\lambda = 0.56\,$Å) are now capable of providing high quality PDF data. The minimum Q determines the longest observable structural correlation. There is no theoretical restriction on $Q_{\min}$, however instrumental constraints mean that ordinary diffractometers (even at central facilities) rarely approach $Q_{\min} = 0.1\,\text{Å}^{-1}$.

As diffuse scattering is weak and spread throughout reciprocal space, it can be difficult to measure and distinguish from the background instrumental scattering. Careful measurement of both the sample and of the instrumental background with adequate statistics are therefore necessary to obtain reliable diffuse scattering.

Processing of total scattering data

The raw diffraction data require processing to obtain the desired $I(Q)$ because a number of additional factors influence the measured data besides the structures (some of which are discussed in Section 2.1.1). Processing of the data includes subtraction of the instrumental background; correction for non-structural scattering effects, *e.g.* absorption (for neutrons and X-rays); Compton scattering (inelastic X-ray scattering); correction for polarisation and instrumental geometry effects; and scaling and merging the data. There are a number of software packages that can carry out these corrections, most importantly PDFGetX/N [300] and GudrunX/N [296, 301]. In this thesis I have used GudrunX.

2.1.3 Analysis of powder diffraction data

Powder diffraction data can be used to determine a wide-range of information about microcrystalline materials [302]. The key facts that one might want to learn about a sample are first, its periodicity, *i.e.* its unit cell parameters; second, its structure; third, the microstructure of the sample and finally, the composition of the sample. These are

broadly determined by respectively, the positions of the Bragg peaks, their relative intensities, the width and shape of the peaks, and the relative intensity of Bragg peaks from different phases. Powder diffraction data can also be used to monitor the evolution of these parameters with external stimuli, including temperature and pressure [303, 304] or through a reaction *in situ* reactions [305] or even devices *in operando* [237]. Least-squares whole pattern refinement, known as 'Rietveld' refinement [306] when structural information is included and 'Pawley' [307] or 'Le Bail' [308] where only periodicity is used, is the overwhelmingly most important method for extracting these structural parameters. The one-dimensional nature of powder diffraction data means that Bragg peaks, especially at higher Q, often overlap. It is therefore not possible to refine the intensities of all the Bragg peaks independently, necessitating the refinement of the entirety of the diffraction data at once.

Determination of periodicity

This is the first step of any analysis of powder diffraction data from an unknown sample, and is known as 'indexing'. Initially, accurate positions for a number of low Q reflections (*i.e.* those corresponding to long periodicities) must be determined. Assuming all reflections belong to only one crystalline phase, these reflections can then be used to determine the six unit cell parameters. There are now a number of well-established algorithms for this process [309–311].

The proposed unit cell parameters determined through the indexing process can be verified through 'structure-free' refinement, the aforementioned Pawley and Le Bail algorithms. Pawley and Le Bail refinements do not restrain the relative intensities of the reflections, only their positions. They are therefore also useful for the accurate determination of lattice parameters, extracting peak intensities for structure solution and also for establishing what the best possible quality fit would be.

Determination of structure

Structure solution from powder diffraction data is still not routine and relies on high quality data. The standard techniques of structure solution for single-crystal diffraction data can be applied to powder diffraction data (*e.g.* direct methods [312, 313] and charge

flipping [314]) but peak overlap reduces the reliability of the high Q reflections that are necessary for these methods. Structure solution from powder thus makes extensive use of real space methods, where chemical information can be included through constraints and restraints [315, 316].

Very often, a reasonable structural model is already known for the material: whether from single-crystal diffraction or an already solved structural analogue. This can then be used as a starting point for Rietveld refinement to establish more accurate structural parameters. Rietveld refinement differs from Pawley and Le Bail refinements in that information about atomic positions and their ADPs are now included in the refinement. Just as with structure solution, constraints and restraints are useful for making sure the refined models are chemically sensible.

Microstructural information

During a whole-pattern refinement it is also necessary to refine parameters that do not relate to the crystal structure, for example the background, the peak shape and often parameters due to the instrument, such as small calibration errors. Where the data are of sufficiently high quality, these parameters, and in particular the peak shape, can contain useful information. The peak shape is a convolution of a contribution due to the instrument (which can be measured) and a contribution from the sample itself. The sample contribution is determined by the microstructure of the sample, in particular the strain distribution and the particle/domain size and shape. Line profile analysis can therefore yield very important structural information [317]. Correlated disorder can also be detected through the shape of the peaks, for example, low-dimensional ordering is associated with the asymmetric 'Warren' line-shape [318].

Quantitative phase analysis

Powder diffraction can be very valuable for the analysis of mixtures—both for *in situ* reactions [305] and for monitoring of industrial or environmental processes [6]. In these cases the most important question is often the composition of the mixture. The most reliable technique for quantitative phase analysis is multi-phase Rietveld refinement, where the relative scale factors of the different phases are allowed to vary [319]. Quantitative

phase analysis can be very susceptible to systematic errors, particularly those due to absorption [320, 321].

2.1.4 Anomalous scattering

I have so far assumed that radiation is scattered only elastically. While this is generally a good approximation for X-rays, it breaks down where the energy of the photons approach the energy of an absorption edge of an element within the sample*. In those cases, photons interact much more strongly with the atom and so can undergo a number of other processes in addition to ordinary elastic scattering, including absorption, fluorescence, that is absorption and rapid re-emission at a lower energy, and anomalous scattering, where the photon is absorbed and re-emitted at the same energy. Anomalous scattering can be modelled by altering the form factor of the anomalously scattering element by an additive factor Δf—crucially also introducing an imaginary component (f''). The scatterer density will now be complex

$$\Delta f(Q,E) = f'(Q,E) + \mathrm{i}\, f''(Q,E). \tag{2.15}$$

An important consequence of the phase shift in anomalous diffraction is that Friedel's law, $I(\mathbf{Q}) = I(-\mathbf{Q})$ is no longer obeyed. This can be seen by the derivation of Friedel's law.

$$I(\mathbf{Q}) = |F(\mathbf{Q})F(\mathbf{Q})^*|, \tag{2.16}$$

which is simply the Fourier transform of the electron density, $\rho(\mathbf{r})$, so

$$I(\mathbf{Q}) = \left|\left[\int \rho(\mathbf{r})\exp(i\mathbf{Q}\cdot\mathbf{r})d\mathbf{r}\right]\cdot\left[\int \rho(\mathbf{r})^*\exp(-i\mathbf{Q}\cdot\mathbf{r})d\mathbf{r}\right]\right|. \tag{2.17}$$

where $\rho(\mathbf{r})$ is real, $\rho(\mathbf{r}) = \rho^*(\mathbf{r})$, and so Eqn. 2.17 reduces to:

$$I(\mathbf{Q}) = \left|\left[\int \rho(\mathbf{r})\exp(i\mathbf{Q}\cdot\mathbf{r})d\mathbf{r}\right]\cdot\left[\int \rho(\mathbf{r})\exp(-i\mathbf{Q}\cdot\mathbf{r})d\mathbf{r}\right]\right| = |F(\mathbf{Q})F(-\mathbf{Q})|. \tag{2.18}$$

$I(\mathbf{Q})$ is thus invariant to the interchange of $\mathbf{Q}$ and $-\mathbf{Q}$. Where anomalous scattering is significant, $\rho(\mathbf{r})$ is complex, and so this simplification is not possible. Anomalous scattering

*There are similar inelastic and resonance effects for neutrons, but they are less common and will not be discussed further.

therefore is widely used to determine the absolute configuration of crystals [322].

Anomalous diffraction is element specific—only atoms with absorption edges close to the energy of the radiation will scatter anomalously. By measuring diffraction patterns at different energies it is therefore possible to systematically vary the form factors of particular elements within a sample and thus gain additional structural information. A simple example of how anomalous scattering could be used to provide structural information is give below, using rutile structured TiO_2. In rutile, the Ti atoms form a body-centered sublattice [323] and so Ti does not contribute to reflections which break the systematic absence condition for body centring, *i.e.* $h + k + l = 2n$, n an integer. Were diffraction measurements carried out at and away from the K-absorption edge for Ti, those reflections would be unchanged, thus allowing for the determination of the Ti sublattice centering. The additional information that can be gained through multiple anomalous diffraction (MAD) has led to the widespread adoption of MAD phasing for difficult crystal structures, particularly in structural biology [324].

Chapter 3

Parametrising the INVERT approach

In Sections 1.5.4 and 1.6, I outlined the difficulties faced when trying to produce data-driven models of amorphous and nano-structured materials, using *a*-Si as an exemplar. I introduced the idea that a characteristic failure of RMC-based models is an unfeasible diversity in coordination environments, and hence by introducing restraints to minimise the variation between local atomic environments it is possible to produce significantly improved models of amorphous materials, without requiring *ad-hoc* constraints relying on prior knowledge of local geometry [148].

This problem of amorphous structure refinement from PDF can be divided into two distinct but interrelated challenges: the uniqueness of the solution and its accessibility. These can be thought of as features of the multidimensional fitting landscape, where χ^2 varies as a function of the parameters of the configuration (in this case, the atomic coordinates), analogous to a conventional energy surface [Fig. 3.1]. The first, and most fundamental problem, is that the χ^2 landscape possesses multiple, equally deep minima. That is to say, the importance of higher order correlations means that the PDF alone does not contain sufficient information to distinguish between sensible structural solutions [147]. The second problem is that the correct solutions correspond to narrow minima and so occupy a relatively small area of configurational space. In this context, the nanostructure problem becomes how to transform the energy landscape, using generic and transferrable methods, to ensure that the meaningful solutions both lie in the deepest minima and are configurationally accessible.

In this Chapter, drawn from work published in Ref. 290, I explore in greater detail the mechanism by which INVERT actually guides nanostructure refinement, and thus shine light on this second problem of the unfavourable 'kinetics' of RMC refinement, with a view to establishing how the approach might be best developed and applied in future

studies. I begin by describing some of the different possible implementations of the central algorithm and then proceed to explore the question of algorithmic weighting: namely, how does one balance the variance term with respect to the fit-to-data, and how is this balance affected by the presence of more than one type of chemical environment? In addressing this question, I quantify the relative contributions of variance and fit-to-data terms during structure refinement, and this leads us to study the roles of density fluctuations and configurational jamming in the RMC fitting process. I present a parametric study of PDF solution space for the three case studies taken in the original work: C_{60}, *a*-Si and *a*-SiO_2, which serves to highlight the difficulties faced in developing a transferable weighting scheme. I conclude with a discussion of the major challenges and opportunities associated with developing further the INVERT approach in future studies.

3.1 Implementation

At its heart, the INVERT concept involves minimising the variance amongst the individual atomic PDFs, $g_i(r)$, for atoms in equivalent environments. The variance is therefore, for

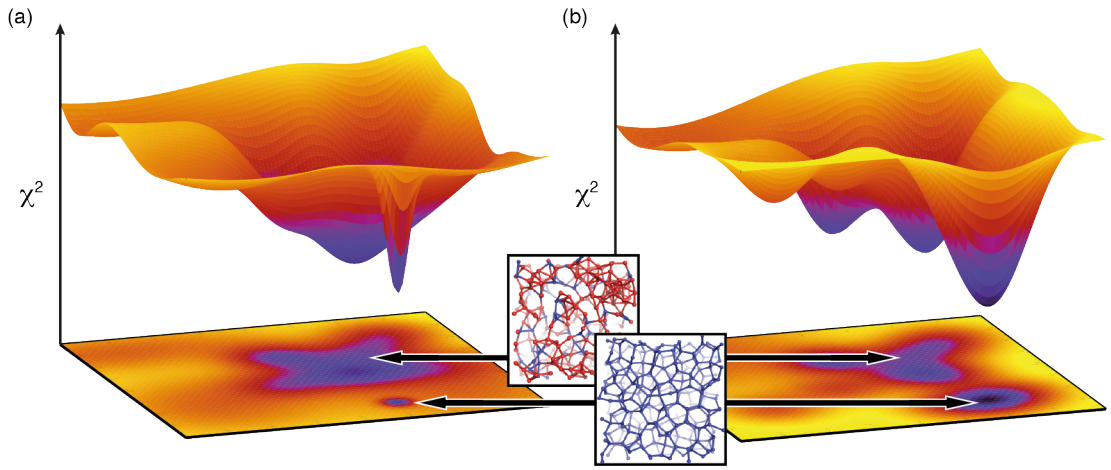

Figure 3.1: Schematic representation of the PDF refinement landscape. (a) Physically unreasonable (mostly red; incorrect local coordination) and sensible (blue; correct local coordination) configurations give rise to equally deep wells in configuration space, but the former are often more accessible. (b) The goal of nanostructure determination algorithms is to reshape solution space so as to increase the relative depth *and* breadth of those minima associated with meaningful solutions.

a single-environment system:

$$\begin{aligned} \mathrm{Var}[g(r)] &= \frac{1}{N}\sum_i \left[g_i(r) - \langle g(r)\rangle\right]^2 \quad (3.1) \\ &= \langle g_i(r)^2\rangle - \langle g(r)\rangle^2. \quad (3.2) \end{aligned}$$

In the limit of zero variance, all of the $g_i(r)$ are equal to the same average $\langle g(r)\rangle$, and hence if this average PDF is also to represent a good fit to the experimental PDF $G_{\mathrm{expt}}(r)$, then this constraint also ensures that each $g_i(r)$ also matches $G_{\mathrm{expt}}(r)$. This suggests a natural implementation of the INVERT approach in the case of a single environment, where the configuration quality is measured by the similarity of each atomic PDF to the experimental function:

$$\chi^2_{\mathrm{INVERT}} = \sum_r \left\{ \frac{1}{N}\sum_i \left[g_i(r) - G_{\mathrm{expt}}(r)\right]^2 \right\}. \quad (3.3)$$

The definition of $g(r)$ and $G(r)$ is important, because the differences amongst the $g_i(r)$ have a r^{-1} dependence for glassy systems [325]; in this work I use the definitions of Ref. 16, which enable direct comparison as suggested above. Recognising then that the standard RMC algorithm involves minimising the function

$$\chi^2_{\mathrm{expt}} = \sum_r \left[\langle g(r)\rangle - G_{\mathrm{expt}}(r)\right]^2, \quad (3.4)$$

it is straightforward to show that Eq. (3.3) reduces to

$$\chi^2_{\mathrm{INVERT}} = \chi^2_{\mathrm{expt}} + \sum_r \mathrm{Var}[g(r)]. \quad (3.5)$$

An extension to multiple environments also follows, assuming initially that the experimental PDF can be decomposed into its constituent partial PDFs $G^{\alpha\beta}_{\mathrm{expt}}(r)$:

$$G_{\mathrm{expt}}(r) = \sum_{\alpha,\beta} c_\alpha c_\beta b_\alpha b_\beta G^{\alpha\beta}_{\mathrm{expt}}(r). \quad (3.6)$$

Here α and β index the different environments (or atom types), and c and b are the corresponding relative concentrations and scattering strengths of those environments re-

spectively. The standard RMC penalty is

$$\chi^2_{\text{expt}} = \sum_r \left\{ \sum_{\alpha,\beta} (c_\alpha c_\beta b_\alpha b_\beta)^2 \left[\langle g^{\alpha\beta}(r) \rangle - G^{\alpha\beta}_{\text{expt}}(r) \right]^2 \right\}, \tag{3.7}$$

and hence

$$\chi^2_{\text{INVERT}} = \chi^2_{\text{expt}} + \sum_r \left\{ \sum_{\alpha,\beta} (c_\alpha c_\beta b_\alpha b_\beta)^2 \, \text{Var}[g^{\alpha\beta}(r)] \right\}. \tag{3.8}$$

This suggests that $(c_\alpha c_\beta b_\alpha b_\beta)^2$ are natural weightings for the variance in each partial atomic PDF $g_i^{\alpha\beta}(r)$. This weighting strategy can be applied even if the individual $G^{\alpha\beta}_{\text{expt}}(r)$ are not experimentally separable.

In deriving the above equations, the implicit assumption is made that the $g_i(r)$ are directly comparable in a meaningful way. In a real material, $g_i(r)$ is a time integral, and so each atomic $g_i(r)$ could resemble the time and configurational average $\langle g(r) \rangle$. The same is not true of course for the static atomistic configurations employed in RMC refinements: the calculated $g_i(r)$ consist of a series of delta functions that can be taken to represent an instantaneous $g_i(r,t)$. Ergodicity allows comparison of the configurational average $\langle g(r) \rangle$ with the experimental $G_{\text{expt}}(r)$, but the same comparison is not meaningful for the $g_i(r,t)$ themselves [Fig. 3.2].

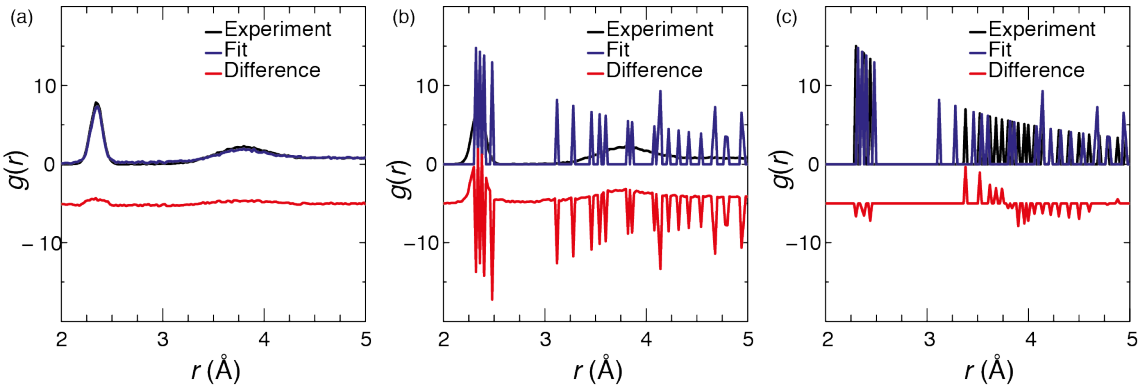

Figure 3.2: Three possible methods for fitting the PDF G_{expt} (black curve): (a) using the configurational average $\langle g(r) \rangle$, which is continuous in r. (b) using an individual atomic PDF $g_i(r)$, which gives rise to a discrete and unhelpful difference function. (c) using a distance list, which gives a discrete but meaningful difference function well suited to atomistic refinement. In each case the fit is shown in blue, and the difference function in red.

One possible approach to resolving this problem is to convolve the $g_i(r,t)$ with a broadening function that represents the effect of thermal motion. For real materials, this motion is correlated and so the corresponding r-dependence would also need to be taken into account [326, 327]. Indeed, the sensitivity of the PDF to some directionality in the phonon dispersion also implies that additional orientation considerations may be required [42, 328]. The only method of unambiguously defining such a function is via direct calculation from a suitable lattice dynamical model [329]—a tractable, if unattractive, solution. However the broadening function is defined, the key disadvantage of this approach is the computational cost of the convolution operation, which must be carried out for each atomic PDF at each step in the refinement.

An alternative approach—and the one I have mostly adopted—is to reformulate the PDF in terms of a distance list. This function is a discretised version of the PDF, which takes integral arguments: $d_{\mathrm{expt}}(n)$ can be defined as the distance r_n for which

$$\int_0^{r_n} 4\pi r^2 \rho\, G_{\mathrm{expt}}(r)\,\mathrm{d}r = n, \tag{3.9}$$

where ρ is the number density. A similar approach has been used in the Liga algorithm described elsewhere [330, 331]. The corresponding INVERT implementation can take one of two forms. Both involve calculating for each atom i of type α the set of distances $d_i^{\alpha\beta}(n)$ to successive shells n of neighbours of type β. The first possibility is to add to the standard χ^2_{expt} function an additional variance term of the form

$$\chi^2_{\mathrm{INVERT}} = \sum_n \sum_{\alpha,\beta} \left\{ \frac{A_{\alpha\beta}}{\langle d^{\alpha\beta}(n)\rangle^2} \sum_i \left[d_i^{\alpha\beta}(n) - \langle d^{\alpha\beta}(n)\rangle \right]^2 \right\}. \tag{3.10}$$

Here the $A_{\alpha\beta}$ represent a suitable weighting for the various partial PDFs (such as discussed above), and the additional $\langle d^{\alpha\beta}(n)\rangle^{-2}$ weighting is included to account for r^2 dependence of the number of neighbours [Fig. 3.2(c)]. I have used this approach for refining *a*-Si configurations. The second possibility is to fit the $d_i(n)$ directly to the $d_{\mathrm{expt}}(n)$ extracted from $G_{\mathrm{expt}}(r)$:

$$\chi^2_{\mathrm{INVERT}} = \sum_n \left\{ \langle d_{\mathrm{expt}}(n)\rangle^{-2} \sum_i \left[d_i(n) - d_{\mathrm{expt}}(n) \right]^2 \right\}. \tag{3.11}$$

This is the general approach I have taken for small molecular clusters (C_{60} and S_{12}), where the experimental $G_{\rm expt}(r)$ function is itself highly discrete and hence ineffective at guiding refinement.

A third possibility for comparing discrete individual PDFs to a time- or configurationally-averaged experimental PDF is to calculate the cumulative PDFs

$$g_i'(r) = \frac{1}{r}\int_0^r g_i(r')\,\mathrm{d}r' \tag{3.12}$$

$$G_{\rm expt}'(r) = \frac{1}{r}\int_0^r G_{\rm expt}(r')\,\mathrm{d}r'. \tag{3.13}$$

This has proved particularly useful for disordered network systems where the configuration box has relatively few atoms: the fluctuations that impede direct fitting to $G_{\rm expt}(r)$ are now smoothed by the integral. In this work, I have applied this cumulative integral approach to the structure solution of *a*-SiO_2.

3.2 Fitting process

While the formulations given in the preceding section suggest a natural weighting for the fit-to-data and variance χ^2 contributions, I was also interested in understanding better the interplay between these two terms during the RMC fitting process, in particular, answering two questions. First, to what extent does each term actually drive the refinement? And second, do the two terms behave similarly for different systems: molecules *vs* networks; systems with a single atom environments *vs* those with multiple-atom environments?

Considering first the "nanostructured" cluster C_{60}, my starting point is a large box containing 60 randomly-distributed C atoms. Because the system is molecular, I do not make use of periodic boundary conditions. The experimental PDF data used in the fit consist only of the portion that corresponds to intermolecular correlations (*i.e.* $r < 7$ Å) [330], and I apply the distance-list implementation of the INVERT variance function as described by Eq. (3.11). The variation in χ^2 components as a function of number of accepted moves is shown in Fig. 3.3(a). What is clear is that the two components behave differently throughout the refinement process. The largest initial changes are found in the $\chi^2_{\rm INVERT}$ term; it is only when this has reached equilibrium that substantive reductions

in $\chi^2_{\rm expt}$ are observed at all. Examination of the configuration at different points in the refinement suggests that the initial decrease in $\chi^2_{\rm INVERT}$ corresponds to the formation of a single contiguous cluster of approximately spherical shape. The solution of the actual chemical structure of C_{60} appears to be almost wholly driven by fitting to the PDF from this point onwards. Consequently, the failure of native RMC approaches to solve the structure of C_{60} from PDF data [148] may largely reflect the difficulty of bringing the atoms together as a single cluster from their initial, random positions.

The corresponding behaviour for the disordered network solids *a*-Si and *a*-SiO_2 is illustrated in Fig. 3.3(b,c). In contrast to the trends observed for C_{60} it seems that improvements to the fit-to-data and variance terms are more strongly coupled in these systems. If there is an obvious difference it is that the variance component in *a*-SiO_2 shows a more gradual and sustained improvement throughout the refinement. This may reflect the more complex set of variance terms associated with a two-component system. In many ways the trend in $\chi^2_{\rm expt}$ is remarkably similar for the two refinements: a period of rapid initial improvement in fit-to-data (up to *ca* 5000 moves) is followed by a sustained, but noticeably more gradual, improvement that persists throughout the remainder of the refinement.

I will next proceed to demonstrate that for *a*-Si these two refinement regimes reflect a period of initial density redistribution followed by subsequent small reorganisation of an essentially-jammed configuration. The starting point is to consider the evolution in

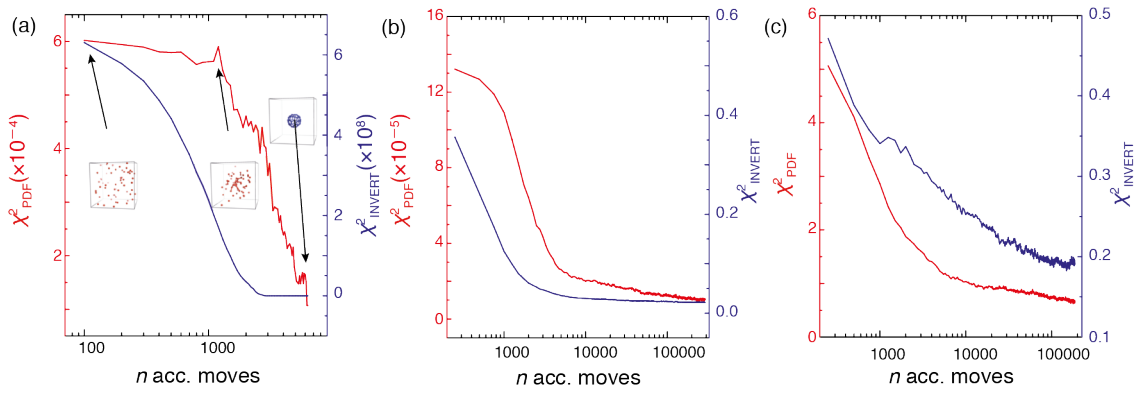

Figure 3.3: Evolution of fit-to-data and variance contributions to χ^2 during RMC refinement of (a) C_{60}, (b) *a*-Si and (c) *a*-SiO_2.

density variance throughout the refinement, which was calculated as follows. The RMC box was subdivided into a set of $50 \times 50 \times 50$ equally-sized voxels (*ca* 0.4 Å each side). The number of Si atoms contained within each voxel was counted, determining a voxel number density $\rho(i, j, k)$, where i, j, k label the voxel in question. The density variance is then given by

$$\mathrm{Var}(\rho) = \sum_{i,j,k} [\rho(i, j, k) - \rho_0]^2, \tag{3.14}$$

where ρ_0 is the total number density. The evolution of $\mathrm{Var}(\rho)$ as a function of accepted moves is shown in Fig. 3.4(a), from which it is clear that the first 5000-move phase of the refinement involves a monotonic reduction in density variance to a level that remains essentially unchanged thereafter. This initial configurational reorganisation is the only phase of the refinement for which large atom moves are accepted; the variation in mean "velocity" (= atom displacement per move) as a function of accepted moves also reflects this result [Fig. 3.4(b)].

That the configuration is essentially jammed after the first 5000 accepted moves is reflected in the histogram of trajectory lengths calculated for different regimes of the refinement [Fig. 3.5]. Considering first the displacements between initial and final atom positions, the median reveals that most atoms have moved approximately 2 Å during the total course of the refinement (145 000 accepted moves). The same histogram calculated for the final 140 000 moves shows a markedly lower median value of less than 1 Å; whereas the corresponding histogram for the first 5000 moves is very similar to the total function, with a median displacement of 1.6 Å. Summing in quadrature yields a total displacement of 1.9 Å, indicating that there is very little correlation between moves in the two phases. So the displacements after 5000 moves reflect small structural reorganisations without any significant changes to network topology. A final comment with respect to this refinement concerns the number of accepted moves themselves. The logarithm of the number of accepted moves is not a linear function of the logarithm of the number of generated moves, but rather is linear over two separate regimes that correspond to fewer than, and more than, 5000 accepted moves.

So what are the implications of the existence of these two regimes of RMC refinement? The obvious concern is that the system does not have the requisite flexibility to explore

configurational space adequately. This means that the atom positions in the final configuration are likely to depend strongly on the fluctuations present in the initial starting configuration. To test this hypothesis, I set up a refinement for *a*-Si for which the initial configuration was based on the structure of crystalline silicon itself. The system was unable to eradicate the bias of its initial periodicity, giving a fit-to-data that was approximately 10% worse than for refinements set up using random initial configurations. The final variance term is similar for both types of refinement (of course χ^2_{INVERT} is initially zero-valued for the crystalline starting configuration), so it is clear that refinement is actually jammed because the total χ^2 value is higher than it might otherwise be. It might be hoped that the appropriate choice of move strategy would be able to reduce the propensity of the refinement to jam. I therefore tried a variety of different maximum move sizes, and also experimented with including a small chance of large moves. This made little difference to the final configurations. Perhaps the most interesting conclusion to be drawn here is that the behaviour of the variance term in the early refinement region—where it is acting to

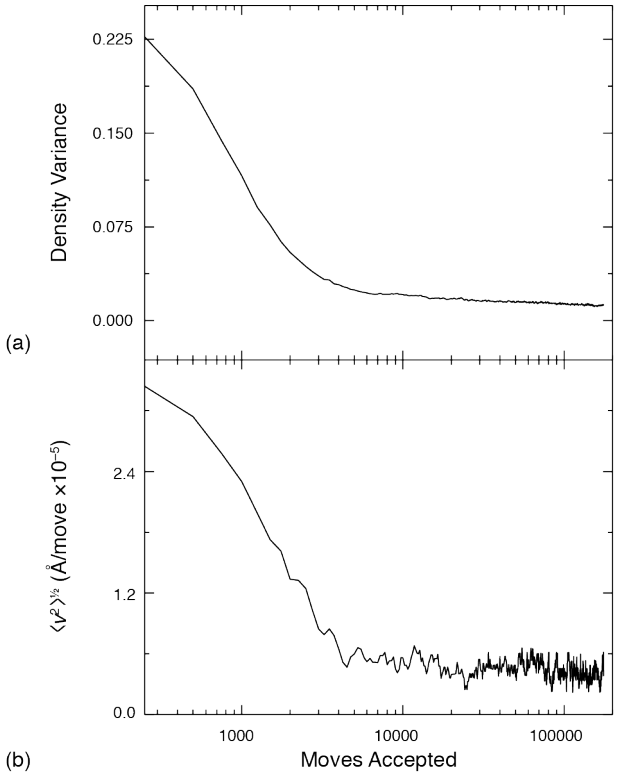

Figure 3.4: Evolution of (a) density variance and (b) root mean squared displacement per accepted move (velocity, v) during RMC refinement of *a*-Si.

increase homogeneity—is advantageous in the case of a molecular system, but may in fact contribute to the jamming problem for networks.

3.3 Solution spaces

I now return to the problem of optimising the relative weights of fit-to-data and local variance χ^2 terms. In previous work, described in Section 1.6, we used an *ad hoc* method to explore the parameter space created by the weightings of these terms. While we obtained satisfactory refinements, it was unclear whether the weightings we had chosen were the optimum values, or indeed how sensitive the solution space was to variation in those parameters. This sensitivity becomes especially important for multi-environment systems where there is no unique transferrable weighting scheme. To understand this, I have explored the refinement "success" for C_{60}, *a*-Si and *a*-SiO_2 as a function of data and variance weightings. The ultimate interest is in the quality of the configuration, rather

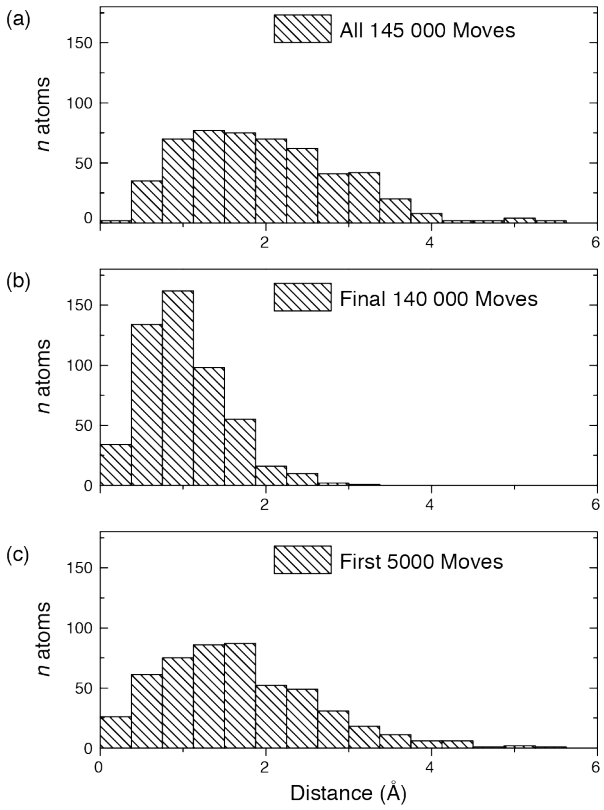

Figure 3.5: Trajectory length distributions for the (a) total, (b) final, and (c) initial RMC refinement regimes of *a*-Si.

than the magnitude of χ^2 (which will vary with relative weightings) and so the number of atoms with the correct coordination number were used as a proxy metric. In the case of C_{60}, configurations with 60 (or nearly 60) threefold-coordinated C atoms universally correspond to good structural models with the expected truncated icosahedral shape. For the network solids, coordination number remains a useful metric, although it is blind to many other unphysical features, such as the existence of triangular ring structures.

C_{60}

The solution space for C_{60} shows a remarkably well-defined plateau that extends across some 14 orders of magnitude of different weighting values [Fig. 3.6(a)]. Convergence appears to be predicated primarily on the INVERT constraint: in particular, in its absence there appears to be no prospect of structure solution. The ability of the INVERT term to drive structure solution by itself is surely a result of the specific implementation used in

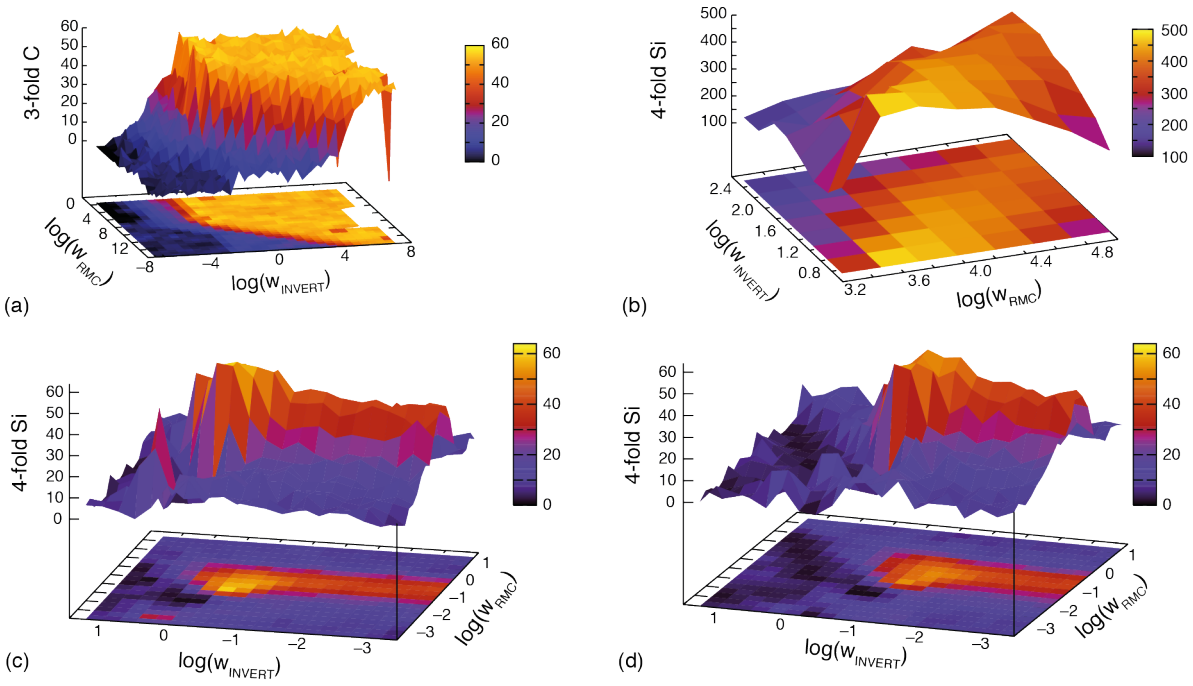

Figure 3.6: . Representations of the solution spaces for refinements of (a) C_{60}, (b) *a*-Si, and (c,d) *a*-SiO_2. Panel (a) shows the number of triply-coordinated C atoms in RMC configurations for C_{60} after 10^6 proposed moves; panel (b) gives the number of fourfold coordinated Si atoms in configurations of *a*-Si (total 512 atoms); panels (c) and (d) give the number of fourfold coordinated Si atoms in configurations of *a*-SiO_2 (total 64 Si atoms and 128 O atoms) with pariwise variance terms weighted equally in (c) but by the relevant $b_i b_j c_i c_j$ terms in (d).

this case: the χ^2 formalism of Eq. (3.11) includes an implicit fit-to-data term. Indeed, the only effect of weighting the data contribution more strongly is to reduce the likelihood of obtaining the correct solution. So it appears that, in this instance, the natural weighting of INVERT and fit-to-data is precisely that needed to obtain a reproducible and accurate structure solution.

Network solids

As suggested by their different refinement behaviour, the parameterisation plots obtained for *a*-Si and *a*-SiO_2 show very different sensitivities to that observed for C_{60} [Fig. 3.6(b,c)]. For both of the network solids, there appears to exist a well-defined optimum set of weights that is not obviously related between the two systems. Moreover, the region of maximum coordination number exists only over a relatively narrow range of weightings, and—especially in the case of *a*-SiO_2—it can also lie adjacent to other regions of very poor solution quality (note the rapid variation in final coordination number observed for different values of $\log(w_{\mathrm{PDF}})$ at $\log(w_{\mathrm{INVERT}}) \sim -1$. As these refinements make use of the INVERT implementation outlined in Eq. (3.10), which does not contain any implicit fit-to-data component, sufficiently high weightings of χ^2_{INVERT} lead to unphysical structures.

Because *a*-SiO_2 contains atoms that exist in two different local environments (Si and O), this system can be used to establish the extent to which its solution space is affected by different weighting schemes for the various pairwise variance terms. I explored two schemes in particular: the first makes use of identical weights for each of the four variance terms; the second applies a weighting based on the $c_i c_j b_i b_j$ terms outlined on page 66. The corresponding solution space plots are given in Fig. 3.6(c,d), where it is clear that their overall form is essentially unchanged by the variation in weighting scheme. Intriguingly, the variation with fit-to-data weighting is almost identical in the two approaches; instead the most obvious difference is the location of the global maximum along the INVERT weighting axis. The difference in optimal $\log(w_{\mathrm{INVERT}})$ values (*ca* 0.75) is much smaller than the logarithm of the square of the $c_i c_j b_i b_j$ terms used (*ca* 3). Consequently, the effective INVERT weighting at the maximum in Fig. 3.6(d) is larger than that at the maximum in Fig. 3.6(c). This suggests that the crucial pairwise variance is relatively weakly weighted amongst the $c_i c_j b_i b_j$. The smallest of these corresponds to the Si/Si

pairs, so the implication here is that it is the arrangement of Si atoms around each other that is critical in defining the structure of a-SiO_2.

Box size

Having established the effects of the various weightings employed during an RMC+INVERT refinement, I subsequently explored the role of configuration box size. To this end, I compared the outcomes for a-Si refinements based on configurations containing 64 and 512 atoms. The variation in box size has a number of consequences for the refinement strategy. Clearly the speed of convergence is much faster for small boxes but there are more subtle differences in the refinement process as well. The quantity of data used in the fit also differs, for example, because $r_{\max} \propto N^{1/3}$, and the discreteness of the calculated PDF will also vary with N. These factors cannot necessarily be straightforwardly adjusted for. Nevertheless, the optimal ratio of data and INVERT weighting for both 64 and 512 atom systems is roughly similar (the logarithmic difference between the two weightings is 2.55 for the former and 3.3 for the latter). Consequently the shape of the solution space appears to be largely unaffected by configuration box size.

Data quality

A further question about any kind of data-driven refinement is the extent to which experimental data quality influences the result of refinement. In previous work we showed that it is possible to solve the structure of C_{60} from both idealised data and high quality experimental neutron PDF data (albeit containing a very small number of coordination defects) [Fig. 3.7(a,b)] [148, 330]. To explore this further, I carried out a refinement using PDF data collected on a laboratory Ag-anode X-ray total scattering diffractometer by Dr Milen Gateshki (PANalytical). The much lower flux available from laboratory X-ray sources combined with the intrinsically lower intensity available to X-rays at high-Q due to the Q dependent form factor mean that the resultant PDF had significantly degraded real space resolution. This lower resolution meant that firstly, many of the peaks that were separable in the neutron data were not resolved and secondly, correcting for the intramolecular contribution to the PDF was less straightforward. Despite the lower quality of the data obtained, it was still possible using INVERT+RMC refinement to recreate the

overall shape of the C_{60} molecule, although much of the detailed local structure is incorrect [Fig. 3.7(c)]. The principal difficulty is a consequence of extracting the distance list from experimental PDF data. Small errors introduced into the baseline, when summed, cause significant shifts in the positions of neighbours in the distance list, precluding the complete solution of the molecular structure. This problem is also encountered in the Liga algorithm, which also makes use of distance lists to aid structure solution [155]. The need for care both when measuring experimental data and processing it thus applies just as much to INVERT+RMC refinement as to existing approaches.

The success that this method had in reproducing the general shape of the molecule even where the distance list contains errors led me to try the most extreme case of low resolution, that is, a spherical shell. The PDF of a spherical shell is constant up to the diameter of the sphere, that is $G_{\mathrm{sphere}}(r) = \frac{\rho}{l}$ for $r \leq l$ and is 0 otherwise, where l is the diameter. Using this calculating spherical 'PDF' as the input data for the INVERT+RMC algorithm I obtained, as might be expected, a model that lacked all the characteristic features of the local structure of C_{60}, with neither icosahedral symmetry or the three-fold coordination. Nevertheless, INVERT+RMC was able to reliably recover the spherical shape of the C_{60} molecule, suggesting that PDF-based approaches may be useful for recovering large-scale structural features from data which do not possess atomic resolution.

$\mathbf{S}_{12}$

I conclude this section by flagging the existence of a range of interesting near-solutions in the case of S_{12}. S_{12} was first investigated as an example of a small nanostructured system with a single type of atom in two environments: its ring structure contains equatorial and axial S atoms that have similar nearest-neighbour distances but slightly-different next-nearest-neighbour separations. While the global minimum in configurational space does indeed correspond to the correct structure, the small molecule size results in a number of distinct local minima with intriguing structures (a number of which are shown in Fig. 3.8). Clearly the chemistry of these candidate structures would be very different! I have highlighted their existence here to provide a caveat for small-molecule structure solution using PDF data that the solution space may be densely populated with diverse candidates that have surprisingly similar PDFs, yet have different three-dimensional structures.

3.4 Outlook and conclusions

Arguably one of the most appealing features of the INVERT approach when it was first proposed was the apparent transferability of the same simple idea across the very different "nanostructure" problems of molecular phases and disordered networks. Yet perhaps the clearest results of this extended study have been the demonstration that INVERT can work very differently in these systems and that the balance between favouring local structural invariance on the one hand, and producing the best-quality fit to data on the other hand, is not only fine but is also system-dependent. Furthermore, I have shown that RMC refinement becomes effectively jammed after a relatively small number of accepted moves, such that configurational space is largely unexplored. This has the important consequence that structure solutions may depend on features of the initial configuration; and so the question of whether nanostructure "solution" is possible at all using PDF methods is still unresolved.

But I have also tried to show that there are many feasible implementations of the

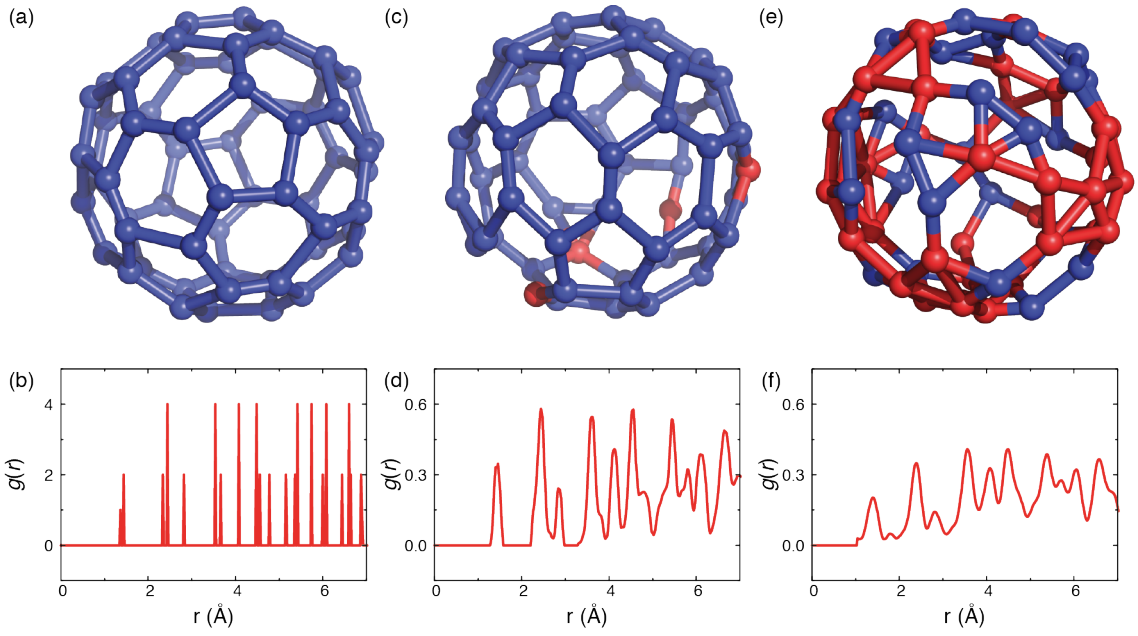

Figure 3.7: The effect of data quality of the INVERT+RMC refined models of C_{60}. A topologically perfect solution is obtained (a) using idealised data (b) but some defects are introduced into the solution (c) when real neutron diffraction data is used (d). The refined model (e) from laboratory total scattering data reproduces only the overall shape of the molecule (f). Neutron data are taken from Ref. 330.

INVERT approach—even within the limited definition of pairwise correlations explored here. It is obvious that the approach is already capable of helping guide refinement (C_{60} being a particularly successful example), and one obvious avenue for further research is to determine more robustly which of the various χ^2_{INVERT} formalisms is most effective in this respect. It may also prove beneficial to re-evaluate the RMC move strategy: in particular, is it possible to sample configurational space more effectively than with small individual moves, thus avoiding the difficulties associated with jammed refinements? For direct, *i.e.* energy based, model building approaches it is already clear that the choice of move is very important to ensure that models are well equilibrated — for example the effectiveness of the WWW algorithm stems from the physical nature of the bond-switch move itself [332] — and similarly, identifying moves that are natural in configurational space could allow for more efficient RMC refinement.

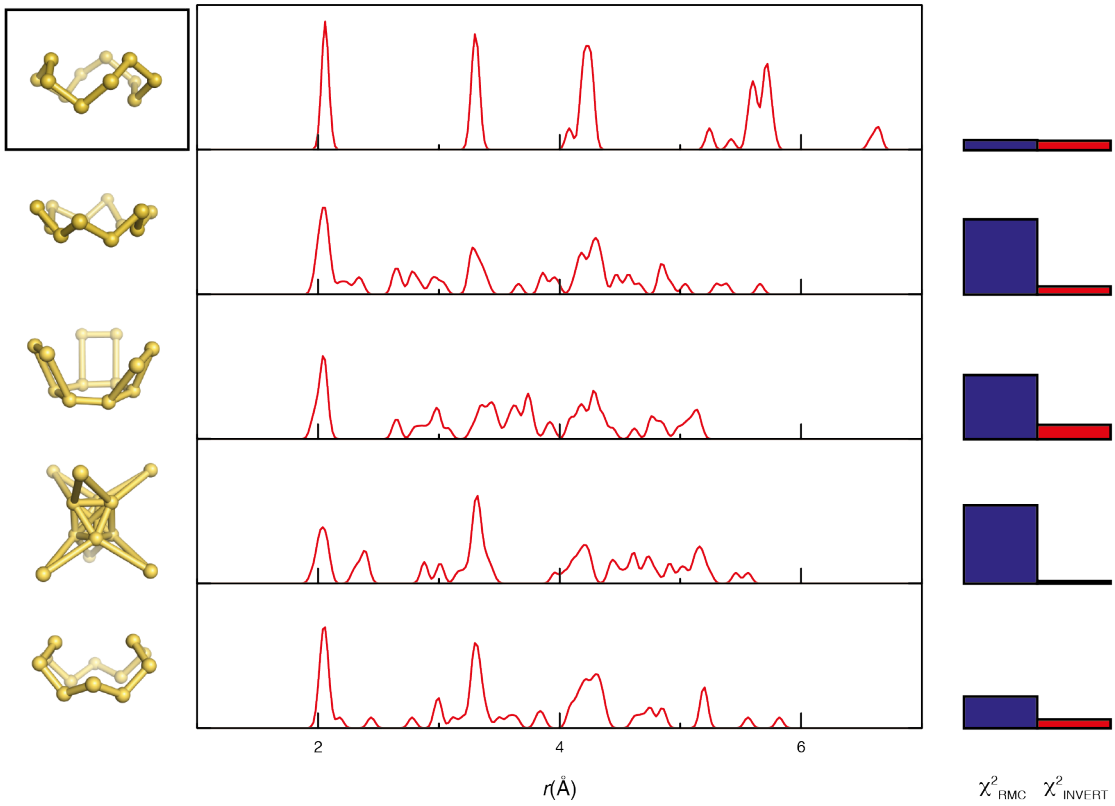

Figure 3.8: Illustrations of molecular geometries and PDFs associated with local minima in the INVERT-weighted configuration space for S_{12}. The blue and red vertical bars represent the corresponding relative magnitudes of, respectively, the χ^2_{expt} and χ^2_{INVERT} terms. The global minimum occurs for the correct geometry, which is highlighted at the top.

Thus far, I have been considering only the simplest possible realisation of the idea of structure invariance, that is, minimising the variance in the atomic PDFs. The clearest limitation of this implementation of the INVERT algorithm is therefore the reliance sole of pair correlations as a descriptor of structural features. One route for improving data-driven models of amorphous materials is therefore extending the concept of structural invariance to include higher-order correlation functions.

Chapter 4

Structural simplicity in disordered materials

In the previous Chapter I explored the extent to which the idea of 'invariance of environment' can act as an effective constraint on the data-driven refinement of the structures of disordered materials. I showed that although this "INVERT" approach is able to produce significantly better models of *a*-Si and *a*-SiO_2, the implementation of this idea as a constraint minimising the variance between atomic PDFs still produced models of amorphous materials that included significant unphysical features. These failures are obvious in both the higher order correlation functions, *e.g.* the bond-angle distribution, and the high level of structural complexity of the refined models.

In this Chapter I show the 'INVERT' approach can be generalised to the idea of simplicity as a constraint on structure and explore how this can be used to understand the higher-order correlations. I will first suggest two new measures for assessing the quality of atomistic configurations: both of which are based on quantifying the orientational distribution of neighbours around each atom in the configuration. The first is geometric invariance: *i.e.* the extent to which the neighbour arrangements are as similar as possible for different atoms, allowing for variations in frame of reference. I describe two possible implementations of this metric. The second metric concerns the degree of local symmetry. I propose that for a set of configurations with equivalent pair correlations, ranking highly those configurations with low geometric invariance and high local symmetry selects for structural simplicity in a way that does not rely on formal group theoretical language (and hence long-range periodic order). I show that these metrics rank a range of SiO_2 and *a*-Si configurations in an intuitive manner, and are also significantly more sensitive to unphysical features of those configurations in a way that metrics based on pair correlations are not. I finally demonstrate that by implementing these metrics as constraints in an RMC refinement against pair distribution function data it is possible to produce more realistic atomistic models of *a*-Si and that, in particular, these models recover characteristic features

of the true higher-order correlations functions. I end by discussing some of the challenges that still need to be tackled for RMC to become a viable method for the structure solution of amorphous materials.

I have made use of the Smooth Overlap of Atomic Positions (SOAP) distance metric developed by Dr Albert Bartók-Partay and coworkers [333]. Dr Bartók-Partay kindly provided access to his implementation of this metric, which I have incorporated within my own RMC implementation. The spherical harmonics calculations described here made use of the freely available software archive SHTOOLS (*shtools.ipgp.fr*), for which I am also grateful. Much of the work in this Chapter has been published in Ref. 291. I would also like to acknowledge fruitful discussions with Prof. David Drabold and Joe Paddison.

4.1 Introduction

The process of translating the PDF into a three-dimensional structural model in many ways equates to the problem of extracting high-order correlation functions from the first- and second-order correlations (to which diffraction data are sensitive, whether a material is long-range ordered or otherwise). That the PDF constrains the two-body correlations is clear: the nearest-neighbour distances can of course be read directly from the function itself. But a meaningful three-dimensional model requires at the very least an accurate depiction of bond and torsion angles, and the extent to which these higher-order correlations are constrained by the PDF has been questioned for some time [118, 146]. In the limiting cases of long-range periodic order on the one hand, and vanishing two-body correlations on the other, the level of constraint is clear: the higher-order correlations are completely fixed in the former and completely free in the latter (see Section 1.5.4 and Ref. 118). Real disordered materials will lie between these two extremes, corresponding to the situation where a number of meaningfully-different three-dimensional models reflect the PDF equally well.

The question is thus how to sort through these different models to find those most characteristic of the real material. I have argued the number and distribution of atomic environments—information available in principle (and for *a*-Si, in practice) from NMR measurements—provides a powerful constraint on the possible structures of amorphous

materials. The empirical observation that there are only a limited range of atomic environments in any real material is not a new insight, and indeed has been formalised for crystalline materials in 'Pauling's rule of Parsimony'* [334]. This observation itself suggests that for a series of models of a material, all of which are consistent with experimental data, those which are simplest are likely the most realistic. This can be thought of as a instantiation of an even older principle: 'Ockham's Razor'.

INVERT is, as a metric of geometric invariance, able to produce models that are significantly more realistic than previous data-driven algorithms. However, examination of the INVERT refined models reveals that their higher order correlation functions, although significantly improved, *e.g.* there are a lower number of Si_3 triangles, are still unphysical. This failure can be understood simply as the failure of the atomistic PDF as a descriptor able to accurately characterise the three-dimensional local geometry. Just as for the material as a whole, the PDF (or distance list) for a single atomic environment in general underdetermines the three dimensional structure [335]. The atomic pair distribution function is therefore an unsatisfactory descriptor of the local geometry and an incomplete distance metric for the similarity between two local geometries. To be able to fully realise the potential of simplicity as a constraint on structure it is therefore necessary to devise a more intrinsically '3D' measure of local geometry.

This generalised concept of structural simplicity does not simply reduce to the inverse of structural diversity: there are a number of other features that might be regarded as signatures of simplicity. One of those would be symmetry. Amorphous materials are, on the macroscopic scale, completely isotropic and thus possess the point symmetry of a sphere. Locally, however, the environments of the atoms within the material are anisotropic, and thus formally their 'site symmetry' is simply 1 (E). Despite this, for many amorphous materials, a-Si included, the local environment resembles very closely that of a higher symmetry: for a-Si, the 'local' symmetry is approximately T_d. In conventional crystallography, the default assumption is to assume a crystal has the highest possible symmetry consistent with the data, to avoid introducing unwarranted complexity in the model. Thus, the local symmetry in a model of an amorphous material could analogously be seen as a measure

*Originally stated as "the number of essentially different kinds of constituents in a crystal tends to be small".

of configurational quality. Devising a metric to quantify local symmetry would also allow a similar kind of structural sorting.

4.2 Descriptors of local geometry and symmetry

This question of how to appropriately quantify a chemical environment is one that stretches across all areas of computational chemistry, from analysis of disordered materials to the parameterisation of interatomic potentials and fitting of potential energy surfaces [336–338]. The appropriate representation of an environment will depend on the intended application.

As these metrics of local environment are intended to be non-system specific, robust to a wide-range of environments, and, as the ultimate aim is to make use of these metrics in refinement, computationally tractable, my starting point is to begin with a relatively simple metric. The local geometry is, to a good approximation, a combination of the distances between an atom and its neighbours and the angular arrangement of those neighbours. Specification of interatomic distances is straightforward (it is the PDF). Angular distributions are most naturally described using spherical harmonics (which are familiar as the angular part of the hydrogenic atomic orbitals [Fig. 4.1(a)]). By projecting the orientational distribution of neighbours onto a spherical harmonic basis, coefficients that characterise the angular component of the distribution are obtained; in this sense we might consider the spherical harmonic coefficients as quantitative "descriptors" of the angular distribution of interatomic vectors. Spherical harmonics also provide a straightforward means by which to address the problem of "registration" for disordered configurations, *i.e.* the absence of a global set of reference axes. By taking the average of the coefficients $q_{l,m}$ for each spherical harmonic $Y_{l,m}$ over all allowed values m for a given index l, then that average becomes a quantitative descriptor that is rotationally invariant, *i.e.* independent of any set of reference axes. A similar approach is used in the field of computer science when addressing the general problem of three-dimensional shape matching [339, 340].

Formally, the atomic environment of a given atom, i, can be represented in terms of the local distribution function $\rho_i(\mathbf{r})$, given as the sum of Dirac delta functions positioned

at each neighbour position

$$\rho_i(\mathbf{r}) = \sum_j \delta(\mathbf{r} - \mathbf{r}_{ij}), \tag{4.1}$$

where j is a neighbour of i and $\mathbf{r}_{ij}$ the vector from atom i to atom j. A 'cut-off' distance criterion is ordinarily used to distinguish neighbours from non-neighbours, however during the process of refinement, atoms can change their coordination. In practice, therefore, an r-dependent weighting term $w(r)$ is included such that the boundary between neighbour and non-neighbour atoms is continuous. For systems where the coordination environment is well understood, as in the simple cases below, it is convenient to simply set $w(r_{ij}) = 1$ where i neighbours j and $w(r_{ij}) = 0$ otherwise. Discussion about the choice of $w(r)$ follows in Section 4.3

$$\rho(\mathbf{r})_i = \sum_j w(|\mathbf{r} - \mathbf{r}_{ij}|)\delta(\mathbf{r} - \mathbf{r}_{ij}). \tag{4.2}$$

The angular part of this distribution is simply:

$$F_i(\theta, \phi) = \sum_j w(r_{ij})\delta(\theta_{ij}, \phi_{ij}). \tag{4.3}$$

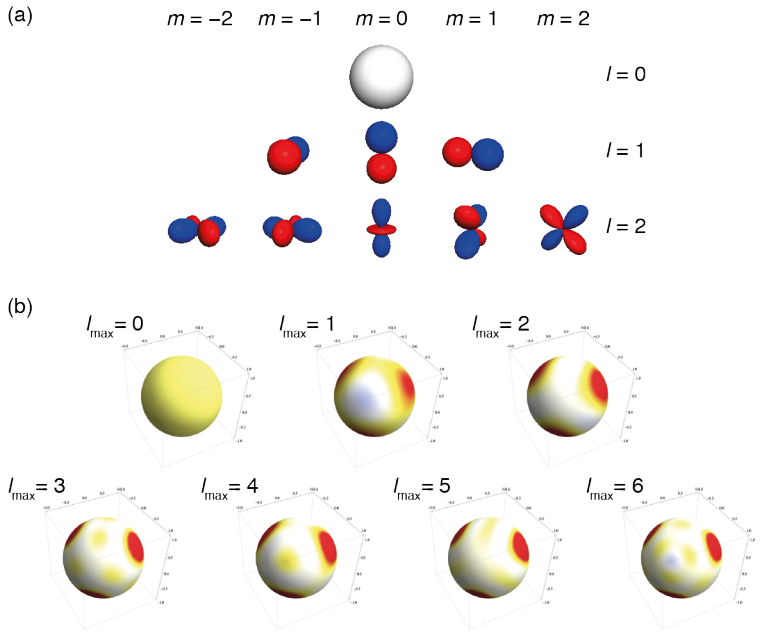

Figure 4.1: (a) Graphical representations of the real forms of the spherical harmonics, displayed as $r = Y_{l,m}$, for values of l up to $l = 2$ (blue represents positive values and red negative values). (b) A demonstration of the reconstruction of a tetrahedral distribution function $F(\theta, \phi)$ by incorporating $q_{l,m}Y_{l,m}(\theta, \phi)$ terms of increasing order l (up to $l = 6$).

Projection onto the spherical harmonics yields the $q_{l,m}$:

$$F_i(\theta,\phi) = \sum_{l=0}^{\infty} \sum_{m=-l}^{l} q_{l,m} Y_{l,m}(\theta,\phi), \tag{4.4}$$

where $Y_{l,m}(\theta,\phi)$ is the spherical harmonic of order l and m. The coefficients $q_{l,m}$ can then be averaged across m and normalised to yield our rotationally-invariant descriptors Q_l:

$$Q_l = \sqrt{\frac{4\pi}{(2l+1)} \left(\sum_{m=-l}^{l} q_{l,m} \right)^2}. \tag{4.5}$$

These Q_l are precisely the quantities used frequently in the fields of amorphous materials and liquids as a means of characterising local geometry [341–343]. There exist relatively intuitive meanings to the Q_l: for example, the $l = 0$ term is a simple measure of the number of neighbours, $l = 1$ describes the extent to which the local environment is polar, and $l = 2$ the extent to which the environment is quadrupolar. The values of Q_l calculated for a variety of common coordination environments are shown in Fig. 4.2.

Having defined this metric Q_l, the degree of dissimilarity between the environments of two atoms i and j the configurational distance $\Delta_{i,j}$ can then be quantified as

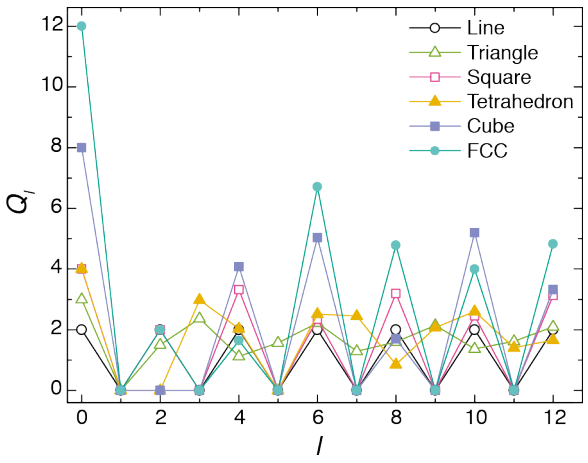

Figure 4.2: Values of the orientationally-invariant descriptors Q_l determined for a range of common high-symmetry local environments.

$$\Delta_{i,j} = \sum_l (Q_l^i - Q_l^j)^2. \tag{4.6}$$

Minimisation of $\mathrm{Var}(Q_l)$ is of course exactly equivalent to minimising the sum over the entire configuration of $\Delta_{i,j}$. An alternative approach for minimising the variation in local geometry would be to devise explicitly a measure of configurational distance without first calculating a descriptor of local geometry. This is the SOAP approach developed in Ref. 333 by Bartók-Partay and coworkers. Perhaps the most general measure of configurational distance between two environments $\rho_i(\mathbf{r})$ and $\rho_j(\mathbf{r})$, is simply the integral over space of their product

$$D(\rho_i(\mathbf{r}), \rho_j(\mathbf{r})) \;=\; \int \rho_i(\mathbf{r})\rho_j(\mathbf{r}) d\mathbf{r}. \tag{4.7}$$

The discrete nature of $\rho(\mathbf{r})$, as defined in Eqn. 4.1, will lead to undesirable discontinuities in D, and to eliminate them $\rho(\mathbf{r})$ is modified by treating each atom as a Gaussian, rather than Dirac delta, function. The modified number density is thus

$$\rho_i(\mathbf{r}) \;=\; \sum_j w(|\mathbf{r} - \mathbf{r}_{ij}|)) \, \exp(-\alpha \, |\mathbf{r} - \mathbf{r}_{ij}|^2). \tag{4.8}$$

The new distance metric D lacks rotational invariance, however, making it unsuitable for application. By integrating Eqn. 4.11 over all possible rotations, $\hat{R}$, a class of new rotationally invariant distance functions can be produced,

$$k_{ij} = k(\rho_i(\mathbf{r}), \rho_j(\mathbf{r})) \;=\; \int \left| D(\rho_i(\mathbf{r}), \rho_j(\hat{R}\,\mathbf{r})) \right|^n d\hat{R}, \tag{4.9}$$

where n is a parameter. For $n = 1$, the order of integration can be reversed and so k reduces to:

$$k_{ij} \;=\; \int g_i(r) g_j(r) dr, \tag{4.10}$$

and so k_{ij} will only provide information about pair correlations. For $n \geq 2$, this simplification is not possible, and so k_{ij} will also contain information about higher order correlation functions. For this work, the simplest case of $n = 2$ was chosen. It is also possible to increase the sensitivity of this measure by raising it to positive power, ζ, which, when

normalised gives the measure

$$K_{ij} = \left(\frac{k_{ij}}{\sqrt{k_{ii}k_{jj}}} \right)^{\zeta}. \tag{4.11}$$

A complete evaluation of k_{ij} would be very computationally intensive. By expanding the angular dependence of k_{ij} as a series of spherical harmonics (as above) and expanding the radial component using a series of orthogonal radial basis functions, it is possible to calculate an approximation to k_{ij}, which can be made arbitrarily accurate by increasing the order of harmonics included. The derivation and exact form of these approximations can be found in Ref. 333. Although in this derivation no descriptor has been assumed, it can be shown that K_{ij} is very closely related to the SO(3) bispectrum descriptor (a descriptor related to the Q_l described above) [333]. K_{ij} is a very appealing measure of configurational distance, as it is derived directly from the intuitive concept that the similarity between two environments is just the 'overlap' between atomic positions. A library for calculating K_{ij} has been implemented by Dr Bartók-Partay and coworkers, to which he has very kindly provided me access.

Having established two implementations of the idea of geometric invariance, I will now develop a third metric that is able to characterise this concept of local symmetry. For crystalline materials, the definitions of local symmetry flow naturally from the formalism of space and point groups. For amorphous materials, this formalism is inapplicable, as they simultaneously have complete isotropic global symmetry and no local site symmetry. A metric for local symmetry therefore must have a number of properties beyond simply being in accord with our ordinary understanding of symmetry: first, like the Q_l it must be rotationally-invariant; second, for two environments with an obvious point group/subgroup relation (*e.g.* tetrahedral and cubic) this ordering should be robustly reflected in the value of the metric; third, the metric should vary in a continuous way for distortions away from ideal point symmetries in order to allow refinement; and, fourth, the metric must be independent of the particular system of interest. This last criterion is necessary to exclude any metrics that have been tailored to a specific geometry—such as tetrahedrality of the angle distribution—because to use such a metric in refinement one would need to decide in advance which metric, and hence which geometry, was appropriate for the system.

The descriptors Q_l already show a number of these essential features: they are rotationally invariant, smooth and system independent. Further, as Q_l are derived from spherical harmonics, they have a natural relationship to symmetry [Fig. 4.2]. For example, for any environment with a centre of symmetry $Q_l = 0$ for l odd.

Inspection of the variation in Q_l for different local symmetries [Fig. 4.2] suggests a possibility for one such metric (although there are likely to be others): namely that the variance in Q_l across l is largest for the most symmetric arrangements. Specifically, higher-symmetry arrangements (*e.g.* cubic or fcc) show a higher degree of variability amongst their Q_l values than lower symmetry environments (*e.g.* triangular). Indeed the requisite point group/subgroup relations also emerge: the cubic arrangement (point group O_h) has many more zero values of Q_l than does the tetrahedral arrangement (point group $T_d \subset O_h$). A large variance in Q_l for high-symmetry environments is straightforwardly rationalised in terms of the observation that such arrangements correspond to a greater degree of "interference" between harmonics, both destructive and constructive. This also suggests that a quantitative measure of symmetry (which we denote S) might be given by the variance of Q_l across l:

$$S^i = \frac{1}{l_{\max}} \sum_{l=1}^{l_{\max}} \left(\frac{Q_l^i}{\bar{Q}^i} - 1 \right)^2, \tag{4.12}$$

where

$$\bar{Q}^i = \frac{1}{l_{\max}} \sum_{l=1}^{l_{\max}} Q_l^i. \tag{4.13}$$

My next step was to verify whether this new metric S quantitatively reflects our understanding of symmetry for real materials. I present here the specific results for the variation in S across a range of tetrahedral SiO_2 polymorphs, but similar results are obtained for many different systems. I focus on silica because of its diversity of polymorph symmetries and also its well-understood group/subgroup relations. Because there are two types of atom in SiO_2 there are in fact four S terms—one for each possible pair of atom types, counting both orderings for each pair individually (*e.g.* arrangement of O atoms around Si atoms; arrangement of Si atoms around O atoms). In all silica polymorphs the tetrahedral SiO_4 geometries are well preserved and so we would expect $S_{\text{Si–O}}$ to remain

essentially constant;* however because the various different polymorphs contain different inter-tetrahedral angles it might be anticipated that $S_{\text{O–O}}$, $S_{\text{O–Si}}$ and $S_{\text{Si–Si}}$ should vary in a manner that depends on the symmetry of the overall crystal packing. These expectations are indeed borne out [Fig. 4.3]. In particular, for all crystalline polymorphs the value of $S_{\text{Si–O}}$ is essentially invariant, and this value is not very much lower in the model of silica glass reported in Ref. 138. For each group/subgroup relation (*e.g.* β-quartz/α-quartz), each of the values decreases. Moreover, the high symmetries of the β-cristobalite and β-tridymite packings (which are well understood to be anomalously high for good physical reasons [50, 344]) are immediately evident from the substantially larger values of $S_{\text{O–O}}$, $S_{\text{O–Si}}$ and $S_{\text{Si–Si}}$. Finally, a random arrangement of Si and O atoms produces very small values of S that essentially represent the uncertainty associated with our calculations.

4.3 Case-study: *a*-Si

Having established suitable metrics both for local geometry and local symmetry, I now proceed to explore how these might be applied to understanding and refining the structure of the canonical disordered system *a*-Si. In our analysis, we make use of six different *a*-Si configurations, each of which contains the same number of atoms and is of the same physical dimensions. The atomic coordinates in these configurations have been chosen

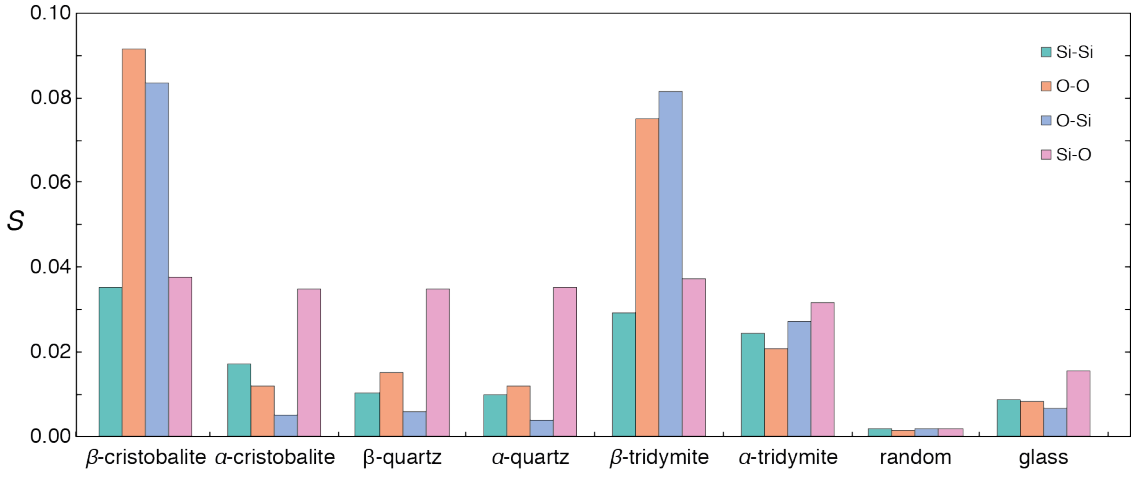

Figure 4.3: Values of the symmetry descriptor S for a number of SiO_2 polymorphs.

*The configurations are based on the average structure for each polymorph, so there are no geometric distortions other than those already present in the crystal structure itself.

or refined in the following ways: (i) randomly; (ii) randomly but with the constraint that no two atoms approach each other more closely than 2 Å; (iii) by fitting this same random configuration to an ideal *a*-Si PDF using RMC; (iv) by fitting to the same PDF using RMC+INVERT; (v) taken from a high-quality WWW model; and (vi) taken from a model of crystalline silicon (modified to have the number density of *a*-Si). For clarity, models (iii), (iv) and (v) all share essentially the same PDF, whereas models (i) and (ii) are too random and model (vi) is too ordered.

I begin by first examining the values of Q_l. As discussed above, for real systems, there are a number of different possible methods for ensuring that Q_l refers to the local environment, corresponding to a choice of the weighting function $w(r)$. Fig. 4.4 compares the successive values of Q_l for each of these six models for three different choices of $w(r)$: first, a hard cut-off at $r_{\mathrm{cut}} = 2.7$ Å, second $w(r) = r^{-4}$ and finally $w(r) = \frac{1}{\sigma\sqrt{2\pi}}\exp(-\frac{1}{2}(\frac{r}{\sigma})^2)$, σ = 1.53 Å. It is immediately clear that the more ordered configurations correspond to more

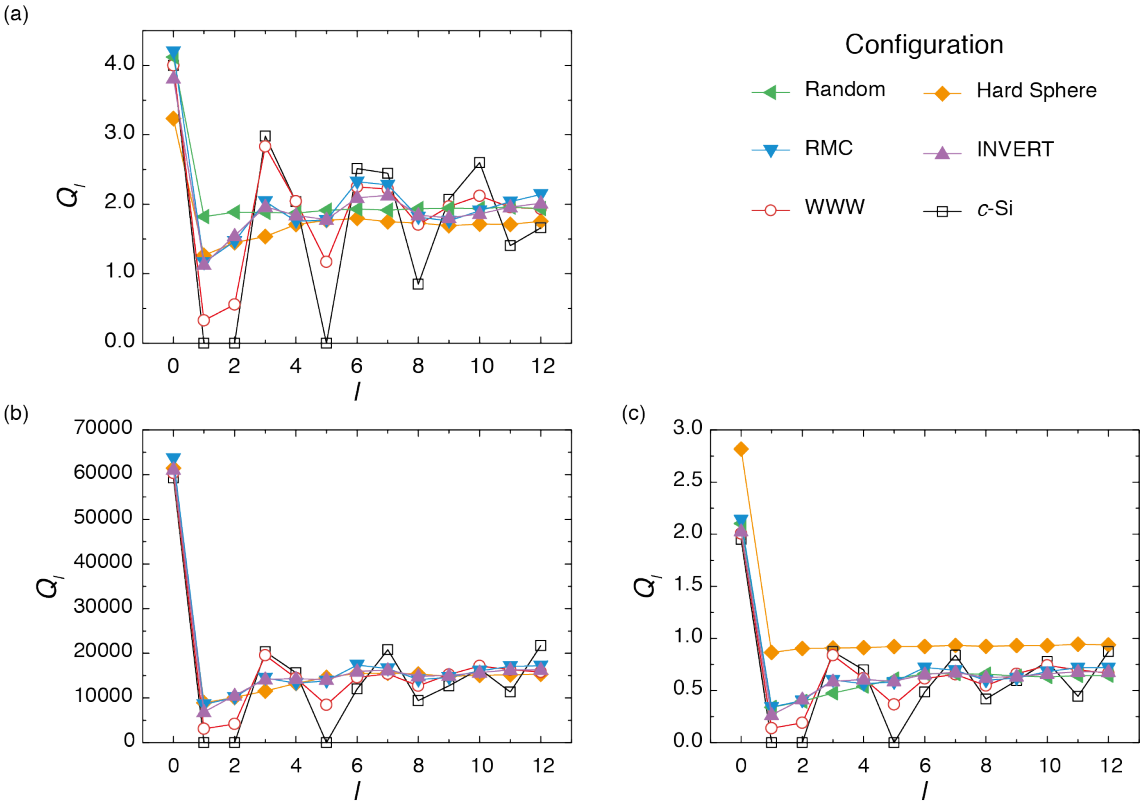

Figure 4.4: Values of Q_l determined for all six Si configurations using different weighting functions $w(r)$: (a) nearest-neighbours only, with $r_{\mathrm{cut}} = 2.7$ Å, (b) all neighbours, $w(r) = r^{-4}$. (c) all neighbours, $w(r) = \exp(-\frac{1}{2}(\frac{r}{\sigma})^2)$ σ = 1.53 Å.

strongly-varying Q_l series. Importantly, while models (iii)–(v) share the same PDF there is a substantial difference in the extent of orientational order in models (iii) and (iv) on the one hand, and model (v) on the other hand. Thus this metric is discriminating for quality of structural model in a way that is not possible using either fit-to-data or local bond length variance as metrics. The choice of $w(r)$ does not have a large effect on the qualitative properties or the ordering of Q_l, although for completeness I note that the value of Q_0 is very sensitive to the choice of weighting.

While Fig. 4.4 shows that Q_l is capable of distinguishing between different configurations of Si, the values of Q_l cannot be used directly as a general constraint on refinement—setting a target value for Q_l is equivalent to assuming the target geometry. Therefore to incorporate this geometric information in refinement I will adopt the assumptions of structural simplicity: by first *minimising* the variance in Q_l values amongst all atoms in the

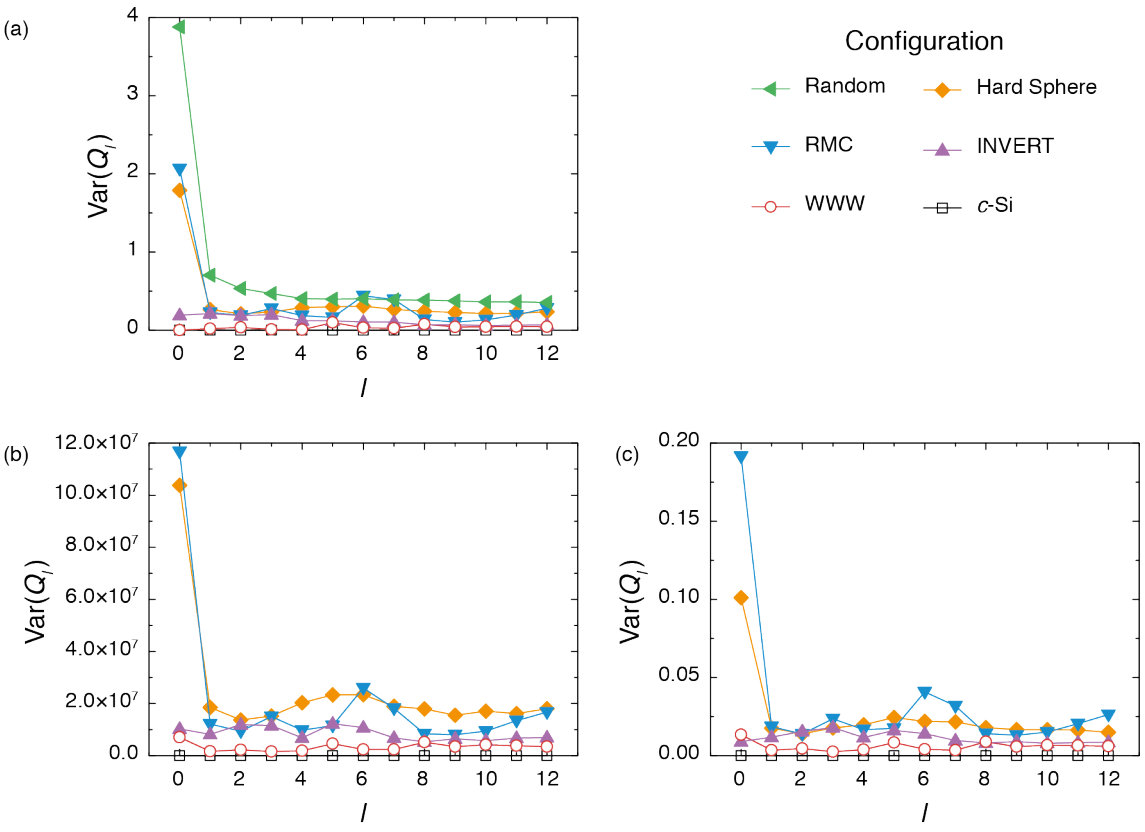

Figure 4.5: Values of Var(Q_l) determined for all six Si configurations using different weighting functions $w(r)$: (a) nearest-neighbours only, with $r_{\mathrm{cut}} = 2.7$,Å, (b) all neighbours, $w(r) = r^{-4}$. (c) all neighbours, $w(r) = \exp(-\frac{1}{2}(\frac{r}{\sigma})^2)$ $\sigma = 1.53$ Å. The random configuration is omitted for (b) and (c) as it is off the scale.

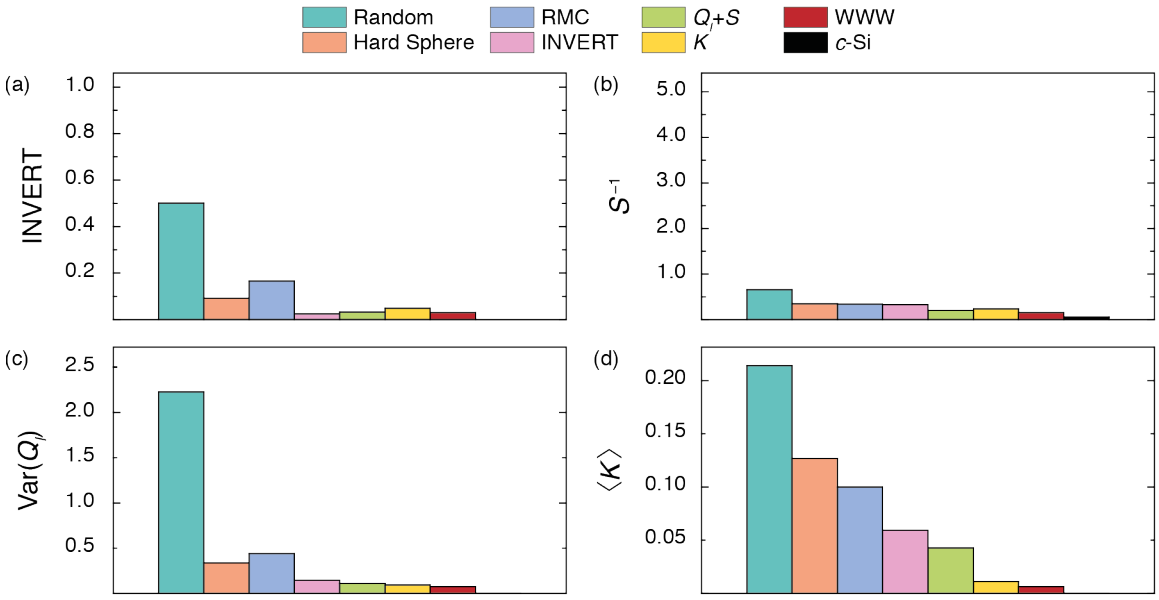

Figure 4.6: Benchmarking of the four metrics of structural invariance using a range of configurations of *a*-Si, arranged from least to most ordered. For each plot the overall scale has been adjusted such that the height of the WWW bar is equal to allow for straightforward comparison. The metrics are: (a) the INVERT PDF variance constraint [148], (b) S^{-1}, the spherical harmonics symmetry measure, (c) $\mathrm{Var}[Q_l]$, the spherical harmonics variance constraint, with a Gaussian r-dependence and (d) $\langle K \rangle$, the SOAP distance measure. The configurations shown consist of models (i) through (vi) described in the main text and two configurations refined using RMC with the new simplicity based measures ($Q_l + S$ and K).

configuration, to ensure that the local geometries are as similar as possible; and secondly by *maximising* the variance in the total (average) Q_l across different values of l, to ensure that this shared geometry has the highest possible local symmetry. While the data shown in Fig. 4.4 suggest that the latter metric behaves appropriately for our five configurations, in order to evaluate the former it is necessary to determine the atomic variance in Q_l for these same configurations. These data are given in Fig. 4.5. Again the expected trend is observed: specifically, the greater the structural simplicity, the lower the $\mathrm{Var}(Q_l)$ values. Note that $\mathrm{Var}(Q_0)$ corresponds to the variance in coordination number; that this value is so large for the RMC configuration helps explain why RMC+INVERT performs so well at improving the RMC-only coordination number distribution [148].

An equivalent comparison can be performed for the symmetry metric S (noting that, in this case, because there is only one atom type there is only one such value for each configuration). The values of S obtained are plotted in Fig. 4.6, together with the variance terms obtained by summing the individual $\mathrm{Var}(Q_l)$ terms of Fig. 4.6. This again leads to

the expected conclusion that S increases as the material becomes more symmetric. Perhaps more surprisingly, the value of S for the RMC+INVERT configuration is very similar to that obtained for the RMC-only refinement, suggesting that the INVERT implementation of Ref. 148 does little to increase the symmetry of Si arrangements. This is illustrated by Fig. 4.7, which shows a section of an RMC+INVERT configuration coloured according to the three metrics: the original INVERT term that characterises variance in interatomic separations, the variance in local Q_l values, and the symmetry metric S. This reveals that the three metrics are orthogonal: parts of the configuration that are ranked highly by one are often ranked poorly by another. It is also clear that the symmetry metric S has substantially different character to the two variance constraints. This is a promising result, since it suggests that the symmetry metric captures some important aspect of local structure in real CRNs that must surely be maximised in any eventual refinement strategy.

The ability of the SOAP distance metric, K, to effectively distinguish between atomic environments has been previously demonstrated for a number of molecular clusters [333]. The logical extension, therefore, is to consider how K compares to the Q_l based simplicity metrics for a-Si. Calculation of K for the set of six Si configurations (i)-(vi) revealed that it was very effective at discriminating between the local geometries in a-Si, suggesting that it might be successful as a constraint used alone [Fig. 4.6].

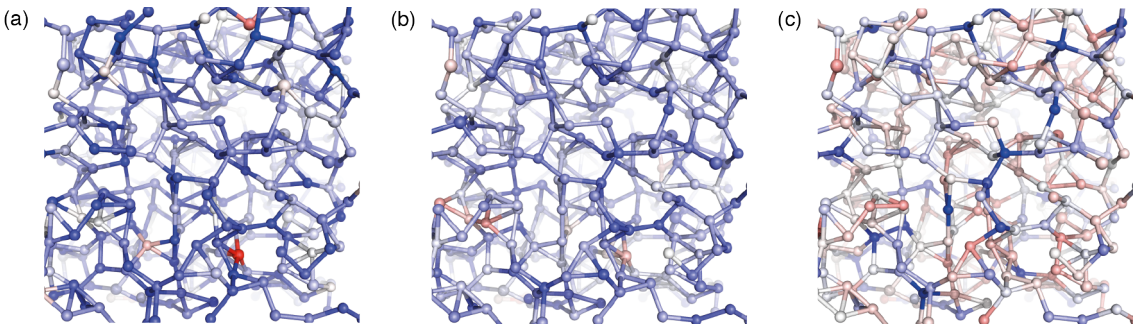

Figure 4.7: A single configuration of *a*-Si produced using the INVERT+RMC of Ref. 148, with each panel coloured according to the goodness of fit for each of three metrics (red is worse, blue is better): (a) PDF variance, (b) $Q(l)$ variance, and (c) S symmetry measure.

4.4 Refinement

The final step was then to implement these new metrics as constraints within an RMC refinement. As before, I used *a*-Si, as a model system, as it is perhaps the simplest system in which higher-order correlations dominate the structural motifs. Use of this system also facilitates direct comparison with the previous work carried out on *a*-Si, and as such I am using an identical configuration size to those of Chapter 3 and Section 1.6.

4.4.1 Constraining with INVERT+Var(Q_l)+S

I began by exploring the implementation of the metrics based on Q_l. Initial trials suggested that the 'non-collinearity' of the INVERT, Var(Q_l) and S metrics highlighted in Fig. 4.7 is also borne out through the process of refinement. In order to maximise structural simplicity it is therefore necessary to incorporate all three of these local metrics as constraints on refinement. This yields the following overall cost function, noting that in this instance that the metric S is to be *increased* rather than decreased during refinement:

$$\begin{aligned}\chi^2 = & w_{\mathrm{PDF}} \sum_r [G(r) - \langle g_i(r) \rangle]^2 + w_{\mathrm{INVERT}} \sum_r \mathrm{Var}_i[g_i(r)] \\ & + w_{Q_l} \mathrm{Var}_i[Q_{l,i}] + \frac{w_S}{\langle S \rangle}.\end{aligned} \tag{4.14}$$

The initial trial refinements suggested that a sensible choice of weighting scheme is very important. I found that the straightforward r cut-off approach was not suitable for use in refinements and also that the r^{-4} weighting—theoretically attractive due to its relationship with the r-dependence of neighbour density and the ease of calculation—was also unsuccessful in producing well-converged refinements. This appears to be due to the asymptotic behaviour as $r \to 0$, and so the Gaussian weighting was chosen (as it tends to a finite limit at low r). This weighting scheme will incur a computational penalty, as the calculation of exponential functions is relatively slow. For this algorithm, the slowest step is the calculation of the coefficients $q_{l,m}$ and so the additional computation due to the weighting proved insignificant in terms of algorithmic speed.

By making use of this Gaussian weighting function and composite objective function,

it was possible to produce refined configurations that had begun to minimise the values of the individual contributions to χ^2. As in the previous Chapter, I found that the refined configurations were very sensitive to the chosen relative weightings of these different metrics. This meant producing a set of weightings where all four constraints were able to direct the refinement was crucial. Unfortunately, as there are now four distinct contributions to χ^2, the parameter space is very large and so an exhaustive grid search parametrisation (as was shown for a-Si and a-SiO_2 in Chapter 3) would be prohibitively slow. The calculation of the $q_{l,m}$ coefficients also imposed a significant speed penalty on the evaluation of χ^2 relative to pure RMC or RMC+INVERT refinements. Additionally, the inclusion of these additional geometry based metrics did very little to avoid the problems associated with 'jamming' described in Chapter 3, which meant that a very large number of proposed moves was necessary to produce models near the minimum associated with a choice of weightings. I therefore adopted a limited design-of-experiments type approach in an attempt to produce a set of relative weightings of the constraints able to produce the highest quality configuration. Despite the difficulties outlined above, it proved possible to find a set of weightings that produced refined configurations where all four contributions to χ^2 began to approach those expected for an ideal configuration.

4.4.2 Constraining with K

The apparent success of the SOAP K metric in distinguishing different models of Si led me to test it as the sole additional constraint on RMC refinement, utilising the following cost function:

$$\chi^2 = w_{\mathrm{PDF}} \sum_r [G(r) - \langle g_i(r) \rangle]^2 + w_K \sum_{ij} K_{ij}. \tag{4.15}$$

As there was now only one relative weighting parameter to adjust, parametrisation of the weightings was much more tractable, and after identifying the range of weightings where both the PDF and the SOAP constraint control the refinement a series of long-duration refinements were carried out. The same kinetic difficulties associated with creating CRNs from random configurations through refinement mean that refinements in excess of 250,000 proposed moves (per atom) are required to produce configurations

which both fit the PDF data acceptably and have values of $\langle K \rangle$ comparable to that of realistic models. Various methods were tried to streamline the refinement, including adjusting move sizes and adjusting the sampling distribution on the basis of the $\langle K \rangle$. I found, however, that simple simulated annealing, together with a dynamic adjustment of the weightings to maintain $w_{PDF}\chi_{PDF} \approx w_{\langle K \rangle}\chi_{\langle K \rangle}$ were the only methods that with any significant effect on the resultant configuration quality. Through implementing these methods it was possible to produce configurations that fit the PDF comparably well to those obtained through unconstrained RMC, and had values of $\langle K \rangle$ about 50% above the reference WWW configuration.

4.4.3 Refined configurations

Despite the difficulties in ensuring complete convergence, I was able to produce models that were consistent with the PDF data and were approaching the levels of structural simplicity seen the WWW models, by the metrics of structural simplicity, both by combining the INVERT, Var(Q_l) and S constraints and by using the SOAP distance, K, alone [Table. 4.1].

But are these configurations also more physical than those produced by INVERT+RMC? Examination of the higher-order correlation functions, in particular the bond angle distribution reveals both configurations have bond angle distributions dominated by a single peak at $\cos(\theta) = -0.3$, *i.e.* centred at the tetrahedral angle [Fig. 4.8]. In contrast to the previous models, the peak at $\cos(\theta) = 0.5$, corresponding to the presence of Si_3 triangles, is practically absent, showing that a number of the unphysical features associated with previous models are disappearing. Evaluation of the energy of these configurations using the Stillinger-Weber potential, a widely-used classical potential, revealed that as expected, the WWW configuration has the lowest energy of the noncrystalline configurations, but that the SOAP constrained configuration has the lowest energy of all the data-driven configurations, followed by that of the combined Q_l+S configuration [Table 4.2] [132]. The improvement in energy is particularly notable in the 3-body potential.

The improvement in the models is also clear from their electronic properties calculated using a tight-binding model [137, 345] [Fig. 4.9]. Although the K and $Q_l + S$ models are still metallic, the major features of the a-Si density of states can now be distinguished.

The lack of band-gap in the data-driven models is not surprising, as the large number of coordinative defects (*ca* 15%) will introduce a large number of gap states [346]. These configurations do demonstrate that the combination of the experimental PDF and density with 'structural parsimony' does allow for the extraction of information about higher order correlation terms, even for systems lacking in long-range order.

Configuration	$\log_{10}\chi^2_{PDF}$	$\log_{10}\langle K\rangle$	$\log_{10}\langle Q_l\rangle$	$\log_{10} S^{-1}$	$\log_{10}$ INVERT
WWW	−4.58	−2.19	−1.11	−0.82	−1.52
c-Si	−1.76	†	†	−1.26	†
Random	−3.86	−0.67	0.35	−0.18	−0.30
Hard Sphere	−3.89	−0.90	−0.47	−0.46	−1.03
RMC	−5.93	−1.00	−0.35	−0.47	−0.78
INVERT	−5.17	−1.22	−0.83	−0.48	−1.61
$Q(l)$+S	−5.18	−1.37	−0.95	−0.69	−1.49
$\langle K\rangle$	−6.08	−1.95	−1.03	−0.63	−1.31

† 0 to numerical precision.

Table 4.1: Summary of the key fit metrics for a variety of configurations. The high value of χ^2_{PDF} for the WWW configuration results from its narrowed nearest neighbour peak compared to the larger 4096 atom, configuration used to calculate the reference PDF.

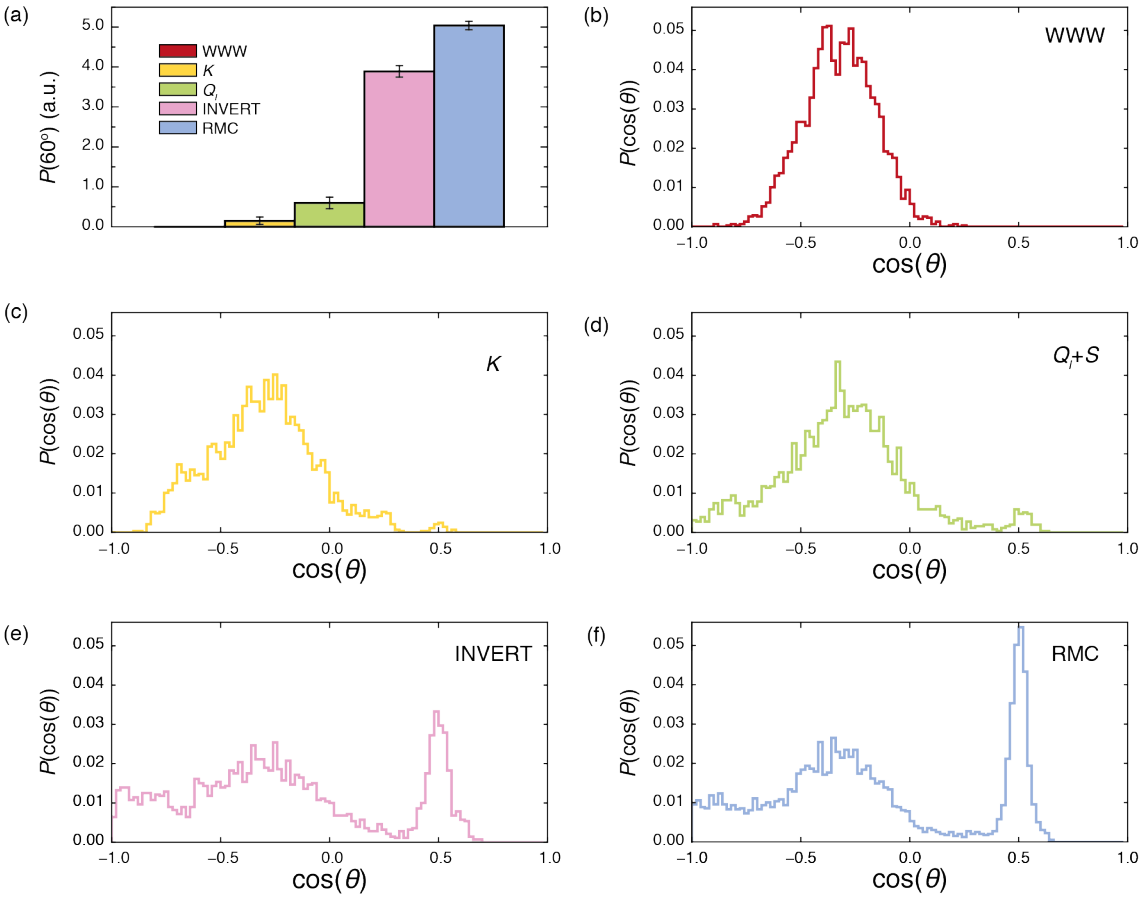

Figure 4.8: The angle distributions of the four RMC refined configurations compared with that of the reference WWW model. (a) The height of the peak at 60°, corresponding to the presence of Si_3 triangles for all five configurations. Values, and standard errors, were derived through Gaussian fitting of the distribution. Histograms of cos(θ) for: (b) WWW and configurations refined against the PDF and constrained by (c) $\langle K \rangle$ (SOAP) (d) Q_l, S and INVERT, (e) INVERT and (f) no additional constraints.

Configuration	E_{pair} (kJ mol^{-1})	E_{tri} (kJ mol^{-1})	E_{tot} (kJ mol^{-1})
WWW	−423	25	−397
c-Si	−418	0	−418
Random	−350	1066	717
Hard Sphere	−440	278	−162
RMC	−457	278	−180
INVERT	−415	187	−227
$Q(l)$+S	−417	76	−341
$\langle K \rangle$	−431	73	−358

Table 4.2: Summary of the calculated energy per Si for a variety of configurations.

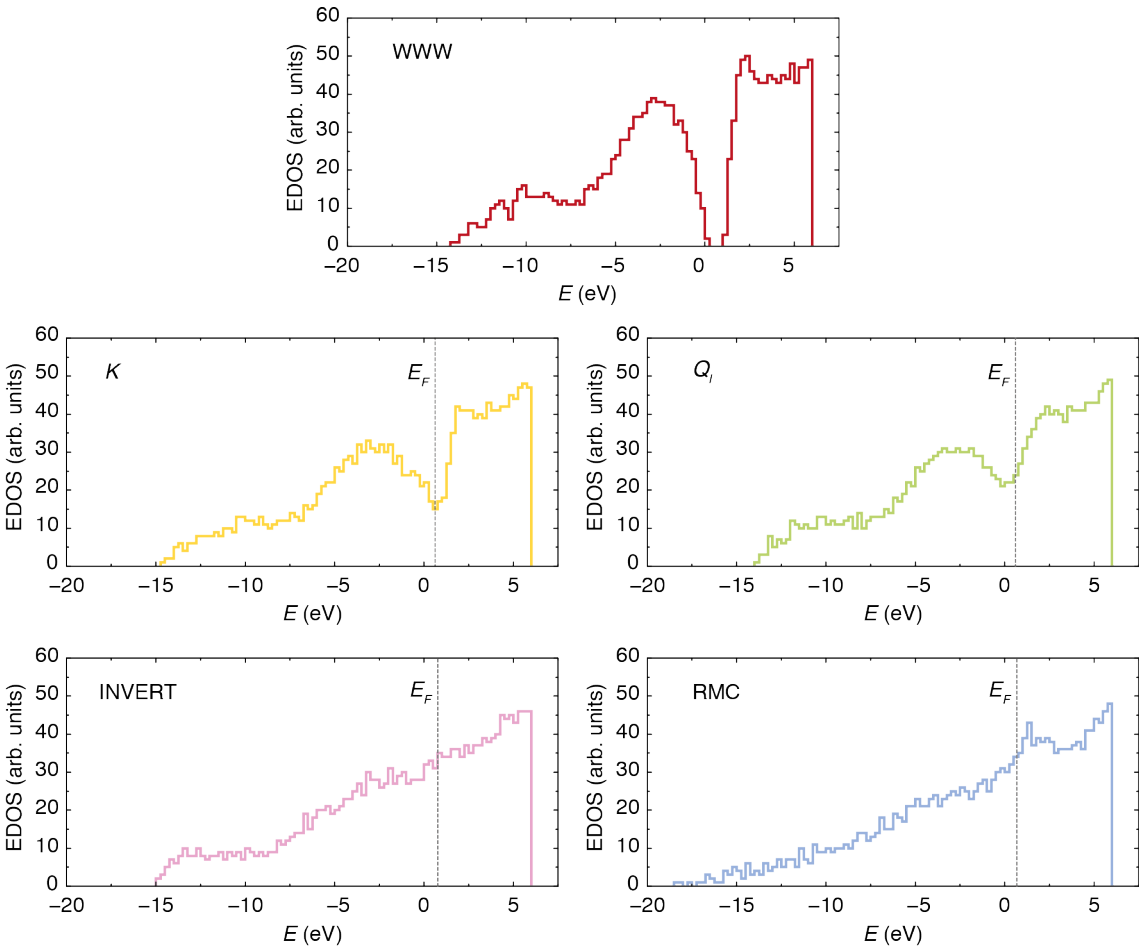

Figure 4.9: The electronic density of states (EDOS) calculated using a tight-binding model of the four RMC refined configurations compared with that of the reference WWW model. (a) WWW and configurations refined against the PDF and constrained by (b) $\langle K \rangle$ (SOAP) (c) Q_l, S and INVERT, (d) INVERT and (e) no additional constraints. The Fermi energy (E_F) is marked by a dotted grey line.

4.5 Conclusions

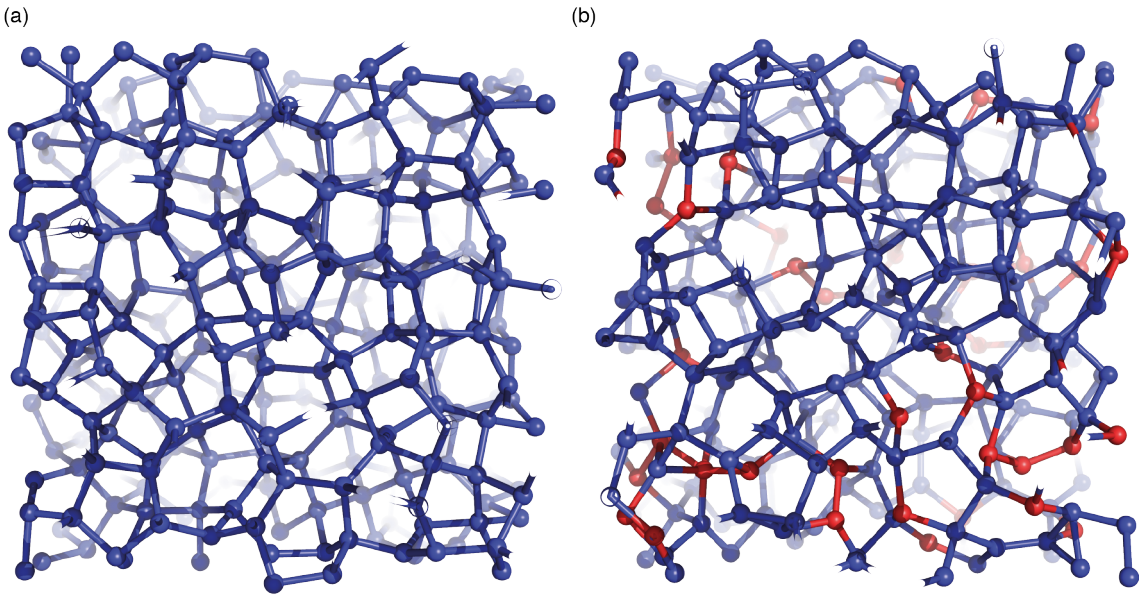

Figure 4.10: Section through the (a) WWW and (b) K configurations. Colour scheme: four-coordinate blue, otherwise red.

The two key results of this work are firstly the demonstration of the existence of meaningful metrics that characterise the local arrangement of neighbours in configurations of highly disordered materials. This approach is independent of "ideal" geometry such that the methods as developed here should be equally applicable to CRNs of arbitrary local symmetry. Secondly, I also introduce the idea of "parsimony"-driven refinement strategy for disordered materials, whereby solutions that are equally consistent with diffraction data are discriminated on the basis of structural simplicity. These new metrics then provide the mechanism by which that level of simplicity can be determined, and show proof of principle that this parsimony-driven approach can be used to produce more realistic configurations and hence extract information about the higher-order correlation functions present in a system, by creating the first data-driven tetrahedral model of a-Si [Fig. 4.10].

The focus here has been on chemically simple systems, but I anticipate that these same general concepts will extend naturally to more complex systems. One such example is plastic phases, in which the constituent molecules have translational order but are orientationally disordered [77]. In such cases one can easily envisage that the orientational distribution functions show strong order over short length scales, and that these distribu-

tions are similar from one site to the next despite the inevitable variation in local reference frame. Finally, these invariants may provide a valuable route for configurational analysis irrespective of whether they are used to drive refinement itself.

Chapter 5

Correlated defect nano-regions in a MOF

In the previous Chapters I have explored how we might use diffraction data to understand the structures of very disordered materials, and shown that structural simplicity can act as a generally applicable guiding principle for refinement. In this Chapter, and the following, I focus on crystalline MOFs, and in particular their potential for correlated disorder. I will demonstrate that we can use diffraction data to uncover the existence of correlated defects in MOFs, that we can exert chemical control over these defects, and that through this control we can influence the physical properties of MOFs.

The material that I have used for this demonstration is hafnium oxohydroxy terephthalate UiO-66(Hf) [347]. The UiO-66 family of materials were amongst the first examples of very chemically and thermally stable MOFs and as such have been the subject of intensive investigation [174]. UiO-66(Hf) is assembled from $Hf_6O_4(OH)_4$ clusters connected by linear terephthalate ligands (1,4-benzenedicarboxylate, bdc^{2-}) in the face-centered cubic **fcu** topology [Fig. 5.1]. This unusually high connectivity has been implicated in the stability of UiO-66 [348]. In addition to its stability, UiO-66 is attractive because of the ease of producing isoreticular analogues—it is facile to substitute both the metal (M = Zr, Hf, Ti, U, Th, Ce, Y or Tb) [174, 347, 349–352] and the ligand [174, 176]. This chemical variation has produced an equivalent diversity in potential applications, from radioactive waste scavenging [347] and CAT scan contrast agent agents [353] to O_2 sensing [354] and Lewis acid catalysis [355]. Many of these more complex materials cannot be synthesised without the addition of acid 'modulators' to the reaction mixture [356]. Modulators, which are typically monocarboxylic acids, such as acetic or benzoic acid, were originally included in MOF syntheses to alter material morphology [357] or control crystallite size [358], but have also proved crucial to synthesising crystalline UiO-66-analogue MOFs [356].

There had been long-standing hints of non-stochiometry in UiO-66 [288], which were

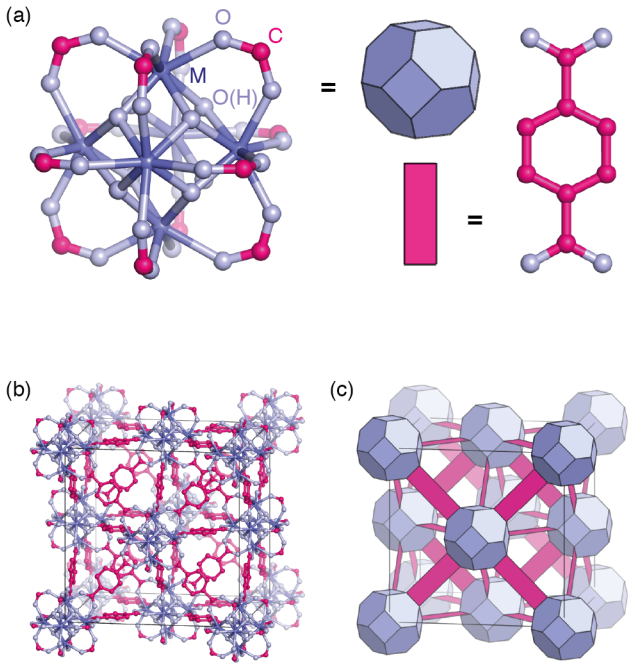

Figure 5.1: Structural description of UiO-66 metal–organic frameworks. (a) The fundamental building unit of the UiO-66 framework type is a six-centre metal cluster, in which eight-coordinate cations (M) are connected *via* carboxylate linkers in an octahedral arrangement. Capping the faces of each M_6 octahedron are eight μ^3-O bridges, of which four are protonated in order to account for charge balance. M atoms are shown in dark blue, O atoms in light blue, and C atoms in magenta. Terephthalate (1,4-benzenedicarboxylate) linkers (a, right) connect these units such that the clusters adopt an expanded face-centred cubic (**fcu**) arrangement, as shown in panel (b). In this topology, each cluster is connected to twelve neighbouring clusters by terephthalate linkers. The colour scheme is as in (a); hydrogen atoms are omitted for clarity. (c) A simplified polyhedral representation of the same network structure. The blue truncated octahedra and magenta rectangles correspond, respectively, to M_6 cluster coordination polyhedra and terephthalate linkers.

confirmed when samples of UiO-66(Zr) and UiO-66(Hf) synthesised with large quantities of modulator were found by neutron diffraction and TGA to contain up to 10% ligand-absence defects [201, 202]. These defects were also found to greatly increase the surface area [202, 212] and the catalytic activity [201].

These early reports of ligand absence vacancies gave no indication that defect correlation could be important for the chemistry of UiO-66. My attention was drawn to UiO-66 because of the presence of structured diffuse scattering in a number of reported PXRD patterns [347, 359–361]. This diffuse scattering takes the form of weak, broad superlattice peaks centred on scattering positions associated with primitive (hkl) reflections that are systematically forbidden for the face-centred cubic structure of the parent framework. The presence of structured diffuse scattering provides a clear signal of the presence of

correlated disorder in UiO-66(Hf). In this Chapter I make use of a range of experimental and computational techniques to uncover the origin of the correlated disorder in UiO-66(Hf). I show that the diffuse scattering observed experimentally cannot be understood completely in terms of guest inclusion and/or linker vacancies but arises instead from correlated vacancies of Hf_6 clusters. By varying the relative concentrations of modulator and linker components, I observe systematic changes in both the coherence length and volume fraction of defect nano-regions. In this way I demonstrate not only that correlated defect structures indeed occur within this MOF, but also that the particular form of these defect structures can be controlled synthetically. This Chapter concludes with details of the experimental and analytical methods used.

5.1 Results

5.1.1 Superlattice reflections

I first synthesised a series of samples of polycrystalline UiO-66(Hf), adapting the methods of Ref. 202, 347 by making use of formic acid as a modulator (see Section 5.3.1 for details). I found that when using a very great excess of formic acid relative to H_2bdc (> 150 fold), the measured diffraction patterns showed features very similar to that of Ref. 347; that is,

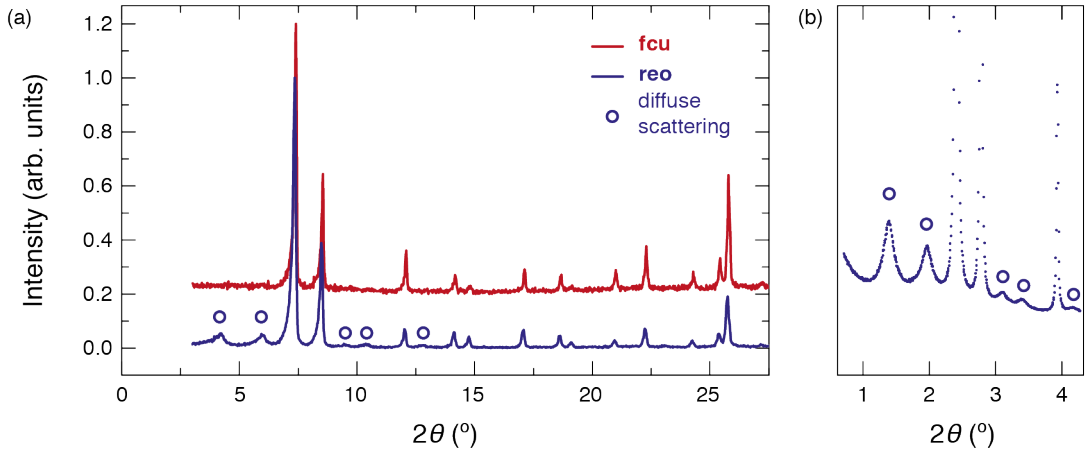

Figure 5.2: (a) PXRD patterns of samples synthesised with (nano-**reo**, blue) and without (**fcu**, red) formic acid modulator added to the reaction mixture. For the sample synthesised with large excess of formic acid, structured diffuse scattering is present in the diffraction pattern in the form of broad, primitive, superlattice reflections (indicated by circles). (b) Synchrotron PXRD pattern of UiO-66(Hf) reported in Ref. 347 ($\lambda = 0.50114$ Å). Diffuse scattering highlighted by circles.

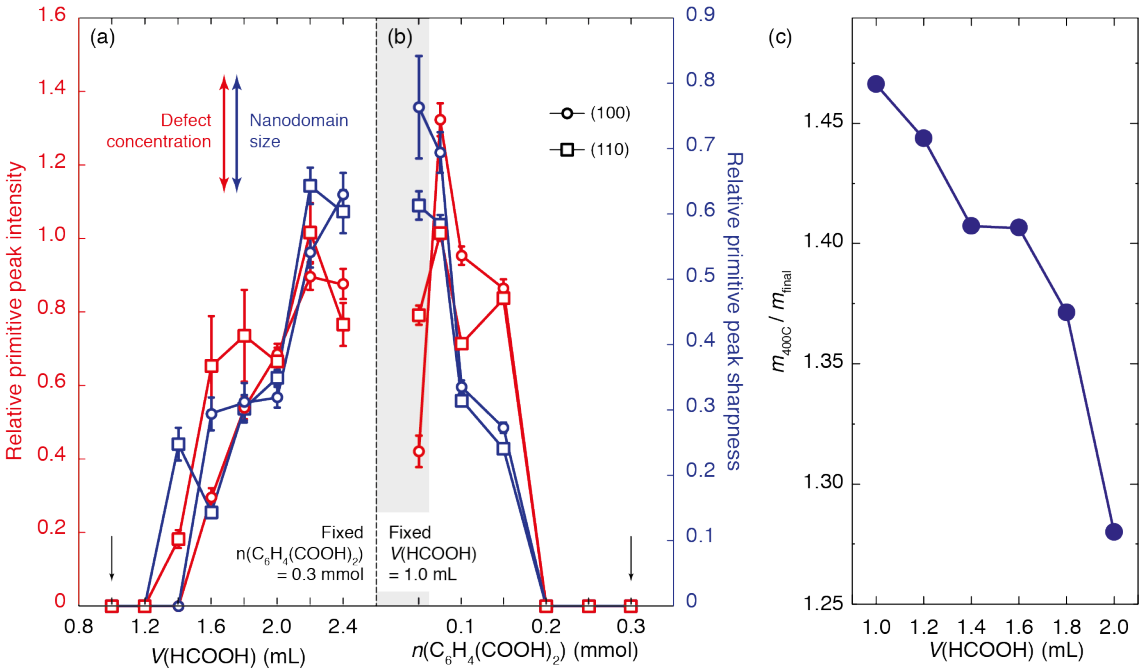

Figure 5.3: Chemical control over defect nano-region concentration and domain size. (a) Increasing modulator (formic acid) concentration for fixed linker concentration during synthesis results in a higher concentration of **reo** nano-regions of increasing domain size, as does (b) decreasing linker concentration for fixed modulator concentration. Points of identical composition are indicated by arrows; the shaded region in (b) corresponds to compositions for which additional phases are present. (c) TGA evidence also shows smaller mass losses on heating for samples synthesised with more formic acid, providing further evidence of defects. Relative primitive peak sharpness values (blue data points) were determined as the ratio of peak widths $\sigma(111)/\sigma(100)$ and $\sigma(111)/\sigma(110)$ extracted from Pawley profile fitting; relative primitive peak intensities (red data points) were determined as the ratio of observed primitive peak intensity to the extrapolated value at maximum defect concentration. The error bars represent standard uncertainties in the mean values.

in addition to the sharp Bragg peaks, the diffraction pattern contains structured diffuse scattering in the form of weak, broad superlattice reflections in primitive positions ($h + k, k + l$, or $h + l = 2n + 1$) [Fig. 5.2]. By varying the concentration of formic acid and H_2bdc in the reaction mixture, it was also possible to systematically alter both the intensity and the breadth of the diffuse scattering: higher concentrations of formic acid and lower concentrations of H_2bdc favoured sharper and more intense diffuse scattering reflections. These superlattice reflections therefore changed in concert with the concentration of ligand absence defects as assessed by TGA [Fig. 5.3].

That this measured diffuse scattering originated from the same phase as the Bragg

scattering was verified by electron diffraction measurements carried out by Prof. Xiaodong Zou and Dr Wei Wan at the University of Stockholm. Although the samples of UiO-66(Hf) were too unstable in the electron beam for high-resolution electron microscopy, electron diffraction measurements showed the presence of both lattice and superlattice reflections in the same crystal [Fig. 5.4(a,b)]. These findings have subsequently been independently verified by Øien *et al.*, in their report of the first synthesis of large single crystals of UiO-66(Zr) [362].

In previous studies of UiO-66 that reported diffraction data containing diffuse scattering, it was speculated that it might arise from the ordering of solvent molecules within the frameworks pores [347]. The scattering occurs at low-Q (0.3–0.5 Å^{-1}) and in systematically forbidden positions, suggesting both that the ordering occurs over a long length scale (on the order of nanometres) and that this order is not solely due to solvent ordering by the framework pore structure. To test this hypothesis I carried out a series of chemical and thermal stability studies. Samples of defective UiO-66(Hf) showing structured diffuse scattering were heated to 300 °C or treated with 1 M acid or base solutions for two weeks. In all cases the superlattice reflections persisted. On this basis I was able to eliminate solvent as the primary cause of the correlated disorder [Fig. 5.5].

As ligand-absence defects are well-known in UiO-66(Hf), and moreover TGA evidence indicated the presence of defects within these samples, their ordering is a logical explana-

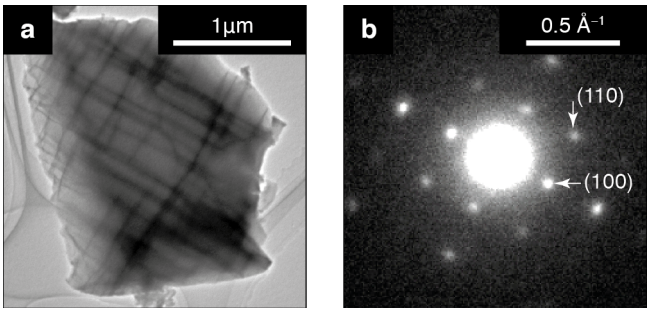

Figure 5.4: (a) Transmission electron microscopy of UiO-66(Hf) crystallites shows a complex microstructure (domain size *ca* 0.1–0.4 μm) with domain walls oriented perpendicular to the $\langle 100 \rangle$ crystal axes. The dark lines at domain boundaries correspond to planes of mass contrast viewed in cross-section and are too thin to contribute to the diffraction pattern. (b) The selected-area electron diffraction (SAED) pattern of the same crystallite shows that the primitive superlattice peaks identified in Fig. 5.2 (i) do not arise from a separate phase and (ii) retain cubic symmetry. The particular example shown here is for the sample with largest defect concentration and nanodomain size.

tion for the observed structured diffuse scattering. The combination of X-ray and electron diffraction measurements put a powerful constraint on the possible ordering structures, as they indicated that there was no evidence for symmetry lowering below primitive cubic. With these constraints on symmetry there are only a limited number of ideal ordering patterns, none of which were able to account for the experimental patterns of diffraction intensity. In particular, the intensity of the (110), and all (hhl) superlattice reflections, was consistently too small across all models [Fig. 5.6].

I therefore examined the possibility that, in addition to ligand vacancies, hafnium cluster vacancies might be present and ordering in such a way as to produce the observed structured diffuse scattering. To demonstrate that hafnium ordering is present in the samples of UiO-66(Hf) I carried out an anomalous scattering experiment, measuring PXRD patterns of UiO-66(Hf) both at the Hf K-edge ($\lambda = 65.3\,\text{keV}$), and away from it ($\lambda = 55\,\text{keV}$). This revealed a subtle but reproducible alteration in the intensities of the primitive superlattice reflections, indicating that Hf ordering must contribute to the observe structured diffuse scattering [Fig. 5.7(a,b)]. The possibility that the Hf cluster itself might be restructuring was dismissed by the use of in-house X-ray total scattering measurements, which confirmed that the cluster remained intact between the defective and non-defective samples of UiO-66(Hf) [Fig. 5.7(c)]. Through this combination of experiments, I was therefore able to establish that UiO-66(Hf) does contain correlated Hf cluster absences.

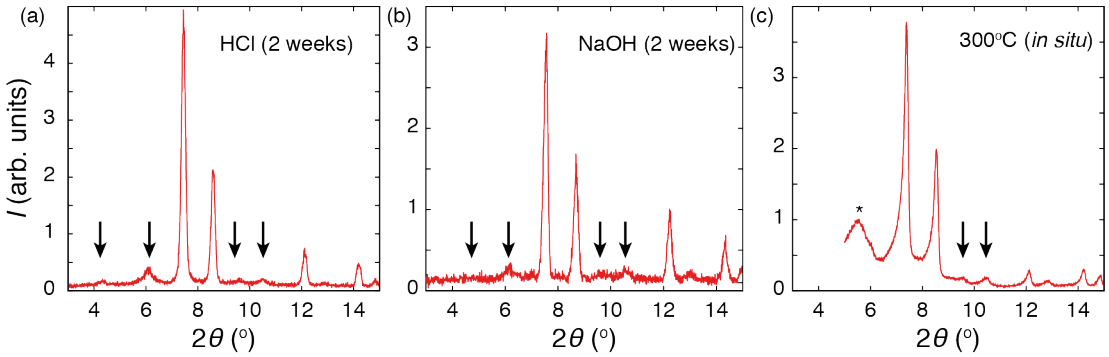

Figure 5.5: Low angle-regions of PXRD patterns of nano-**reo** UiO-66(Hf) after having been treated with (a) 1 M HCl for two weeks; (b) 1 M NaOH for two weeks and (c) heated to 300 ∘C. The locations of primitive reflections are marked by arrows. A broad peak due to instrumental background is marked by an asterisk.

5.1.2 Structural description of defect nano-regions

The question remains, however: what exactly are the short-range correlations responsible for the observed diffuse scattering? Just as systematic absences in the Bragg diffraction patterns of long-range-ordered materials place strong constraints on the corresponding real-space structures, the form of the observed diffuse scattering equally allows for inferences to be made about the short-range correlations present in these UiO-66(Hf) samples. The cubic symmetry of the structure again severely contraints the range of models possible. Coarse-grained Fourier maps reconstructed from the low-angle diffraction intensities of Fig. 5.2 also suggest decreasing cluster occupation at the unit cell origin relative to the face-centred sites with increasing defect concentration [Fig. 5.7(d)].

It can be shown that there are only two possible cluster vacancy modifications to the face-centred cubic structure that preserve cubic symmetry and do not require expanding the unit cell. These are characterised by periodicities along the $\langle 100 \rangle^*$ directions. In the limit of completely absent clusters, one model would consist of vacancies ordered on the

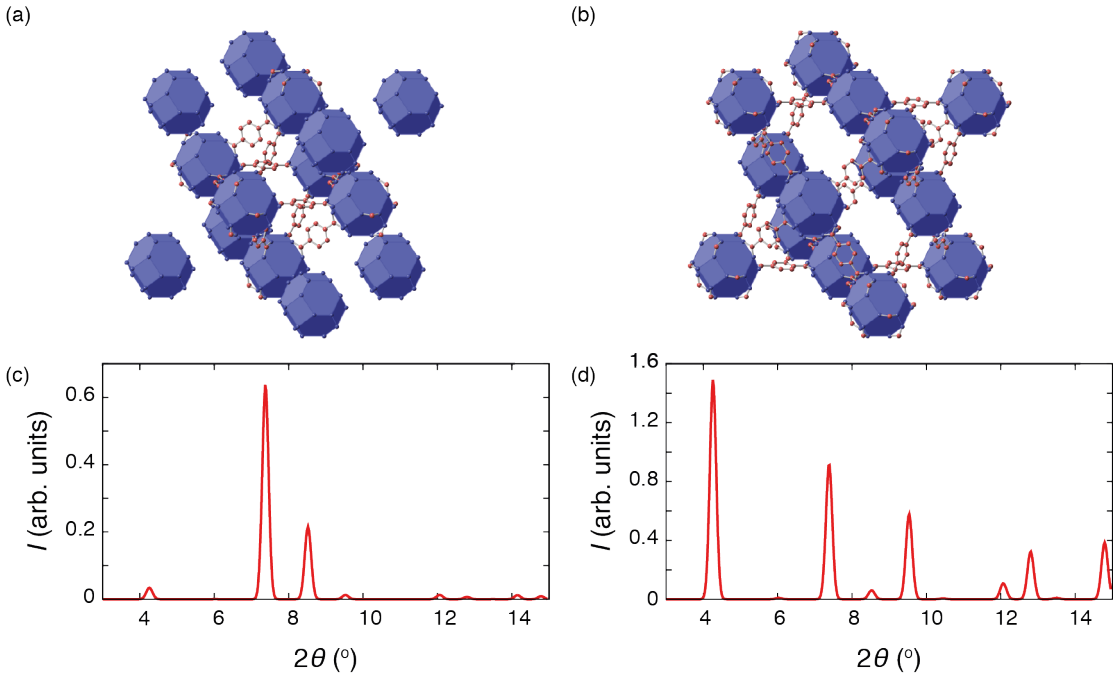

Figure 5.6: Calculated Cu Kα1 PXRD patterns for UiO-66(Hf) based on the two different ligand vacancy regimes consistent with the crystal symmetry determined by electron diffraction. In both cases an additional superlattice reflection—the (100)—is present at *ca* 4° but there is no significant intensity in the (110) position (*ca* 6°).

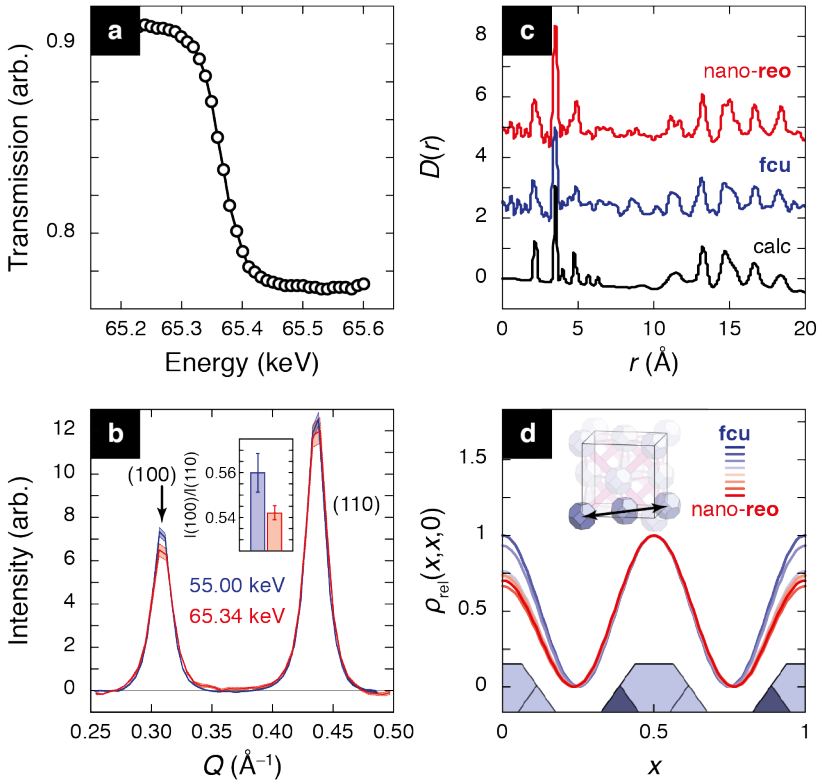

Figure 5.7: (a) Location of the X-ray absorption edge associated with the Hf K transition, determined using transmission measurements of the nano-**reo** UiO-66(Hf) phase. (b) Anomalous X-ray scattering at the Hf K-edge (65.34 keV) results in a small (1–5%) variation in background-subtracted diffraction intensities relative to off-edge measurements (here, 55 keV) for those peaks to which Hf scattering contributes, seen here to include the superlattice reflections. The inset shows the difference in the ratio $I(100)/I(110)$ at these two energies. (c) As a result of the large Hf X-ray scattering cross-section, X-ray PDF measurements are dominated by Hf pair correlations; these correlations show the local Hf coordination environment (*i.e.* cluster geometry) is similar in nano-**reo** (top, raised by 5 units) and non-defective **fcu** (middle, raised by 2.5 units) UiO-66(Hf) samples, and is well-modelled by the structure determined crystallographically (bottom). (d) Coarse-grained Fourier maps reconstructed from the low-angle diffraction patterns of Fig. 5.2 reveal a systematic decrease in scattering intensity at the unit cell origin with increasing defect concentration that is consistent with short-range ordering of cluster vacancies on the primitive cubic lattice.

face-centered sites, leaving Hf_6 clusters at the corners of the unit cell; the other is its inverse, where vacancies order on the corners of the unit cell, leaving the Hf_6 clusters to form a locally eight-connected net with **reo** topology [Fig. 5.9(a)]. The former is clearly unphysical because it would require isolated clusters to remain spatially correlated across nanometre-scale voids, whereas a long-range ordered version of the latter is actually known to occur in the related DUT-51(Zr) framework [363]. Quantum mechanical calculations further confirmed the stability of a long-range ordered **reo** model [Section 5.3.8].

The logical question is whether this short-range (nano-correlated) **reo** model is actually able to quantitatively account for the observed structured diffuse scattering. There are two primary parameters to determine: the fraction of cluster vacancies and the **reo** domain size. These are constrained by respectively, the relative intensities and width of the four principal diffuse scattering peaks (*i.e.* eight measurable quantities). Comparison of observed and calculated diffuse peak widths and intensities allow for estimation of an effective vacancy fraction and **reo** domain size for the UiO-66(Hf) sample shown in Fig. 5.2 of 0.13(5) and 7(3) nm, respectively [Section 5.3.7]. From these parameters can be constructed an atomistic model that accounts successfully *both* for the sharp Bragg peaks *and* for the broad diffuse scattering component in the PXRD pattern [Fig. 5.8].

5.1.3 Defect formation and quantum-mechanical calculations

Inspection of the model [Fig. 5.9] helps explain the microscopic mechanism responsible for ordered vacancy inclusion. Approximately 50% of the Hf_6 clusters are located within or adjacent to **reo**-type nano-regions, with individual domains dispersed throughout a continuous 12-coordinate **fcu** network. There are four equally-populated domain orientations corresponding to the four lattice sites in the face-centred cubic cell [Fig. 5.9(c)]. Within

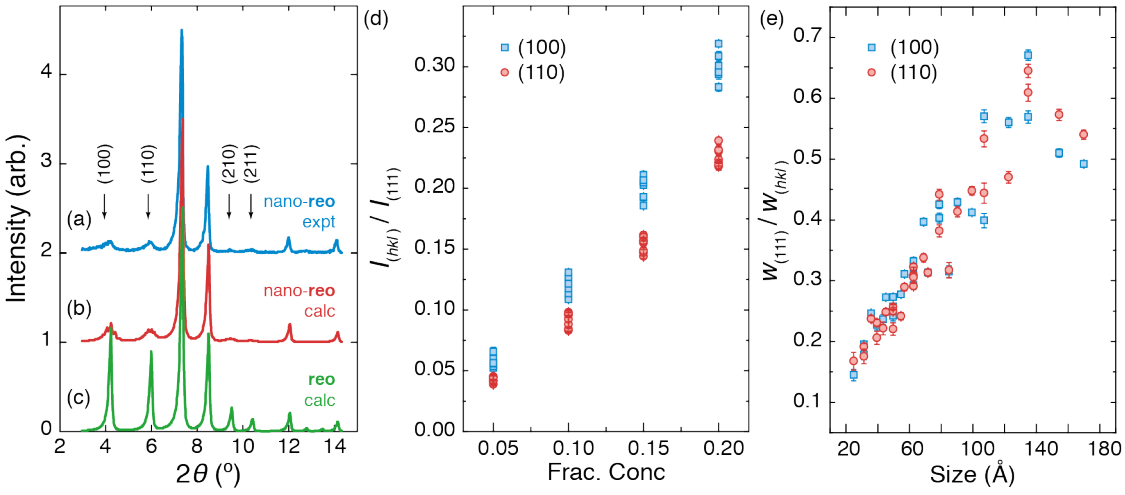

Figure 5.8: (a) The experimentally observed PXRD pattern of nano-**reo** UiO-66(Hf). (b) Calculated diffraction pattern from a model generated using the defect nano-domain growth method. (c) Calculated diffraction pattern of the hypothetical fully ordered **reo** UiO-66(Hf). (d) Calibration plot for the concentration of cluster absence defects against observed intensity of the broad superlattice reflections. (e) Calibration plot for the size of defect nanodomains against the observed width of the broad superlative reflections.

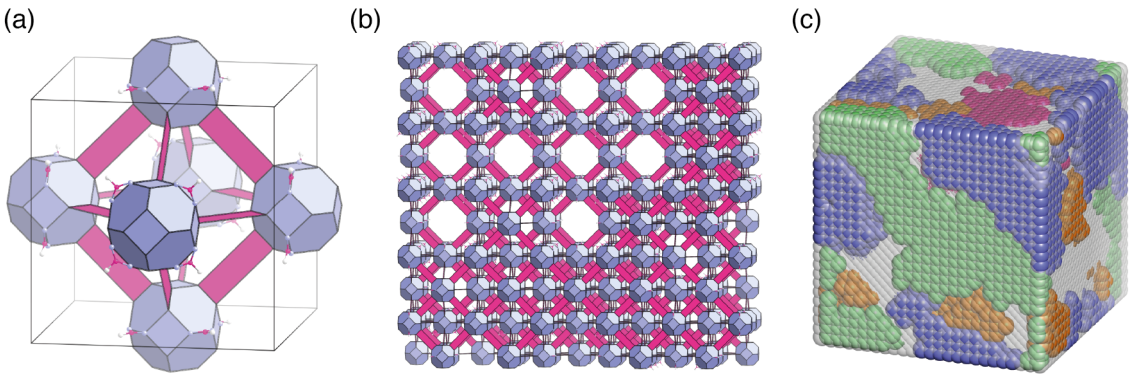

Figure 5.9: Structural description of defect nano-regions in UiO-66(Hf). (a) A polyhedral representation of a single unit cell of the (ordered) **reo** defect structure, using the same colour scheme employed in Fig 5.1(c) and making use of the atomic coordinates and unit cell parameters extracted from the equilibrium structure obtained through quantum chemical calculations [Appendix Section A1.3]. (b) A representative section of the atomistic model from which the simulated diffraction pattern shown in Fig. 5.8(b) is generated. Defect-rich nano-regions are dispersed throughout a matrix of defect-free **fcu** framework. (c) The defect concentration and domain size parameters determined experimentally can be used to generate atomistic representations of defect nano-regions in UiO-66(Hf). The representation given here is for a 6×6×6 supercell of the **fcu** unit cell (total edge length 12.4 nm), chosen for clarity to be smaller by a factor of 4^3 than those configurations used to calculate the diffraction pattern shown in Fig. 5.8(b). There are four possible orientations of the **reo** defect structure relative to the bulk **fcu** framework, corresponding to the four cluster positions in the **fcu** unit cell. In the representation used here, individual clusters are not shown but nano-domains corresponding to each of these four orientations are represented by blue, green, orange, and magenta regions. Grey-coloured regions correspond to defect-free **fcu** framework.

each **reo** domain, the Hf_6 clusters are coordinated by eight terephthalate linkers (noting that additional linker vacancies may reduce this number further). The sensitivity of the X-ray diffraction intensities to the nature of the species bound at the remaining coordination sites is very low, but both chemical reasonableness and computational studies indicate that formate, as a carboxylate, is the most likely ligand [364]. The tendency to adopt a lower effective cluster coordination number in the presence of increased formate concentration is therefore likely controlled by the following equilibrium reaction

$$[Hf_6O_4(OH)_4][C_6H_4(COO)_2]_{12/2} + x[HCOO]^- \rightleftharpoons [Hf_6O_4(OH)_4][HCOO]_x[C_6H_4(COO)_2]_{(12-x)/2} + \frac{x}{2}[C_6H_4(COO)_2]^{2-}, \quad (5.1)$$

and so the additional formate is likely to drive the equilibrium towards the **reo** structure. The observed balance between ordered and nano **reo**/**fcu** structures suggests that sterics and solvation effects, along with the kinetics of domain nucleation, growth, and ligand dif-

fusion may well play a role in determining product composition. This, in combination with the dependence of the formate concentration on the extent of DMF decomposition, likely explains why diffuse primitive reflections have sometimes been observed and sometimes not in previous experiments [174, 347]. A further important point is that the presence of sharp Bragg reflections at d-spacings corresponding to the parent face-centered matrix implies that there must be a very close lattice match between the **reo** and **fcu** domains—this is confirmed by quantum chemical calculations, which find the difference in lattice parameter to be less than 0.05% [Appendix Section A1.3].

5.2 Discussion

The model developed here differs from previous interpretations of disorder in the UiO family in two important respects. The first—and most crucial—is that vacancy inclusion in UiO-66(Hf) is correlated: the position of one vacancy affects the likelihood of a vacancy at neighbouring sites. This demonstrates *for the first time* the possibility of designing MOFs that support correlated disordered states, such as are currently exploited in charge transport, catalysis, mechanical and optical responses of other longer-established solid-state materials families [27]. Moreover, I have shown how these correlated states might be controlled from a synthetic viewpoint, and have explored their microscopic origin. It is improbable that UiO-66(Hf) is the only MOF to contain correlated defect nano-regions; rather, the relative difficulty of interpreting diffuse scattering patterns may have prevented more routine characterisation of nanoscale structural complexity in a variety of MOF phases [365].

The second difference is that vacancies are present at both the metal cluster and the linker sites—the entire network is more defective than had previously been imagined. This has important consequences for the properties of UiO-66(Hf), and may explain some of the difficulties in interpreting the gas sorption and TGA data [202]. The presence of cluster vacancies highlights an additional difficulty encountered both in TGA and in Bragg intensities, that is, their sensitivity only to the cluster:ligand ratio, rather than their absolute values. The average structure derived through Rietveld refinement in Ref. 202 for UiO-66(Zr) synthesised using acetic acid as a modulator, containing 11% ligand vacancies is thus indistinguishable from a **reo**-type cluster vacancy model with a 33% volume fraction

(*i.e.* 8% cluster vacancies), and it is only the absence of diffuse scattering that allows us to rule out cluster–vacancy ordering.

A further consequence of this correlated defect nano-region model of UiO-66 is the demonstration that defect-inclusion can lead to widespread heterogeneity in MOF structure, above and beyond what might be expected from a single ligand substitution. The correlations between defects lead to ligand order between H_2bdc and formate around the metal clusters, and thus there will be two different kinds of $Hf_6O_4(OH)_4$ cluster, with different cluster symmetries. The presence of nanodomains inevitably implies the presence of interfaces between them. These domain walls are likely to be high-energy internal 'surfaces', with elevated reactivity compared to the domain bulk. The presence of reactive internal surface is consistent with the unusual solid-state postsynthetic ligand exchange reported in UiO-66 [188]. Finally, this nanoscale heterogeneity appears to be implicated in the formation of more complex microstructure: electron diffraction measurements reveals the formation of hafnium and oxygen rich {100}-type planes within the structure [Fig. 5.4(b)]. The separation between planes is orders-of-magnitude larger than that accessible through wide-angle diffraction measurements, nevertheless, these may play an important role in the bulk properties of this material, particulary for catalytic activity, conductivity and sorption. This may explain in part the unusually low surface areas that this series of samples showed [Fig. 5.15].

This 'correlated defect nano-region' model of UiO-66(Hf) may be considered a MOF analogue of the Schottky defect phases of the early transition metal monoxides discussed in Section 1.4.1. In particular, if the **fcu** structure is thought of as analogous to the ordinary rock-salt structured transition-metal monoxides, then the **reo** structure resembles the primitive **reo** ordering common to these Schottky defect phases [31]. Just as defect correlations play a crucial role in the electronic conductivity of transition metal monoxides, one might expect qualitatively similar effects on the band structures and reciprocal-space properties of UiO-66. Indeed, our *ab-initio* calculations of compressibilities suggest that **reo** will be approximately twice as flexible as non-defective **fcu** UiO-66(Hf) [Appendix Tables A1.13 and A1.14]. This reduced rigidity suggests that correlated defect inclusion could be used to introduce anomalous mechanical properties, such as pressure-induced amorphisation and negative thermal expansion [366].

5.3 Methods

5.3.1 Sample preparation

All reagents were obtained from commercial suppliers and used as supplied. Microcrystalline powders of UiO-66(Hf) were prepared using a solvothermal approach. Standard conditions for synthesis were as follows. $HfCl_4$ (0.3 mmol, 96 mg) and terephthalic acid (H_2bdc; 0.3 mmol, 50 mg) were added to a PTFE-lined Parr reaction vessel (23 ml capacity), followed by *N,N*-dimethylformamide (DMF; 4 ml) and formic acid (95%, 1 ml). The vessel was sealed, heated at 120 °C for 48 h, then removed from the oven and allowed to cool to room temperature. The reaction mixture was subsequently filtered under vacuum and washed (acetone) to yield UiO-66(Hf) as a white microcrystalline powder. Analogous reactions in which $HfCl_4$ was replaced by an equimolar quantity of $ZrCl_4$ produced comparable results. The use of acetic acid as modulator does not produce the nano-**reo** phase under these conditions, in agreement the findings of Ref. 367. For the concentration studies shown in Fig. 5.3 I adopted this basic procedure, modified as described below.

Formic acid concentration study

The quantity of formic acid was systematically varied from 1 to 2.4 ml in order to obtain the series of compounds on which Figs. 5.3(a,c) are based, with each concentration point repeated in duplicate. As a consequence the total reaction mixture volume (solvent + formic acid) varied across the series. When more than 2.5 ml formic acid is included in the reaction mixture additional impurity phases are formed [Appendix B].

H_2bdc (mmol)	Formic acid (ml)	$HfCl_4$ (mmol)	DMF (ml)
0.3	1–2.4	0.3	4

H_2bdc concentration study

In a similar way the quantity of H_2bdc was systematically varied from 0.05 mmol to 0.3 mmol to obtain the series of compounds on which Fig. 5.3(b) is based. Again all preparations were performed in duplicate. When the quantity of H_2bdc in the reaction mixture is below approximately 0.1 mmol, additional impurity phases are formed [Appendix B].

BDC (mmol)	Formic acid (ml)	$HfCl_4$ (mmol)	DMF (ml)
0.05–0.3	1	0.3	4

Large-scale synthesis

Larger scale syntheses were also carried out to furnish sufficient material for stability studies. Standard synthetic conditions were as follows. $HfCl_4$ (3 mmol, 960 mg) and H_2bdc (3 mmol, 498 mg) were added to a Schott bottle (250 ml capacity), followed by DMF (40 ml) and formic acid (95%, 20 ml). The vessel was sealed, heated at 120 °C for 24 h, then removed from the oven and allowed to cool to room temperature. The reaction mixture was subsequently filtered under vacuum and washed (acetone) to afford the required product as a white microcrystalline powder. This procedure produced the material shown in Fig. 5.2.

5.3.2 Stability of nano-structured UiO-66(Hf)

The chemical and thermal stability of UiO-66(Hf) and its correlated superstructure under a range of conditions was assessed as follows.

Chemical stability

UiO-66(Hf) was synthesised according to the larger-scale protocol and then treated with water, aqueous 1 M NaOH, 1 M HCl or 1 M formic acid for two weeks. The retention of crystallinity before and after exposure was demonstrated by PXRD [Fig. 5.5(a,b)].

Thermal stability

UiO-66(Hf) synthesised according to the larger scale protocol was Soxhlet washed in refluxing EtOH for 10 hours followed by either heat treatment at 250 °C in air for 5 days; at 300 °C in He for 4 h or at 150 °C *in vacuo* for 5 days. Sample crystallinity was assessed using PXRD [Fig. 5.5(c)].

Resistance to post-synthetic reactions

Post-synthetic modification of UiO-66(Hf) was also attempted, following the methods of Kim *et al.* in an attempt to modify the defect concentration of samples of both defec-

tive and non-defective UiO-66(Hf) [188]. Two sets of conditions were tried to introduce defects into non-defective UiO-66(Hf), and one set of conditions to remove defects from nanostructured defective UiO-66(Hf). This proved unsuccessful.

The elimination of defects was attempted by heating 50 mg of activated, nano structured defective UiO-66(Hf) in 4 ml 0.2 M aqueous terephthalic acid solution (prepared by dissolving terephthalic acid in a basic sodium hydroxide solution before neutralisation with an equimolar quantity of HCl) at 85 °C for 4 days in a screwtop glass vial. The product was again filtered and PXRD patterns measured. No conversion was observed [Fig. 5.10(a)].

The introduction of defects was attempted by heating 50 mg of activated, non-defective UiO-66(Hf) in 2 ml of aqueous solution of formic acid (95%, 50%, 25%, 10%, 2.5%) or ammonium formate (containing 200 mg (3.17 mmol), 100 mg (1.59 mmol), 50 mg (0.79 mmol), 25 mg (0.40 mmol)) at 85 °C for four days in a screwtop glass vial. The vials were left

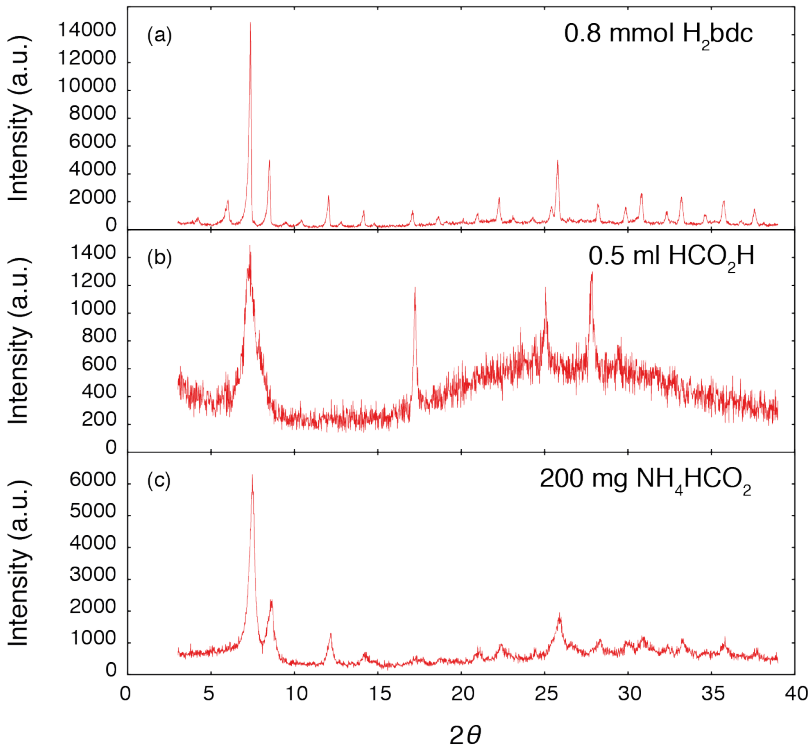

Figure 5.10: PXRD of the product after attempted post-synthetic modification of UiO-66(Hf). (a) 50 mg nano-**reo** UiO-66(Hf) reacted with 0.8 mmol H_2bdc. (b) 50 mg **fcu** UiO-66(Hf) reacted with 0.5 ml HCO_2H. (c) 200 mg **fcu** UiO-66(Hf) reacted with 200 mg NH_4HCO_2.

to cool to room temperature before the product was isolated via vacuum filtration. The product was then assessed by PXRD (except for 50% and 100% formic acid, where no appreciable solid remained). No conversion was observed, although concentrated formic acid was able to degrade the framework [Fig. 5.10(b,c)].

5.3.3 Powder diffraction measurements and analysis

PXRD measurement

All samples were assessed for crystallinity and purity via their X-ray powder diffraction patterns, measured using a Philips PW1730 diffractometer (Cu Kα radiation, $\lambda = 1.541\,\text{Å}$) over the angular ($2\theta$) range 3–39°, using a step size of 0.02° and a scan speed of $0.02°\,\text{s}^{-1}$. For quantitative analysis of peak widths and intensities, higher quality diffraction patterns were collected using a PANalytical X'Pert PRO diffractometer (Cu Kα1 radiation, $\lambda = 1.54060\,\text{Å}$). Diffraction data were measured over the angular range 3–8°, with a step size of 0.002° and a scan speed of $0.006°\,\text{s}^{-1}$. Diffraction patterns at elevated temperatures were collected in the angular range 3–70° using a Siemens D5000 diffractometer (Cu Kα radiation, $\lambda = 1.541\,\text{Å}$) equipped with an Anton Paar HTK1200 furnace, under a flowing He atmosphere.

Powder diffraction analysis

Structural refinements were performed using the Pawley strategy in Topas Academic version 4.1 structure refinement software [315]. The powder diffraction pattern presented in Fig. 5.2 of the main text was analysed using conventional crystallographic methods. Firstly, a Pawley fit to the pattern was carried out using the higher-symmetry $Fm\bar{3}m$ space group. This yielded a lattice parameter of $a = 20.7339(9)\,\text{Å}$, $R_{\text{wp}} = 17.192$, However, this model clearly left a number of diffraction peaks unaccounted for. Lowering the symmetry to $Pm\bar{3}m$ improved the fit, accounting for these additional superlattice peaks, and yielded a lattice parameter of $a = 20.7342(6)\,\text{Å}$, $R_{\text{wp}} = 12.750$. The Pawley fit still failed to account for the additional width of these diffraction peaks, so a two-phase fit—with all the superlattice peaks fitted by a separate phase with a different peak shape—was carried out, yielding a final lattice parameter of $a = 20.712(9)\,\text{Å}$, $R_{\text{wp}} = 11.213$. This model accounts for all significant features in the diffraction pattern [Fig. 5.11].

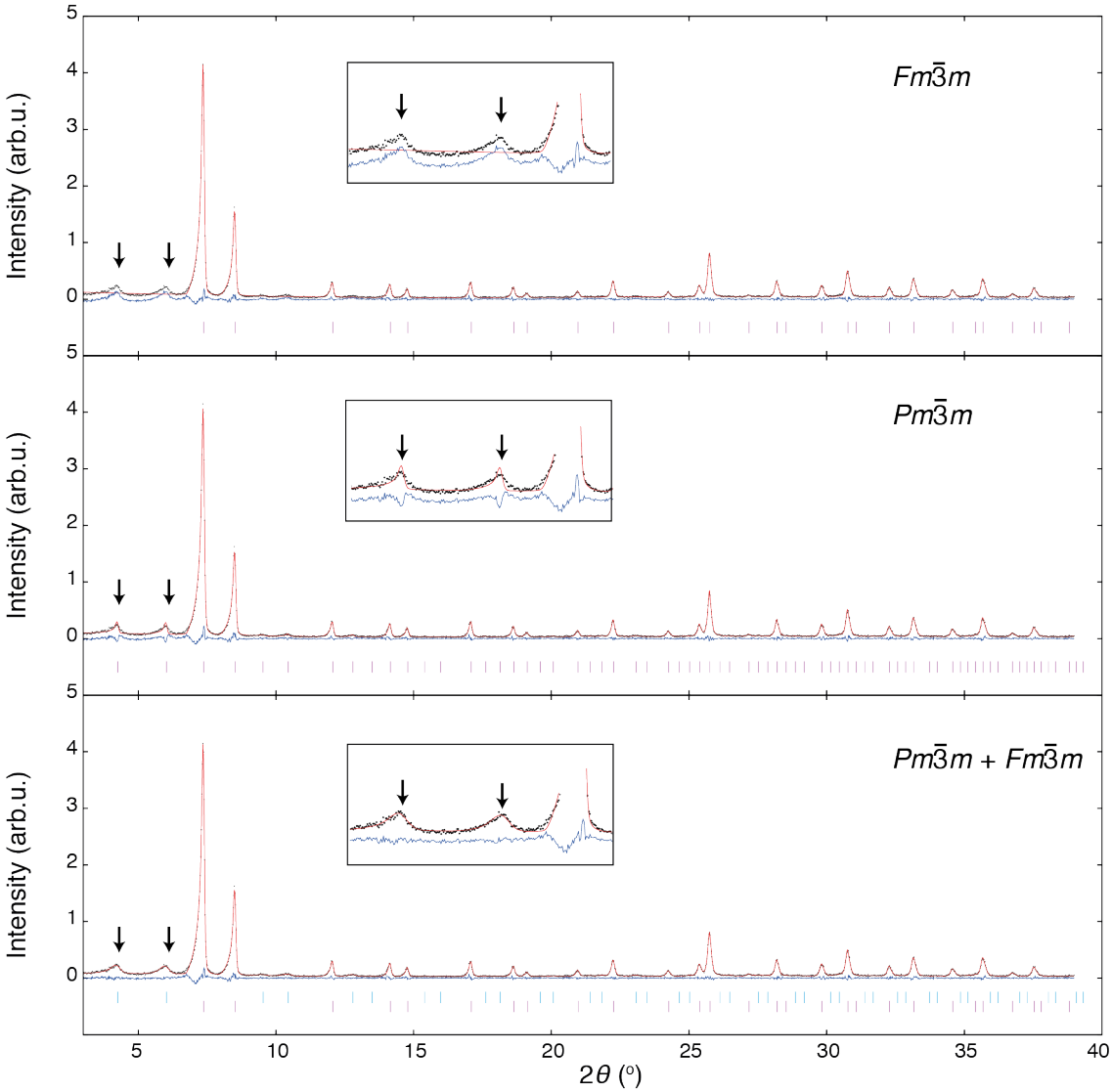

Figure 5.11: Pawley fits to experimental diffraction data for nano-structured UiO-66(Hf). From top to bottom: a fit using $Fm\bar{3}m$, $Pm\bar{3}m$ and a fit using a joint $Fm\bar{3}m$ and $Pm\bar{3}m$ model with two sets of peak shape parameters.

Peak fitting

Extraction of quantitative peak information was not carried out within the context of a given structural model; rather, the pattern was fitted in terms of three independent peaks and a single background term. The weaker (100) and (110) reflections were modelled as Gaussians and the (111) as a split Pearson VII-type peak. In the case that a peak was clearly absent from the diffraction pattern, it was not included in the fitting process. For some samples, such as those synthesised using very high concentrations of formic acid (*i.e.* > 2.4 ml for the conditions above) and/or very low concentrations of terephthalic acid (*i.e.* < 0.1 mmol for the conditions above), additional impurity peaks appeared in the diffraction pattern. These peaks are a result of what appear to be hafnium formate phases [Appendix A1.3] and were included in the model wherever appropriate. These do, however, cause substantial variation in the intensity of nano-**reo** superlattice reflections, making interpretation of the data for these extreme cases more complex.

5.3.4 Electron microscopy

Electron microscopy measurements were carried out by Dr Wei Wan and Prof. Xiaodong Zou (University of Stockholm). In order to prepare the sample for TEM observation, the UiO-66(Hf) powder was dispersed in ethanol and the suspension was sonicated for a period of 4 min. A single drop of the suspension was then transferred to a copper grid coated with holey carbon and dried in air. The TEM observations were made on a JEOL JEM-2100 microscope equipped with a LaB_6 electron gun and operated at 200 kV. The TEM images and electron diffraction patterns were recorded on a Gatan ES500W side-entry CCD camera.

5.3.5 High-energy anomalous scattering

Anomalous synchrotron X-ray powder diffraction measurements were performed at the I15 beamline, Diamond Light Source, in collaboration with Dr Heribert Wilhelm, Dr Annette Kleppe, Dr Phil Chater, Dr Matt Tucker (Diamond Light Source) and Prof. Andrew Goodwin. A finely-ground polycrystalline sample of nano-**reo** UiO-66(Hf) was mixed in equal mass proportions with a ceria calibration standard in a 1 mm quartz capillary and

mounted in vertical geometry on the diffractometer. Angular dispersive powder diffraction data were collected using 240 s exposures first at 55 keV and then at intervals of 5 eV for a 50 eV range across the Hf K-edge (located *via* an I/I_0 scan using diodes placed before and after the sample) using a Perkin Elmer flat panel detector mounted 1.124 m downstream of the sample. X-ray energies were selected using a Si(111) double crystal monochromator with a divergence limited bandpass of 10^{-3}. The X-ray beam was subsequently focussed to 65 μm×65 μm and passed through a pinhole 70 μm in diameter. Diffraction patterns were measured at three different sample heights (offset from each other by 0.1 mm) at both 55 keV and 65.340 keV to account for any potential sample inhomogeneity.

Two-dimensional powder diffraction data were calibrated using the Bragg reflections of the ceria internal standard using DAWN data analysis software [369]. The two-dimensional data were masked to remove contributions from dead pixels and the beamstop, and reduced to one dimensional $(2\theta, I)$ data using PyFAI [370]. Integrated intensities were then extracted for the lowest angle peaks (the (100) and (110) reflections) by subtracting a symmetric quartic background term; the corresponding raw data are given in Table 5.1. The extracted intensities showed no evidence of systematic sample inhomogeneity. On analysis of the sample it became clear that the sample exhibited reasonably strong beam sensitivity both at (65.34 keV) and well away (55 keV) from the edge and that the effect of

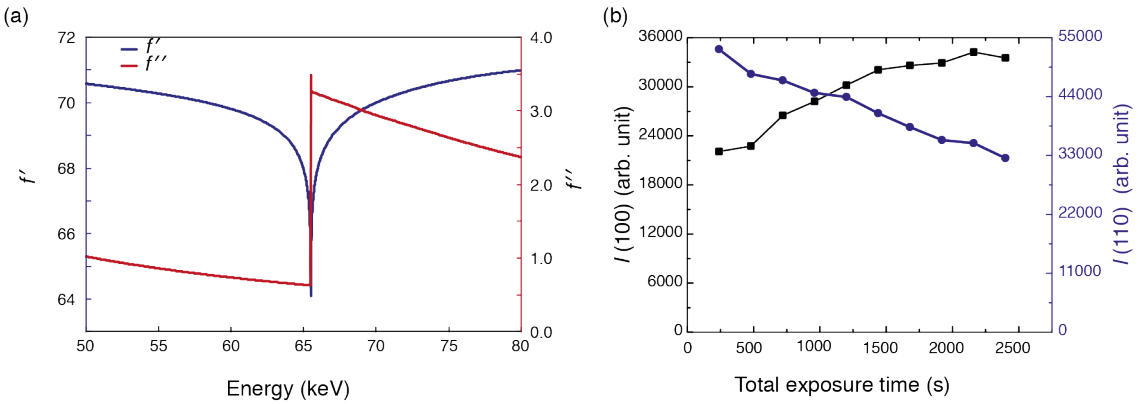

Figure 5.12: (a) Predicted variation of the anomalous components of the Hf form factor with energies of 50 keV to 80 keV. Data were generated using the DABAX database in XOP [368]. The experimental absorption maximum occurred for an energy of 65.365 keV, which is close to the predicted position of 65.540 keV. Variations in edge positions are expected as a result of variation in electronic states and Hf coordination environment. (b) Variation in intensity of the two most intense primitive superlattice reflections with beam exposure.

radiation damage over extended exposure was an order of magnitude larger than any effect due to the anomalous scattering [Fig. 5.12(b)]. As a result, all analysis was carried out on diffraction patterns measured on pristine samples that had not previously been exposed to the beam; comparisons were only made between data sets that had been exposed for precisely the same amount of time. This meant that the "on edge" energy we used was slightly below the actual absorption edge, because our measurements at the edge itself were only performed on regions of sample that had previously been exposed to the beam. In spite of this limitation, the predicted value of $\Delta f'$ between 55 keV and 25 eV below the edge is $4.7e^-$, a difference of 7%, and consequently a variation in diffraction intensities of up to 10% is expected by comparing diffraction patterns collected at 55 and 65.34 keV [Fig. 5.12(a)].

5.3.6 X-ray total scattering

X-ray total-scattering measurements were carried out with the help of Dr Nicholas Funnell. X-ray PDF measurements were performed using powder samples of UiO-66(Hf) of varying defect concentration that were loaded in 1 mm quartz capillaries and mounted on a PANalytical Empyrean diffractometer equipped with a Mo X-ray tube ($\lambda = 0.71$ Å, $Q_{\max} = 17.7$ Å^{-1}), Mo focussing mirror and scintillation point detector. Divergence ($\frac{1}{4}^\circ$, Ta), anti-scatter, and Soller (0.02 rad) slits were used to adjust the incident beam profile;

Table 5.1: Experimentally observed peak intensities for nano-**reo** UiO-66(Hf) at 55 and 65.340 keV.

E = 55.000 keV			
Height (mm)	***I*(100) (arb. unit)**	***I*(110) (arb. unit)**	**ratio**
−0.1	33512.4	63718.8	0.5768
−0.2	30925.1	56523.4	0.5471
−0.3	32558.1	58551.5	0.5561
mean ratio			0.560(9)
E = 65.340 keV			
Height (mm)	***I*(100) (arb. unit)**	***I*(110) (arb. unit)**	**ratio**
0.1	28084.5	52193.7	0.5381
0.2	25782.0	47023.5	0.5483
0.3	29230.3	54159.6	0.5397
mean ratio			0.560(9)

Estimated standard errors are given in parentheses.

a programmable receiving slit, set to a height of 1 mm, was used for the diffracted beam. Total scattering data were collected over the angular range $2.75 > 2\theta > 140°$, yielding data with useable $Q_{max} = 15\,Å^{-1}$. These data were corrected for background, Compton, and multiple scattering and beam attenuation by the sample container using the GUDRUNX package [296, 301]. The normalised intensity $F(Q)$ was converted to the PDF in the form of the $D(r)$ function as defined in Ref. 16. Experimental $F(Q)$ and $D(r)$ functions for both the **fcu** and nano-**reo** phases are shown in Fig. 5.13.

In order to check that the measured PDFs were consistent with the average structure of UiO-66(Hf), we fitted the processed $D(r)$ ($G(r)$ in the PDFGui formalism) using the PDFGui programme [103]. As the measured PDFs do not contain information about the longer range correlations, we modelled both the defective and non-defective UiO-66(Hf) using the non-defective average structure of Ref. 174, with Zr substituted by Hf. As hafnium has more electrons than all other atoms in the materials by an order of magnitude, it proved possible to account for nearly all the features of the experimental PDF with just the Hf–Hf and Hf–O partial correlation functions. This was done by refining the lattice parameter, the Hf position and atomic displacement parameter, the O position, an overall scale factor, and a peak sharpening parameter (to allow for the differential broadening within and between clusters) defined with a cut-off of $r_{cut} = 7\,Å$. The corresponding crystallographic details are summarised in Appendix Section A1.1.

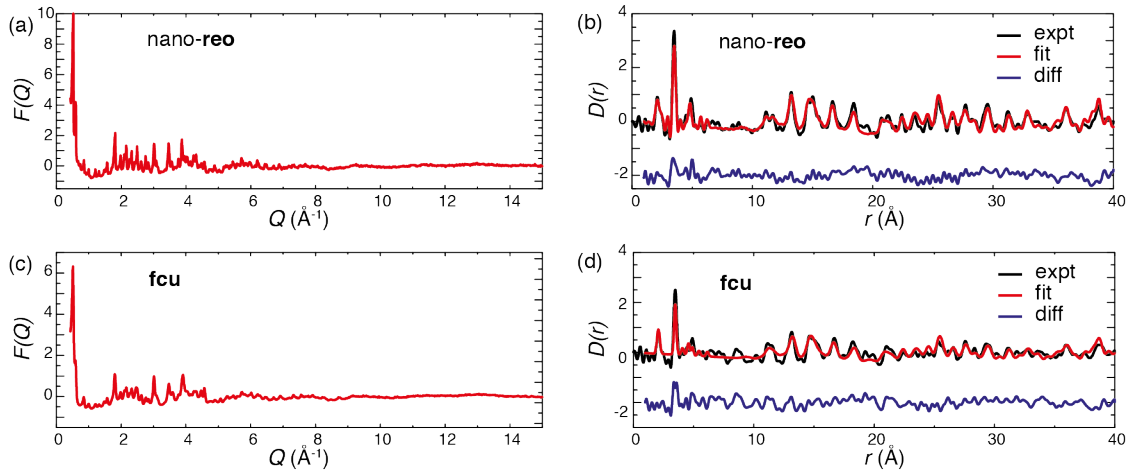

Figure 5.13: Experimental X-ray total scattering functions $F(Q)$ for (a) nano-**reo** UiO-66(Hf) and (b) **fcu** UiO-66(Hf). Experimental (black) and fitted (red) $D(r)$ functions for (c) nano-**reo** UiO-66(Hf) and (d) **fcu** UiO-66(Hf), collected and processed as described in Section 5.3.6.

5.3.7 Modelling of the powder diffraction data

Defect nano-region model generation

The defect nano-region model was produced using a domain growth approach. For a given defect composition and cluster size, a stoichiometric 24×24×24 supercell of the **fcu** (ordered) UiO-66(Hf) structure was taken, and a suitable number of randomly-selected Hf_6 clusters were removed. These incipient vacancy nano-domains were grown using an iterative approach as follows. First, a vacant cluster site was picked at random. Then, if it corresponded to a vacant site on the surface of a nano-domain, a neighbouring cluster site in one of the ⟨100⟩ directions was picked. If the cluster was present and not adjacent to a nano-domain of different orientation, it was removed, otherwise it was left unchanged. This was repeated until the total vacancy concentration reached the desired value. The corresponding X-ray diffraction pattern was then calculated from the remaining atom coordinates, assuming that the contribution from any remnant guest species could be neglected and that the Hf_6 cluster coordination near defect sites was completed with formate counterions.

Modelling of the powder diffraction data

A series of models, consisting of supercells 24×24×24 times the original UiO-66 cell (*i.e.* ∼500 Å in each linear dimension) were produced, with defect concentrations varying from 0.05 to 0.2 in 0.05 steps and numbers of initial cluster-vacancy nuclei from 5 to 400. This produced a wide variety of nano-domain sizes, varying from 2.5 nm up to 17 nm. Powder diffraction patterns of these supercells were then simulated out to a d-spacing of 11 Å ($Q_{\max} = 0.57\,\text{Å}^{-1}$, $2\theta \approx 8°$ for Cu Kα radiation), using a Gaussian peak shape.

The peak widths and intensities of the three reflections in the calculated diffraction patterns were then extracted by fitting using Topas Academic 4.1, using individual Gaussian peaks with no additional background terms [315]. Calibration curves of $I(100)/I(111)$ and $I(110)/I(111)$ as a function of defect concentration, on the one hand, and of $w(111)/w(100)$ and $w(111)/w(110)$ as a function of approximate nano-domain size, on the other hand, are given in Fig. 5.8. Both of these calibration curves are approximately linear as might be expected from simple concentration arguments and the Scherrer equation, except for

models with large domain sizes where finite size effects begin to become important. Interestingly, the peak width as predicted by the Scherrer equation is *ca* twice as large as is observed for these models.

The calculated powder diffraction pattern shown in Fig. 5.8(b) was calculated using a split Pearson VII peak shape to replicate the pronounced instrumental peak asymmetry in the experimentally observed patterns.

5.3.8 Quantum mechanical calculations

Quantum mechanical calculations were carried out by Dr François-Xavier Coudert (Chimie ParisTech–CNRS). The **fcu** and **reo** structures of UiO-66(Hf) were relaxed fully by optimising both atomic positions and unit cell parameters. Quantum mechanical calculations were performed using the density functional theory approach with localised basis sets (CRYSTAL09 code [371]). B3LYP hybrid exchange-correlation functional [372] and all-electron basis sets [288] were used for all atoms except Hf, for which small relativistic effective core potential with twelve outer electrons considered explicitly was used [373]. The mechanical properties of both **fcu** and **reo** phases were calculated in the elastic regime, following the methodology outlined in Ref. 374. Calculations were also carried out for UiO-66(Zr), giving very similar results. The optimised lattice parameters, unit cell and mechanical properties are available in Appendix Tables A1.8 and A1.10 to A1.12.

5.3.9 Thermogravimetric analysis

Samples were prepared for TGA analysis by activation under vacuum (150 °C for 24 h). TGA measurements were performed using a Perkin Elmer TGA 7, with a Perkin Elmer TAC 7/DX thermal analysis controller, from 50 to 650 °C, with a temperature ramp rate of 5 °C min^{-1}. The corresponding TGA traces, normalised against the mass at 650 °C, are shown in Fig. 5.14.

5.3.10 Surface area measurements

Surface area analysis was carried out by Oxford Materials Characterisation Service on a systematic series of samples, prepared using varying formic acid volumes of 1.0 to 2.0 ml. All samples were activated by heating at 150 °C under dynamic vacuum for 12 hours.

Approximately 50 mg of activated sample was then degassed at 150 °C under a nitrogen atmosphere before Brunauer-Emmett-Teller (BET) analysis was carried out using a Micromeritics Gemini V surface area analyser with nitrogen as the adsorbate. Pore diameter measurements were limited to the range 1.7–300 nm. The experimental data showed greater variation than might be anticipated from earlier studies [201, 212, 367]. Perhaps the clearest trend is to be found in the Barrett-Joyner-Halend (BJH) adsorption pore diameters, which show a steady increase in effective pore diameter with defect concentration [Fig. 5.15(a)]. This result is mirrored by the BJH pore diameter volume behaviour, where there emerges a large peak associated with pores of diameter 2.5 nm for defective samples [Fig. 5.15(c,d)]. Taken at face value, these two results would suggest that the UiO samples are becoming increasingly porous with increasing defect concentrations, and yet the measured trend in BET surface area displays erratic behaviour that even suggests accessible pore area decreases for highly defective samples [Fig. 5.15(b)]. In addition there is strong hysteretic behaviour evident in the contrast between adsorption and desorption isotherms that adds to the complexity of the sorption behaviour of nano-**reo** UiO-66(Hf).

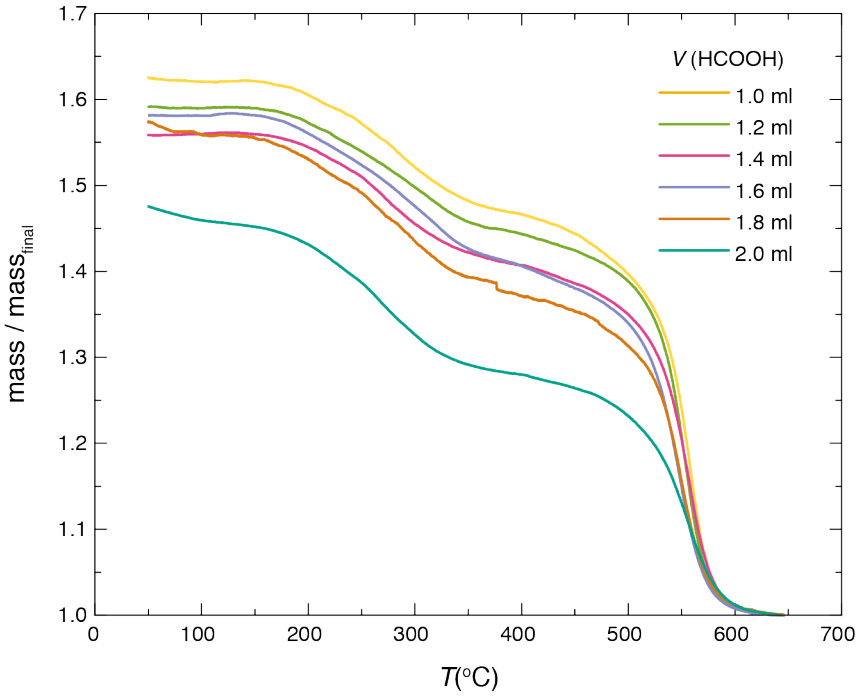

Figure 5.14: TGA traces for samples of UiO-66(Hf) synthesised with varying about of formic acid, normalised to the final mass

One possible explanation for this anomalous result is that the Hf/O-rich defect inclusions observed using electron microscopy—which enclose interior domains of the crystallites—are acting as barriers to gas migration. In this way, on increasing defect concentrations there is an increase in pore diameter but a decrease in overall porosity as the interior of the crystals is impermeable to the probe gas.

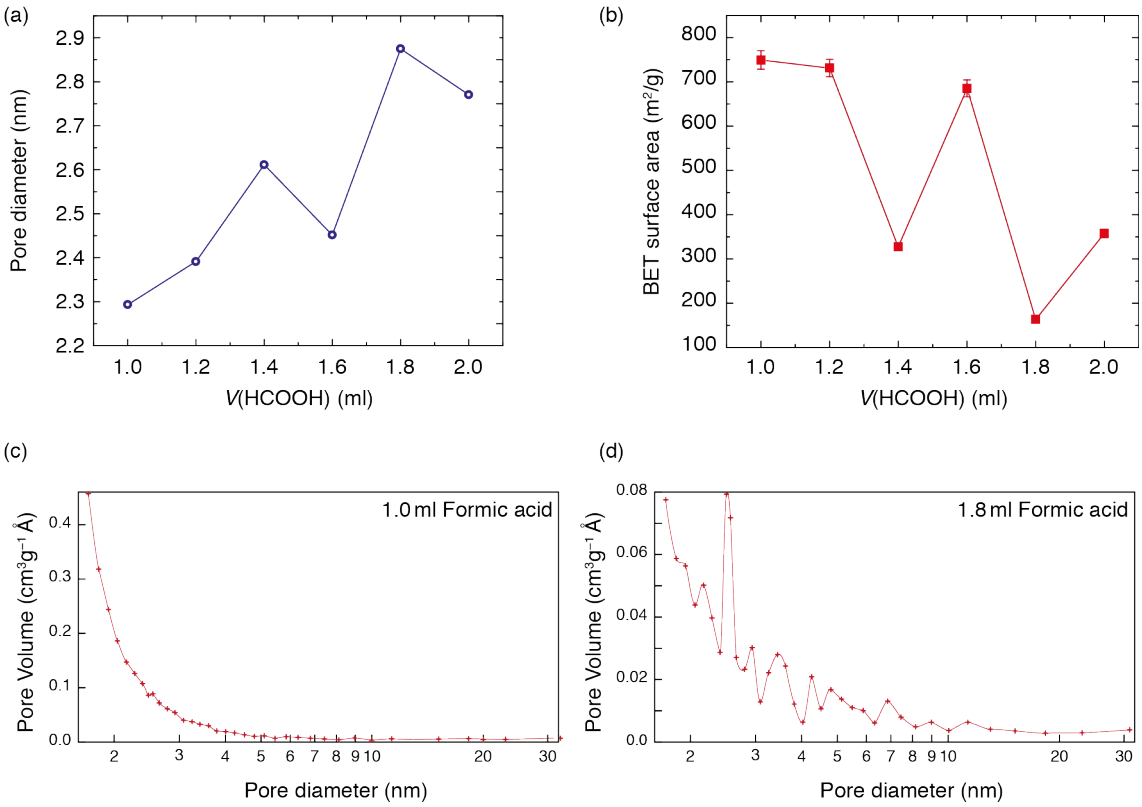

Figure 5.15: (a) Barrett-Joyner-Halenda (BJH) adsorption pore diameter for samples of UiO-66(Hf) synthesised with varying quantities of formic acid (1.0 ml to 2.0 ml). (b) The measured Brunauer Emmett Teller (BET) surface areas for samples synthesised with varying quantities of formic acid (1.0 ml to 2.0 ml). (c,d) Barrett-Joyner-Halenda pore diameter volume plots for the samples synthesised with 1.0 ml (c) and 1.8 ml (d) of formic acid. A large peak at around 2.5 nm is present in the sample with a higher defect concentration.

Chapter 6

Defect-controlled MOF mechanics

In the previous Chapter I demonstrated that defects can be introduced in a MOF in a correlated fashion. In this Chapter I demonstrate that this control over defects leads in turn to control over the physical properties of MOFs, by carrying out a proof-of-principle study using the defect dependence of the thermomechanical behaviour of UiO-66(Hf). The specific choice of physical property and material was driven by the following reasons. Firstly, the thermal response of a framework is both relatively straightforward to assess and reflects the fundamental elastic properties of the material [263, 270, 375]. The range of tuneable unusual thermomechanical that have be found in MOFs thus far, including negative thermal expansion (NTE) [272, 274, 367], thermal amorphisation [139], and dramatic 'breathing' transitions [264, 376] also raises the general expectation that MOFs will show anomalous properties, and that these will be particularly sensitive to the presence of defects. Secondly, UiO-66 is the MOF where we have arguably established the best control over the chemistry of defects [201, 202, 212, 292].

Although the presence of defects leads to modulation of the structure over the scale of nanometers, the local coordination environments the Hf cluster in the defective and non-defective phases are in fact very similar (comparing the ordered **fcu** and **reo** structures[Fig. 6.1(a,c)]). However, these local coordination differences can be amplified by making use of the high temperature (250–300°C) ligand-elimination reaction in UiO-66(Hf) [201, 288, 364, 377]. During this ligand-elimination reaction labile ligands are driven off, exploiting the coordinative flexibility of Hf—for non-defective UiO-66(Hf), two H_2O molecules are lost, whereas for defective **reo** UiO-66(Hf), the four formates will be eliminated. This leads to drastically different coordination environments in the ligand-eliminated phases [Fig. 6.1(b,d)].

Making use of *in situ* variable-temperature synchrotron X-ray diffraction measurements of a series of UiO-66(Hf) samples with a range of defect concentrations, I will demonstrate the following. First, ligand elimination results in framework densification, the magnitude of which is dependent on defect concentration. Quantum mechanical calcula-

tions help interpret the microscopic origin of this volume reduction. Second, all densified-UiO-66(Hf) samples exhibit isotropic NTE behaviour that is many times stronger than that of any other MOF, and in one case even satisfies the condition of "colossal" NTE (its volumetric coefficient of thermal expansion $\alpha_V = \mathrm{d}V/V\mathrm{d}T \simeq -100\,\mathrm{MK}^{-1}$). This is the first report of colossal NTE in an isotropic MOF. Third, the magnitude of NTE can also be tuned systematically by defect concentration. I will then move on to a discussion of the likely mechanisms by which defect inclusion might influence elastic properties of this particular MOF, the challenges posed for understanding NTE in defective materials, and the implications for exploiting defect/property relationships in other MOF systems. This Chapter concludes with the experimental and analytical methods used.

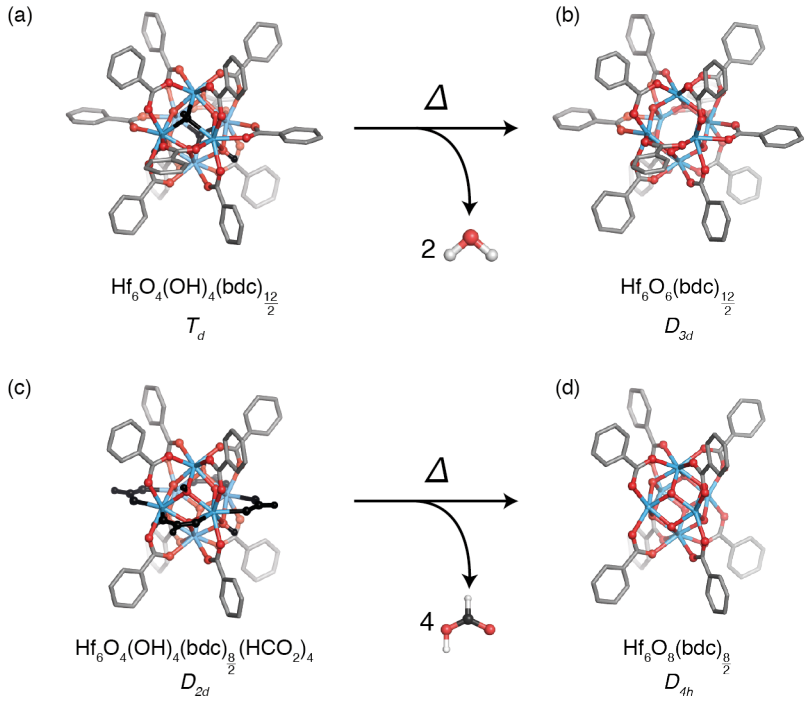

Figure 6.1: The cluster coordination environments in non-defective **fcu** and defective **reo** UiO-66(Hf). In spite of the differences in framework topology, the cluster coordination environments of **fcu** (a) and **reo** (c) UiO-66(Hf) are very similar. After ligand elimination (b,(d) the two cluster types are distinct in both their coordination and symmetry. Atoms are coloured as follows: Hf, blue; O, red; and C, grey. Atoms lost during thermal elimination are coloured black. Coordinates from calculated crystal structures (a,c,d) in Appendix Section A1.3, (b) Ref. 378.

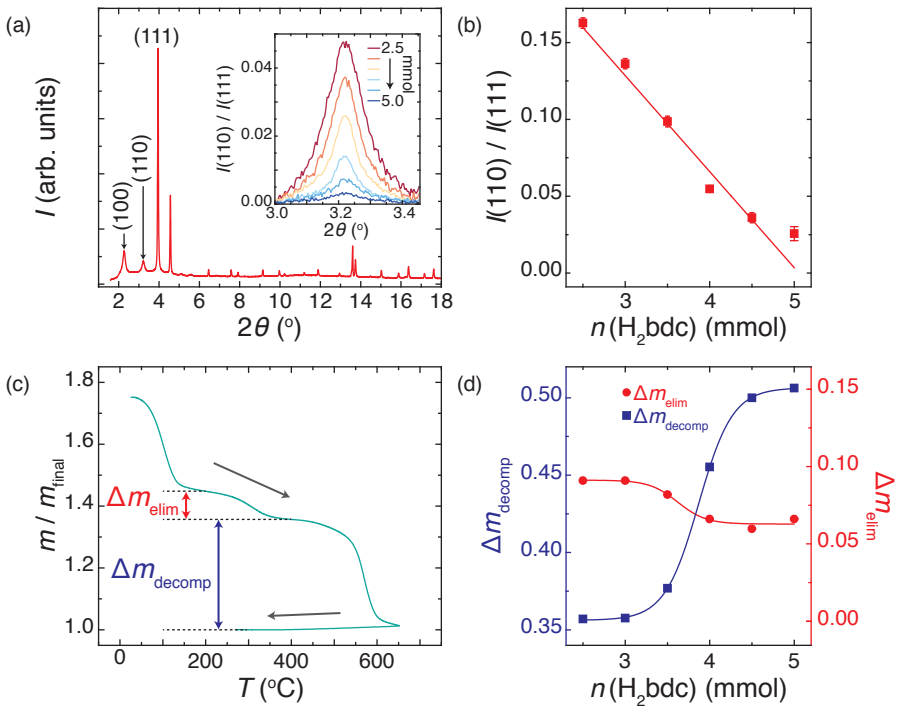

Figure 6.2: (a) A diffraction pattern of the most defective sample of UiO-66(Hf). Structured diffuse scattering located at primitive superlattice positions is a signature of the presence of correlated defects in UiO-66(Hf). The most intense of these broad reflections are the (100) and (110). On increasing the quantity of H_2bdc in the reaction mixture, the concentrations of defects decreases, and so the relative intensity of these primitive reflections decreases ((a) inset and (b)). (c) The TGA trace of UiO-66(Hf) shows three steps corresponding to, in turn, guest volatilisation, ligand elimination and framework decomposition. (d) The decrease in defect concentration is evident in the variation with bdc concentration of normalised mass losses both on ligand elimination (Δm_{elim}), which decreases, and framework decomposition ($\Delta m_{\mathrm{decomp}}$). Fitted curves are included as guides to the eye.

6.1 Results and discussion

After having prepared a series of six samples of nano-**reo** UiO-66(Hf) containing different defect concentrations [Section 6.3.1, my first step was to ascertain whether these samples did contain defects as expected. PXRD measurements revealed that the structured diffuse scattering in the form of broad primitive superlattice reflections was present in all six samples, confirming that all six samples contained correlated cluster vacancies [Fig 6.2(a)]. Further, the relative intensity of the diffuse scattering compared to the Bragg scattering increased in an approximately linear fashion with the concentration of H_2bdc ligand contained in the reaction mixture [Fig 6.2(b)], confirming both control over defect inclusion and that the samples spanned a suitable range of defect concentrations.

The onset temperature of ligand elimination was determined using thermogravimetric

analysis (TGA). The TGA traces of all samples are qualitatively similar and can be interpreted on the basis of previous studies of this system [201, 288, 348]: each shows three distinct mass losses, corresponding in turn to guest desorption (∼100 °C), ligand elimination (250–350 °C) and framework decomposition (550–600 °C) [Figs. 6.2(c)]. Qualitative trends in defect concentrations can be inferred from the relative mass losses associated with the second and third stages [Δm_{elim} and $\Delta m_{\mathrm{decomp}}$, respectively, in Fig. 6.2(c,d)]. Framework decomposition corresponds to the loss of terephthalate (leaving behind HfO_2) and so larger values of $\Delta m_{\mathrm{decomp}}$ are expected for the least defective examples, which should contain the highest relative concentrations of terephthalate. This is precisely what is observed [Fig. 6.2(d)]. Likewise the value of Δm_{elim} should decrease as the defect concentration is reduced (since H_2O is eliminated instead of the heavier HCOOH), and again this trend is observed in practice. So, both X-ray diffraction and TGA measurements point to a systematic variation in defect concentration across the series of UiO-66(Hf) samples.

In order to determine the effect of defect concentration on thermomechanical behaviour, I measured variable-temperature PXRD patterns for all six samples. Because the primary motivation is to determine the thermal expansivity of the ligand-eliminated phases, particular care was paid to ensuring that the samples were heated sufficiently to drive this elimination step but not so far as to initiate framework decomposition. In practice this dictated an experimental protocol of heating each sample to a temperature of 340 °C and then measuring thermal expansivity on subsequent cooling to 100 °C. The temperature range probed in these experiments therefore corresponds to the first two steps seen by TGA.

For all samples the same qualitative behaviour was observed (although, as will form the focus of subsequent discussion, the magnitudes of these changes varied from sample to sample). On heating through the first stage of mass loss (*i.e.* up to 250 °C) the most noticeable changes to the diffraction pattern were in the relative intensities of reflections sensitive to solvent occupation within the framework pores. There was only a very small change (∼0.1%) in the size of the unit cell within this regime. These observations are consistent with our interpretation of the TGA trace and with previous investigations [201, 288]. In contrast, the ligand elimination process that occurs between 250 and 350 °C

resulted in an order-of-magnitude larger decrease in the cubic unit cell parameter that has not previously been observed in defect-free samples [Fig. 6.3(a)]. The diffraction pattern of the densified framework formed at this higher temperature can still be accounted for by a model based on the ambient-temperature structure, adjusted for the change in lattice dimensions; however the scattering intensity in high-angle Bragg peaks was so much reduced that detailed structural refinement was not possible. On subsequent cooling from 340 to 100 °C all samples showed NTE [Fig. 6.3(a,b)]. The two processes of densification and NTE, together with their dependence on defect concentration, are discussed in turn below.

6.1.1 Thermal densification

As the diffraction data were unable to support a detailed structural model of this densified framework, I turned to quantum mechanical calculations to verify that the structural changes associated with formate elimination were consistent with the magnitude of volume collapse observed experimentally. From a computational viewpoint it would have been unfeasible to use *ab initio* methods to relax large atomistic configurations describing the nanodomain defect structure described in Chapter 5. Instead I focussed on the ordered

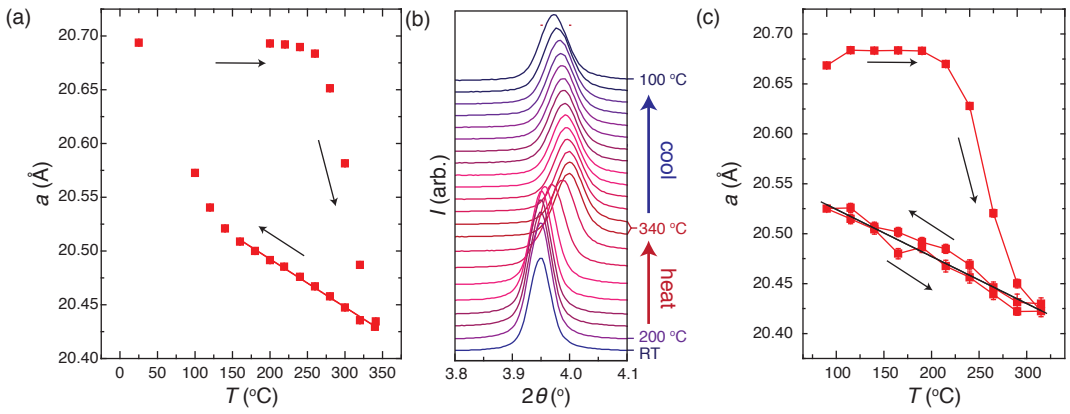

Figure 6.3: (a) Evolution of the lattice parameter of the UiO-66(Hf) sample synthesised with the smallest quantity of H_2bdc (2.5 mmol)—*i.e.* the highest defect concentration—on heating from room temperature to 340 °C then cooling to 100 °C. A linear fit to the lattice parameter over the temperature range 340–160 °C is shown, for the determination of α_V. (b) The evolution of the most intense peak, the (111) reflection, throughout this process. (c) Evolution of the lattice parameter of the same sample of UiO-66(Hf) measured on heating from room temperature up to 315 °C cooling to 85 °, and then reheating under flowing N_2, demonstrating the reversibility of the NTE. These data are of much poorer quality than the synchrotron data shown in (a), as they were collected using a laboratory diffractometer. The reliability of both the refined lattice parameter and the temperature calibration are thus restricted.

reo structure, which was computationally much more tractable. For this model, ligand elimination corresponds to the chemical process

$$Hf_6O_4(OH)_4(bdc)_4(OOCH)_4 \rightarrow Hf_6O_8(bdc)_4 + 4HCOOH\uparrow.$$

In silico relaxation of structural models for the framework compositions represented on either side of this reaction equation suggested that a 1.0% change in lattice parameters is expected upon HCOOH elimination: $a = 20.862\,\text{Å}$ for $Hf_6O_4(OH)_4(bdc)_4(OOCH)_4$ and $20.652\,\text{Å}$ for $Hf_6O_8(bdc)_4$.[‡] In contrast, it is already known that elimination of water from defect-free UiO-66 does not result in any significant volume change [364]. Inspection of the relaxed structural model for $Hf_6O_8(bdc)_4$, reveals that distortions of the Hf_6 octahedra are responsible for this framework densification. Elimination of HCOOH greatly amplifies the tetragonal distortion of Hf_6 octahedra, reducing the effective octahedral volume by 4.2% and bending the cluster–bdc–cluster connection, coupling these local distortions to

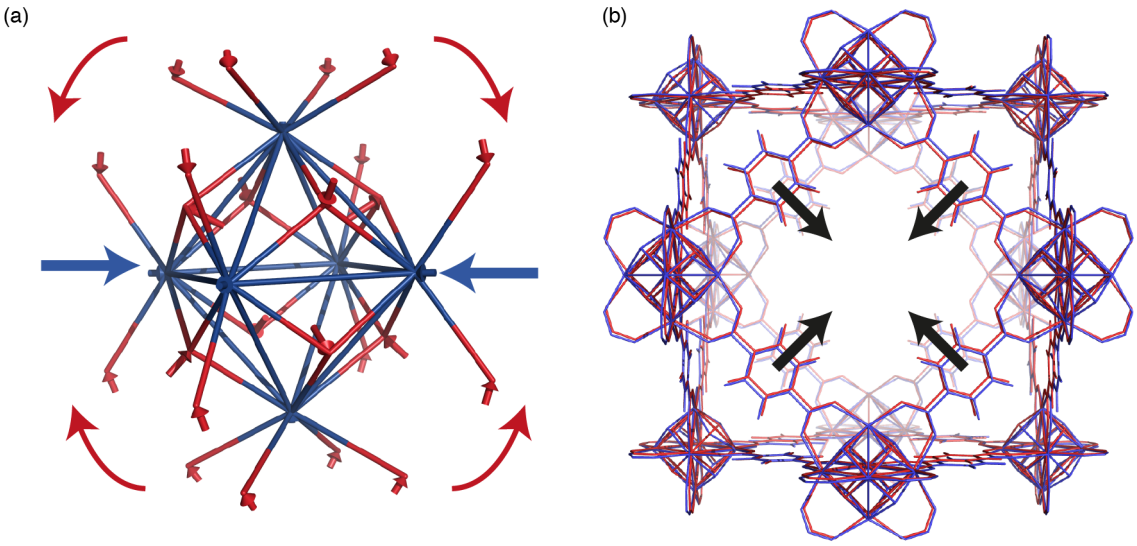

Figure 6.4: Structural changes on ligand-elimination in **reo** UiO-66(Hf) found by *in-silico* relaxation. (a) The Hf_6O_8 cluster after ligand elimination. The largest structural changes are amplification of the tetragonal distortion of the cluster, with accompanying cluster contraction, and translation of the bdc^{2-} ligand relative to the metal cluster edges. Atomic displacements are shown by arrows pointing to each atom. Colour scheme as follows: Hf, blue and O, red. (b) An overlay of the structure before (blue) and after (red) ligand elimination. The most striking change are the translations of the bdc^{2-} linkers, caused by the tetragonal cluster distortions.

[‡]The tendency for calculations to overestimate lattice parameters for organic and organic-containing materials is well-known phenomenon and arises due to the difficulty of correctly accounting for dispersive interactions. It does not impact the analysis of structural and lattice parameter trends in families of materials of similar composition and porosity [379].

macroscopic volume contraction [Fig. 6.4]. The relaxed structural models are included in Appendix Section A1.3.

If, as this analysis would suggest, the process of framework densification depends on the presence of structural defects, then stronger densification in UiO-66(Hf) samples with larger defect concentrations would be expected. By heating the samples to sufficiently-high temperatures to ensure complete densification (and working within the constraints of available synchrotron beam time), this expected property/defect relationship is borne out in practice [Fig. 6.5(a,b)]. The most defective samples showed densifications that were larger by ∼1% (of the total lattice parameter) than for the least defective samples; this result is consistent not only with the results of the *ab initio* calculations but also with previous experimental reports [288].

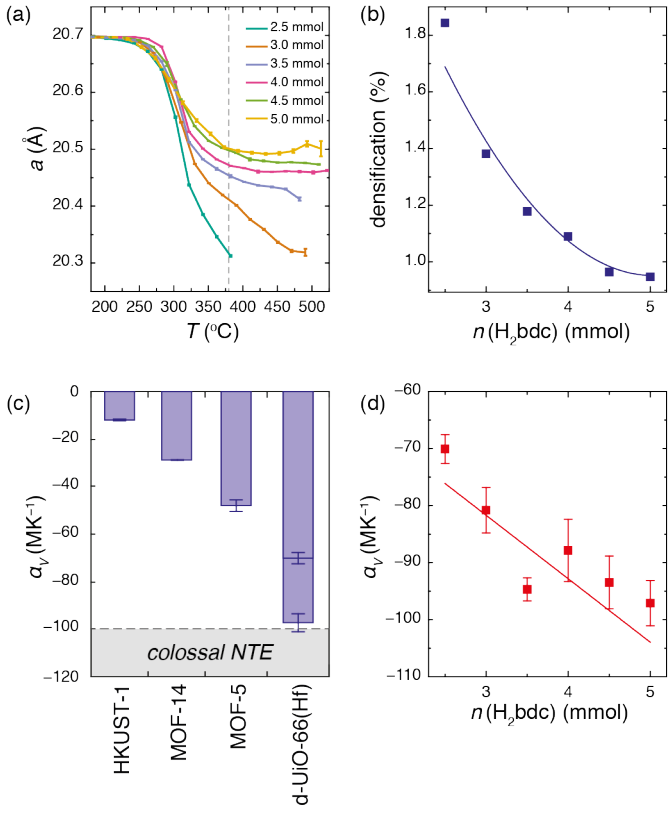

Figure 6.5: (a) The evolution of the lattice parameter through the ligand elimination process for a series of samples with different defect concentrations. To correct for minor variations in the onset temperature of ligand elimination between samples, the curves are offset in temperature such that the maximum change in volume corresponds to 300 °C. (b) The densification (percentage linear decrease) after ligand elimination, measured at 380 °C, highlighted in (a) by a dashed grey line. (c) Coefficients of thermal expansion for isotropic NTE MOFs. The two values given for densified-UiO-66(Hf) correspond to upper and lower defect concentrations [272–274]. (d) Variation in NTE behaviour as a function of decreasing defect concentration (increasing quantity of H_2bdc in the reaction mixture).

6.1.2 Negative thermal expansion

Perhaps the most intriguing physical property of densified-UiO-66(Hf) is its NTE response, which is evident in the increase of the cubic unit cell parameter on cooling from 340 °C [Fig. 6.5(a)] and in the anomalous thermal shifts of Bragg peaks in the raw diffraction data themselves [Fig. 6.5(b)]. While NTE is increasingly frequently observed amongst MOFs, there are two particular aspects of the behaviour observed here that are especially attractive: on the one hand, the cubic crystal symmetry of defective UiO-66 means that its NTE is isotropic—*i.e.* it occurs with equal magnitude in all crystal directions; and, on the other hand, the magnitude itself is very large. The thermal expansion can be quantified via the coefficient of volume thermal expansion, α_V:

$$\alpha_V = \frac{1}{V}\left(\frac{\partial V}{\partial T}\right)_p, \tag{6.1}$$

with typical (positive) thermal expansion of engineering materials corresponding to values of α_V in the range 10–30 $\mathrm{MK^{-1}}$ [380]. For the least defective sample of UiO-66(Hf), the lattice parameter data give a thermal expansivity of $\alpha_V = -97(4)\,\mathrm{MK^{-1}}$ over the temperature range 160–340 °C, which is comparable in magnitude to that of "colossal" thermal expansion materials ($|\alpha| \simeq 100\,\mathrm{MK^{-1}}$) such as $Ag_3[Co(CN)_6]$ [270]. Although an even more rapid increase in lattice parameter is observed on further cooling from 160–100 °C, this feature may arise from re-uptake of guest molecules at these lower temperatures. Separate variable temperature diffraction measurements, carried out under flowing N_2, confirm the reversibility of the NTE behaviour [Fig. 6.5(c)].

Isotropic NTE behaviour of this magnitude is rare indeed. First discovered in ZrW_2O_8 in the late 1960s [381], isotropic NTE is now known to occur in a handful of materials, such as ZrW_2O_8 itself and related substitutional variants [381–383], the perovskite analogues ScF_3 and ReO_3 [384–386], the cuprite–structured oxides Ag_2O and Cu_2O [387], the $Zn_xCd_{1-x}(CN)_2$ family and anhydrous Prussian Blue analogues [388–391], and the three MOFs HKUST-1, MOF-5, and MOF-14 [272–274]*. Of these various systems, single-

*More recently, theoretical studies have suggested that isotropic NTE may occur in a much wider range of MOF materials than known from experiment. These studies also emphasise the central role that topology plays in determining mechanical properties [392].

network $Cd(CN)_2$ is the only colossal NTE material ($\alpha_V = -100.5(15)\,MK^{-1}$) [391]. Despite decades of theoretical and experimental studies there is only general consensus that low-energy transverse vibrational modes play at least some role in the NTE mechanisms for most of these materials. The details of NTE mechanisms remain controversial, with new studies frequently demanding reinterpretation of long-held assumptions as and when they appear [274, 393–395]. I avoid here speculating on a detailed NTE mechanism and focus instead on the measurement and defect dependence of the phenomenon. I note simply that, with its open framework structure of high-nuclearity clusters connected by long, light, and flexible organic linkers, densified-UiO-66(Hf) certainly shares many of the basic design features thought to favour low-energy NTE modes. Fig. 6.5(d) places the isotropic NTE behaviour of UiO-66(Hf) in the context of the three other MOFs known to show the effect [272–274].

As anomalous as the thermal expansion behaviour of densified-UiO-66(Hf) is, a more far-reaching question is whether the magnitude of NTE might be sensitive to defect concentration. What sensitivity, if any, can be expected? An earlier study of the geometric contribution to NTE in molecular frameworks suggested that defects of the type thought to occur in UiO-66(Hf) should actually encourage NTE because they act to increase the relative contribution of NTE vibrational modes to the overall framework dynamics [52]. Likewise, even simple Maxwellian counting suggests that the balance of degrees of freedom and geometric constraints would be tipped increasingly in favour of the former (and hence NTE) as linkers are removed from a three-dimensional network [396]. Not taken into account in either analysis, however, is the observation that defects are also linked to framework densification. Empirically, one finds that higher densities usually result in weaker NTE—this is exactly what is observed in zeolites, Prussian blues, and the $Zn_xCd_{1-x}(CN)_2$ family alike [388, 390, 397]. A further complication to add to this balance of competing effects, is that the ligand elimination process alters the point symmetry of the Hf_6 clusters in a way that may itself affect the dynamics—and hence the NTE—of defective UiO-66(Hf). The point symmetries of both defect-free and defective Hf_6 clusters (D_{3d} and D_{4h}, respectively) are incompatible with one another, as they are with the point symmetry of the crystallographic site on which they both sit (O_h) [Fig. 6.1(c,d)]. Consequently, the effective energy potential governing transverse vibrational motion—which,

by analogy to better-understood NTE materials, is likely to be implicated in NTE—will not be constrained by symmetry and hence will vary from site to site throughout the defective lattice. The effect of defect concentration on the average effective potential, its asymmetry, and its variance together pose an interesting challenge for computational and theoretical methods of understanding NTE lattice dynamics in this system.

What is in practice observed is that the UiO-66(Hf) samples with higher defect concentrations actually show reduced NTE effects relative to defect-poor samples. The coefficients of thermal expansion determined *via* variable-temperature PXRD measurements increase systematically from $-70(2)$ to $-97(4)\,\mathrm{MK}^{-1}$ as defect concentrations are reduced [Fig. 6.5(c)]. So any effect of increased flexibility arising from the reduced framework connectivity at high defect concentrations must be outweighed by the effects of densification and/or local symmetry. Regardless of the microscopic origin of this defect dependence, the chemical control over NTE behaviour observed here would usually be associated with aliovalent substitution, as exploited in conventional solid-state NTE compounds (*e.g.* the $ZrV_xP_{2-x}O_7$ family [382]). That similar control over the physical properties of MOFs can be achieved through the use of defect chemistry is precisely the proof-of-principle needed to demonstrate that defects might be used as a design element in their own right when engineering MOFs with targeted properties.

6.2 Concluding remarks

One of the driving forces for exploring NTE in defective MOFs is the relationship between NTE and other unusual mechanical phenomena, *e.g.* pressure-induced amorphisation [366, 398, 399] or softening [400, 401]. The counterintuitive defect-dependence of the NTE for UiO-66(Hf) hints that similarly unorthodox defect-dependence may hold for its mechanical properties: reduced NTE implies higher stiffness, and so more defective UiO-66 may in fact be more resistant to pressure induced transitions/amorphisation [402]. This may provide a mechanism to improve the mechanical properties of MOFs, such as their machinability and durability under operating conditions. Whether this bizarre relationship of defect-driven toughening actually holds in practice remains to be shown, but what is clear, even at this stage, is that further studies of defect/property relationships in MOFs are set to challenge our collective intuition of the physical consequences of structural disorder.

While I have focussed heavily on the implications of variable NTE in the UiO-66 system, the control over framework densification evident in Fig. 6.5(b) may highlight another means of exploiting defects in MOFs. It has recently been shown that densification of guest-containing MOFs through pressure or mechanical grinding can be an effective method of immobilising dangerous species (*e.g.* radioactive iodine) [403, 404]. The incorporation of defects might therefore allow for simultaneously increasing capacity for adsorption of these guests while also more efficiently trapping guests through lower framework densities.

In summary, I have shown for the first time how the thermomechanical properties of a MOF can be systematically varied *via* controlled incorporation of defects. The thermomechanical properties observed in defective UiO-66(Hf) are extremely unusual, and include the strongest isotropic NTE effect ever observed for a MOF. This property in itself may have application in counteracting the positive thermal expansion behaviour of other engineering materials. Yet the most important result remains a conceptual one: namely that defects might now realistically play a key role in the design of new classes of functional MOFs.

6.3 Methods

6.3.1 Preparation of defective UiO-66(Hf)

I synthesised defective UiO-66(Hf) using the method described for large scale synthesis in Section 5.3.1. The most defective sample was synthesised as follows. $HfCl_4$ (3 mmol, 99.9% (metals basis, $< 0.5\%$ Zr), Alfa Aesar) and terephthalic acid (2.5 mmol, Sigma Aldrich) were added to a 250 ml Schott bottle and dissolved in N,N dimethylformamide (DMF) (40 ml, Sigma Aldrich). This mixture was sonicated until the metal and ligand had dissolved and then formic acid (20 ml, 95%, Sigma Aldrich) was added. The bottle was sealed then placed in an oven at 120 °C for 24 h. The product was isolated by filtration, washed (DMF) and then heated at 60 °C with DMF for 3 days to ensure the removal any residual ligand. Further impurities were removed from the filtered product by Soxhlet extraction (ethanol). The purified product was then dried at 150 °C for 24 h *in vacuo*. Less defective samples were prepared using larger concentrations of terephthalic acid: 3.0, 4.0,

4.5 and 5.0 mmol. All samples were loaded in 0.5 mm quartz glass capillaries with Al_2O_3 as an internal temperature standard (*ca* 50% by mass) and sealed with cotton wool.

6.3.2 Thermogravimetric analysis

Thermogravimetric analysis was carried using a Mettler Toledo TGA/DSC 1 System, heating from 30 °C to 650 °C at a rate of 20 °C min^{-1} before cooling down to room temperature [Fig. 6.6].

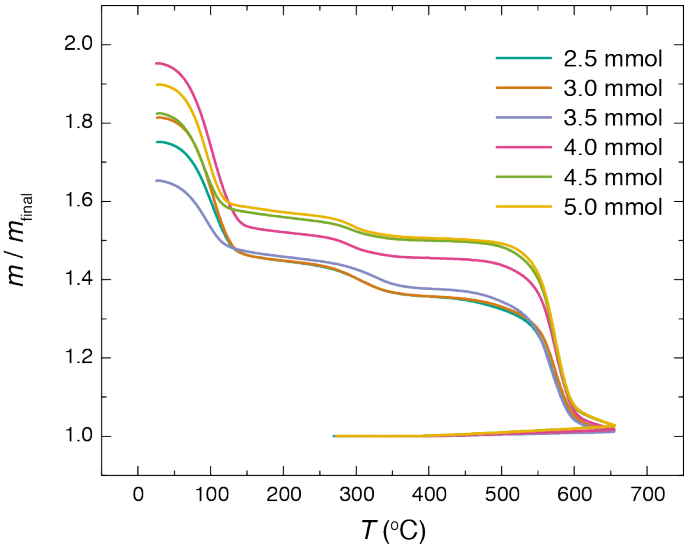

Figure 6.6: TGA traces for all six samples, synthesised with a varying quantity of H_2bdc ligand, summarised in Fig. 6.2(c,d). All masses have been scaled to the lowest mass.

6.3.3 Variable-temperature synchrotron PXRD measurements

The variable temperature synchrotron experiments were carried out with the help of Dr Claire Murray (Diamond Light Source), Joshua Hill and Prof. Andrew Goodwin. Variable temperature PXRD measurements were carried out on the I11 beamline at the Diamond Light Source ($\lambda = 0.82562$ Å) using a position sensitive detector with a Cyberstar hot air blower [405, 406]. Analysis of the data was carried out using Topas Academic version 4.1 [315]. The purity of all samples was checked using a Rietveld fit to the reported structure for UiO-66(Zr) [174], with Hf substituted for Zr. The additional primitive peaks were fitted using a secondary Pawley phase with the same lattice parameter but with additional size broadening as described in Ref. 292. Lattice parameters were determined using Pawley refinement in space group $Fm\bar{3}m$, omitting the low angle region where the

broad primitive reflections make an important contribution. The Pawley refinements were carried out using the previous temperature's refined parameters as the input for the next refinement.

Laboratory PXRD measurements were carried out using a Siemens D5000 diffractometer operating in Bragg-Brentano geometry using Cu Kα radiation ($\lambda = 1.541$ Å), equipped with an Anton Paar furnace under flowing N_2. Refined parameters are available in Appendix Tables A1.3 to A1.6 and displayed in Appendix Fig. A1.1 along with exemplar fits [Appendix Fig. A1.2].

6.3.4 Quantum mechanical calculations

Quantum mechanical calculations were carried out by Dr François-Xavier Coudert (Chimie ParisTech–CNRS). All structures were fully relaxed by optimizing both atomic positions and unit cell parameters. Quantum mechanical calculations were performed using the density functional theory approach with localized basis sets (CRYSTAL14 code [371]). B3LYP hybrid exchange-correlation functional [372] and all-electron basis sets for all atoms [288] were used, except Hf for which a small relativistic effective core potential with 12 outer electrons considered explicitly was used [373]. Full methodological details can be found in Refs. 292 and 374. The optimised structures are included in Appendix Section A1.3.

Chapter 7

Conclusion

In this Thesis I have tried to make the case that we are now in the position to use disorder and defects as design elements in molecular framework materials. I have done this by exploring two distinct aspects of the problem of disorder. In the first half of the Thesis I addressed one of the canonical hard problems of structural science: how to determine the structure of amorphous materials, and showed that diffraction data are more information-rich than conventionally believed. The two key steps taken were: first, demonstrating that information from other techniques, in the form of the number and distribution of atomic environments, can be included in RMC refinements; and second, showing that the constraint on the number of distinct atomic environments can be generalised into the concept of 'structural simplicity'. These two steps can be thought of in the framework of a Bayesian, information-based approach: information about the number of structural environments corresponds to additional observations and structural simplicity provides a more realistic prior probability distribution. Using this approach I was able to demonstrate that information about the higher-order correlation functions can be recovered from PDF data for amorphous materials.

In the second half of this Thesis I focussed instead on a concrete chemical system: demonstrating that disorder plays an important role in the chemistry of MOFs, using the example of disordered defects in the canonical MOF UiO-66(Hf). In Chapter 5 I demonstrated the existence of correlated defects in UiO-66(Hf) and showed that these defects could be controllably introduced in synthesis through the use of an acid modulator. In Chapter 6 I went on to demonstrate that these defects have non-trivial implications for the physical properties of MOFs, in particular that defects can be used to control the remarkable thermomechanical properties of UiO-66(Hf), allowing for tuning of both the large NTE and densification.

One of the threads that binds the Thesis together is the importance of diffraction data and its intimate connection to structure and disorder. The success of conventional crystallography has meant that structures of the overwhelming majority of ordered crystals

can be routinely determined. In contrast, even the most straightforward forms of correlated disorder necessitate considerable effort—optimised data collection, non-trivial structure solution and interpretation of structure often requiring custom software. Our knowledge about disordered materials is thus comparatively restricted. This paucity of knowledge equally suggests that there may be many surprising discoveries yet to be made.

This prompts the question: how should we proceed to best explore disordered materials? Despite the advances demonstrated in this Thesis, it is clear that we have not yet arrived at a proven method for solving the structures of amorphous materials. In Chapter 3 I investigated the limitations of this data-driven approach: it is clear that just like with energy-driven approaches, minimising the structures of amorphous CRN materials is slow. Therefore, even where the algorithm would in theory find the correct solution, it will not reach it in any sensible period of time. It is also true that the models of *a*-Si I have obtained—despite being the highest quality data-driven configurations so far produced—still lack physicality: calculations of their properties will not show the defining feature of *a*-Si, electronic semiconductivity. A final issue that will have to be addressed is how this approach could be applied in the real world: despite continuing improvements in instrumentation, the perfect data I have used will never be experimentally accessible; nearly every amorphous material is more complex than *a*-Si and finally many scientifically and globally important amorphous systems are deeply inhomogeneous. Amorphous structure solution remains a formidable challenge.

To tackle this challenge it will be necessary to marshall the wealth of techniques that we have available to us and develop methods able to combine them effectively. The flexibility of a Bayesian information-based approach is appealing, as it supplies a logical framework for the incorporation of diverse forms of structural information. Crucially, it also allows for robust assessment of how the various included data shape the refined model. Bayesian statistics can therefore help distinguish between structural features that are the result of experimental data, and those that are simply artefacts of the fitting process. Two of the most important sources of information that are not currently directly included in any RMC approach are NMR data and the energy of a system. The INVERT approach is one route for including information derived from NMR. However, this only represents a small subset of the information that can be obtained through NMR. Equally, *ab initio*

calculations are now able to accurately capture the fundamental chemistry of materials but the potentials used to restrain refinements are much more limited. In both cases the obvious barrier is the computational expense of carrying out the calculation. How best to make use of these powerful techniques remains an open question.

Recent advances in coherent radiation sources, including both third-generation synchrotrons [407] and X-ray free electron lasers [408], have shown that it is possible to increase the information available through diffraction techniques, potentially providing data sensitive to higher-order correlation functions. Coherent X-ray diffraction has already proved its capability for imaging and strain mapping of nanocrystals [409, 410], but its utility for understanding the structures of disordered materials is so far unknown [411]. Fluctuation electron microscopy (FEM) is a related technique that also makes use of the coherence of radiation to provide information on the third- and fourth-order correlation functions, in this case through measurements the nanometre scale inhomogeneity [412]. FEM has in fact already been applied to amorphous materials, indicating the existence of greater inhomogeneity in *a*-Si than one might expect from a simplistic CRN model [413]. For these advanced diffraction techniques quantitative data analysis is still its infancy and thus their inclusion in RMC-type approaches remains difficult.

A second challenge for structural refinement is how to explore configurational space more effectively. Despite the ease of implementation and their conceptual simplicity, it is clear that small, translational single-atom moves are not the most efficient route for optimising structures [143]. That the move is a constraining factor in refinement is apparent from the very low move acceptance rate. Developing 'natural' moves that will allow for efficient refinement of big box models would thus be a very substantial step forward.

A further step to be taken is the extension of the simplicity-based approach to the multicomponent, many-element systems that make up the overwhelming majority of chemistry. For simpler cases, *e.g.* *a*-SiO_2, the extension is relatively straightforward: the simplicity of each element type should be maximised. For more complex systems, such as where the material contains molecules, this direct approach may not prove as successful. However, the molecular nature itself provides a solution, as much of the chemical complexity is encoded in the structure of the molecule. As the structures of molecules are

ordinarily both relatively experimentally accessible and parametrisable, the real-space big box approach allows for much of this complexity to be abstracted from the refinement itself. This step would appear at face value to be much more tractable than the previous two.

The way forward for the study of disorder in MOFs is perhaps less opaque: the important role that vacancies and defects play in classical oxide chemistry hints at their potential importance for MOFs. Thus far the overwhelming majority of MOF defect chemistry (including in this thesis) has made use of the ligand fragmentation approach. This is clearly limiting: just as the range of defects in metal oxides extends beyond oxide vacancies, the range of possible defects within MOFs must extend beyond ligand (and now cluster) vacancies. It will be important to expand our methods for control over disorder and defects—can we make use of the burgeoning range of postsynthetic and mechanochemical techniques for this purpose? Many of the most important properties of conventional defective materials rely on the presence of motion, but there have been no reports of the mobility of defects. Extending MOF defect chemistry toward dynamic disorder will therefore be necessary to take full advantage of its potential.

As the range and variety of disorder synthetically accessible in MOF expands, our ability to make of this disorder will correspondingly increase. Defects are now beginning to prove their worth as motifs in functional materials, particularly for gas sorption and catalysis. In this thesis I have also shown the relevance of defects to mechanical properties. Understanding and controlling the interaction between flexibility and gas sorption, such as in gate opening or breathing materials, will very likely depend on our comprehension of the role of defects, especially higher dimensional, plane or line, defects. Dynamic disorder is of course essential for ionic conduction. Exploration of dynamic disorder will therefore also shed light on the possibility of MOFs in electrochemistry, whether as catalysts or battery components. Dynamic disorder is also essential for equilibration and so would open the possibility of MOFs as platforms for systems chemistry. Combinatorially synthesised and dynamically optimised materials (whether through manual iteration or self-assembly) could produce materials with exceptionally high selectivities and affinities for guests, suggesting the possibility of smart sorbents or catalysts. The systems chemistry approach also gives the possibility of replicating and extending the properties of some of the complex

magnetic materials metals and oxides. MOFs would be ideal candidates to, for example, produce mechanical analogues of the emergent phenomena found in magnetism, suggesting applications in areas such as thermoelectrics.

Despite the many advances of materials chemistry, we still have no sure-fire route to create useful new materials—except for exploring new chemical space with eyes wide open. The study of disordered molecular frameworks, by virtue of their diversity and modularity, offer one of the most promising avenues for exploration.

Bibliography

[1] E. R. Caley and J. F. C. Richards, *Theophrastus On Stones*, The Ohio State University, Columbus Ohio, 1956.

[2] L. B. Skinner, S. R. Chae, C. J. Benmore, H. R. Wenk and P. J. M. Monteiro, *Phys. Rev. Lett.*, 2010, **104**, 195502.

[3] G. Xu, Z. Zhong, Y. Bing, Z.-G. Ye and G. Shirane, *Nat. Mater.*, 2006, **5**, 134–140.

[4] D. Loke, T. H. Lee, W. J. Wang, L. P. Shi, R. Zhao, Y. C. Yeo, T. C. Chong and S. R. Elliott, *Science*, 2012, **336**, 1566–1569.

[5] S. Weiner, I. Sagi and L. Addadi, *Science*, 2005, **309**, 1027–1028.

[6] D. L. Bish, D. F. Blake, D. T. Vaniman, S. J. Chipera, R. V. Morris, D. W. Ming, A. H. Treiman, P. Sarrazin, S. M. Morrison, R. T. Downs, C. N. Achilles, A. S. Yen, T. F. Bristow, J. A. Crisp, J. M. Morookian, J. D. Farmer, E. B. Rampe, E. M. Stolper and N. Spanovich, *Science*, 2013, **341**, 1238932.

[7] L. Addadi, S. Raz and S. Weiner, *Adv. Mater.*, 2003, **15**, 959–970.

[8] S. Hull, *Reports Prog. Phys.*, 2004, **67**, 1233–1314.

[9] S. T. Bramwell and M. J. Gingras, *Science*, 2001, **294**, 1495–1501.

[10] J. P. Crutchfield, *Nat. Phys.*, 2011, **8**, 17–24.

[11] D. Ruelle, *Physica*, 1982, **113A**, 619–623.

[12] J. H. E. Cartwright and A. L. Mackay, *Philos. T. Roy. Soc. A*, 2012, **370**, 2807–2822.

[13] R. J. Baxter, *Exactly Solved Models in Statistical Mechanics*, Academic Press, London, 1982.

[14] M. T. Dove, *Structure and Dynamics*, Oxford University Press, Oxford, 2003.

[15] *Fundamentals of Crystallography*, ed. C. Giacovazzo, Oxford University Press, Oxford, 2nd edn., 2011.

[16] D. A. Keen, *J. Appl. Crystallogr.*, 2001, **34**, 172–177.

[17] P. Coppens, in *International Tables for Crystallography*, ed. E. Prince, International Union of Crystallography, 1st edn., 2006, vol. B, ch. 1.2, pp. 10–24.

[18] M. O'Keeffe, M. A. Peskov, S. J. Ramsden and O. M. Yaghi, *Acc. Chem. Res.*, 2008, **41**, 1782–1789.

[19] A. F. Wells, *Structural Inorganic Chemistry*, Oxford University Press, Oxford, 2nd edn., 1984.

[20] J. Colinge and C. Colinge, *Physics of Semiconductor Devices*, Kluwer Academic Publishers, Boston, 2002.

[21] W. L. Bragg and E. J. Williams, *P. Roy. Soc. Lond. A Mat.*, 1934, **145**, 699–730.

[22] J. M. Cowley, *J. Appl. Phys.*, 1950, **21**, 24–30.

[23] S. C. Moss, *J. Appl. Phys.*, 1964, **35**, 3547–3553.

[24] S. Sarkar, X. Ren and K. Otsuka, *Phys. Rev. Lett.*, 2005, **95**, 1–4.

[25] J.-M. Joubert, M. Latroche, R. Černý, A. Percheron-Guégan and Y. K., *J. Alloys Compd.*, 2000, **330–332**, 208–214.

[26] C. Guo, S. Jia, W. Meng, H. Zheng, L. Jin, Y. Liu, J. Shi and J. Wang, *Acta Crystallogr.*, 2013, **B69**, 589–594.

[27] C. N. R. Rao and B. Raveau, *Transition Metal Oxides*, Wiley-VCH, New York, 1998.

[28] J. Bobroff, H. Alloul, S. Ouazi, P. Mendels, A. Mahajan, N. Blanchard, G. Collin, V. Guillen and J.-F. Marucco, *Phys. Rev. Lett.*, 2002, **89**, 157002.

[29] C. P. Adams, J. W. Lynn, Y. M. Mukovskii, A. A. Arsenov and D. A. Shulyatev, *Phys. Rev. Lett.*, 2000, **85**, 3954–3957.

[30] E. S. Božin, S. J. Billinge, G. H. Kwei and H. Takagi, *Phys. Rev. B*, 1999, **59**, 4445–4454.

[31] J. K. Burdett and J. F. Mitchell, *Prog. Solid St. Chem.*, 1995, **23**, 131–170.

[32] M. D. Banus, *Mat. Res. Bull.*, 1968, **3**, 723–734.

[33] J. B. Goodenough, *Phys. Rev. B*, 1972, **5**, 2764–2774.

[34] P. J. Saines, M. G. Tucker, D. A. Keen, A. K. Cheetham and A. L. Goodwin, *Phys. Rev. B*, 2013, **88**, 134418.

[35] T. Suemoto, *Solid State Ionics*, 1986, **21**, 225–229.

[36] C. Tealdi, P. Mustarelli and M. S. Islam, *Adv. Funct. Mater.*, 2011, **22**, 3874–3880.

[37] N. Laurance, *Phys. Rev.*, 1960, **120**, 57–62.

[38] T. A. Miller, J. S. Wittenberg, H. Wen, S. Connor, Y. Cui and A. M. Lindenberg, *Nat. Commun.*, 2012, **4**, 1369.

[39] G. Eckold, K. Funke, J. Kalus and R. Lechner, *Solid State Commun.*, 1976, **37**, 1097–1103.

[40] A. Kvist and R. Tärneberg, *Z. Naturforsch.*, 1970, **25 a**, 257–259.

[41] K. Krynicki, C. D. Green and D. W. Sawyer, *Faraday Discuss. Chem. Soc.*, 1978, **66**, 199–208.

[42] A. L. Goodwin, M. G. Tucker, E. R. Cope, M. T. Dove and D. A. Keen, *Phys. Rev. B*, 2005, **72**, 214304.

[43] M. J. Duer, *Solid–State NMR Spectroscopy: Principles and Applications*, Blackwell Science, Oxford, 2002.

[44] C. Line, B. Winkler and M. Dove, *Phys. Chem. Miner.*, 1994, **21**, 451–459.

[45] M. T. Dove, *Eur. J. Mineral.*, 2002, **14**, 203–224.

[46] A. D. B. Woods, W. Cochran and B. N. Brockhouse, *Phys. Rev.*, 1960, **119**, 980–999.

[47] M. Schwoerer-Böhning, A. Macrander and D. Arms, *Phys. Rev. Lett.*, 1998, **80**, 5572–5575.

[48] T. Ruf, J. Serrano, M. Cardona, P. Pavone, M. Pabst, M. Krisch, M. D'Astuto, T. Suski, I. Grzegory and M. Leszczynski, *Phys. Rev. Lett.*, 2001, **86**, 906–909.

[49] W. W. Schmall, I. P. Swainson, M. T. Dove and A. Graeme-Barber, *Z. Krist.*, 1992, **201**, 125–145.

[50] M. G. Tucker, M. P. Squires, M. T. Dove and D. A. Keen, *J. Phys.: Condens. Matter*, 2001, **13**, 403–423.

[51] G. Shirane, B. Frazer, V. Minkiewicz, J. Leake and A. Linz, *Phys. Rev. Lett.*, 1967, **19**, 234–235.

[52] A. L. Goodwin, *Phys. Rev. B*, 2006, **74**, 134302.

[53] R. W. G. Wyckoff, *Am. J. Sci.*, 1925, **9**, 448–457.

[54] R. W. G. Wyckoff, *Z. Kristallogr Krist.*, 1926, **63**, 507–537.

[55] M. G. Tucker, D. A. Keen and M. T. Dove, *Mineral. Mag.*, 2001, **65**, 489–507.

[56] W. Zhong, D. Vanderbilt and K. M. Rabe, *Phys. Rev. B*, 1994, **73**, 1861–1865.

[57] G. H. Kwei, A. C. Lawson, S. J. L. Billinge and S. W. Cheong, *J. Phys. Chem.*, 1993, **97**, 2368–2377.

[58] M. Holma, N. N. Takesue and H. Chen, *Ferroelectrics*, 1995, **164**, 237–251.

[59] H. D. Megaw and H. P. Rooksby, *Nature*, 1945, **155**, 484–485.

[60] R. Comès, M. Lambert and A. Guinier, *Solid State Commun.*, 1968, **6**, 715–719.

[61] L. Pauling, *J. Am. Chem. Soc.*, 1935, **57**, 2680–2684.

[62] V. E. Fairbank, A. L. Thompson, R. I. Cooper and A. L. Goodwin, *Phys. Rev. B*, 2012, **86**, 104113.

[63] D. P. Shoemaker, R. Seshadri, A. L. Hector, A. Llobet, T. Proffen and C. J. Fennie, *Phys. Rev. B*, 2010, **81**, 144113.

[64] T. Fennell, P. P. Deen, A. R. Wildes, K. Schmalzl, D. Prabhakaran, A. T. Boothroyd, R. J. Aldus, D. F. McMorrow and S. T. Bramwell, *Science*, 2009, **326**, 415–417.

[65] M. Paściak, T. R. Welberry, J. Kulda, M. Kempa and J. Hlinka, *Phys. Rev. B*, 2012, **85**, 224109.

[66] M. T. Dove, *Mineral. Mag.*, 1995, **59**, 629–639.

[67] J. E. Lewis, Jr., C. C. Freyhardt and M. E. Davis, *J. Phys. Chem.*, 1996, **100**, 5039–5049.

[68] H. Morell, K. Angermund, A. R. Lewis, D. H. Brouwer, C. A. Fyfe and H. Gies, *Chem. Mater.*, 2002, **14**, 2192–2198.

[69] L. Karlsson, *Solid State Ionics*, 1995, **76**, 301–308.

[70] M. T. Dove, I. P. Swainson, B. M. Powell and D. C. Tennant, *Phys. Chem. Miner.*, 2005, **32**, 493–503.

[71] Y. Yamada and M. Harada, *J. Phys. Soc. Japan*, 1986, **55**, 4315–4322.

[72] Z.-S. Yao, M. Mito, T. Kamachi, Y. Shiota, K. Yoshizawa, N. Azuma, Y. Miyazaki, K. Takahashi, K. Zhang, T. Nakanishi, S. Kang, S. Kanegawa and O. Sato, *Nat. Chem.*, 2014, **6**, 1079–1083.

[73] R. W. Impey, M. L. Klein and I. R. McDonald, *J. Chem. Phys.*, 1985, **82**, 4690–4698.

[74] M. Jansen, *Angew. Chem. Int. Ed.*, 1991, **30**, 1547–1558.

[75] U. Höchli, K. Knorr and A. Loidl, *Adv. Phys.*, 1990, **39**, 405–615.

[76] K. Binder and J. Reger, *Adv. Phys.*, 1992, **41**, 547–627.

[77] N. P. Funnell, M. T. Dove, A. L. Goodwin, S. Parsons and M. G. Tucker, *J. Phys.: Condens. Matter*, 2013, **25**, 454204.

[78] J. C. W. Folmer, R. L. Withers, T. R. Welberry and J. D. Martin, *Phys. Rev. B*, 2008, **77**, 144205.

[79] L. Yu, *Adv. Drug Deliv. Rev.*, 2001, **48**, 27–42.

[80] C. Dimitrakopoulos and D. Mascaro, *IBM Journal of Research and Development*, 2001, **45**, 11–27.

[81] F. M. Michel, L. Ehm, S. M. Antao, P. L. Lee, P. J. Chupas, G. Liu, D. R. Strongin, M. A. A. Schoonen, B. L. Phillips and J. B. Parise, *Science*, 2007, **316**, 1726–1729.

[82] S. Ding, Y. Liu, Y. Li, Z. Liu, S. Sohn, F. J. Walker and J. Schroers, *Nat. Mater.*, 2014, **13**, 1–7.

[83] L. Zhong, J. Wang, H. Sheng, Z. Zhang and S. X. Mao, *Nature*, 2014, **512**, 177–180.

[84] J. E. Shelby, *Introduction to Glass Science and Technology*, Royal Society of Chemistry, Cambridge, 2005.

[85] A. L. Greer and N. Mathur, *Nature*, 2005, **437**, 1246–1247.

[86] S. Kugler and K. Shimakawa, *Amorphous Semiconductors*, Cambridge University Press, Cambridge, 2015.

[87] P. F. Damasceno, M. Engel and S. C. Glotzer, *Science*, 2012, **337**, 453–457.

[88] L. Rovigatti, F. Smallenburg, F. Romano and F. Sciortino, *ACS Nano*, 2014, **8**, 3567–3574.

[89] S. Bach, V. R. Celinski, M. Dietzsch, M. Panthöfer, R. Bienert, F. Emmerling, J. Schmedt auf der Günne and W. Tremel, *J. Am. Chem. Soc.*, 2015, **137**, 2285–2294.

[90] Los Angeles County Museum of Arts, *Bowl, M.73.5.363*.

[91] A. Walsh, J. L. F. Da Silva and S.-H. Wei, *Chem. Mater.*, 2009, **21**, 5119–5124.

[92] K. S. Thyagarajan and A. Ghatak, *Fiber Optic Essentials*, IEEE Press, Piscataway New Jersey, 2007.

[93] Y. H. Liu, G. Wang, R. J. Wang, D. Q. Zhao, M. X. Pan and W. H. Wang, *Science*, 2007, **315**, 1385–1388.

[94] A. Inoue, B. Shen, H. Koshiba, H. Kato and A. R. Yavari, *Nat. Mater.*, 2003, **2**, 661–663.

[95] W. S. Wong and A. Salleo, *Flexible Electronics: Materials and Applications*, Springer Science & Business Media, New York, 2009, vol. 11.

[96] D. E. Carlson and C. R. Wronski, *Appl. Phys. Lett.*, 1976, **28**, 671–673.

[97] J. Li and D. Drabold, *Phys. Rev. B*, 2003, **68**, 033103.

[98] R. Hasegawa, *Mat. Sci. Eng. A-Struct.*, 2004, **375–377**, 90–97.

[99] S. R. Ovshinky, *Phys. Rev. Lett.*, 1968, **21**, 1450–1453.

[100] D. M. Pai and B. E. Springett, *Rev. Mod. Phys.*, 1993, **65**, 163–211.

[101] K. Nomura, H. Ohta, A. Takagi, T. Kamiya, M. Hirano and H. Hosono, *Nature*, 2004, **432**, 488–492.

[102] H. Hosono, *J. Non. Cryst. Solids*, 2006, **352**, 851–858.

[103] C. L. Farrow, P. Juhas, J. W. Liu, D. Bryndin, E. S. Božin, J. Bloch, T. Proffen and S. J. L. Billinge, *J. Phys.: Condens. Matter*, 2007, **19**, 335219.

[104] E. S. Božin, M. Schmidt, A. J. DeConinck, G. Paglia, J. F. Mitchell, T. Chatterji, P. G. Radaelli, T. Proffen and S. J. L. Billinge, *Phys. Rev. Lett.*, 2007, **98**, 137203.

[105] H. Y. Playford, A. C. Hannon, E. R. Barney and R. I. Walton, *Chem.-Eur. J.*, 2013, **19**, 2803–2813.

[106] D. Prill, P. Juhás, M. U. Schmidt and S. J. L. Billinge, *J. Appl. Crystallogr.*, 2015, **48**, 171–178.

[107] R. B. Neder and T. Proffen, *Diffuse Scattering and Defect Structure Simulations: A cook book using the program DISCUS*, Oxford University Press, New York, 2008.

[108] T. R. Welberry, D. J. Goossens, A. J. Edwards and W. I. F. David, *Acta Crystallogr.*, 2001, **A57**, 101–109.

[109] G. Sala, M. J. Guttman, D. Prabhakaran, D. Pomaranski, C. Mitchelitis, J. B. Kycia, D. G. Porter, C. Castelnovo and J. P. Goff, *Nat. Mater.*, 2014, **13**, 488–493.

[110] R. L. McGreevy and L. Pusztai, *Mol. Simul.*, 1988, **1**, 359–367.

[111] M. G. Tucker, D. A. Keen, M. T. Dove, A. L. Goodwin and Q. Hui, *J. Phys.: Cond. Matt.*, 2007, **19**, 335218.

[112] J. Villain, R. Bidaux, J.-P. Carton and R. Conte, *J. Phys. France*, 1980, **41**, 1263–1272.

[113] V. Krayzman, I. Levin and M. G. Tucker, *J. Appl. Crystallogr.*, 2008, **41**, 705–714.

[114] G. Opletal, T. Petersen, I. Snook and S. Russo, *Comput. Phys. Commun.*, 2013, **184**, 1946–1957.

[115] D. Frenkel and B. Smit, *Understanding Molecular Simulation*, Academic Press, San Diego, 2002.

[116] A. K. Soper, *Phys. Rev. B*, 2005, **72**, 104204.

[117] A. L. Patterson, *Nature*, 1939, **143**, 939–940.

[118] T. R. Welberry and B. D. Butler, *J. Appl. Crystallogr.*, 1994, **27**, 205–231.

[119] A. C. Wright and M. F. Thorpe, *Phys. Status Solidi B*, 2013, **250**, 931–936.

[120] S. R. Elliott, *Physics of Amorphous Materials*, Longman Scientific & Technical, Burnt Mill, Harlow, Essex, 2nd edn., 1990.

[121] J. T. Randall, H. P. Rooksby and B. S. Cooper, *Z. Krist.*, 1930, **75**, 196–214.

[122] B. E. Warren, *J. Chem. Phys.*, 1934, **2**, 551–555.

[123] S. Roorda, W. C. Sinke, J. M. Poate, D. C. Jacobson, S. Dierker, B. S. Dennis, D. J. Eaglesham, F. Spaepen and P. Fuoss, *Phys. Rev. B*, 1991, **44**, 3702–3726.

[124] D. L. Griscom, *J. Non. Cryst. Solids*, 1985, **73**, 51–77.

[125] W. H. Zachariasen, *J. Am. Chem. Soc.*, 1932, **54**, 3841–3851.

[126] W. Rosenhain, *J. Soc. Glass Technol. Trans.*, 1927, **11**, 77.

[127] J. D. Bernal and F. J. L, *Discuss Faraday Soc.*, 1967, **43**, 62–69.

[128] D. E. Polk, *J. Non. Cryst. Solids*, 1971, **5**, 365–376.

[129] M. Long, P. Galison, R. Alben and G. A. N. Connell, *Phys. Rev. B*, 1976, **13**, 1821–1829.

[130] A. Donev, I. Cisse, D. Sachs, E. A. Variano, F. H. Stillinger, R. Connelly, S. Torquato and P. M. Chaikin, *Science*, 2004, **303**, 990–993.

[131] X.-X. Huang, L.-G. Qiu, W. Zhang, Y.-P. Yuan, X. Jiang, A.-J. Xie, Y.-H. Shen and J.-F. Zhu, *Cryst. Eng. Comm.*, 2012, **14**, 1613–1617.

[132] F. H. Stillinger and T. A. Weber, *Phys. Rev. B*, 1985, **31**, 5262–5271.

[133] J. Tersoff, *Phys. Rev. B*, 1988, **37**, 6991–7000.

[134] F. Wooten, K. Winer and D. Weaire, *Phys. Rev. Lett.*, 1985, **54**, 1392–1395.

[135] F. Wooten and D. Weaire, *Solid State Phys.*, 1987, **40**, 1–42.

[136] G. Barkema and N. Mousseau, *Phys. Rev. B*, 2000, **62**, 4985–4990.

[137] D. A. Drabold, *Eur. Phys. J. B*, 2009, **68**, 1–21.

[138] M. G. Tucker, D. A. Keen, M. T. Dove and K. Trachenko, *J. Phys.: Condens. Matter*, 2005, **17**, S67–S75.

[139] T. D. Bennett, A. L. Goodwin, M. T. Dove, D. A. Keen, M. G. Tucker, E. R. Barney, A. K. Soper, E. G. Bithell, J.-C. Tan and A. K. Cheetham, *Phys. Rev. Lett.*, 2010, **104**, 115503.

[140] A. C. Wright, G. Etherington, J. A. E. Desa, R. N. Sinclair, G. A. N. Connell and J. C. Mikkelsen Jr., *J. Non. Cryst. Solids*, 1982, **49**, 63–102.

[141] S. Sastry and C. Austen Angell, *Nat. Mater.*, 2003, **2**, 739–743.

[142] C. Desgranges and J. Delhommelle, *J. Am. Chem. Soc.*, 2011, **133**, 2872–2874.

[143] G. T. Barkema and N. Mousseau, *Phys. Rev. Lett.*, 1996, **77**, 4358–4361.

[144] H. W. Sheng, W. K. Luo, F. M. Alamgir, J. M. Bai and E. Ma, *Nature*, 2006, **439**, 419–425.

[145] S. Kugler, L. Pusztai, L. Rosta, P. Chieux and R. Bellissent, *Phys. Rev. B*, 1993, **48**, 7685–7688.

[146] R. Evans, *Mol. Simul.*, 1990, **4**, 409–411.

[147] O. Gereben and L. Pusztai, *Phys. Rev. B*, 1994, **50**, 14136–14143.

[148] M. J. Cliffe, M. T. Dove, D. A. Drabold and A. L. Goodwin, *Phys. Rev. Lett.*, 2010, **104**, 125501.

[149] P. Biswas, R. Atta-Fynn and D. Drabold, *Phys. Rev. B*, 2004, **69**, 195207.

[150] P. Biswas and D. A. Drabold, *J. Non. Cryst. Solids*, 2008, **354**, 2697–2701.

[151] I. Levin, V. Krayzman and J. C. Woicik, *Phys. Rev. B*, 2014, **89**, 024106.

[152] L. Lichtenstein, C. Büchner, B. Yang, S. Shaikhutdinov, M. Heyde, M. Sierka, R. Włodarczyk, J. Sauer and H.-J. Freund, *Angew. Chem. Int. Ed.*, 2012, **51**, 404–407.

[153] D. M. Dawson and S. E. Ashbrook, *J. Phys. Chem. C*, 2014, **118**, 23285–23296.

[154] W.-L. Shao, J. Shinar, B. C. Gerstein, F. Li and J. S. Lannin, *Phys. Rev. B*, 1990, **41**, 9491–9494.

[155] P. Juhás, L. Granlund, P. M. Duxbury, W. F. Punch and S. J. L. Billinge, *Acta Crystallogr.*, 2008, **A64**, 631–640.

[156] R. D. Johnson, G. Meijer and D. S. Bethune, *J. Am. Chem. Soc.*, 1990, **112**, 8983–8984.

[157] J. Steidel, R. Steudel and A. Kutoglu, *Z. Anorg. Allg. Chem.*, 1981, **476**, 171–178.

[158] A. Phan, C. J. Doonan, F. J. Uribe-Romo, C. B. Knobler, M. O'Keeffe and O. M. Yaghi, *Acc. Chem. Res.*, 2010, **43**, 58–67.

[159] X.-Y. Wang, L. Gan, S.-W. Zhang and S. Gao, *Inorg. Chem.*, 2004, **43**, 4615–4625.

[160] Z. Wang, B. Zhang, T. Otsuka, K. Inoue, H. Kobayashi and M. Kurmoo, *Dalt. T.*, 2004, 2209–2216.

[161] A. B. Cairns and A. L. Goodwin, *Chem. Soc. Rev.*, 2013, **42**, 4881–4893.

[162] M. Eddaoudi, J. Kim, N. Rosi, D. Vodak, J. Wachter, M. O'Keeffe and O. M. Yaghi, *Science*, 2002, **295**, 469–472.

[163] H. Deng, S. Grunder, K. E. Cordova, C. Valente, H. Furukawa, M. Hmadeh, F. Gandara, A. C. Whalley, Z. Liu, S. Asahina, H. Kazumori, M. O'Keeffe, O. Terasaki, J. F. Stoddart and O. M. Yaghi, *Science*, 2012, **336**, 1018–1023.

[164] G. Hautier, C. Fischer, V. Ehrlacher, A. Jain and G. Ceder, *Inorg. Chem.*, 2011, **50**, 656–663.

[165] F. Denis Romero, A. Leach, J. S. Möller, F. Foronda, S. J. Blundell and M. A. Hayward, *Angew. Chem. Int. Ed.*, 2014, **53**, 7556–7559.

[166] C. Tassel, Y. Goto, Y. Kuno, J. Hester, M. Green, Y. Kobayashi and H. Kageyama, *Angew. Chem. Int. Ed.*, 2014, **53**, 10377–10380.

[167] L. J. Wang, H. Deng, H. Furukawa, F. Gandara, K. E. Cordova, D. Peri and O. M. Yaghi, *Inorg. Chem.*, 2013, **53**, 5881–5883.

[168] M. I. Breeze, G. Clet, B. C. Campo, A. Vimont, M. Daturi, J.-M. Grenèche, A. J. Dent, F. Millange and R. I. Walton, *Inorg. Chem.*, 2013, **52**, 8171–8182.

[169] T.-H. Park, K. Koh, A. G. Wong-Foy and A. J. Matzger, *Cryst. Growth Des.*, 2011, **11**, 2059–2063.

[170] D. N. Bunck and W. R. Dichtel, *Chem.-Eur. J.*, 2013, **19**, 818–827.

[171] H. Li, M. Eddaoudi, M. O'Keeffe and O. M. Yaghi, *Nature*, 1999, **402**, 276–279.

[172] H. Deng, C. J. Doonan, H. Furukawa, R. B. Ferreira, J. Towne, C. B. Knobler, B. Wang and O. M. Yaghi, *Science*, 2010, **327**, 846–850.

[173] J. Gascon, U. Aktay, M. D. Hernandez-Alonso, G. P. M. van Klink and F. Kapteijn, *J. Catal.*, 2009, **261**, 75–87.

[174] J. H. Cavka, S. Jakobsen, U. Olsbye, N. Guillou, C. Lamberti, S. Bordiga and K. P. Lillerud, *J. Am. Chem. Soc.*, 2008, **130**, 13850–13851.

[175] S. J. Garibay and S. M. Cohen, *Chem. Commun.*, 2010, **46**, 7700–7702.

[176] A. Schaate, P. Roy, T. Preusse, S. J. Lohmeier, A. Godt and P. Behrens, *Chem.-Eur. J.*, 2011, **17**, 9320–9325.

[177] N. L. Rosi, J. Kim, M. Eddaoudi, B. Chen, M. O'Keeffe and O. M. Yaghi, *J. Am. Chem. Soc.*, 2005, **127**, 1504–1518.

[178] C. Wang, J. L. Wang and W. Lin, *J. Am. Chem. Soc.*, 2012, **134**, 19895–19908.

[179] N. Calvo Galve, E. Coronado, M. Giménez-Marqués and G. Mínguez Espallargas, *Inorg. Chem.*, 2014, **53**, 4482–4490.

[180] X.-L. Qi, S.-Y. Liu, R.-B. Lin, P.-Q. Liao, J.-W. Ye, Z. Lai, Y. Guan, X.-N. Cheng, J.-P. Zhang and X.-M. Chen, *Chem. Commun.*, 2013, **49**, 6864–6866.

[181] D. J. Lun, G. I. N. Waterhouse and S. G. Telfer, *J. Am. Chem. Soc.*, 2011, **133**, 5806–5809.

[182] J. G. Nguyen and S. M. Cohen, *J. Am. Chem. Soc.*, 2010, **132**, 4560–4561.

[183] W. Li, M. R. Probert, M. Kosa, T. D. Bennett, A. Thirumurugan, R. P. Burwood, M. Parinello, J. A. K. Howard and A. K. Cheetham, *J. Am. Chem. Soc.*, 2012, **134**, 11940–11943.

[184] J. Gopalakrishnan, *Chem. Mater.*, 1995, **7**, 1265–1275.

[185] K. K. Tanabe and S. M. Cohen, *Chem. Soc. Rev.*, 2011, **40**, 498–519.

[186] P. Deria, J. E. Mondloch, O. Karagiaridi, W. Bury, J. T. Hupp and O. K. Farha, *Chem. Soc. Rev.*, 2014, **43**, 5896–5912.

[187] E. M. Sletten and C. R. Bertozzi, *Angew. Chem. Int. Ed.*, 2009, **48**, 6974–6998.

[188] M. Kim, J. F. Cahill, Y. Su, K. A. Prather and S. M. Cohen, *Chem. Sci.*, 2012, **3**, 126–130.

[189] C. J. Doonan, W. Morris, H. Furukawa and O. M. Yaghi, *J. Am. Chem. Soc.*, 2009, **131**, 9492–9493.

[190] S. Pullen, H. Fei, A. Orthaber, S. M. Cohen and S. Ott, *J. Am. Chem. Soc.*, 2013, **135**, 16997–17003.

[191] J. Aguilera-Sigalat and D. Bradshaw, *Chem Commun.*, 2014, **50**, 4711–4713.

[192] A. Demessence, D. M. D'Alessandro, M. L. Foo and J. R. Long, *J. Am. Chem. Soc.*, 2009, **131**, 8784–8786.

[193] K. M. L. Taylor-Pashow, J. Della Rocca, Z. Xie, S. Tran and W. Lin, *J. Am. Chem. Soc.*, 2009, **131**, 14261–14263.

[194] R. K. Deshpande, J. L. Minnaar and S. G. Telfer, *Angew. Chem. Int. Ed.*, 2010, **49**, 4598–4602.

[195] O. Karagiaridi, M. B. Lalonde, W. Bury, A. A. Sarjeant, O. K. Farha and J. T. Hupp, *J. Am. Chem. Soc.*, 2012, **134**, 18790–18796.

[196] H. Fei, J. F. Cahill, K. A. Prather and S. M. Cohen, *Inorg. Chem.*, 2013, **52**, 4011–4016.

[197] T. Li, M. T. Kozlowski, E. A. Doud, M. N. Blakely and N. L. Rosi, *J. Am. Chem. Soc.*, 2013, **135**, 11688–11691.

[198] R. Wasserman, in *The Stanford Encyclopedia of Philosophy*, ed. E. N. Zalta, URL = http://plato.stanford.edu/archives/spr2015/entries/material-constitution, Spring 2015.

[199] P. Brown, in *Shakespeare's Local*, Macmillan, London, 2012, pp. 52–53.

[200] A. F. Gross, E. Sherman and J. J. Vajo, *Dalton Trans.*, 2012, **41**, 5458–5460.

[201] F. Vermoortele, B. Bueken, G. Le Bars, B. Van de Voorde, M. Vandichel, K. Houthoofd, A. Vimont, M. Daturi, M. Waroquier, V. Van Speybroeck, C. Kirschhock and D. E. De Vos, *J. Am. Chem. Soc.*, 2013, **135**, 11465–11468.

[202] H. Wu, Y. S. Chua, V. Krungleviciute, M. Tyagi, P. Chen, T. Yildirim and W. Zhou, *J. Am. Chem. Soc.*, 2013, **135**, 10525–10532.

[203] K. M. Choi, H. J. Jeon, J. K. Kang and O. M. Yaghi, *J. Am. Chem. Soc.*, 2011, **133**, 11920–11923.

[204] S. Yang, X. Lin, W. Lewis, M. Suyetin, E. Bichoutskaia, J. E. Parker, C. C. Tang, D. R. Allan, P. J. Rizkallah, P. Hubberstey, N. R. Champness, K. M. Thomas, A. J. Blake and M. Schröder, *Nat. Mater.*, 2012, **11**, 710–716.

[205] D. N. Bunck and W. R. Dichtel, *Chem. Eur. J.*, 2013, **19**, 818–827.

[206] B. Tu, Q. Pang, D. Wu, Y. Song, L.-H. Weng and Q. Li, *J. Am. Chem. Soc.*, 2014, **136**, 14465–14471.

[207] N. E. A. El-Gamel, *Eur. J. Inorg. Chem.*, 2015, **2015**, 1351–1358.

[208] J. Park, Z. U. Wang, L.-B. Sun, Y.-P. Chen and H.-C. Zhou, *J. Am. Chem. Soc.*, 2012, **134**, 20110–20116.

[209] G. Barin, V. Krungleviciute, O. Gutov, J. T. Hupp, T. Yildirim and O. K. Farha, *Inorg. Chem.*, 2014, **53**, 6914–6919.

[210] Z. Fang, J. P. Dürholt, M. Kauer, W. Zhang, C. Lochenie, B. Jee, B. Albada, N. Metzler-Nolte, A. Pöppl, B. Weber, M. Muhler, Y. Wang, R. Schmid and R. A. Fischer, *J. Am. Chem. Soc.*, 2014, **136**, 9627–9636.

[211] O. Kozachuk, I. Luz, F. X. Llabrés I Xamena, H. Noei, M. Kauer, H. B. Albada, E. D. Bloch, B. Marler, Y. Wang, M. Muhler and R. A. Fischer, *Angew. Chem. Int. Ed.*, 2014, **53**, 7058–7062.

[212] M. J. Katz, Z. J. Brown, Y. J. Colón, P. W. Siu, K. A. Scheidt, R. Q. Snurr, J. T. Hupp and O. K. Farha, *Chem. Commun.*, 2013, **49**, 9449–9451.

[213] T. Fukushima, S. Horike, H. Kobayashi, M. Tsujimoto, S. Isoda, M. L. Foo, Y. Kubota, M. Takata and S. Kitagawa, *J. Am. Chem. Soc.*, 2012, **134**, 13341–13347.

[214] A. M. Katzenmeyer, J. Canivet, G. Holland, D. Farrusseng and A. Centrone, *Angew. Chem. Int. Ed.*, 2014, **53**, 2852–2856.

[215] K. Koh, A. G. Wong-Foy and A. J. Matzger, *Chem. Commun.*, 2009, 6162–6164.

[216] P. V. Dau and S. M. Cohen, *Chem. Commun.*, 2014, **50**, 12154–12157.

[217] X. Kong, H. Deng, F. Yan, J. Kim, J. A. Swisher, B. Smit, O. M. Yaghi and J. A. Reimer, *Science*, 2013, **341**, 882–885.

[218] *Introduction to Zeolite Science and Practice*, ed. J. Čejka, Elsevier, Amsterdam, 2007.

[219] B. Hoskins and R. Robson, *J. Am. Chem. Soc.*, 1989, **111**, 5962–5964.

[220] O. Yaghi, G. Li and H. Li, *Nature*, 1995, **378**, 703–706.

[221] S. Kitagawa, M. Munakata and T. Tanimura, *Inorg. Chem.*, 1992, **31**, 1714–1717.

[222] O. K. Farha, I. Eryazici, N. C. Jeong, B. G. Hauser, C. E. Wilmer, A. A. Sarjeant, R. Q. Snurr, S. T. Nguyen, A. O. Yazaydin and J. T. Hupp, *J. Am. Chem. Soc.*, 2012, **134**, 15016–15021.

[223] L. Sarkisov, *Adv. Mater.*, 2012, **24**, 3130–3133.

[224] A. G. Wong-Foy, A. J. Matzger and O. M. Yaghi, *J. Am. Chem. Soc.*, 2006, **128**, 3494–3495.

[225] Y. H. Hu and L. Zhang, *Adv. Mater.*, 2010, **22**, 117–130.

[226] L. J. Murray, M. Dincă and J. R. Long, *Chem. Soc. Rev.*, 2009, **38**, 1294–1314.

[227] J.-R. Li, R. J. Kuppler and H.-C. Zhou, *Chem. Soc. Rev.*, 2009, **38**, 1477–1504.

[228] J. Lee, O. K. Farha, J. Roberts, K. A. Scheidt, S. T. Nguyen and J. T. Hupp, *Chem. Soc. Rev.*, 2009, **38**, 1450–1459.

[229] A. C. McKinlay, R. E. Morris, P. Horcajada, G. Férey, R. Gref, P. Couvreur and C. Serre, *Angew. Chem. Int. Ed.*, 2010, **49**, 6260–6266.

[230] E. D. Bloch, W. L. Queen, R. Krishna, J. M. Zadrozny, C. M. Brown and J. R. Long, *Science*, 2012, **335**, 1606–1610.

[231] T. M. McDonald, J. A. Mason, X. Kong, E. D. Bloch, D. Gygi, A. Dani, V. Crocellà, F. Giordanino, S. O. Odoh, W. S. Drisdell, B. Vlaisavljevich, A. L. Dzubak, R. Poloni, S. K. Schnell, N. Planas, K. Lee, T. Pascal, L. F. Wan, D. Prendergast, J. B. Neaton, B. Smit, J. B. Kortright, L. Gagliardi, S. Bordiga, J. A. Reimer and J. R. Long, *Nature*, 2015, **519**, 303–308.

[232] D. Britt, H. Furukawa, B. Wang, T. G. Glover and O. M. Yaghi, *Proc. Natl. Acad. Sci. U.S.A.*, 2009, **106**, 20637–20640.

[233] A. M. Rasero-Almansa, A. Corma, M. Iglesias and F. Sánchez, *ChemCatChem*, 2013, **5**, 3092–3100.

[234] K. Manna, T. Zhang, M. Carboni, C. W. Abney and W. Lin, *J. Am. Chem. Soc.*, 2014, **136**, 13182–13185.

[235] H.-l. Jiang, B. Liu, T. Akita, M. Haruta, H. Sakurai, K. U. V, N. Ku, E. V. Sciences, T. Metropolitan and V. Uni, *J. Am. Chem. Soc.*, 2009, **131**, 11302–11303.

[236] G. Lu, S. Li, Z. Guo, O. K. Farha, B. G. Hauser, X. Qi, Y. Wang, X. Wang, S. Han, X. Liu, J. S. DuChene, H. Zhang, Q. Zhang, X. Chen, J. Ma, S. C. J. Loo, W. D. Wei, Y. Yang, J. T. Hupp and F. Huo, *Nat. Chem.*, 2012, **4**, 310–316.

[237] H. Liu, F. C. Strobridge, O. J. Borkiewicz, K. M. Wiaderek, K. W. Chapman, P. J. Chupas and C. P. Grey, *Science*, 2014, **344**, 1252817.

[238] M. Fujita and Y. Kwon, *J. Am. Chem. Soc.*, 1994, **116**, 1151–1152.

[239] K. Schlichte, T. Kratzke and S. Kaskel, *Microporous Mesoporous Mater.*, 2004, **73**, 81–88.

[240] U. Ravon, M. E. Domine, C. Gaudillère, A. Desmartin-Chomel and D. Farrusseng, *New J. Chem.*, 2008, **32**, 937–940.

[241] F. Vermoortele, M. Vandichel, B. Van de Voorde, R. Ameloot, M. Waroquier, V. Van Speybroeck and D. E. De Vos, *Angew. Chem. Int. Ed.*, 2012, **51**, 4887–4890.

[242] P. Horcajada, T. Chalati, C. Serre, B. Gillet, C. Sebrie, T. Baati, J. F. Eubank, D. Heurtaux, P. Clayette, C. Kreuz, J.-S. Chang, Y. K. Hwang, V. Marsaud, P.-N. Bories, L. Cynober, S. Gil, G. Férey, P. Couvreur and R. Gref, *Nat. Mater.*, 2010, **9**, 172–178.

[243] S. Diring, D. O. Wang, C. Kim, M. Kondo, Y. Chen, S. Kitagawa, K. Kamei and S. Furukawa, *Nat. Commun.*, 2013, **4**, 2684.

[244] A. C. McKinlay, P. K. Allan, C. L. Renouf, M. J. Duncan, S. J. Warrender, D. Dawson, S. E. Ashbrook, B. Gil, D. Tina, J. J. Williams, C. Charrier, D. Mercer, S. J. Teat and R. E. Morris, *APL Mater.*, 2014, **2**, 124108.

[245] P. Jain, V. Ramachandran, R. J. Clark, D. Z. Hai, B. H. Toby, N. S. Dalal, H. W. Kroto and A. K. Cheetham, *J. Am. Chem. Soc.*, 2009, **131**, 13625–13627.

[246] Y. Inokuma, S. Yoshioka, J. Ariyoshi, T. Arai, Y. Hitora, K. Takada, S. Matsunaga, K. Rissanen and M. Fujita, *Nature*, 2013, **495**, 461–466.

[247] P. G. de Gennes and J. Prost, *The Physics of Liquid Crystals*, Clarendon Press, Oxford, 1993.

[248] W. Zhang and R.-G. Xiong, *Chem. Rev.*, 2012, **112**, 1163–95.

[249] P. Jain, N. S. Dalal, B. H. Toby, H. W. Kroto and A. K. Cheetham, *J. Am. Chem. Soc.*, 2008, **130**, 10450–10451.

[250] X. H. Zhao, X. C. Huang, S. L. Zhang, D. Shao, H. Y. Wei and X. Y. Wang, *J. Am. Chem. Soc.*, 2013, **135**, 16006–16009.

[251] K. Otsubo, Y. Wakabayashi, J. Ohara, S. Yamamoto, H. Matsuzaki, H. Okamoto, K. Nitta, T. Uruga and H. Kitagawa, *Nat. Mater.*, 2011, **10**, 291–295.

[252] C. H. Hendon, D. Tiana and A. Walsh, *Phys. Chem. Chem. Phys.*, 2012, **14**, 13120–13132.

[253] D. Sheberla, L. Sun, M. A. Blood-Forsythe, S. Er, C. R. Wade, C. K. Brozek, A. Aspuru-Guzik and M. Dincă, *J. Am. Chem. Soc.*, 2014, **136**, 8859–8862.

[254] A. A. Talin, A. Centrone, A. C. Ford, M. E. Foster, V. Stavila, P. Haney, R. A. Kinney, V. Szalai, F. El Gabaly, H. P. Yoon, F. Léonard and M. D. Allendorf, *Science*, 2014, **343**, 66–69.

[255] S. Ferlay, T. Mallah, R. Ouahès, P. Veillet and M. Verdaguer, *Nature*, 1995, **378**, 701–703.

[256] D. Tiana, C. Hendon and A. Walsh, *Chem. Commun.*, 2014, **50**, 13990–13993.

[257] W. Kaneko, M. Ohba and S. Kitagawa, *J. Am. Chem. Soc.*, 2007, **129**, 13706–13712.

[258] G. J. Halder, C. J. Kepert, B. Moubaraki, K. S. Murray and J. D. Cashion, *Science*, 2002, **298**, 1762–1765.

[259] P. D. C. Dietzel, Y. Morita, R. Blom and H. Fjellvåg, *Angew. Chem. Int. Ed.*, 2005, **44**, 6354–6358.

[260] P. Canepa, Y. J. Chabal and T. Thonhauser, *Phys. Rev. B*, 2013, **87**, 094407.

[261] S. Horike, S. Shimomura and S. Kitagawa, *Nat. Chem.*, 2009, **1**, 695–704.

[262] S. Bourrelly, P. L. Llewellyn, C. Serre, F. Millange, T. Loiseau and G. Férey, *J. Am. Chem. Soc.*, 2005, **127**, 13519–13521.

[263] J. M. Ogborn, I. E. Collings, S. A. Moggach, A. L. Thompson and A. L. Goodwin, *Chem. Sci.*, 2012, **3**, 3011–3017.

[264] C. Serre, F. Millange, C. Thouvenot, M. Noguès, G. Marsolier, D. Louër and G. Férey, *J. Am. Chem. Soc.*, 2002, **124**, 13519–13526.

[265] C. Serre, C. Mellot-Draznieks, S. Surblé, N. Audebrand, Y. Filinchuk and G. Férey, *Science*, 2007, **315**, 1828–1831.

[266] Y.-S. Wei, K.-J. Chen, P.-Q. Liao, B.-Y. Zhu, R.-B. Lin, H.-L. Zhou, B.-Y. Wang, W. Xue, J.-P. Zhang and X.-M. Chen, *Chem. Sci.*, 2013, **4**, 32–35.

[267] K. Biradha and M. Fujita, *Angew. Chem. Int. Ed.*, 2002, **41**, 3392–3395.

[268] S. A. Moggach, T. D. Bennett and A. K. Cheetham, *Angew. Chem. Int. Ed.*, 2009, **48**, 7087–7089.

[269] S. B. Choi, H. Furukawa, H. J. Nam, D. Y. Jung, Y. H. Jhon, A. Walton, D. Book, M. O'Keeffe, O. M. Yaghi and J. Kim, *Angew. Chem. Int. Ed.*, 2012, **51**, 8791–8795.

[270] A. L. Goodwin, M. Calleja, M. J. Conterio, M. T. Dove, J. S. O. Evans, D. A. Keen, L. Peters and M. G. Tucker, *Science*, 2008, **319**, 794–797.

[271] C. Yang, X. Wang and M. A. Omary, *Angew. Chem. Int. Ed.*, 2009, **48**, 2500–2505.

[272] Y. Wu, A. Kobayashi, G. J. Halder, V. K. Peterson, K. W. Chapman, N. Lock, P. D. Southon and C. J. Kepert, *Angew. Chem. Int. Ed.*, 2008, **47**, 8929–8932.

[273] Y. Wu, V. K. Peterson, E. Luks, T. A. Darwish and C. J. Kepert, *Angew. Chem. Int. Ed.*, 2014, **53**, 5175–5178.

[274] W. Zhou, H. Wu, T. Yildirim, J. R. Simpson and A. R. Hight Walker, *Phys. Rev. B*, 2008, **78**, 054114.

[275] W. Cai and A. Katrusiak, *Nat. Commun.*, 2014, **5**, 4337.

[276] A. B. Cairns and A. L. Goodwin, *arXiv*, 2015, 1502.00846.

[277] T. D. Bennett and A. K. Cheetham, *Acc. Chem. Res.*, 2014, **47**, 1555–1562.

[278] D. Umeyama, S. Horike, M. Inukai, T. Itakura and S. Kitagawa, *J. Am. Chem. Soc.*, 2015, **137**, 864–870.

[279] A. J. Graham, A. M. Banu, T. Düren, A. Greenaway, S. C. McKellar, J. P. S. Mowat, K. Ward, P. A. Wright and S. A. Moggach, *J. Am. Chem. Soc.*, 2014, **136**, 8606–8613.

[280] S. Cao, T. D. Bennett, D. A. Keen, A. L. Goodwin and A. K. Cheetham, *Chem. Commun.*, 2012, **48**, 7805–7807.

[281] C. J. Kepert, T. J. Prior and M. J. Rosseinsky, *J. Am. Chem. Soc.*, 2000, **122**, 5158–5168.

[282] C.-B. Tian, R.-P. Chen, C. He, W.-J. Li, Q. Wei, X.-D. Zhang and S.-W. Du, *Chem. Commun.*, 2014, **50**, 1915–1917.

[283] J. Mart-Rujas, N. Islam, D. Hashizume, F. Izumi, M. Fujita and M. Kawano, *J. Am. Chem. Soc.*, 2011, **133**, 5853–5860.

[284] M. Ghoreishi Amiri, A. Morsali and M. Zeller, *Z. Anorg. Allg. Chem.*, 2009, **635**, 1673–1677.

[285] S. Kitagawa and M. Kondo, *Bull. Chem. Soc. Jpn.*, 1998, **71**, 1739–1753.

[286] T. D. Bennett, S. Cao, J. C. Tan, D. A. Keen, E. G. Bithell, P. J. Beldon, T. Friščić and A. K. Cheetham, *J. Am. Chem. Soc.*, 2011, **133**, 14546–14549.

[287] T. D. Bennett, P. Simoncic, S. A. Moggach, F. Gozzo, P. Macchi, D. A. Keen, J.-C. Tan and A. K. Cheetham, *Chem. Commun.*, 2011, **47**, 7983–7985.

[288] L. Valenzano, B. Civalleri, S. Chavan, S. Bordiga, M. H. Nilsen, S. Jakobsen, K. P. Lillerud and C. Lamberti, *Chem. Mater.*, 2011, **23**, 1700–1718.

[289] H.-X. Deng, S.-H. Wei, S.-S. Li, J. Li and A. Walsh, *Phys. Rev. B*, 2013, **87**, 125203.

[290] M. J. Cliffe and A. L. Goodwin, *J. Phys.: Condens. Matter*, 2013, **25**, 454218.

[291] M. J. Cliffe and A. L. Goodwin, *Phys. Status Solidi B*, 2013, **250**, 949–956.

[292] M. J. Cliffe, W. Wan, X. Zou, P. A. Chater, A. K. Kleppe, M. G. Tucker, H. Wilhelm, N. P. Funnell, F.-X. Coudert and A. L. Goodwin, *Nat. Commun.*, 2014, **5**, 4176.

[293] M. J. Cliffe, J. A. Hill, C. A. Murray, F.-X. Coudert and A. L. Goodwin, *Phys. Chem. Chem. Phys.*, 2015, **17**, 11586—11592.

[294] B. E. Warren, H. Krutter and O. Morningstar, *J. Am. Ceram. Soc.*, 1936, **19**, 202–206.

[295] T. Egami and S. J. L. Billinge, *Underneath the Bragg Peaks, Structural Analysis of Complex Materials*, Pergamon, Oxford, 2003.

[296] S. E. McLain, D. T. Bowron, A. C. Hannon and A. K. Soper, *GudrunN and GudrunX: Programs for correcting raw neutron and X-ray diffraction data to differential scattering cross section*, Rutherford Appleton Laboratory Technical Report RAL-TR-2011-013, 2011.

[297] H. Lipson, J. I. Langford and H.-C. Hu., in *International Tables for Crystallography*, ed. E. Prince, International Union of Crystallography, 1st edn., 2006, vol. C, ch. 6.2, pp. 596–598.

[298] P. W. Stephens, *J. Appl. Crystallogr.*, 1999, **32**, 281–289.

[299] O. B. Zeldin, S. Brockhauser, J. Bremridge, J. M. Holton and E. F. Garman, *Proc. Natl. Acad. Sci. U. S. A.*, 2013, **110**, 20551–20556.

[300] P. Juhás, T. Davis, C. L. Farrow and S. J. L. Billinge, *J. Appl. Crystallogr.*, 2013, **46**, 560–566.

[301] A. K. Soper and E. R. Barney, *J. Appl. Cryst.*, 2011, **44**, 714–726.

[302] A. K. Cheetham and A. L. Goodwin, *Nat. Mater.*, 2014, **13**, 760–762.

[303] Z. Huang, J. E. Auckett, P. E. R. Blanchard, B. J. Kennedy, W. Miiller, Q. Zhou, M. Avdeev, M. R. Johnson, M. Zbiri, G. Garbarino, W. G. Marshall, Q. Gu and C. D. Ling, *Angew. Chem. Int. Ed.*, 2014, **53**, 3414–3417.

[304] W. Zhang, A. R. Oganov, A. F. Goncharov, Q. Zhu, S. E. Boulfelfel, A. O. Lyakhov, E. Stavrou, M. Somayazulu, V. B. Prakapenka and Z. Konôpková, *Science*, 2013, **342**, 1502–1505.

[305] R. I. Walton and D. O'Hare, *Chem. Commun.*, 2000, **2000**, 2283–2291.

[306] H. Rietveld, *J. Appl. Crystallogr.*, 1969, **2**, 65–71.

[307] G. S. Pawley, *J. Appl. Crystallogr.*, 1981, **14**, 357–361.

[308] A. Le Bail, *Powder Diffr.*, 2005, **20**, 316–326.

[309] A. Le Bail, *Powder Diffr.*, 2004, **19**, 249–254.

[310] V. Favre-Nicolin and R. Cerný, *J. Appl. Crystallogr.*, 2002, **35**, 734–743.

[311] A. Coelho, *J. Appl. Crystallogr.*, 2003, **36**, 86–95.

[312] I. L. Karle and J. Karle, *Acta Crystallogr.*, 1964, **17**, 835–841.

[313] G. M. Sheldrick, *Acta Crystallogr.*, 2007, **A64**, 112–122.

[314] G. Oszlányi and A. Suto, *Acta Crystallogr.*, 2004, **A60**, 134–141.

[315] A. Coelho, *TOPAS - Academic: General Profile and Structure Analysis Software for Powder Diffraction Data., Version 4.1*, Brisbane, Australia, 2007.

[316] W. I. F. David, K. Shankland, J. Van De Streek, E. Pidcock, W. D. S. Motherwell and J. C. Cole, *J. Appl. Crystallogr.*, 2006, **39**, 910–915.

[317] D. Balzar, N. Audebrand, M. R. Daymond, A. Fitch, A. Hewat, J. I. Langford, A. Le Bail, D. Louër, O. Masson, C. N. McCowan, N. C. Popa, P. W. Stephens and B. H. Toby, *J. Appl. Crystallogr.*, 2004, **37**, 911–924.

[318] B. E. Warren, *Phys. Rev.*, 1941, **59**, 693–698.

[319] D. L. Bish and S. A. Howard, *J. Appl. Crystallogr.*, 1988, **21**, 86–91.

[320] I. C. Madsen, N. V. Y. Scarlett, L. M. D. Cranswick and T. Lwin, *J. Appl. Crystallogr.*, 2001, **34**, 409–426.

[321] N. V. Y. Scarlett, I. C. Madsen, L. M. D. Cranswick, T. Lwin, E. Groleau, G. Stephenson, M. Aylmore and N. Agron-Olshina, *J. Appl. Crystallogr.*, 2002, **35**, 383–400.

[322] J. M. Bijvoet, A. F. Peerdeman and A. J. van Bommel, *Nature*, 1951, **168**, 271–272.

[323] W. H. Baur, *Acta Crystallogr.*, 1956, **9**, 515–520.

[324] W. A. Hendrickson and C. M. Ogata, *Methods Enzymol.*, 1997, **276**, 494–523.

[325] V. A. Levashov, S. J. L. Billinge and M. F. Thorpe, *Phys. Rev. B*, 2005, **72**, 024111.

[326] I.-K. Jeong, T. Proffen, F. Mohiuddin-Jacobs and S. J. L. Billinge, *J. Phys. Chem. A*, 1999, **103**, 921–924.

[327] I.-K. Jeong, R. H. Heffner, M. J. Graf and S. J. L. Billinge, *Phys. Rev. B*, 2003, **67**, 104301.

[328] A. L. Goodwin, M. G. Tucker, M. T. Dove and D. A. Keen, *Phys. Rev. Lett.*, 2004, **93**, 075502.

[329] E. R. Cope and M. T. Dove, *J. Appl. Crystallogr.*, 2007, **40**, 589–594.

[330] P. Juhás, D. M. Cherba, P. M. Duxbury, W. F. Punch and S. J. L. Billinge, *Nature*, 2006, **440**, 655–658.

[331] P. Juhás, L. Granlund, S. R. Gujarathi, P. M. Duxbury and S. J. L. Billinge, *J. Appl. Crystallogr.*, 2010, **43**, 623–629.

[332] N. Mousseau and G. T. Barkema, *Phys. Rev. B*, 2000, **61**, 1898–1906.

[333] A. P. Bartók, R. Kondor and G. Csányi, *Phys. Rev. B*, 2013, **87**, 184115.

[334] L. Pauling, *J. Am. Chem. Soc.*, 1929, **51**, 1010–1026.

[335] B. Hendrickson, *SIAM J. Optim.*, 1995, **5**, 835–857.

[336] J. Behler and M. Parrinello, *Phys. Rev. Lett.*, 2007, **98**, 146401.

[337] L. Raff, R. Komanduri, M. Hagan and S. Bukkapatnam, *Networks in Chemical Reaction Dynamics*, Oxford University Press, New York, 2012.

[338] B. J. Braams and J. M. Bowman, *Int. Rev. Phys. Chem.*, 2009, **28**, 577–606.

[339] M. Novotni and R. Klein, Proceedings of the eighth ACM symposium on Solid modeling and applications - SM '03, New York, New York, USA, 2003, pp. 216–225.

[340] M. Kazhdan, T. Funkhouser and S. Rusinkiewicz, Eurographics Symposium on Geometry Processing, 2003.

[341] P. Steinhardt, D. Nelson and M. Ronchetti, *Phys. Rev. B*, 1983, **28**, 784–805.

[342] A. Baranyai, A. Geiger, P. R. Gartrell-Mills, K. Heinzinger, R. McGreevy, G. Plinks and I. Ruff, *J. Chem. Soc. Farad. T. 2*, 1987, **83**, 1335–1365.

[343] S. Le Roux and V. Petkov, *J. Appl. Crystallogr.*, 2010, **43**, 181–185.

[344] M. T. Dove, A. K. A. Pryde and D. A. Keen, *Mineral. Mag.*, 2000, **64**, 267–283.

[345] W. A. Harrison, *Electronic Structure and the Properties of Solids: The Physics of the Chemical Bond*, Dover, New York, 1980.

[346] D. Weaire, *Phys. Rev. Lett.*, 1971, **26**, 1541–1543.

[347] S. Jakobsen, D. Gianolio, D. S. Wragg, M. H. Nilsen, H. Emerich, S. Bordiga, C. Lamberti, U. Olsbye, M. Tilset and K. P. Lillerud, *Phys. Rev. B*, 2012, **86**, 125429.

[348] G. C. Shearer, S. Chavan, J. Ethiraj, J. G. Vitillo, S. Svelle, U. Olsbye, C. Lamberti, S. Bordiga and K. P. Lillerud, *Chem. Mater.*, 2014, **26**, 4068–4071.

[349] C. Falaise, C. Volkringer, J.-F. Vigier, N. Henry, A. Beaurain and T. Loiseau, *Chem.-Eur. J.*, 2013, **19**, 5324–5331.

[350] C. Falaise, J.-S. Charles, C. Volkringer and T. Loiseau, *Inorg. Chem.*, 2015, **54**, 2235—2242.

[351] A. M. Ebrahim and T. J. Bandosz, *ACS Appl. Mater. Inter.*, 2013, **5**, 10565–10573.

[352] D. X. Xue, A. J. Cairns, Y. Belmabkhout, L. Wojtas, Y. Liu, M. H. Alkordi and M. Eddaoudi, *J. Am. Chem. Soc.*, 2013, **135**, 7660–7667.

[353] K. E. deKrafft, W. S. Boyle, L. M. Burk, O. Z. Zhou and W. Lin, *J. Mater. Chem.*, 2012, **22**, 18139–18144.

[354] S. M. Barrett, C. Wang and W. Lin, *J. Mater. Chem.*, 2012, **22**, 10329–10334.

[355] F. Vermoortele, R. Ameloot, A. Vimont, C. Serre and D. De Vos, *Chem. Commun.*, 2011, **47**, 1521–1523.

[356] A. Schaate, P. Roy, A. Godt, J. Lippke, F. Waltz, M. Wiebcke and P. Behrens, *Chem.-Eur. J.*, 2011, **17**, 6643–6651.

[357] T. Tsuruoka, S. Furukawa, Y. Takashima, K. Yoshida, S. Isoda and S. Kitagawa, *Angew. Chem. Int. Ed.*, 2009, **48**, 4739–4743.

[358] S. Diring, S. Furukawa, Y. Takashima, T. Tsuruoka and S. Kitagawa, *Chem. Mater.*, 2010, **22**, 4531–4538.

[359] M. Kandiah, M. H. Nilsen, S. Usseglio, S. Jakobsen, U. Olsbye, M. Tilset, C. Larabi, E. A. Quadrelli, F. Bonino and K. P. Lillerud, *Chem. Mater.*, 2010, **22**, 6632–6640.

[360] C. Zlotea, D. Phanon, M. Mazaj, D. Heurtaux, V. Guillerm, C. Serre, P. Horcajada, T. Devic, E. Magnier, F. Cuevas, G. Férey, P. L. Llewellyn and M. Latroche, *Dalton Trans.*, 2011, **40**, 4879–4881.

[361] G. Cmarik, M. Kim, S. M. Cohen and K. S. Walton, *Langmuir*, 2012, **28**, 15606–15613.

[362] S. Øien, D. Wragg, H. Reinsch, S. Svelle, S. Bordiga, C. Lamberti and K. P. Lillerud, *Cryst. Growth Des.*, 2014, **14**, 5370–5372.

[363] V. Bon, V. Senkovskyy, I. Senkovska and S. Kaskel, *Chem. Commun.*, 2012, **48**, 8407–8409.

[364] M. Vandichel, J. Hajek, F. Vermoortele, M. Waroquier, D. E. De Vos and V. Van Speybroeck, *CrystEngComm*, 2015, **17**, 395–406.

[365] T. K. Prasad and M. P. Suh, *Chem.-Eur. J.*, 2012, **18**, 8673–8680.

[366] A. U. Ortiz, A. Boutin, A. H. Fuchs and F.-X. Coudert, *J. Phys. Chem. Lett.*, 2013, **4**, 1861–1865.

[367] H. Wu, Y. Yildirim and W. Zhou, *J. Phys. Chem. Lett.*, 2013, **4**, 925–930.

[368] M. Sánchez del Río and R. J. Dejus, *Proc. S.P.I.E.*, 2004, **5536**, 171–174.

[369] *DAWN*, `http://www.dawnsci.org/`.

[370] J. Kieffer and D. Karkoulis., *J. Phys.: Conf. Ser.*, 2013, **425**, 202012.

[371] R. Dovesi, R. Orlando, B. Civalleri, C. Roetti, V. R. Saunders and C. M. Zicovich-Wilson, *Z. Krist.*, 2005, **220**, 571–573.

[372] A. D. Becke, *J. Chem. Phys.*, 1993, **98**, 5648–5652.

[373] D. Muñoz Ramo, J. L. Gavartin, A. L. Shluger and G. Bersuker, *Phys. Rev. B*, 2007, **75**, 205336.

[374] A. U. Ortiz, A. Boutin, A. H. Fuchs and F.-X. Coudert, *J. Chem. Phys.*, 2013, **138**, 174703.

[375] I. E. Collings, M. G. Tucker, D. A. Keen and A. L. Goodwin, *CrystEngComm*, 2014, **16**, 3498–3506.

[376] S. Henke, A. Schneemann and R. Fischer, *Adv. Funct. Mater.*, 2013, **23**, 5990–5996.

[377] G. C. Shearer, S. Forselv, S. Chavan, S. Bordiga, K. Mathisen, M. Bjørgen, S. Svelle and K. P. Lillerud, *Top. Catal.*, 2013, **56**, 770–782.

[378] A. D. Wiersum, E. Soubeyrand-Lenoir, Q. Yang, B. Moulin, V. Guillerm, M. B. Yahia, S. Bourrelly, A. Vimont, S. Miller, C. Vagner, M. Daturi, G. Clet, C. Serre, G. Maurin and P. L. Llewellyn, *Chem. Asian J.*, 2011, **6**, 3270–3280.

[379] V. Haigis, Y. Belkhodja, F.-X. Coudert, R. Vuilleumier and A. Boutin, *J. Chem. Phys.*, 2014, **141**, 064703.

[380] R. S. Krishnan, R. Srinivasan and S. Devanarayanan, *Thermal Expansion of Crystals*, Pergamon, Oxford, 1979.

[381] C. Martinek and F. A. Hummel, *J. Am. Ceram. Soc.*, 1968, **51**, 227–228.

[382] V. Korthuis, N. Khosrovani, A. W. Sleight, N. Roberts, R. Dupree and W. W. Warren Jr., *Chem. Mater.*, 1995, **7**, 412–417.

[383] S. E. Tallentire, F. Child, I. Fall, L. Vella-Zarb, I. R. Evans, M. G. Tucker, D. A. Keen, C. Wilson and J. S. O. Evans, *J. Am. Chem. Soc.*, 2013, **135**, 12849–12856.

[384] E. E. Rodriguez, A. Llobet, T. Proffen, B. C. Melot, R. Seshadri, P. B. Littlewood and A. K. Cheetham, *J. Appl. Phys.*, 2009, **105**, 114901.

[385] T. Chatterji, P. F. Henry, R. Mittal and S. L. Chaplot, *Phys. Rev. B*, 2008, **78**, 134105.

[386] B. K. Greve, K. L. Martin, P. L. Lee, P. J. Chupas, K. W. Chapman and A. P. Wilkinson, *J. Am. Chem. Soc.*, 2010, **132**, 15496–15498.

[387] W. Tiano, M. Dapiaggi and G. Artioli, *J. Appl. Crystallogr.*, 2003, **36**, 1461–1463.

[388] A. L. Goodwin and C. J. Kepert, *Phys. Rev. B*, 2005, **71**, 140301.

[389] A. L. Goodwin, K. W. Chapman and C. J. Kepert, *J. Am. Chem. Soc.*, 2005, **127**, 17980–17981.

[390] K. W. Chapman, P. J. Chupas and C. J. Kepert, *J. Am. Chem. Soc.*, 2006, **128**, 7009–7014.

[391] A. E. Phillips, A. L. Goodwin, G. J. Halder, P. D. Southon and C. J. Kepert, *Angew. Chem. Int. Ed.*, 2008, **47**, 1396–1399.

[392] L. Bouëssel du Bourg, A. U. Ortiz, A. Boutin and F.-X. Coudert, *APL Mat.*, 2014, **2**, 124110.

[393] N. Lock, Y. Wu, M. Christensen, L. J. Cameron, V. K. Peterson, A. J. Bridgeman, C. J. Kepert and B. B. Iversen, *J. Phys. Chem. C*, 2010, **114**, 16181–16186.

[394] N. Lock, M. Christensen, Y. Wu, V. K. Peterson, M. K. Thomsen, R. O. Piltz, A. J. Ramirez-Cuesta, G. J. McIntyre, K. Norén, R. Kutteh, C. J. Kepert, G. J. Kearley and B. B. Iversen, *Dalton Trans.*, 2013, **42**, 1996–2007.

[395] L. H. N. Rimmer, M. T. Dove, A. L. Goodwin and D. C. Palmer, *Phys. Chem. Chem. Phys.*, 2014, **16**, 21144–21152.

[396] M. F. Thorpe, in *Encyclopedia of Complexity and Systems Science*, ed. R. A. Meyers, Springer, New York, 2009, pp. 6013–24.

[397] P. Lightfoot, D. A. Woodcock, M. J. Maple, L. A. Villaescusa and P. A. Wright, *J. Mater. Chem.*, 2001, **11**, 212–216.

[398] G. N. Greaves, F. Meneau, A. Sapelkin, L. M. Colyer, I. ap Gwynn, S. Wade and G. Sankar, *Nat. Mater.*, 2003, **2**, 622–629.

[399] D. A. Keen, A. L. Goodwin, M. G. Tucker, M. T. Dove, J. S. O. Evans, W. A. Crichton and M. Brunelli, *Phys. Rev. Lett.*, 2007, **98**, 225501.

[400] K. W. Chapman and P. J. Chupas, *J. Am. Chem. Soc.*, 2007, **129**, 10090–10091.

[401] H. Fang, A. E. Phillips, M. T. Dove, M. G. Tucker and A. L. Goodwin, *Phys. Rev. B*, 2013, **88**, 144103.

[402] B. Van de Voorde, I. Stassen, B. Bueken, F. Vermoortele, D. De Vos, R. Ameloot, J.-C. Tan and T. D. Bennett, *J. Mater. Chem. A*, 2015, **3**, 1737–1742.

[403] T. D. Bennett, P. J. Saines, D. A. Keen, J.-C. Tan and A. K. Cheetham, *Chem.-Eur. J.*, 2013, **19**, 7049–7055.

[404] D. F. Sava, M. A. Rodriguez, K. W. Chapman, P. J. Chupas, J. A. Greathouse, P. S. Crozier and T. M. Nenoff, *J. Am. Chem. Soc.*, 2011, **133**, 12398–12401.

[405] S. P. Thompson, J. E. Parker, J. Potter, T. P. Hill, A. Birt, T. M. Cobb, F. Yuan and C. C. Tang, *Rev. Sci. Instrum.*, 2009, **80**, 075107.

[406] S. P. Thompson, J. E. Parker, J. Marchal, J. Potter, A. Birt, F. Yuan, R. D. Fearn, A. R. Lennie, S. R. Street and C. C. Tang, *J. Synchrotron Radiat.*, 2011, **18**, 637–648.

[407] I. A. Vartanyants and A. Singer, *New J. Phys.*, 2010, **12**, 035004.

[408] N. Patel, *Nature*, 2002, **415**, 110–111.

[409] I. Robinson and R. Harder, *Nat. Mater.*, 2009, **8**, 291–298.

[410] J. M. Zuo, I. Vartanyants, M. Gao, R. Zhang and L. A. Nagahara, *Science*, 2003, **300**, 1419–1421.

[411] S. O. Hruszkewycz, M. Sutton, P. H. Fuoss, B. Adams, S. Rosenkranz, K. F. Ludwig, W. Roseker, D. Fritz, M. Cammarata, D. Zhu, S. Lee, H. Lemke, C. Gutt, A. Robert, G. Grübel and G. B. Stephenson, *Phys. Rev. Lett.*, 2012, **109**, 185502.

[412] M. M. J. Treacy and J. M. Gibson, *Acta Crystallogr.*, 1996, **A52**, 212–220.

[413] M. M. J. Treacy and K. B. Borisenko, *Science*, 2012, **335**, 950–953.

[414] H. T. Stokes, D. M. Hatch and B. J. Campbell, *ISOTROPY Software Suite*.

[415] W. Liang, R. Babarao, M. J. Murphy and D. M. D'Alessandro, *Dalton Trans.*, 2015, **44**, 1516–1519.

Appendix A

A1 Experimental

A1.1 UiO-66(Hf)

UiO-66(Hf) PDF Refinements

Table A1.1: Summary of crystallographic details for nano-**reo** UiO-66(Hf) obtained by PDFGui refinement against X-ray total scattering data.

Number of constraints	1539		
Number of refined parameters	9		
Number of fixed parameters	8		
R_w	41.2%		
a (Å)	20.725(18)		
Scale	0.168(14)		
low-r peak sharpening (Å)	0.23(19)		
Atom	x	y	z
Hf1	0.1193 (7)	0	0
O1	0.546 (3)	0.046(3)	0.546(3)
O2	0.335(4)	0.102(4)	0.5
Atom	U_{11} (Å^2)	U_{22} (Å^2)	U_{33} (Å^2)
Hf1	0.0074(13)	0.030(9)	0.030 9)
O1	0.05	0.05	0.05
O2	0.05	0.05	0.05

Estimated standard errors are given in parentheses.

Table A1.2: Summary of crystallographic details for **fcu** UiO-66(Hf) obtained by PDFGui refinement against X-ray total scattering data.

Number of constraints	1539		
Number of refined parameters	9		
Number of fixed parameters	8		
R_w	58.0%		
a (Å)	20.69 (3)		
Scale	0.125(14)		
low-r peak sharpening(Å)	0.40(9)		
Atom	x	y	z
Hf1	0.119 (12)	0	0
O1	0.560 (5)	0.440 (5)	0.560 (5)
O2	0.334 (7)	0.086 (7)	0.5
Atom	U_{11} (Å^2)	U_{22} (Å^2)	U_{33} (Å^2)
Hf1	0.007 (13)	0.030 (9)	0.030 (9)
O1	0.05	0.05	0.05
O2	0.05	0.05	0.05

Estimated standard errors are given in parentheses.

n BDC (mmol)	$I(110)$ / $I(111)$	$a_{200°C}$ / $a_{380°C}$ -1 (%)	$\alpha_a(\mathrm{MK}^{-1})$
2.5	0.163(3)	1.843(12)	$-23.4(8)$
3	0.136(3)	1.381(5)	$-26.9(1.3)$
3.5	0.099(3)	1.178(7)	$-31.6(7)$
4	0.055(3)	1.089(2)	$-29.3(1.8)$
4.5	0.036(3)	0.964(5)	$-31.2(1.5)$
5	0.026(5)	0.946(6)	$-32.4(1.3)$

Table A1.3: Summary of the variation in thermomechanical properties with defect concentration presented in Fig. 6.5

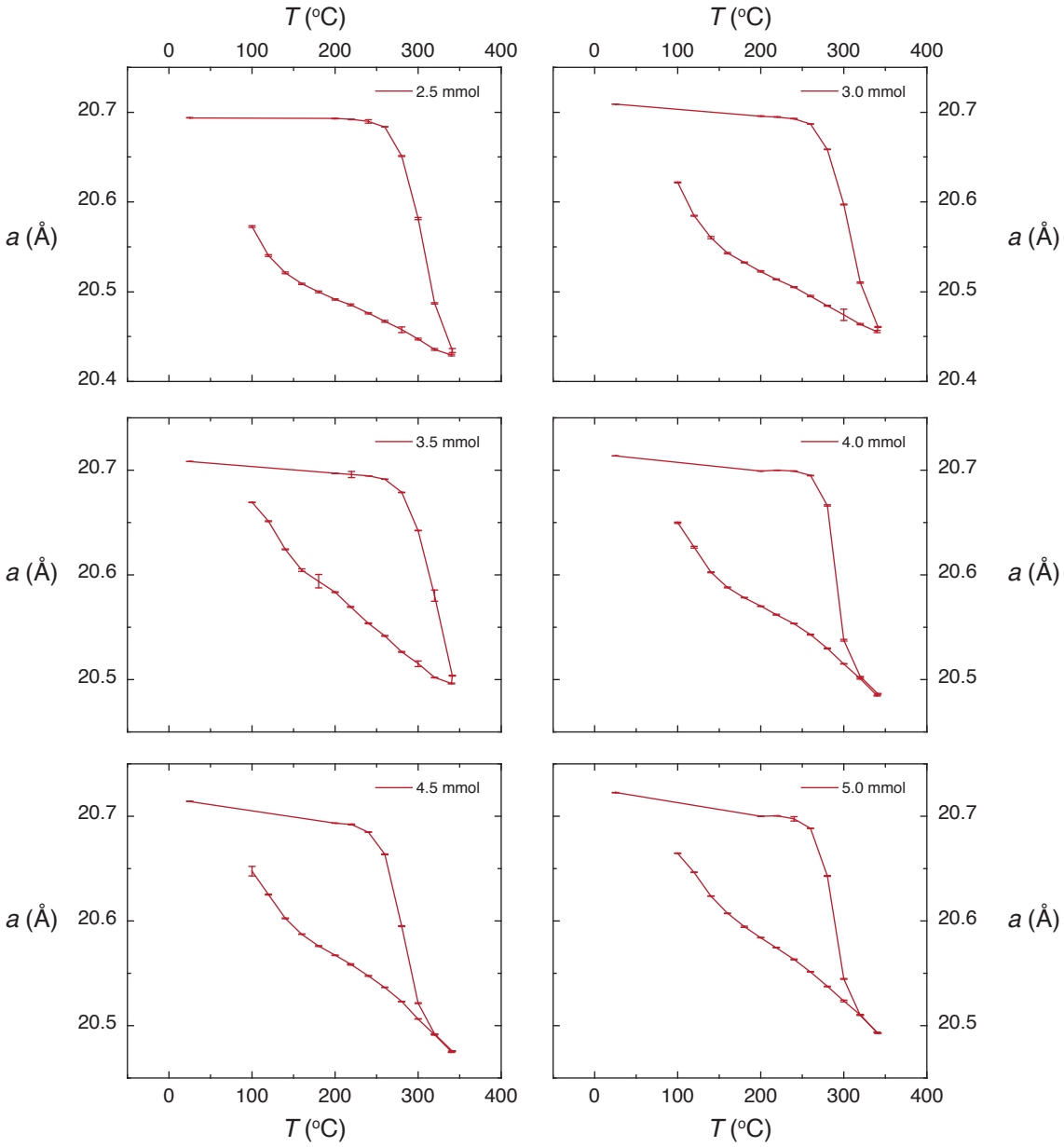

Figure A1.1: Synchrotron PXRD diffraction measurements of the variation in lattice parameter for defective UiO-66(Hf), on heating from 200–340 °C followed by cooling to 100 °C. These measurements were used to calculated the values shown in Fig. 4(c,d) in the main text.

n (BDC) (mmol)	2.5			3.0		3.5		4.0		4.5		5.0	
T(°C)	a (Å)	error	T(°C)	a (Å)	error	a (Å)	error	a (Å)	error	a (Å)	error	a (Å)	error
100	20.6981	0.0002	25	20.7047	0.0004	20.6942	0.0001	20.7131	0.0001	20.7026	0.0007	20.7165	0.0003
100	20.6983	0.0003	200	20.7019	0.0003	20.7040	0.0001	20.7075	0.0001	20.6945	0.0002	20.7251	0.0007
120	20.6974	0.0002	220	20.7012	0.0002	20.7031	0.0002	20.7077	0.0001	20.6936	0.0003	20.7218	0.0015
140	20.6972	0.0002	240	20.6987	0.0002	20.7020	0.0001	20.7044	0.0004	20.6887	0.0003	20.7072	0.0017
160	20.6963	0.0002	260	20.6923	0.0002	20.6988	0.0001	20.6907	0.0002	20.6770	0.0003	20.6880	0.0022
180	20.6950	0.0002	280	20.6740	0.0002	20.6891	0.0002	20.6288	0.0007	20.6472	0.0034	20.6504	0.0025
200	20.6940	0.0002	300	20.6241	0.0004	20.6612	0.0003	20.5410	0.0003	20.5848	0.0004	20.6096	0.0025
220	20.6913	0.0006	320	20.5519	0.0006	20.6106	0.0003	20.5114	0.0003	20.5380	0.0003	20.5782	0.0025
240	20.6885	0.0003	340	20.4786	0.0002	20.5197	0.0003	20.4924	0.0001	20.5122	0.0004	20.5549	0.0025
260	20.6828	0.0001	360	20.4449	0.0003	20.4892	0.0003	20.4812	0.0003	20.4995	0.0004	20.5313	0.0019
280	20.6689	0.0011	380	20.4242	0.0009	20.4726	0.0018	20.4772	0.0003	20.4911	0.0004	20.5249	0.0019
300	20.6369	0.0005	400	20.4063	0.0010	20.4593	0.0022	20.4711	0.0018	20.4795	0.0019	20.5220	0.0018
320	20.5530	0.0014	420	20.3814	0.0010	20.4496	0.0005	20.4706	0.0002	20.4767	0.0010	20.5198	0.0018
340	20.4342	0.0010	440	20.3639	0.0013	20.4435	0.0005	20.4717	0.0005	20.4740	0.0004	20.5209	0.0024
360	20.3822	0.0011	460	20.3414	0.0013	20.4407	0.0009	20.4711	0.0016	20.4745	0.0004	20.5249	0.0030
380	20.3431	0.0013	480	20.3261	0.0022	20.4368	0.0011	20.4697	0.0021	20.4732	0.0005	20.5374	0.0048
400	20.3094	0.0016	500	20.3236	0.0062	20.4194	0.0029	20.4730	0.0010	20.4705	0.0008	20.5289	0.0135

Table A1.4: Lattice parameters, derived from Pawley fitting, for the initial variable temperature measurements used for the determination of densification. Shown in Fig. 6.5(a,b).

n (BDC) (mmol)	2.5		3.0		3.5		4.0		4.5		5.0	
T(°C)	a (Å)	error	a (Å)	error	a (Å)	error	a(Å)	error	a (Å)	error	a (Å)	error
25	20.6937	0.0002	20.7090	0.0002	20.7082	0.0001	20.7136	0.0000	20.7141	0.0003	20.7226	0.0001
200	20.6930	0.0002	20.6957	0.0002	20.6970	0.0001	20.6991	0.0001	20.6935	0.0001	20.7001	0.0001
220	20.6921	0.0002	20.6947	0.0002	20.6958	0.0031	20.7000	0.0000	20.6921	0.0004	20.7005	0.0001
240	20.6897	0.0018	20.6928	0.0002	20.6946	0.0001	20.6992	0.0001	20.6848	0.0001	20.6975	0.0021
260	20.6835	0.0002	20.6869	0.0002	20.6913	0.0001	20.6948	0.0001	20.6636	0.0003	20.6883	0.0000
280	20.6513	0.0005	20.6585	0.0003	20.6787	0.0002	20.6662	0.0007	20.5953	0.1706	20.6429	0.0004
300	20.5815	0.0011	20.5972	0.0004	20.6423	0.0003	20.5375	0.0007	20.5215	0.0003	20.5447	0.0003
320	20.4870	0.0007	20.5102	0.0005	20.5804	0.0054	20.5028	0.0002	20.4921	0.0003	20.5101	0.0001
340	20.4345	0.0021	20.4607	0.0006	20.5039	0.0004	20.4864	0.0003	20.4758	0.0004	20.4928	0.0002
340	20.4294	0.0009	20.4557	0.0014	20.4961	0.0004	20.4848	0.0003	20.4751	0.0007	20.4934	0.0002
320	20.4355	0.0010	20.4637	0.0007	20.5020	0.0003	20.5009	0.0003	20.4913	0.0004	20.5102	0.0004
300	20.4474	0.0009	20.4743	0.0063	20.5151	0.0026	20.5150	0.0003	20.5064	0.0003	20.5236	0.0010
280	20.4577	0.0032	20.4845	0.0006	20.5266	0.0004	20.5297	0.0003	20.5229	0.0003	20.5375	0.0002
260	20.4671	0.0009	20.4952	0.0006	20.5418	0.0004	20.5429	0.0003	20.5365	0.0003	20.5513	0.0002
240	20.4759	0.0009	20.5052	0.0004	20.5537	0.0004	20.5535	0.0003	20.5476	0.0003	20.5634	0.0004
220	20.4853	0.0009	20.5137	0.0006	20.5693	0.0004	20.5619	0.0003	20.5586	0.0006	20.5745	0.0003
200	20.4916	0.0008	20.5226	0.0006	20.5836	0.3518	20.5701	0.0003	20.5672	0.0003	20.5840	0.0002
180	20.4999	0.0009	20.5325	0.0006	20.5938	0.0064	20.5782	0.0002	20.5760	0.0003	20.5945	0.0006
160	20.5087	0.0009	20.5430	0.0006	20.6044	0.0012	20.5879	0.0004	20.5873	0.0003	20.6073	0.0002
140	20.5209	0.0010	20.5602	0.0013	20.6242	0.0004	20.6025	0.0003	20.6026	0.0004	20.6236	0.0002
120	20.5404	0.0009	20.5846	0.0006	20.6514	0.0004	20.6264	0.0010	20.6252	0.1154	20.6464	0.0002
100	20.5726	0.0009	20.6216	0.0006	20.6693	0.0003	20.6499	0.0006	20.6474	0.0045	20.6646	0.0003

Table A1.5: Lattice parameters, derived from Pawley fitting, for the final variable temperature measurements used for determination of the coefficients of NTE shown in Fig. 6.5(c,d) of the main text. These data are displayed in Fig. A1.1.

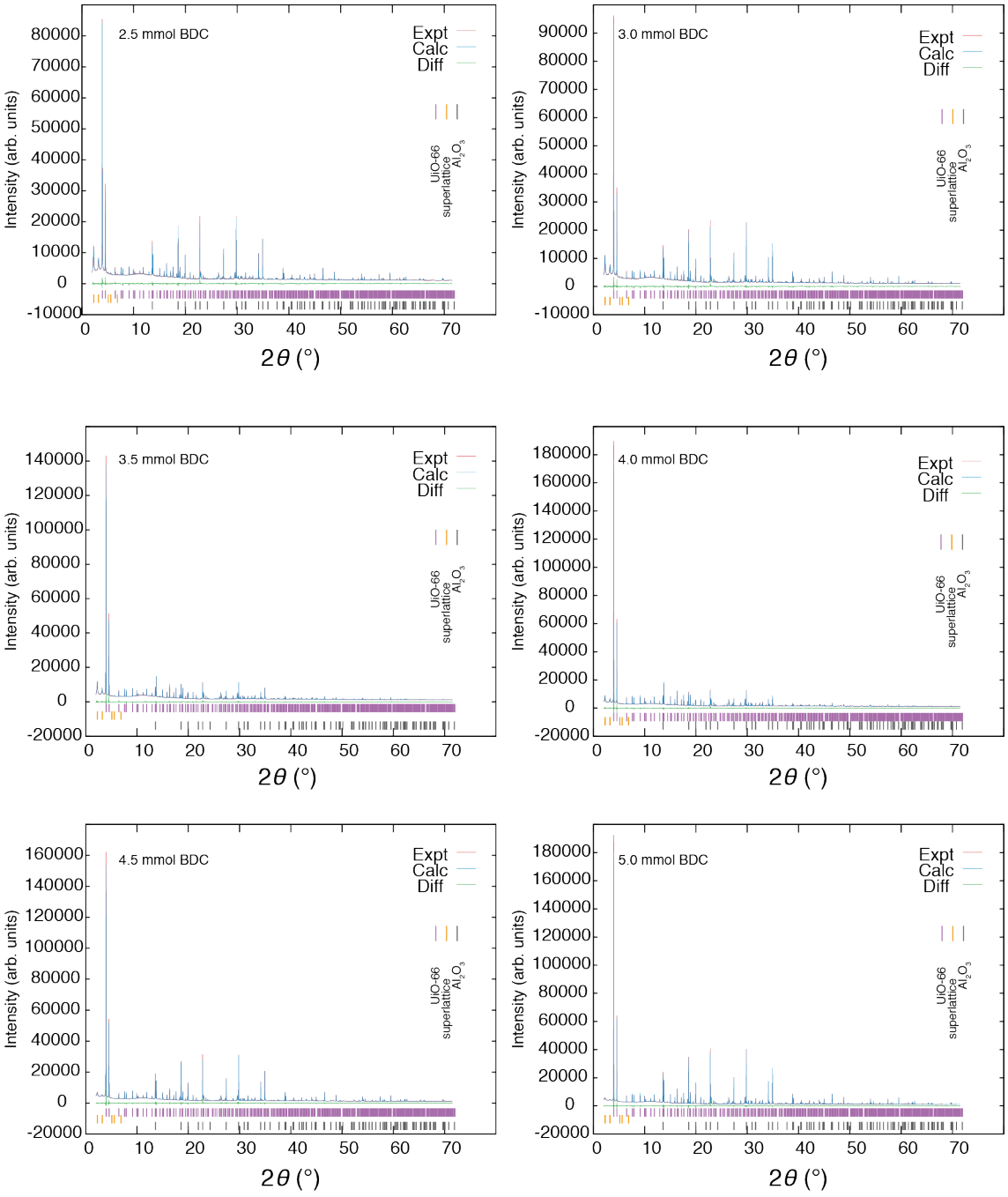

Figure A1.2: Rietveld fits for each sample at 200 °C. The data were fit with three phases: **fcu**-UiO-66(Hf), Al_2O_3 and a Pawley phase accounting for the broad superlattice reflections, using the same cell parameter as for the UiO-66(Hf) Rietveld phase.

n(BDC) mmol	R_{wp}	a (Å)	σ	Hf x	σ	Hf U_{iso} (Å^{-2})	σ	non-Hf U_{iso} (Å$^{-2)}$	σ
2.5	3.004	20.69023	0.00009	0.11953	0.00005	0.02434	0.0002	0.074	0.002
3.0	2.976	20.69383	0.00008	0.11958	0.00005	0.02197	0.0002	0.064	0.002
3.5	3.122	20.69589	0.00007	0.11954	0.00004	0.019265	0.00016	0.0630	0.0016
4.0	3.340	20.69789	0.00006	0.11953	0.00003	0.017477	0.00013	0.0502	0.0013
4.5	3.477	20.69164	0.00008	0.11954	0.00004	0.022260	0.00019	0.0523	0.0016
5.0	3.446	20.69926	0.00005	0.11944	0.00004	0.017085	0.00014	0.0458	0.0013

Table A1.6: Refined parameters for the Rietveld fits shown in Fig. A1.2.

A1.2 Hafnium formate

Table A1.7: Atomic coordinates for the model of α hafnium formate derived from X-ray powder diffraction data.

Radiation	Cu $K\alpha_1$, $\lambda = 1.54056$ Å			
Formula	$Hf_6O_{32}C_{12}$			
M (g mol^{-1})	1727			
Z	4			
Crystal System	Orthorhombic			
Space Group	$Cmcm$			
a (Å)	9.9784(3)			
b (Å)	19.6126(8)			
c (Å)	19.6759(7)			
V (Å^3)	3850.6(2)			
Atom	x	y	z	B_{eq} (Å^2)
Hf1	−0.1768(3)	0.02008(12)	0.08739(13)	2.88(7)
Hf2	0	−0.12231(19)	0.02889(19)	3.4(1)
O1	0	−0.04177	0.093714	3
O2	0	0.0697	0.0663	3
O3	0.16821	−0.0556	0.0119	3
O4	−0.10914	0.03878	0.19543	3
O5	−0.25425	−0.07154	0.14486	3
O6	−0.14657	−0.16251	0.10401	3
O7	−0.24558	0.12558	0.10699	3
O8	−0.13095	0.19252	0.03582	3
O9	0.3923	0.00616	0.05526	3
C1	0.7991	0.8742	0.1555	3
C2	−0.2316	0.1783	0.0749	3
C3	0.8101	0.0367	0.25	3
C4	0.5	0.0067	0.0919	3

Estimated standard errors are given in parentheses.

A1.3 Computational Structures

Table A1.8: Atomic coordinates for the optimised structure of **reo** UiO-66(Hf).

Crystal System	Cubic		
Space Group	$P\bar{4}3m$		
a (Å)	20.862		
V (Å^3)	9080		
Atom	x	y	z
C1	0.1512	0.4935	−0.1512
C2	0.2027	−0.2975	0.0062
C3	0.2676	−0.0068	0.3148
C4	−0.3482	−0.0040	−0.1518
C5	−0.2325	−0.0064	−0.1854
H1	0.1884	0.4881	−0.1884
H2	0.3652	−0.2803	0.0068
H3	0.1350	−0.2199	0.0062
H4	0.0940	0.0940	0.4063
O1	0.1704	−0.0023	0.4063
O2	0.0494	0.0494	−0.4507
O3	0.0674	−0.0674	−0.4330
O4	−0.0941	0.1711	0.4966
O5	−0.3297	−0.0025	−0.0937
Hf1	−0.3808	0.0000	0.0000
Hf2	0.1195	0.0000	−0.5000

Table A1.9: Atomic coordinates for the optimised structure of **reo** UiO-66(Hf) after ligand elimination.

Crystal System	Cubic		
Space Group	$P\bar{4}3m$		
a (Å)	20.6521		
V (Å^3)	8808		
Atom	x	y	z
C1	-0.3549	-0.0000	-0.1563
C2	0.2087	-0.3046	0.0000
C3	-0.2389	0.0002	-0.1914
C4	0.2743	-0.0002	0.3220
H1	0.3729	-0.2873	0.0003
H2	0.1405	-0.2261	-0.0003
Hf1	-0.3841	0.0000	0.0000
Hf2	0.1121	0.0000	0.5000
O1	0.0612	0.0612	-0.4417
O2	0.0613	-0.0613	-0.4417
O3	0.1746	-0.0000	0.4148
O4	-0.3347	0.0000	-0.0986

Table A1.10: Atomic coordinates for the optimised structure of **fcu** UiO-66(Hf).

Crystal System	Cubic		
Space Group	$F\bar{4}3m$		
a (Å)	20.872		
V (Å^3)	9092		
Atom	x	y	z
C1	0.1518	0.4958	0.1518
C2	0.0064	0.2026	0.2974
C3	−0.2325	0.1854	−0.0068
H1	−0.2198	0.0067	−0.1350
H2	0.0939	0.0939	−0.4061
O1	−0.0026	0.3296	−0.0938
O2	0.4507	−0.0493	−0.0493
O3	−0.0672	−0.0672	−0.4328
Hf1	0.3807	0.0000	0.0000

Table A1.11: Atomic coordinates for the optimised structure of **reo** UiO-66(Zr).

Crystal System	Cubic		
Space Group	$P\bar{4}3m$		
a (Å)	20.9689		
V (Å^3)	9220		
Atom	x	y	z
C1	0.2029	0.7028	0.0060
C2	0.2675	0.9933	0.3144
C3	0.6523	0.9961	0.8477
C4	0.1517	0.4937	0.8483
C5	0.7674	0.9940	0.8143
H1	0.0939	0.0939	0.4063
H2	0.1887	0.4887	0.8113
H3	0.3646	0.7199	0.0069
H4	0.1355	0.7800	0.0056
O1	0.9052	0.1714	0.4966
O2	0.0496	0.0496	0.5494
O3	0.0675	0.9325	0.5670
O4	0.1707	0.9977	0.4055
O5	0.6707	0.9975	0.9055
Zr1	0.6203	0.0000	0.0000
Zr2	0.1206	0.0000	0.5000

Table A1.12: Atomic coordinates for the optimised structure of **fcu** UiO-66(Zr).

Crystal System	Cubic		
Space Group	$F\bar{4}3m$		
a (Å)	20.9768		
V (Å^3)	9220		
Atom	x	y	z
C1	0.0062	0.7029	0.7971
C2	0.1523	0.9959	0.6523
C3	0.7674	0.1857	0.9935
H1	0.0938	0.5938	0.0938
H2	0.7800	0.0064	0.8645
O1	0.9974	0.3293	0.9054
O2	0.9506	0.9506	0.4506
O3	0.4327	0.9327	0.0673
Zr1	0.3796	0.0000	0.0000

Table A1.13: Calculated mechanical properties for UiO-66(Hf). Elastic constants (C_{11},C_{12} and C_{44}), polycrystalline aggregate mechanical moduli (K, E, G) according to the Voigt–Reuss–Hill averaging scheme, and extremal values of the directional Young's modulus and shear moduli. Also shown for reference are the results for non-defective UiO-66(Hf) from Ref. 367.

	simul. **fcu**	Zhou et al. (simul. **fcu**)	simul. **reo**
space group	$F\bar{4}3m$	$F\bar{4}3m$	$P\bar{4}3m$
C_{11} (GPa)	59.8	58.4	28.6
C_{12} (GPa)	29.6	30	13.2
C_{44} (GPa)	20.2	18	10
Bulk modulus (K) (GPa)	39.6		18.3
Youngs modulus (E) (GPa)	46.8		23.3
Shear modulus (G) (GPa)	18		9
E_{min} (GPa)	40.2		20.3
E_{max} (GPa)	51.8		25.5
G_{min} (GPa)	15.1		7.7
G_{max} (GPa)	20.2		10

Table A1.14: Calculated mechanical properties for UiO-66(Zr). Elastic constants (C_{11},C_{12} and C_{44}), polycrystalline aggregate mechanical moduli (K, E, G) according to the Voigt–Reuss–Hill averaging scheme, and extremal values of the directional Young's modulus and shear moduli. Also shown for reference are the results for non-defective UiO-66(Zr) from Ref. !367.

	simul. **fcu**	Zhou et al. (simul. **fcu**)	simul. **reo**
space group	$F\bar{4}3m$	$F\bar{4}3m$	$P\bar{4}3m$
C_{11} (GPa)	59.9	59.4	28.6
C_{12} (GPa)	29.3	31.8	13.1
C_{44} (GPa)	19.9	17.6	10.0
Bulk modulus (K) (GPa)	39.5		18.3
Youngs modulus (E) (GPa)	46.6		23.3
Shear modulus (G) (GPa)	17.8		9.0
E_{min} (GPa)	40.5		20.4
E_{max} (GPa)	51.0		25.4
G_{min}(GPa)	15.3		7.7
G_{max} (GPa)	19.9		10.0

Appendix B

B1 Synthesis

Synthesis of α-hafnium formate

$HfCl_4$ (1g, 0.35 mmol) was dissolved in H_2O (5 ml), 10 ml DMF was added, followed by 20 ml formic acid (warning, exothermic). This was refluxed overnight, where a white precipitate was formed, filtered under vacuum, and washed on the filter with acetone, yielding a white microcrystalline powder. An X-ray powder diffraction pattern of this phase and Rietveld fit are shown in Fig. B1.3(a).

Synthesis of β-hafnium formate

$HfCl_4$ (1g, 0.35 mmol) was added to 10 ml DMF, followed by the addition of 2 ml formic acid. This was refluxed for 3 h, forming a white precipitate. This was filtered under vacuum, and washed on the filter with acetone, yielding a white microcrystalline powder. An X-ray powder diffraction pattern of this phase can be seen in Fig.B1.3(b).

B2 Structure solution of the α phase

A structural model for α hafnium formate was determined by the following method. First the cell dimensions were determined by the standard indexing algorithm implemented in Topas Academic version 4.1 [315]. An approximate structure in the $P1$ space group was obtained by a simulated annealing approach (again using Topas), in which only Hf_6O_8 clusters were included. The space group of the resulting arrangement was then determined from this structure using the FINDSYM programme [414] and formate ligands were subsequently included in chemically reasonable positions. The positions and isotropic atomic

displacement parameters of the Hf atoms were then allowed to refine, but the rest of the model kept fixed, as refinement of their locations proved unstable. Crystallographic details are summarised in Appendix Section A1.7; the positions of the formate ligands are to be regarded as approximate. The topology of the structure is in accordance with a subsequently published single crystal structure of α-Zr formate [415]. The corresponding fit-to-data is shown in Fig. B1.3(a); the quality of fit was given by $R_{\mathrm{wp}} = 20.8\%$. Two representative views of the crystal structure are shown in Appendix Figures B2.4 and B2.5.

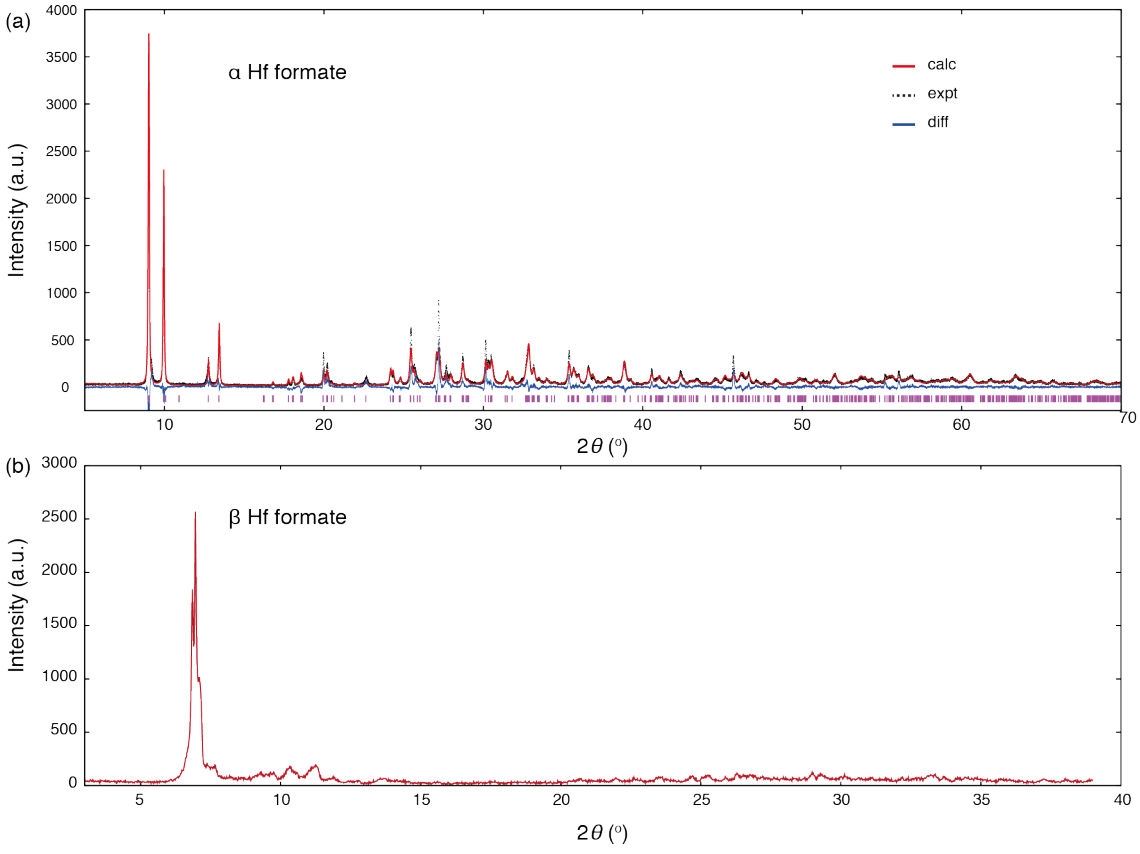

Figure B1.3: (a) Rietveld fit to model structure of hafnium formate α. Black points are experimental data, red line is the fit, blue line is the difference curve, pink lines are tick marks marking the positions of peaks. (b) Powder diffraction pattern of Hafnium formate β.

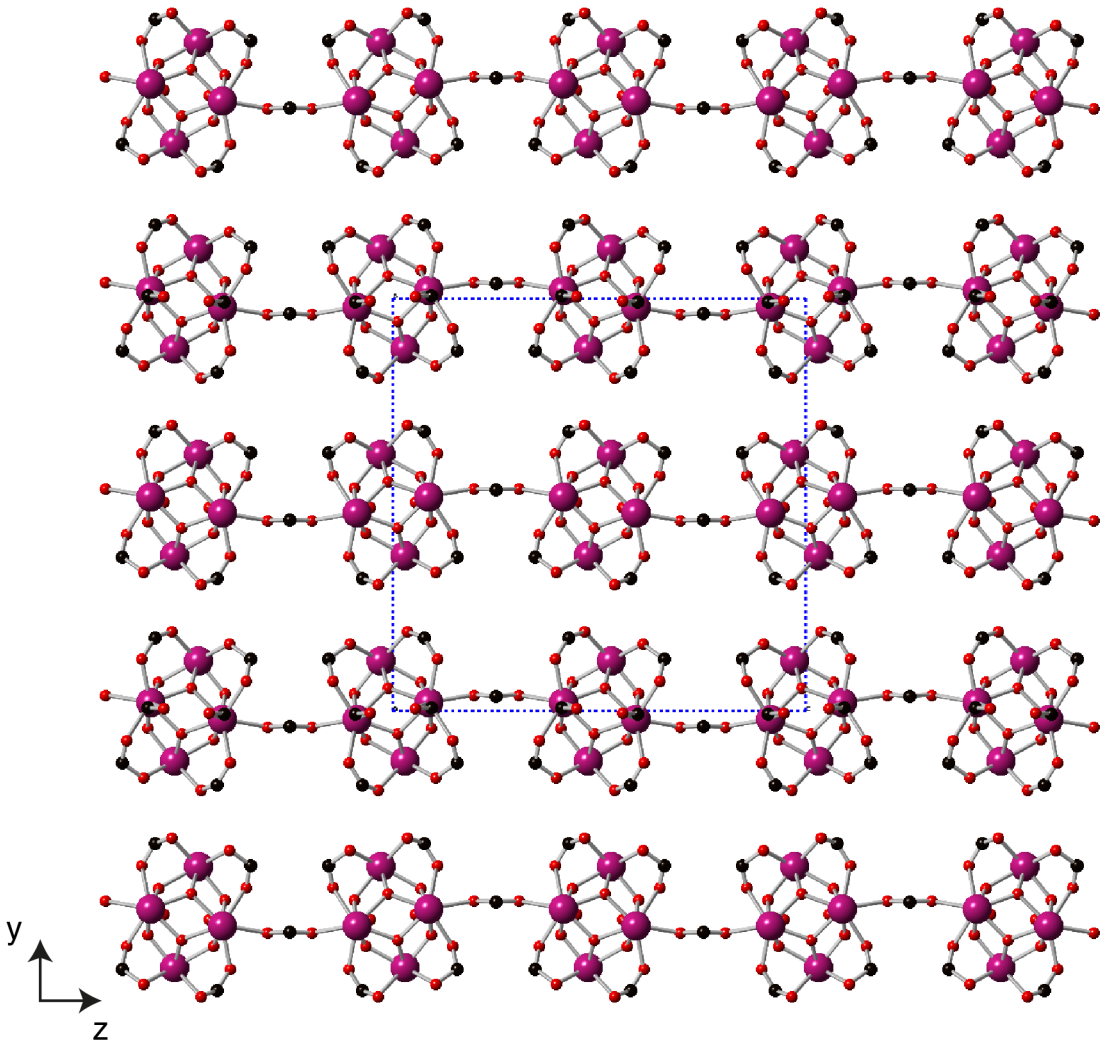

Figure B2.4: A representation of the α-hafnium formate structure, viewed along the [100] direction. Colour scheme as follows: Hf, purple; C, black and O, red. The blue dotted lines indicate the unit cell.

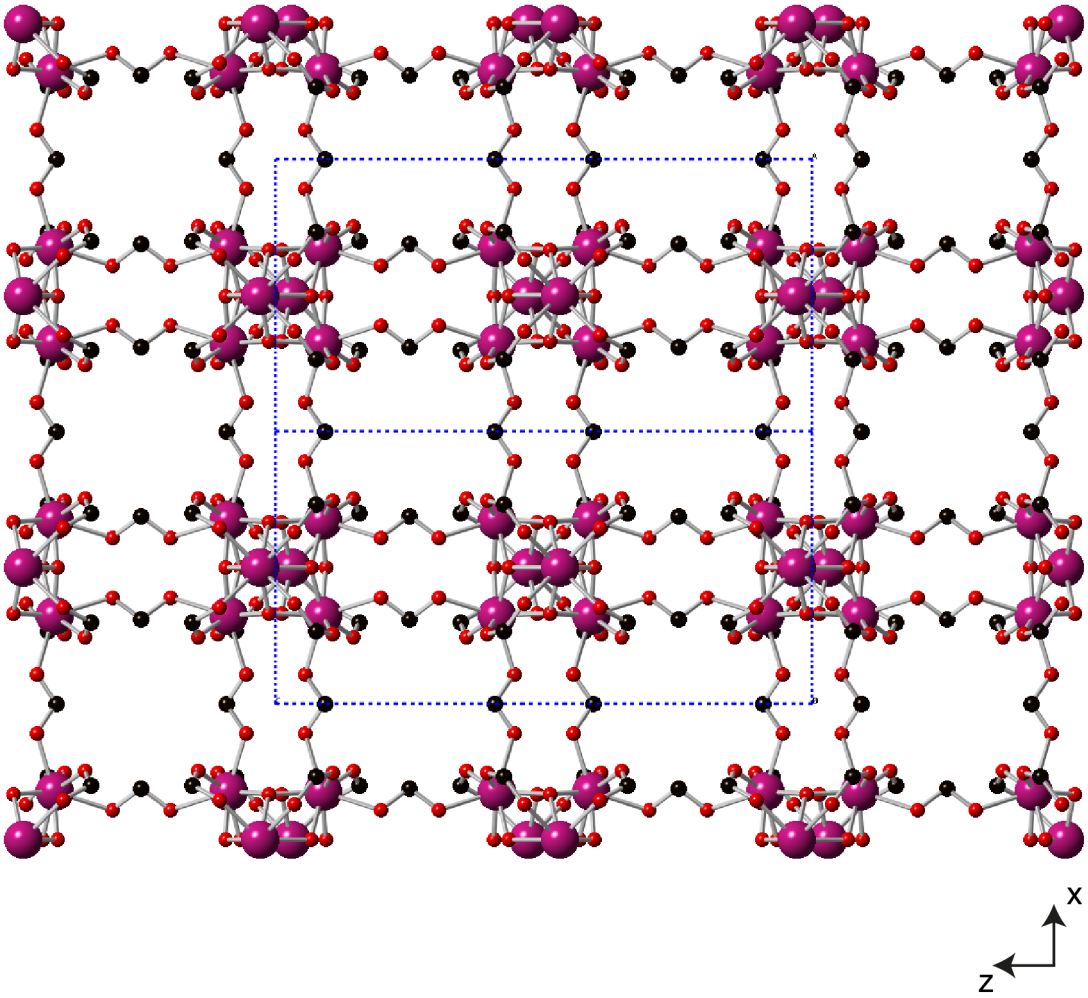

Figure B2.5: A representation of the α-hafnium formate structure, viewed along the [010] direction. Colour scheme as follows: Hf, purple; C, black and O, red. The blue dotted lines indicate the unit cell.

Appendix C

In this Thesis I have concentrated on the role that disorder and defects play in framework structures. A secondary direction of my research during my DPhil concerns the (thermo)mechanical properties of molecular frameworks. This work is detailed in the published papers included in this appendix.

C1 PASCal: a principal axis strain calculator for thermal expansion and compressibility determination

The first included paper describes a web-tool PASCal (www.pascal.chem.ox.ac.uk) that I developed to allow for the calculation of the (thermo)mechanical properties of a crystal from the temperature/pressure dependence of its lattice parameters. PASCal calculates the principal strains and fits these strains with a variety of simple equations of state to extract the relevant thermodynamic parameters. For high symmetry systems, this process is trivial, as the unit cell angles are fixed by symmetry and so the principal strains and the derived hydrostatic compressibilities or thermal expansivities can be completely described through the changes in the unit cell lengths. For monoclinic and triclinic systems, the cell angles can change and the cell axis directions are now arbitrary as they are unconstrained by symmetry. Analysis of how the structure changes along cell axes will therefore give different coefficients for different choices of unit cell and moreover, an arbitrary choice of unit cell will always underestimate the degree of mechanical anisotropy, potentially missing anomalous mechanical properties such as NTE or negative (linear) compressibilities. The most complete description of the strain (and derived properties) is the strain tensor, which can be easily diagonalised to yield its eigenvalues and eigenvectors—*i.e.* the principal strains and the principal axes along which they lie. Although the calculation

these principal strains and axes is been very well understood and routinely carried out in many scientific communities, particularly geosciences, they are underexploited by materials chemists. PASCal is designed as a web tool to make it easy for materials chemists to carry out these calculations and so make the most of their experimental data. This paper also contains three of published variable temperature or pressure lattice parameter data where principal axis calculations provide additional insight into a materials' behaviour.

Journal of
Applied Crystallography
ISSN 0021-8898

Received 13 April 2012
Accepted 15 October 2012

PASCal: a principal axis strain calculator for thermal expansion and compressibility determination

Matthew J. Cliffe and Andrew L. Goodwin*

Inorganic Chemistry Laboratory, Department of Chemistry, University of Oxford, South Parks Road, Oxford OX1 3QR, UK. Correspondence e-mail: andrew.goodwin@chem.ox.ac.uk

This article describes a web-based tool (*PASCal*; principal axis strain calculator; http://pascal.chem.ox.ac.uk) designed to simplify the determination of principal coefficients of thermal expansion and compressibilities from variable-temperature and variable-pressure lattice parameter data. In a series of three case studies, *PASCal* is used to reanalyse previously published lattice parameter data and show that additional scientific insight is obtainable in each case. First, the two-dimensional metal–organic framework $[Cu_2(OH)(C_8H_3O_7S)(H_2O)]\cdot 2H_2O$ is found to exhibit the strongest area negative thermal expansion (NTE) effect yet observed; second, the widely used explosive HMX exhibits much stronger mechanical anisotropy than had previously been anticipated, including uniaxial NTE driven by thermal changes in molecular conformation; and third, the high-pressure form of the mineral malayaite is shown to exhibit a strong negative linear compressibility effect that arises from correlated tilting of SnO_6 and SiO_4 coordination polyhedra.

© 2012 International Union of Crystallography
Printed in Singapore – all rights reserved

1. Introduction

The mechanisms by which crystalline materials respond to changes in temperature and pressure are as important for the valuable insight they provide into the fundamental chemistry of the solid state as they are for a range of practical applications. Topical examples include negative thermal expansion (NTE) in metal–organic frameworks (MOFs) (Wu *et al.*, 2008; Lock *et al.*, 2010), negative linear compressibility (NLC) in molecular co-crystals (Fortes *et al.*, 2011) and extreme gating responses to guest sorption in microporous materials (Serre *et al.*, 2002; Mulfort *et al.*, 2010; Walton *et al.*, 2011). From an experimental viewpoint, crystallographic techniques offer a direct and straightforward measure of any structural variation: the evolution of unit-cell parameters describes the bulk mechanical response of the material, with the corresponding changes in atomic positions indicating the microscopic mechanism responsible for this response. Thus, for any given system, determination of the temperature and/or pressure dependence of its unit-cell parameters is a simple but effective means of diagnosing anomalous (and useful) mechanical behaviour.

Because the unit cell is a construct of convention rather than uniqueness, the question as to whether variations in unit-cell geometry actually reflect the fundamental mechanical response[1] of a material is an important one. Put differently, can we be certain that an alternative choice of unit cell, however unconventional, would yield the same lattice expansivities and/or compressibilities? The answer, of course, is that the values determined nearly always depend on the particular unit cell chosen. A canonical example is given by a simple two-dimensional molecular framework (Fig. 1*a*) {a lower-dimensional analogue, perhaps, of MIL-53 (Serre *et al.*, 2002) or $Ag_3[Co(CN)_6]$ (Goodwin *et al.*, 2008)}. The dominant deformation mechanism of this framework might involve a 'wine-rack'-like expansion in one direction that couples to a contraction in a perpendicular direction (Baughman *et al.*, 1998): a mechanism that is reflected in the lattice parameter variation of the orthogonal (rectangular) unit cell shown in Fig. 1. For the related rhombic cell (Fig. 1*b*), there is no apparent change in the values of the lattice parameters a and b; instead the important variation occurs in the angle β, which is less readily interpreted. By analogy, in real materials of low crystal symmetry the key science can be hidden within the variation of the entire ensemble of lattice parameters a, b, c, α, β, γ, making analysis much less straightforward than would otherwise be hoped (or indeed is often assumed).

The tensor algebra that resolves this issue is well established but is perhaps used more widely within some communities than others. The central concept is that for any system there exists a unique set of orthogonal axes (the principal axes) along which the material responds in a purely linear fashion, either expanding or contracting, with the response along other directions involving some nonzero shear component. It is the expansion or contraction along the principal axes that describes the fundamental mechanical response of the system. Predictably, crystal symmetry plays a crucial role in determining the orientation of these axes.

For systems of orthorhombic symmetry or higher the principal and (conventional) crystallographic axes coincide (Nye, 1957).[2] Hence the variation in lattice parameters ℓ with temperature (T) and pressure

[1] In this manuscript we use the term 'mechanical response' to refer to those mechanical properties most readily measured crystallographically: hydrostatic compressibilities, the bulk modulus, the pressure derivative of the bulk modulus and the thermal expansivities. In other contexts, the same term is sometimes equated with the full elastic tensor and includes *e.g.* the elastic compliances, Poisson's ratio and shear moduli (Nye, 1957).

[2] For uniaxial systems (*i.e.* with three-, four- or sixfold rotational symmetry), two of the three principal axes are related by this rotational symmetry; these axes define a unique plane in which the mechanical response is invariant. Cubic systems are isotropic.

(p) can be related directly to the bulk expansivities α_ℓ and compressibilities K_ℓ:[3]

$$\alpha_\ell = +\frac{1}{\ell}\left(\frac{\partial \ell}{\partial T}\right)_p, \quad (1)$$

$$K_\ell = -\frac{1}{\ell}\left(\frac{\partial \ell}{\partial p}\right)_T. \quad (2)$$

For monoclinic and triclinic crystal classes, however, the principal axes are not necessarily related to the unit-cell axes[4] and must instead be determined as the eigenvectors of the full strain tensor. In particular, because the principal expansivities and compressibilities now depend in a complex fashion on the variation in unit-cell lengths and angles, the values determined using equations (1) and (2) no longer carry any physical significance. Returning to the example of Fig. 1, the discrepancy in lattice thermal expansivities arises because the principal axes coincide with the axes of the rectangular unit cell rather than the rhombic cell.

Variable-temperature (or -pressure) unit-cell data contain all the information necessary to identify the principal axes and hence the principal coefficients of thermal expansion (or compressibilities), but for low-symmetry systems the process of calculating these is a problem best suited to automation. A number of software packages are capable of carrying out this calculation: notably *STRAIN* (Ohashi, 1982) and its successor *WINSTRAIN* (unpublished but available for download from http://www.rossangel.com), *DEFORM* (Filhol *et al.*, 1987), and *ElAM* (Marmier *et al.*, 2010). Yet for much of the materials chemistry community, the many features offered by these packages can in some cases require more detailed experimental data than are available (*e.g.* elastic constant measurements) and/or provide a level of analysis beyond what is necessary to identify expansivity and compressibility anomalies.

We have developed a new web-based tool, *PASCal* (= principal axis strain calculator; available at http://pascal.chem.ox.ac.uk), that accepts variable-temperature or variable-pressure lattice parameter data as input and simply returns as output the principal axis expansivities/compressibilities and the orientation of the principal axes relative to the crystallographic axes. The pressure dependence of the unit-cell volume is also fitted to equations of state, from which the bulk modulus and its pressure derivative are determined. This output enables the user to identify quickly any anomalous mechanical properties (*e.g.* NTE, NLC, pressure-induced softening) and to understand their geometric relationship to the structure itself. At all times, our particular focus has been on providing a simple tool usable by experts in elastic property calculations and non-experts alike.

Our paper is arranged as follows: in §2, we describe the particular implementation of strain tensor calculations used by the program and provide a summary of the most important aspects of the program input and output. What follows subsequently is a series of three case studies – focusing on one MOF, one molecular crystal and one mineral – where we have used *PASCal* to reanalyse previously published lattice parameter data. In all cases we are able to develop the relevant science as a result of considering the principal compressibilities or expansivities. In this way, we hope to demonstrate not only that routine application of *PASCal* to parametric crystallographic studies is feasible but also that the program is capable of adding substantive scientific value to the field.

2. Computational detail

2.1. Theory

The calculations at the heart of *PASCal* involve determination of the orthogonal strains. Our starting point is the transformation from crystallographic axes $\mathbf{A}_i$ to orthogonal axes $\mathbf{E}_i$ [with notation as in Giacovazzo *et al.* (2011)]. The orientation of the $\mathbf{E}_i$ axes is arbitrary: we make use of the Institute of Radio Engineers convention where $\mathbf{E}_3$ is parallel to the $\mathbf{c}$ crystallographic axis, $\mathbf{E}_1$ is parallel to $\mathbf{a}^*$, and $\mathbf{E}_2 = \mathbf{E}_3 \times \mathbf{E}_1$. The corresponding change-of-basis transformation is described by the square matrix $\mathbf{M}$:

$$\mathbf{E} = \mathbf{M} \times \mathbf{A}. \quad (3)$$

The strain $\boldsymbol{\varepsilon}$ corresponding to a pair of initial and final conditions (*i.e.* temperature or pressure values) is given as the symmetric part of the product of $\mathbf{M}$ at the first condition with its inverse at the second condition: defining

$$\mathbf{e} \equiv \mathbf{M}_{\rm final}^{-1} \times \mathbf{M}_{\rm initial} - \mathbf{I}, \quad (4)$$

we have

$$\boldsymbol{\varepsilon} = \tfrac{1}{2}(\mathbf{e} + \mathbf{e}^{\rm T}). \quad (5)$$

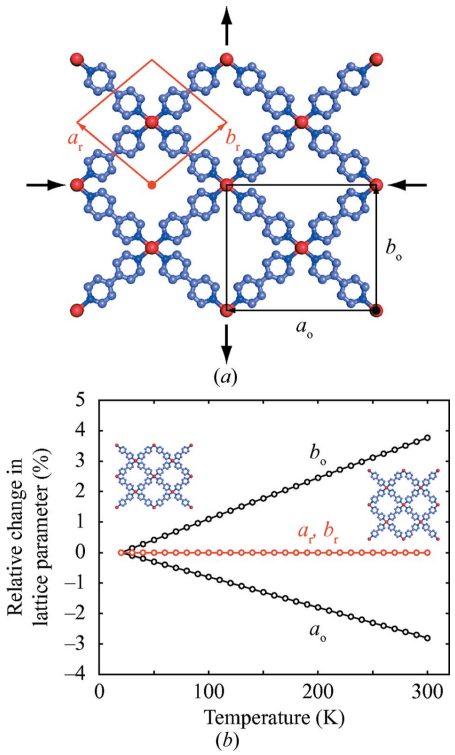

Figure 1
An illustrative example of the effect of unit-cell choice on lattice parameter expansivity determination. (*a*) A hypothetical two-dimensional molecular framework, with both a rhombic and an orthogonal unit-cell indicated. (*b*) A plot of the relative change in lattice parameter determined for each of these two cells for the concerted lattice deformation indicated by arrows in (*a*). The rhombic cell shows no variation in unit-cell length, whereas the changes in orthogonal cell lengths reflect the underlying bulk material response.

[3] Note that there is more than one convention widely in use for the symbols for compressibility and its inverse the bulk modulus. In key solid-state physics texts (*e.g.* Ashcroft & Mermin, 1976; Kittel, 2005) K is used to denote compressibility and B the bulk modulus. Confusingly, the primary reference for mechanical properties of crystals (Nye, 1957) uses K to denote the bulk modulus and β the compressibilities. Here, we follow the physics convention in order to remove any ambiguity regarding the lattice parameter β.

[4] For monoclinic classes in the conventional setting, one principal axis lies parallel to **b**.

The eigenvalues ε_i and eigenvectors $\mathbf{x}_i$ of the matrix $\boldsymbol{\varepsilon}$ are then the principal strains and the principal axes. The derivatives of these principal strains with respect to temperature and/or pressure give the principal coefficients of thermal expansion and/or compressibilities:

$$\alpha_i = +\left(\frac{\partial \varepsilon_i}{\partial T}\right)_p, \tag{6}$$

$$K_i = -\left(\frac{\partial \varepsilon_i}{\partial p}\right)_T. \tag{7}$$

Formally, the definitions we have given here correspond to infinitesimal Lagrangian strains; this is the standard approach applied in texts such as Nye (1957). We note, however, that infinitesimal strains are quantitatively exact only in the limit of small variations in lattice parameters. Consequently, slightly different definitions of strain can be more meaningful in other situations (*e.g.* finite strain for lattice discontinuities at a phase transition). There is scope within *PASCal* to calculate these alternative strains; interested readers are referred to Giacovazzo *et al.* (2011), Schlenker *et al.* (1978) and Zotov (1990) for further details regarding the choice of strain and the associated calculations. In practice the use of different strain definitions can give quantitatively significant differences in principal axis expansivity/compressibility values but is unlikely to affect the diagnosis of qualitative features, such as the existence or otherwise of NTE or NLC. Implementation of all strain calculations within *PASCal* is as a Fortran90 routine that makes use of the LAPACK and MINPACK libraries (Anderson *et al.*, 1999; Moré *et al.*, 1984).

2.2. Program input

We have tried to simplify the required input for *PASCal* as much as possible. Parametric data are entered as a series of whitespace- or comma-separated values in sequential columns: temperature (K) or pressure (GPa) values; the uncertainty in these values; followed by the corresponding lattice parameters a, b, c, α, β, γ. At this stage, estimated errors in cell parameters are neither required nor taken into account, as the errors in all subsequently calculated parameters are nearly always dominated by errors in temperature or pressure values and scatter in the data themselves.

As an aside, we note that the use of standard errors on lattice parameters to determine standard errors in derived parameters has been the subject of a number of detailed investigations. First, it is well established that standard uncertainties are underestimated by both single-crystal and powder (Rietveld) refinement, with reported errors smaller by up to an order of magnitude than the real values determined by multiple measurements (Taylor & Kennard, 1986; Herbstein, 2000). Second, the avoidance of bias in derived orthogonal cells arising from angular uncertainty is a well recognized problem for monoclinic and triclinic systems (Haestier, 2009). Third, the covariances necessary for accurate error propagation are rarely quoted or included in deposited CIFs. Some of these issues can be overcome with careful treatment – *e.g.* by using repeat measurements to obtain experimental distributions of cell parameters – hence providing physically meaningful estimates of standard uncertainties. A thorough investigation of one such approach is detailed by Angel (2000). However, in order to maintain a simple interface and in order not to give an impression of misleading precision, the error-propagation algorithms within *PASCal* have been implemented in a way that is likely to provide a small overestimation of uncertainties. For specific instances demanding greater control over error treatment, the user is referred to more specialist code (*e.g. STRAIN*; Ohashi, 1982).

In Fig. 2 we show an example set of input data for both expansivity and compressibility measurements of the high-pressure phase $Ag_3[Co(CN)_6]$-II (Goodwin *et al.*, 2008).

2.3. Program output

For variable-temperature data, *PASCal* calculates the principal thermal expansivities across the entire temperature range for which

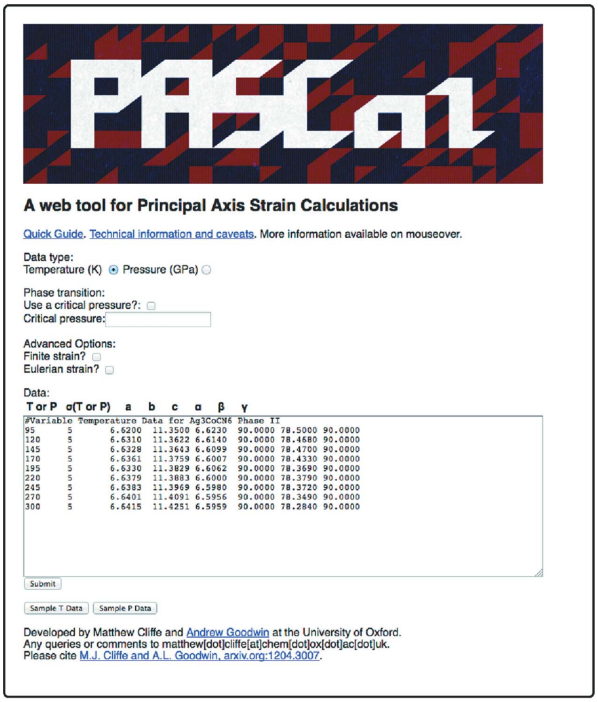

(*a*)

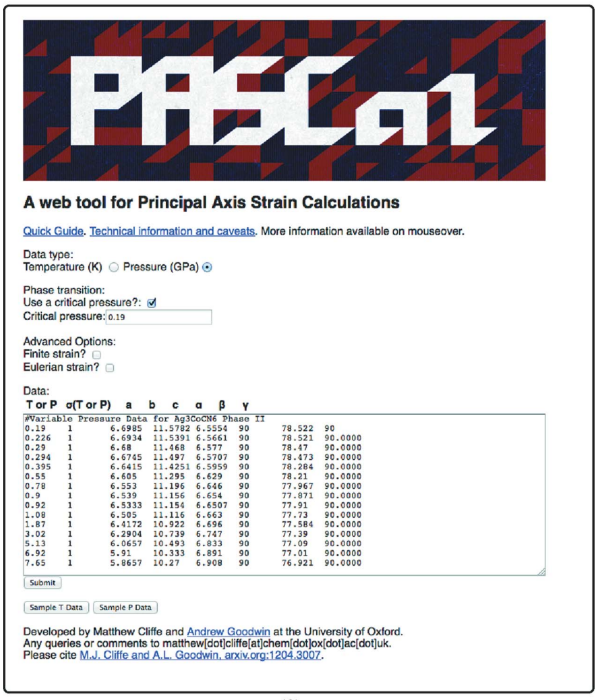

(*b*)

Figure 2
Sample *PASCal* input for (*a*) variable-temperature and (*b*) variable-pressure lattice parameter data measured for $Ag_3[Co(CN)_6]$-II (Goodwin *et al.*, 2008).

data are provided. No attempt is made to fit the expansivity data at any level of complexity beyond a simple linear dependence: $\ell_i(T) = \ell_0(1 + \alpha_i T)$. More complex fitting approaches, such as using a Debye model for thermal expansion, are prone to instabilities in the absence of very high quality data that extend to low temperatures ($T \ll \Theta_D$; David *et al.*, 1993). We are of the view that complex fits are most likely to be of interest to specialist users, with simple linear coefficients of thermal expansion of greatest value to the broadest user base. In any case, the principal strains are given in tabular format for each temperature point, with the intention that more complex fits might easily be performed using any third-party fitting software of choice.

The relationship between principal axes and the crystallographic axes is also described in the *PASCal* output, where we give the normalized components of the principal axes projected onto the crystallographic axes. The thermal expansivity tensor is represented visually in the form of the expansivity indicatrix. The expansivity indicatrix is a smoothly varying surface centred at the unit-cell origin, where the distance between the surface and the origin in a given direction **r** is equal to the magnitude of α in that direction (taking negative values as appropriate) (Belousov & Filatov, 2007; Durka *et al.*, 2011; Krashnenko *et al.*, 2000; Vershinin *et al.*, 2005). Perhaps the more traditional method of visualizing the expansivity or compressibility tensor would be *via* either the representation quadric or the strain ellipsoid (Nye, 1957). The particular advantage of the expansivity/compressibility indicatrix over these other representations – and the reason behind its inclusion in the *PASCal* output – lies in the ease with which crystallographic directions corresponding to mechanical behaviour of particular interest can be identified (*e.g.* α very large and positive, very large and negative, or zero). We illustrate this point explicitly in Fig. 3, where we show together the expansivity indicatrix, the quadric and the strain ellipsoid for the $Ag_3[Co(CN)_6]$-II system. For this material, comparison of the expansivity indicatrix with the crystal structure shows, in accord with the original study (Goodwin *et al.*, 2008), that NTE occurs along the layer-stacking axis and that the covalent Co—C—N—Ag—N—C—Co linkages are oriented along directions for which the expansivity essentially vanishes. The actual *PASCal* output for this same system is shown in Fig. 4.

The output provided for variable-pressure data is more detailed. At the simplest level, median principal compressibilities, their uncertainties and the corresponding principal axes are calculated according to equation (7) using a linear fit to the strains. While thermal expansion data are usually approximately linear across typical measurement ranges, a linear pressure dependence is rarely observed for variable-pressure data (and thermodynamically forbidden over large pressure ranges). In our experience of relatively highly compressible materials such as molecular frameworks, axial compressibilities are often much better characterized using an empirical fit of the form $\ell(p) = \ell_0 + \lambda(p - p_c)^{\nu}$ (Goodwin *et al.*, 2008; Cairns *et al.*, 2012). Accordingly, *PASCal* also outputs fitted values of λ and ν for each principal axis and, because compressibility now varies with pressure, $K_i(p)$ for each pressure point and their uncertainties are both plotted graphically and listed in tabular form (Fig. 5).

There is valuable thermodynamic information in the pressure dependence of the unit-cell volume, in the form of the bulk modulus $B = (-V\mathrm{d}p/\mathrm{d}V)_T$ and its (dimensionless) pressure derivative $B' = (\mathrm{d}B/\mathrm{d}p)_T$. The parameter B' can be an indicator of unusual mechanical behaviour; for example, a large B' is often indicative of a rapid stiffening characteristic of layered materials (Munn, 1972) and a negative B' can indicate the presence of a dynamic instability (Chapman & Chupas, 2007). Accordingly, unit-cell volumes are fitted in *PASCal* using Birch–Murnaghan equations of state (Birch, 1947) of various degrees of complexity, with the ultimate choice left to the user, perhaps guided by the quality of fits obtained or by construction of a so-called *f–F* plot (Angel, 2000). Defining the parameter

$$\eta \equiv (V_0/V)^{1/3}, \tag{8}$$

where V_0 is the zero-pressure unit-cell volume, the second- and third-order Birch–Murnaghan fits correspond to the equations of state

$$p(V) = \frac{3B}{2}\left(\eta^7 - \eta^5\right) \tag{9}$$

and

$$p(V) = \frac{3B_0}{2}\left(\eta^7 - \eta^5\right)\left[1 + \frac{3}{4}(B' - 4)(\eta^2 - 1)\right], \tag{10}$$

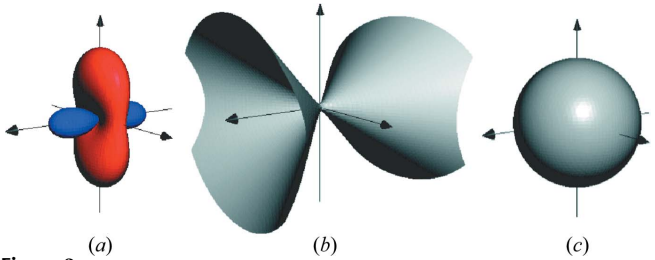

(*a*) (*b*) (*c*)

Figure 3
A comparison of three methods for representing an expansivity tensor, using the variable-temperature $Ag_3[Co(CN)_6]$-II data of Goodwin *et al.* (2008). (*a*) The thermal expansivity indicatrix, with positive thermal expansion shown in red and NTE in blue; (*b*) the thermal expansivity quadric; (*c*) the strain ellipsoid (shown here for the maximum strain obtained in order to emphasize the difficulty associated with perceiving asphericity). The directions and relative magnitudes of large positive and negative thermal expansion are obvious in the expansivity indicatrix representation but are obscured in the other, more traditional, representation surfaces.

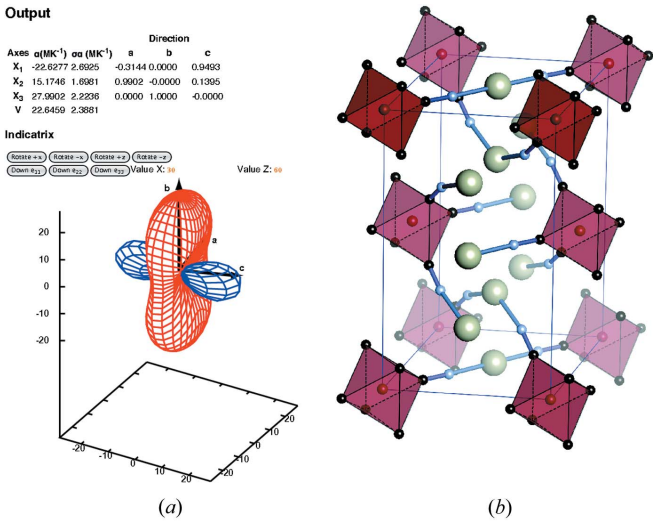

(*a*) (*b*)

Figure 4
(*a*) The key *PASCal* output obtained for the input data shown in Fig. 2(*a*), showing the principal components of the expansivity tensor and the expansivity indicatrix representation as discussed in the text. (*b*) A representation of the crystal structure of $Ag_3[Co(CN)_6]$-II shown with axes in the same orientation as the expansivity indicatrix in (*a*). The layer of Ag^+ cations (shown as large spheres) corresponds to the large positive thermal expansion component of the expansivity indicatrix, which is shown in red; the perpendicular (stacking) axis of $Ag_3[Co(CN)_6]$-II then corresponds to the large NTE component of the expansivity indicatrix (shown in blue). The Co—C—N—Ag—N—C—Co linkages, shown in ball-and-stick representation, are oriented in the set of directions for which the expansivity indicatrix has a near-zero value.

respectively. In equation (10), B_0 can be interpreted as the value of B at zero pressure. For completeness, the option is provided to use finite Eulerian rather than infinitesimal Lagrangian strains, as the former is used in the derivation of the Birch–Murnaghan equation of state (Birch, 1947). We note, however, that this formalism was derived for isotropic crystals and need not describe equally well the behaviour of anisotropic systems. Consequently Birch–Murnaghan fits for anisotropic systems should be interpreted with this caveat in mind.

For high-pressure phases that are unstable below some critical pressure $p_c > 0$, even the third-order Birch–Murnaghan equation of state does not capture the elastic behaviour fully, as it assumes that both V and B are continuous functions of p for all $p > 0$. In *PASCal*, we have incorporated the option to fit a modified version, which now takes into account the existence of a nonzero critical pressure p_c (Sata *et al.*, 2002):

$$p(V) = \eta^5\left[p_c - \frac{1}{2}(3B - 5p_c)(1-\eta^2) + \frac{9}{8}B_0\left(B' - 4 + \frac{35p_c}{9B_0}\right)(1-\eta^2)^2\right]. \quad (11)$$

In fitting equation (11) the assumption is made that p_c is less than or equal to the lowest pressure value for which data are given. The user is given the option to include a fixed value of p_c in their analysis.

For the example of $Ag_3[Co(CN)_6]$-II discussed above and shown in Fig. 2, it is meaningful to fix the value of p_c at the phase-I/II transition pressure of 0.19 GPa. A good fit to the experimental $V(p)$ data is then obtained by *PASCal*, as shown in Fig. 5. The fundamental parameters we extract in this fit show some discrepancy with those reported by Goodwin *et al.* (2008): here we obtain $B_0 = 14.2\ (14)$ GPa and $B' = 10.9\ (13)$ [the previously reported values are 11.8 (7) GPa and 13.5 (12), respectively]. The origin of this discrepancy appears to be the extremely large parametric covariances within the third-order Birch–Murnaghan equation of state, resulting in different convergence behaviour with different minimization routines [the values reported by Goodwin *et al.* (2008) were determined using the solver routine within Microsoft *Excel*]. A fit using the program *EOS-FIT* (Angel, 2001) (which automatically constrains $p_c = 0$ and hence gives a slightly different set of parameters yet again) returns covariance terms with magnitudes greater than 0.94, indicating that the system of equations is very poorly constrained. It is actually the case for many well studied systems that there exist a variety of B, B' and V_0 values that result in very similar fits to experimental compressibility data, and we reiterate here the caution of *e.g.* Jackson (1998) by emphasizing the covariance amongst these parameters, especially for data with large scatter.

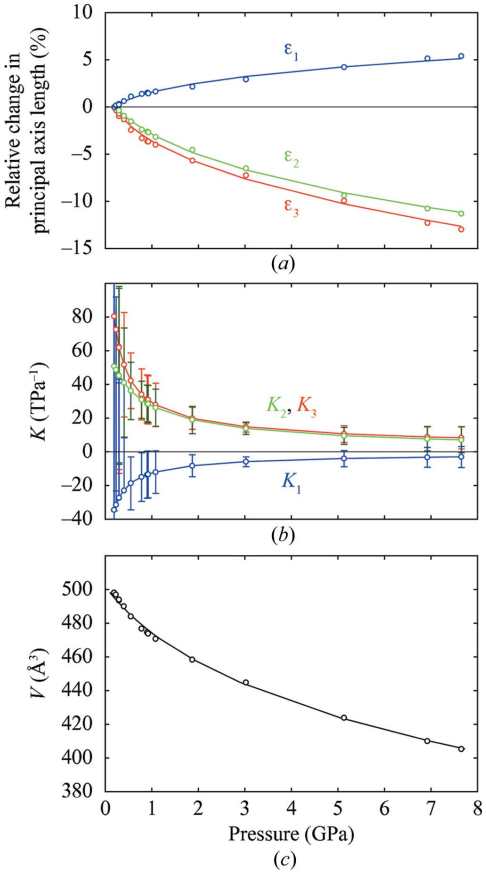

Figure 5
Calculated fits to variable-pressure $Ag_3[Co(CN)_6]$-II lattice parameter data obtained using *PASCal*: (*a*) relative changes in length for the three principal axes, (*b*) the corresponding principal compressibilities and (*c*) the modified third-order Birch–Murnaghan fit to the unit-cell volumes.

3. Case studies

3.1. A metal–organic framework: Cu-SIP-3

The first of our case studies concerns the flexible metal–organic framework $[Cu_2(OH)(C_8H_3O_7S)(H_2O)]\cdot 2H_2O$ (abbreviated to Cu-SIP-3·3H_2O). This is a material of particular currency for its potential applications as a biomedical agent for controlled nitrous oxide (NO) release (Xiao *et al.*, 2009; Hinks *et al.*, 2010). Under ambient conditions its structure can be considered as a stack of two-dimensional covalently connected 'sheets': each such sheet is assembled from what is technically a distorted square (4,4)-net of tetrameric Cu_4 clusters connected *via* 5-sulfoisophthalate linkers (although a description in terms of hexagonal close packing of the same clusters might be considered equally valid) (Fig. 6*a*). Adjacent sheets interact only very weakly, *via* axial $Cu^{2+}\cdots O_3SR$ contacts [$r(Cu\cdots O) > 2.8$ Å], such that if only strong covalent bonds are considered then the network of the solid as a whole has two-dimensional rather than three-dimensional connectivity.

Variable-temperature (150–365 K) lattice parameter data for this ambient phase were reported by Allan *et al.* (2010) as part of a detailed study into a reversible reconstructive phase transition that occurs on desolvation/resolvation. Because Cu-SIP-3·3H_2O crystallizes in the monoclinic space group $P2_1/n$, this is an example of a system where not all of the coefficients of thermal expansion determined from lattice parameters correspond to principal expansivities. Nonetheless there are hints even in the lattice parameter measurements that the system exhibits anomalous thermal expansion behaviour: the *b* unit-cell parameter decreases on increasing temperature, and there is a negligible change in unit-cell volume over the temperature range studied.

We have used the lattice parameter data of Allan *et al.* (2010) as input for *PASCal* in order to determine the fundamental thermal expansion properties of this interesting material; our results are summarized in Table 1. Perhaps the most unexpected finding here is that two of the three principal expansivities are in fact negative. Therefore not only does Cu-SIP-3·3H_2O become one of the few known materials to show an area NTE effect, but this effect is very large indeed. In fact the area coefficient of thermal expansion $\alpha_A = \alpha_1 + \alpha_2 = -76\ MK^{-1}$ is essentially an order of magnitude more negative than corresponding values in previously studied area

Table 1
Principal coefficients of thermal expansion and corresponding principal axes determined for Cu-SIP-3·3H_2O.

		Component of $\mathbf{x}_i$ along the crystallographic axes			
Principal axis, i	α_i (MK^{-1})	a	b	c	Approximate axis
1	−55 (7)	0	−1	0	[010]
2	−21 (7)	−0.7932	0	0.6090	[$\bar{1}$01]
3	+60 (9)	0.8260	0	0.5637	[101]

Table 2
Principal coefficients of thermal expansion and corresponding principal axes determined for β-HMX.

		Component of $\mathbf{x}_i$ along the crystallographic axes			
Principal axis, i	α_i (MK^{-1})	a	b	c	Approximate axis
1	+101 (3)	0	−1	0	[010]
2	+37 (3)	−0.5570	0	0.8305	[$\bar{2}$03]
3	−15 (3)	−0.8419	0	−0.5397	[302]

NTE materials: *e.g.* the $Ni(CN)_2$ family ($\alpha_A = -11$ to $-16\ MK^{-1}$; Hibble *et al.*, 2007, 2011), graphite ($\alpha_A = -2.4\ MK^{-1}$; Bailey & Yates, 1970) and low-temperature arsenic ($\alpha_A = -4.0\ MK^{-1}$; Munn, 1972).

Clues as to the microscopic driving force responsible for this unusual behaviour can be found in the orientation of the principal axes relative to the crystal structure. The set of directions in which NTE is observed lies perpendicular to the $\mathbf{x}_3$ principal axis (*i.e.* the plane containing the $\mathbf{x}_1$ and $\mathbf{x}_2$ axes). Hence the orientation of $\mathbf{x}_3$ must carry some special significance. We find that $\mathbf{x}_3$ is approximately parallel to the [101] crystal axis, which is in fact the layer-stacking direction [*i.e.* normal to the layer shown in Fig. 6(*a*)]. Hence, on heating, the framework Cu-SIP-3 expands in a direction parallel to the stacking axis, but contracts in every perpendicular direction.

The general propensity for layered materials to exhibit area NTE was in fact predicted 60 years ago (Lifshitz, 1952): the lowest energy phonon branches correspond to 'rippling' of the layers, a displacement pattern that causes the interlayer separation to increase and the effective layer area to decrease (Fig. 6*b*). The actual magnitude of NTE response observed then depends on the elastic stiffness of the sheets (*i.e.* how easily they might be corrugated). We would suggest that the use of flexible organic linkers is responsible for the large NTE effect we find here by virtue of the low energy cost associated with flexing of the layers. Finally we comment that, in the light of an emerging correspondence between negative thermal expansion and negative compressibility in framework materials (Goodwin *et al.*, 2008; Fortes *et al.*, 2011; Cairns *et al.*, 2012), one might expect Cu-SIP-3 to exhibit the elusive property of negative area compressibility under hydrostatic pressure (Baughman *et al.*, 1998).

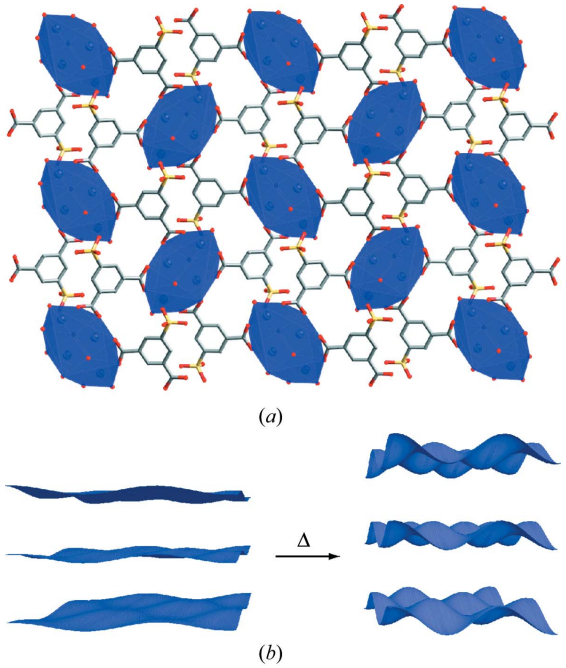

Figure 6
Negative thermal expansion in Cu-SIP-3·3H_2O. (*a*) A single covalently bonded layer in the material, viewed down the [101] axis (the single principal axis associated with positive thermal expansion). (*b*) The general mechanism responsible for area NTE in layered materials: the lowest energy deformations correspond to 'rippling' of the layers, which results in an increased interlayer separation but a smaller effective layer area.

3.2. A molecular crystal: HMX

Anisotropy in thermal expansion can be of considerable importance in materials applications, particularly when the avoidance of cracking is important. One such application is the development of high-performance explosive materials, where cracking can increase the propensity for accidental detonation: *i.e.* the sensitivity of the explosive (Bennett *et al.*, 1998; McGrane *et al.*, 2009; Ramaswamy *et al.*, 1996). Like many molecular crystals, explosives often crystallize in low-symmetry crystal systems. Consequently in order to determine the degree of anisotropy in their mechanical response it is rarely sufficient to consider the temperature dependence of the unit-cell lengths alone. Indeed since the principal coefficients of thermal expansion correspond to the extrema of mechanical response, the use of unit-cell length variation to characterize mechanical anisotropy will always underestimate its maximum extent.

One of the most important and widely used explosives is cyclotetramethylenetetranitramine (HMX) (Agrawal, 2010). HMX is known to crystallize in any one of four polymorphs (α, β, γ, δ), of which the β phase (space group $P2_1/n$) is the most important because it is the only stable polymorph under ambient conditions (Fig. 7*a*) (Cady *et al.*, 1963; Choi & Boutin, 1970). A recent thermal expansion study of β-HMX, aimed at characterizing its mechanical anisotropy, revealed a large difference in the lattice coefficients of thermal expansion: $\alpha_a, \alpha_b, \alpha_c = 33$, 99 and $0.43\ MK^{-1}$, respectively (Deschamps *et al.*, 2011).

Using the variable-temperature lattice parameter data of Deschamps *et al.* (2011) as input for *PASCal*, we have been able to determine the principal coefficients of thermal expansion; the *PASCal* output is summarized in Table 2. We find a subtle but important difference between the principal and lattice coefficients of thermal expansion: namely that there exists NTE along one of the principal axes ($\mathbf{x}_3$). This is important because the degree of anisotropy in some directions is now substantially larger than anticipated from the lattice parameters alone; for example, the lattice expansivities underestimate anisotropy in the (010) plane by *ca* 40%.

At a molecular level, the driving force for the NTE effect that we observe appears to be a flattening of the eight-membered ring of each HMX molecule at higher temperatures. There are two different ring orientations within the β-HMX crystal structure, which are related by the space-group symmetry. For each orientation the four ring N atoms are coplanar, so a vector normal to this plane characterizes the ring orientation. We find that an average of the two orientation vectors coincides with the NTE principal axis $\mathbf{x}_3$ to within 1% (Fig. 7*b*). A simple measure of the degree of ring puckering is given by the mean-

squared displacement of the four C atoms away from the N-atom plane defined above. On the basis of the atomic coordinates given by Deschamps *et al.* (2011), this quantity appears to decrease with temperature – *i.e.* the HMX rings become flatter at higher temperatures – providing a feasible explanation for the reduction in crystallite size in a direction perpendicular to these C_4N_4 rings.

3.3. A mineral: malayaite

Our final case study concerns the mineral malayaite ($CaSnOSiO_4$), which is a calcium tin silicate closely related to titanite ($CaTiOSiO_4$) that, when doped with chromium, finds application as a pink glaze for ceramics (Ingham & Bradford, 1961; Higgins & Ribbe, 1976). From a fundamental science viewpoint, the comparative critical behaviour of the malayaite–titanite family is of general interest in helping to understand the interplay between mechanical and electronic properties in framework silicates (Salje *et al.*, 1993; Zhang *et al.*, 1999). In titanite itself, second-order Jahn–Teller distortions of the d^0 Ti^{4+} ion lead to local polarizations of the TiO_6 octahedra [such as is observed in key ferroelectrics such as $BaTiO_3$ (Shirane *et al.*, 1967)]; this effect is reduced on substitution with Sn^{4+}. An interest in understanding the effects of pressure and temperature on the interplay between these off-centre distortions and structural transitions has led to a number of variable-temperature and variable-pressure studies on both systems (Kek *et al.*, 1997; Kunz *et al.*, 2000).

The structure of malayaite consists of chains of vertex-sharing SnO_6 octahedra. These chains are connected *via* SiO_4 tetrahedra to form a three-dimensional anionic network structure. Calcium ions occupy a set of voids within this framework such that each Ca^{2+} is 'coordinated' by six or seven O atoms (the Ca—O separations being sufficiently large that identification of the coordination sphere is somewhat arbitrary). At a pressure of 4.95 (1) GPa, malayaite transforms from its ambient monoclinic $A2/a$ phase into a triclinic $P\overline{1}$ phase (Rath *et al.*, 2003). The distortion mechanism associated with this transition and the structural changes observed on further compression within the triclinic phase offer insight into the key dynamical properties of malayaite. For example, the high-pressure crystallographic study of Rath *et al.* (2003) documents, amongst other things, the effective compressibilities of SiO_4 tetrahedra (not very compressible), SnO_6 octahedra (more compressible) and CaO_x coordination polyhedra (very compressible): the implication being that vibrational modes resulting in large changes in Ca—O distances play a significant role in the dynamics of ambient-phase malayaite.

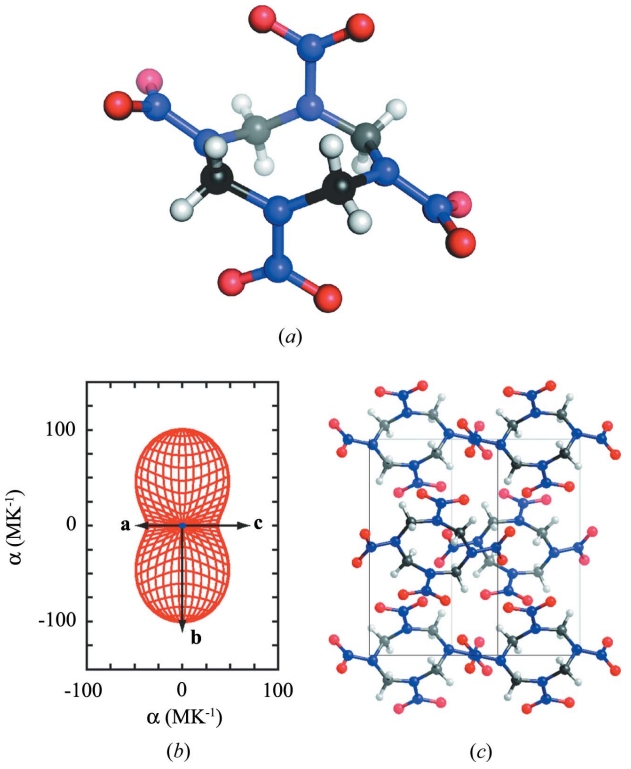

Figure 7
(*a*) A representation of the molecular geometry of HMX in its β phase. (*b*) The thermal expansivity indicatrix viewed down the axis of NTE (*i.e.* for the x_1x_2 plane). The negative-valued lobe of the expansivity indicatrix is small and projects from the centre of the expansivity indicatrix towards the viewer. (*c*) A representation of the crystal structure of β-HMX viewed in the same orientation as for the expansivity indicatrix in (*b*). A flattening of the central eight-membered C_4N_4 rings at higher temperatures causes an expansion in the $\mathbf{x}_1$ and $\mathbf{x}_2$ directions but a contraction in the $\mathbf{x}_3$ direction (*i.e.* along the viewing direction).

Table 3
Principal compressibilities and corresponding principal axes determined for the high-pressure ($P\overline{1}$) phase of malayaite.

		Component of $\mathbf{x}_i$ along the crystallographic axes			
Principal axis, i	K_i (TPa^{-1})	a	b	c	Approximate axis
1	+7.6 (4)	−0.6482	−0.5429	0.5339	$[1\overline{1}1]$
2	+2.28 (10)	−0.5846	−0.0820	−0.8072	[203]
3	−3.1 (3)	−0.6270	0.7591	0.1747	$[\overline{4}41]$

Making use of the variable-pressure lattice parameter data reported by Rath *et al.* (2003) for the high-pressure triclinic phase of malayaite, we have been able to extend their analysis to the determination of orthogonal strains. Using first a linear fit to these data, *PASCal* obtains the principal compressibilities and principal axes given in Table 3. Of particular note is the NLC behaviour along $\mathbf{x}_3$: *i.e.* approximately parallel to the $[\overline{4}41]$ crystallographic axis. We find that the compression mechanism is dominated by concerted rigid-body rotations and translations of the SnO_6 and SiO_4 polyhedra that cause a contraction within the plane perpendicular to the $[\overline{4}41]$ axis. The polyhedral 'rocking' associated with this compression translates to an expansion in a perpendicular direction: the NLC axis. In this process the CaO_x coordination environment undergoes substantive changes in geometry, which might suggest that the coordination flexibility of Ca^{2+} allows a particularly anisotropic mechanical response to network compression.

For completeness, we show in Fig. 8 the nonlinear parameterized fits to the principal strains obtained using *PASCal* and the derived compressibilities. What is apparent from these plots is that the value of K_2 increases with pressure – even in this post-transition phase – which could suggest the existence of an incipient dynamic instability at yet higher pressures. This conclusion is reflected also in the thermodynamic quantities obtained from a third-order Birch–Murnaghan fit to the $V(p)$ data: here we find $B_0 = 170$ (40) GPa and $B' = -3$ (5). Given the magnitude of the uncertainties involved, we cannot be sure that the value of B' is really negative, but if it were then the implication is that the material is becoming mechanically softer on compression: a feature also associated with dynamic instabilities (Chapman & Chupas, 2007; McConnell *et al.*, 2000). To some extent this was discussed by Rath *et al.* (2003), but caution led the authors to constrain their fit to a second-order Birch–Murnaghan equation of state. If we perform a similar fit, *PASCal* obtains a value of $B = 119$ (2) GPa, which is in close agreement with the value obtained by Rath *et al.* (2003) [$B = 118.3$ (7) GPa]. Intriguingly, Rath (2002) reports indications of a second high(er)-pressure phase transition in titanite at *ca* 10 GPa, suggesting that the dynamical anomalies we

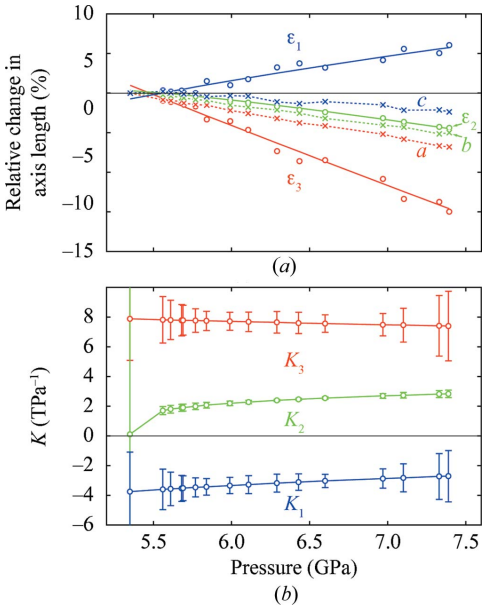

Figure 8
Compressibility of high-pressure malayaite. (*a*) Relative changes in the lengths of the principal axes (open circles, solid lines) and $P\bar{1}$ unit-cell axes (crosses and dashed lines) under compression. The variation in unit-cell axes is substantially more moderate than the variation in principal axes. (*b*) The corresponding principal linear compressibilities. The increase in the magnitude of K_2 observed at increasing pressure reflects a dynamical instability.

observe here for malayaite might signal the existence of a similar incipient transition. This putative phase transition could provide an explanation for the observed NLC, as has been observed in other oxide frameworks (Angel & Bismayer, 1999; Angel *et al.*, 2004).

4. Conclusion

Our aim has been to develop a simple tool that enables rapid and straightforward calculation of the principal coefficients of thermal expansion and compressibilities from variable-p/T lattice parameter data. On the one hand, this will allow users to screen easily for anomalous mechanical responses: *e.g.* NTE, NLC and pressure-induced softening. On the other hand, the reporting of principal axes means that any such effects can be related back to the underlying crystal structure. While we are aware that *PASCal* replicates some functionalities of existing codes, it is our hope that the straightforward input format, web accessibility and ease of output interpretation will mean that a greater scientific audience can make use of orthogonal strain calculations than is currently the case.

The three case studies discussed above illustrate some of the ways in which scientific value might be added through routine lattice parameter analysis with *PASCal*. In the case of the metal–organic framework Cu-SIP-3, we have shown it exhibits the strongest area NTE effect yet reported and have been able to relate this effect back to low-energy acoustic modes of its layer-like structure. Analysis of thermal expansion data for the explosive material HMX reveals a much stronger mechanical anisotropy than had otherwise been determined: a result that may have implications for strain propagation and cracking of polycrystalline HMX preparations. Finally, we have shown that high-pressure malayaite exhibits two thermodynamic anomalies: it expands in one direction on compression, and it becomes mechanically softer on increasing pressure.

These three systems are unlikely to be isolated examples. Indeed, we anticipate that, with a more widespread application of principal axis strain calculations, phenomena such as NTE and NLC will be observed with increasing frequency. Irrespective of the prevalence of such effects, the mechanisms responsible will almost always provide important insight into the dominant dynamical properties of materials. It is our particular hope that the ready availability of programs such as *PASCal* might help develop our understanding of dynamics in classes of solid materials for which strain calculations have not yet played a central role.

The authors gratefully acknowledge financial support from the EPSRC (grant No. EP/G004528/2) and the ERC (grant No. 279705), and wish to thank D. A. Keen and M. G. Tucker (ISIS) and W. Li (Cambridge) for their assistance in testing the code.

References

Agrawal, J. P. (2010). *High Energy Materials Propellants, Explosives and Pyrotechnics*. Weinheim: Wiley-VCH.
Allan, P. K., Xiao, B., Teat, S. J., Knight, J. W. & Morris, R. E. (2010). *J. Am. Chem. Soc.* **132**, 3605–3611.
Anderson, E., Bai, Z., Bischof, C., Blackford, S., Demmel, J., Dongarra, J., Du Croz, J., Greenbaum, A., Hammarling, S., McKenney, A. & Sorensen, D. (1999). *LAPACK Users' Guide*. Society for Industrial and Applied Mathematics, Philadelphia, USA.
Angel, R. J. (2000). *Rev. Min. Geochem.* **41**, 35–64.
Angel, R. J. (2001). *EOS-FIT*. Version 5.2. Virginia Polytechnic Institute and State University, Blacksburg, VA, USA.
Angel, R. J. & Bismayer, U. (1999). *Acta Cryst.* B**55**, 896–901.
Angel, R. J., Bismayer, U. & Marshall, W. G. (2004). *Acta Cryst.* B**60**, 1–9.
Ashcroft, N. W. & Mermin, N. D. (1976). *Solid State Physics*. Ithaca: Thomson Learning Inc.
Bailey, A. C. & Yates, B. (1970). *J. Appl. Phys.* **41**, 5088–5091.
Baughman, R. H., Stafstrom, S., Cui, C. & Dantas, S. O. (1998). *Science*, **279**, 1522–1524.
Belousov, R. I. & Filatov, S. K. (2007). *Glass Phys. Chem.* **33**, 271–275.
Bennett, J. G., Haberman, K. S., Johnson, J. N. & Asay, B. W. (1998). *J. Mech. Phys. Solids*, **46**, 2303–2322.
Birch, F. (1947). *Phys. Rev.* **71**, 809–824.
Cady, H. H., Larson, A. C. & Cromer, D. T. (1963). *Acta Cryst.* **16**, 617–623.
Cairns, A. B., Thompson, A. L., Tucker, M. G., Haines, J. & Goodwin, A. L. (2012). *J. Am. Chem. Soc.* **134**, 4454–4456.
Chapman, K. W. & Chupas, P. J. (2007). *J. Am. Chem. Soc.* **129**, 10090–10091.
Choi, C. S. & Boutin, H. P. (1970). *Acta Cryst.* B**26**, 1235–1240.
David, W. I. F., Ibberson, R. M. & Matsuo, T. (1993). *Proc. R. Soc. London Ser. A*, **442**, 129–146.
Deschamps, J. R., Frisch, M. & Parrish, D. (2011). *J. Chem. Cryst.* **41**, 966–977.
Durka, K., Hoser, A. A., Kamiński, R., Luliński, S., Serwatowski, J., Koźmiński, W. & Woźniak, K. (2011). *Cryst. Growth Des.* **11**, 1835–1845.
Filhol, A., Lajzerowicz, J. & Thomas, M. (1987). Unpublished software.
Fortes, A. D., Suard, E. & Knight, K. S. (2011). *Science*, **331**, 742–746.
Giacovazzo, C., Monaco, H. L., Artioli, G., Viterbo, D., Milanesio, M., Ferraris, G., Gilli, G., Gilli, P., Zanotti, G. & Catti, M. (2011). *Fundamentals of Crystallography*. New York: Oxford Science.
Goodwin, A. L., Keen, D. A. & Tucker, M. G. (2008). *Proc. Natl Acad. Sci. USA*, **105**, 18708–18713.
Haestier, J. (2009). *J. Appl. Cryst.* **42**, 798–809.
Herbstein, F. H. (2000). *Acta Cryst.* B**56**, 547–557.
Hibble, S. J., Chippindale, A. M., Bilbé, E. J., Marelli, E., Harris, P. J. & Hannon, A. C. (2011). *Inorg. Chem.* **50**, 104–113.
Hibble, S. J., Chippindale, A. M., Pohl, A. H. & Hannon, A. C. (2007). *Angew. Chem. Int. Ed.* **46**, 7116–7118.
Higgins, J. B. & Ribbe, P. H. (1976). *Am. Mineral.* **61**, 878–888.
Hinks, N. J., McKinlay, A. C., Xiao, B., Wheatley, P. S. & Morris, R. E. (2010). *Microporous Mesoporous Mater.* **129**, 330–334.
Ingham, F. T. & Bradford, E. F. (1961). *Am. Mineral.* **46**, 768–769.
Jackson, I. (1998). *Geophys. J. Int.* **134**, 291–311.
Kek, S., Aroyo, M., Bismayer, U., Schmidt, C., Eichhorn, K. & Krane, H. G. (1997). *Z. Kristallogr.* **212**, 9–19.

Kittel, C. (2005). *Introduction to Solid State Physics*. Hoboken: John Wiley and Sons.
Krasnenko, T. I., Zolotukhina, L. V. & Andrianova, L. V. (2000). *Inorg. Mater.* **36**, 1032–1035.
Kunz, M., Arlt, T. & Stolz, J. (2000). *Am. Mineral.* **85**, 1465–1473.
Lifshitz, I. M. (1952). *Zh. Eks. Teor. Fiz.* **22**, 475–486.
Lock, N., Wu, Y., Christensen, M., Cameron, L. J., Peterson, V. K., Bridgeman, A. J., Kepert, C. J. & Iversen, B. B. (2010). *J. Phys. Chem. C*, **114**, 16181–16186.
Marmier, A., Lethbridge, Z. A. D., Walton, R. I., Smith, C. W., Parker, S. C. & Evans, K. E. (2010). *Comput. Phys. Commun.* **181**, 2102–2115.
McConnell, J. D. C., McCammon, C. A., Angel, R. J. & Seifert, F. (2000). *Z. Kristallogr.* **215**, 669–677.
McGrane, S. D., Grieco, A., Ramos, K. J., Hooks, D. E. & Moore, D. S. (2009). *J. Appl. Phys.* **105**, 073505.
Moré, J. J., Sorensen, D. C., Hillstrom, K. E. & Garbow, B. S. (1984). *Sources and Development of Mathematical Software*, edited by W. J. Cowell, pp. 88–111. Englewood Cliffs: Prentice Hall.
Mulfort, K. L., Farha, O. K., Malliakas, C. D., Kanatzidis, M. G. & Hupp, J. T. (2010). *Chem. Eur. J.* **16**, 276–281.
Munn, R. W. (1972). *J. Phys. C*, **5**, 535–542.
Nye, J. F. (1957). *Physical Properties of Crystals.* Oxford University Press.
Ohashi, Y. (1982). *Comparative Crystal Chemistry*, edited by R. M. Hazen & L. W. Finger, pp. 92–102. New York: Wiley.
Ramaswamy, A. L., Shin, H., Armstrong, R. W., Lee, C. H. & Sharma, J. (1996). *J. Mater. Sci.* **31**, 6035–6042.
Rath, S. (2002). PhD thesis, ETH Zürich, Switzerland.
Rath, S., Kunz, M. & Miletich, R. (2003). *Am. Mineral.* **88**, 293–300.
Salje, E., Schmidt, C. & Bismayer, U. (1993). *Phys. Chem. Miner.* **19**, 502–506.
Sata, N., Shen, G., Rivers, M. & Sutton, S. (2002). *Phys. Rev. B*, **65**, 104114.
Schlenker, J. L., Gibbs, G. V. & Boisen, M. B. (1978). *Acta Cryst.* A**34**, 52–54.
Serre, C., Millange, F., Thouvenot, C., Noguès, M., Marsolier, G., Louër, D. & Férey, G. (2002). *J. Am. Chem. Soc.* **124**, 13519–13526.
Shirane, G., Frazer, B. C., Minkiewicz, V. J. & Leake, J. A. (1967). *Phys. Rev. Lett.* **19**, 234–235.
Taylor, R. & Kennard, O. (1986). *Acta Cryst.* B**42**, 112–120.
Vershinin, A. D., Selivanov, E. N., Gulyaeva, R. I. & Sel'menskikh, N. I. (2005). *Inorg. Mater.* **41**, 882–887.
Walton, R. I., Munn, A. S., Guillou, N. & Millange, F. (2011). *Chem. Eur. J.* **17**, 7069–7079.
Wu, Y., Kobayashi, A., Halder, G. J., Peterson, V. K., Chapman, K. W., Lock, N., Southon, P. D. & Kepert, C. J. (2008). *Angew. Chem. Int. Ed.* **47**, 8929–8932.
Xiao, B., Byrne, P. J., Wheatley, P. S., Wragg, D. S., Zhao, X., Fletcher, A. J., Thomas, K. M., Peters, L., Evans, J. S., Warren, J. E., Zhou, W. & Morris, R. E. (2009). *Nat. Chem.* **1**, 289–294.
Zhang, M., Salje, E. & Bismayer, U. (1997). *Am. Mineral.* **82**, 30–35.
Zotov, N. (1990). *Acta Cryst.* A**46**, 627–628.

C2 Negative area compressibility in silver(I) tricyanomethanide

The second paper, Section C2 describes the variable pressure behaviour of silver (I) tricyanomethanide (Ag(tcm)), and reports the first example of a crystal that displays negative area compressibility (*i.e.* a material with negative hydrostatic compressibilities in two orthogonal directions). This paper is the culmination of work carried out by two Part II students in the Goodwin Group, Sarah Hodgson and Sarah Hunt. My contribution to this paper was helping to analyse the variable pressure diffraction data collected on this sample.

ChemComm

COMMUNICATION

View Article Online
View Journal | View Issue

Open Access Article. Published on 09 December 2013. Downloaded on 25/08/2014 13:27:25.
This article is licensed under a Creative Commons Attribution 3.0 Unported Licence.

Negative area compressibility in silver(I) tricyanomethanide†

Cite this: *Chem. Commun.*, 2014, **50**, 5264

Received 13th September 2013,
Accepted 9th December 2013

DOI: 10.1039/c3cc47032f

www.rsc.org/chemcomm

Sarah A. Hodgson,[a] Jasper Adamson,[a] Sarah J. Hunt,[a] Matthew J. Cliffe,[a] Andrew B. Cairns,[a] Amber L. Thompson,[a] Matthew G. Tucker,[bc] Nicholas P. Funnell[a] and Andrew L. Goodwin*[a]

The molecular framework Ag(tcm) (tcm$^-$ = tricyanomethanide) expands continuously in two orthogonal directions under hydrostatic compression. The first of its kind, this negative area compressibility behaviour arises from the flattening of honeycomb-like layers during rapid pressure-driven collapse of the interlayer separation.

In the absence of a structural phase transition, it is a thermodynamic requirement that a system reduce its volume under hydrostatic pressure.[1] The phenomenon of negative compressibility is the counterintuitive effect whereby this volume reduction couples to an expansion of the material in at least one linear dimension.[2] Examples of such behaviour are rare even amongst anisotropic materials because buckling and bond compression mechanisms are almost always more effective at reducing crystal volume than is uniaxial or biaxial lattice expansion. Not only does the existence of negative compressibility challenge our understanding of the ways in which materials can respond to external stimuli, but the phenomenon is also of practical importance. It promises a means of developing artificial muscles, nanoscale actuators and high-performance pressure sensors for sonar and altitude measurements.[2,3] In principle, the most extreme such response allowed thermodynamically is that of negative area compressibility (NAC), whereby a material expands along two orthogonal directions on increasing hydrostatic pressure. The possibility that tetragonal $PbTiO_3$ might show an extremely weak NAC effect has been raised[4] and disputed;[5] similarly weak effects are thought to occur at high pressure in NaV_2O_5 (ref. 6) and are predicted for $TlGaSe_2$.[7] Instead the remarkably few negative compressibility materials that have been characterised unambiguously expand only along one principal axis when compressed hydrostatically (*i.e.*, negative linear compressibility, NLC).[8–12] The distinction between NLC and NAC is more fundamental than magnitude alone: NAC materials increase their surface area under hydrostatic pressure, and so they can be used as substrates to provide order-of-magnitude amplification of piezoelectric response in *e.g.* ferroelectric sensors.[2]

One strategy for identifying negative compressibility candidates is to target framework materials that exhibit anisotropic negative thermal expansion (NTE): a material that shrinks in one direction on heating is likely to expand in that same direction on compression.[13] While there is no requirement that deformation mechanisms under temperature and pressure be identical,[14] there is empirical evidence of such a correspondence amongst molecular framework materials.[8,9,12,15] The natural strategy then for identifying NAC candidates is to investigate framework materials that exhibit area-NTE. It is for this reason that we chose to investigate silver(I) tricyanomethanide, Ag(tcm): its layer-like network topology [Fig. 1(a)] is of a form often associated with area-NTE.[16,17] In this compound, each Ag^+ cation is coordinated by three tcm$^-$ anions in an approximately trigonal arrangement; likewise each tcm$^-$ anion is coordinated by three Ag^+ centres.[18,19] The resulting hexagonal (6,3) topology is sufficiently open that two honeycomb networks interpenetrate within each layer of the crystal structure [Fig. 1(b)]. Adjacent layers interact *via* long Ag···N contacts [d(Ag···N) > 3 Å] that are sufficiently weak that the material behaves essentially as a two-dimensional framework, capable even of intercalation chemistry.[19]

Using single-crystal X-ray diffraction, we first established the thermal expansion behaviour of Ag(tcm) to verify whether or not the material exhibits area-NTE. Because the material crystallises in the orthorhombic (polar) space group *Ima*2,[18] its thermal expansivity is uniquely determined by the relative rate of change of the unit cell lengths with temperature.[17] We observe essentially linear thermal variation in these parameters over the

[a] *Department of Chemistry, University of Oxford, Inorganic Chemistry Laboratory, South Parks Road, Oxford OX1 3QR, UK. E-mail: andrew.goodwin@chem.ox.ac.uk; Fax: +44 (0)1865 274690; Tel: +44 (0)1865 272137*
[b] *ISIS Facility, Rutherford Appleton Laboratory, Chilton, Didcot, OX11 0QX, UK*
[c] *Diamond Light Source, Harwell Campus, Didcot, OX11 0DE, UK*

† Electronic supplementary information (ESI) available: Synthesis; experimental methods; X-ray single-crystal diffraction refinement details (variable-temperature and variable-pressure); neutron powder diffraction refinement details; calculations. CCDC 961474–961482. For ESI and crystallographic data in CIF or other electronic format see DOI: 10.1039/c3cc47032f

This journal is © The Royal Society of Chemistry 2014

Open Access Article. Published on 09 December 2013. Downloaded on 25/08/2014 13:27:25.
This article is licensed under a Creative Commons Attribution 3.0 Unported Licence.

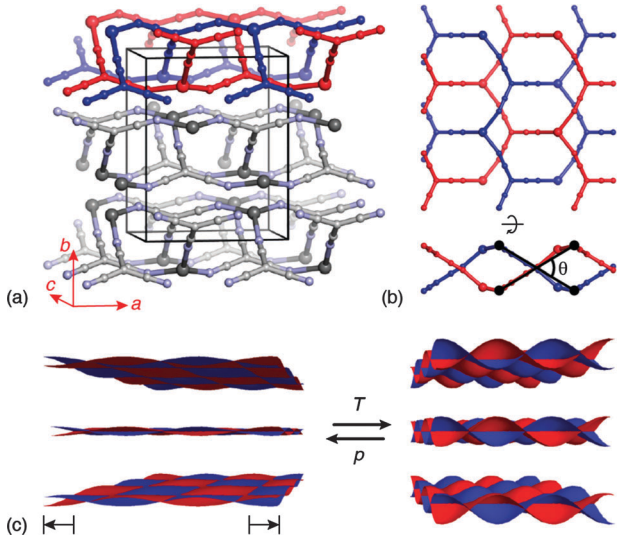

Fig. 1 (a) The crystal structure of Ag(tcm) is composed of stacked, doubly-interpenetrating (6,3)-nets in which both Ag^+ (large spheres) and tcm^- ions (smaller spheres) function as trigonal nodes. (b) The extent of rippling of layers (viewed along *b* and *a* in the top and bottom parts of this panel, respectively) can be quantified by the inter-network angle θ (see ESI†). (c) The generic mechanical response of a layered material links volume expansion to increasing interlayer separation and increasing layer rippling. The cross-sectional area of each layer is maximised by reducing θ, and hence increases during volume reduction under hydrostatic compression.

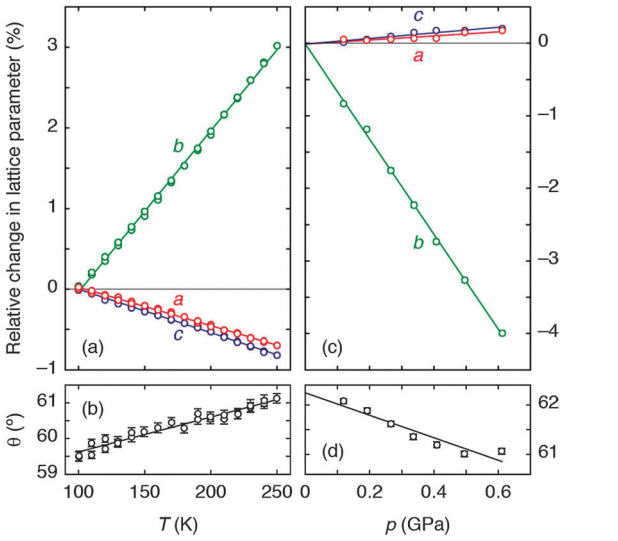

Fig. 2 (a) The thermal variation of lattice parameters, determined using single-crystal X-ray diffraction measurements, is illustrated here for ease of comparison as a % change relative to the extrapolated value at 100 K. Solid lines are weighted linear fits to the data obtained using the program PASCal.[17] (b) The corresponding variation in inter-network angle θ indicates an increase in layer rippling on heating. (c) The pressure dependence of lattice parameters, measured using variable-pressure neutron diffraction, is represented as a % change relative to the extrapolated value at 0 GPa. (d) The corresponding variation in θ now indicates a decrease in layer rippling under compression.

temperature range 100–250 K [Fig. 2(a)], yielding coefficients of thermal expansion of −48(3), +200(2) and −54.0(4) MK^{-1} along the *a*, *b*, and *c* axes, respectively.[17] As is increasingly found to be the case for molecular frameworks,[13,20] the magnitudes of these values are large compared to those obtained for traditional engineering materials, for which one expects linear coefficients of thermal expansion in the vicinity of +20 MK^{-1} (*i.e.*, a 0.2% increase in linear dimension for each 100 K temperature rise).[21] What is clear is that Ag(tcm) does exhibit area-NTE, with an area coefficient of thermal expansion for the (*a*,*c*)-plane, $\alpha_{(010)}$ = −102(3) MK^{-1}, that is the most extreme negative value reported for a layered material. The material undergoes a 1% reduction in area for each 100 K rise in temperature—more than an order of magnitude larger than the corresponding values for area-NTE systems such as graphite and $Ni(CN)_2$ (α_A = −2.4 and −13 MK^{-1}, respectively).[17,22,23]

The microscopic mechanism responsible for this behaviour can be deduced from the variation in framework geometry during heating. The established model of area-NTE in layered materials predicts coupling between NTE and the extent of layer 'rippling', as quantified by the inter-network torsion angle θ [Fig. 1(b and c)].[16] Our measurements indeed indicate an increase in θ with temperature [Fig. 2(b)].[24] Using simple geometric arguments, the temperature dependence of θ can be used to estimate the value of α_A attributable to layer rippling:

$$\alpha_A^{\mathrm{calc}} = -\theta \tan\left(\frac{\theta}{2}\right)\alpha_\theta, \qquad (1)$$

where $\alpha_\theta = \mathrm{d}(\ln\theta)/\mathrm{d}T$ (see ESI† for derivation). Our data give α_A^{calc} = −101 MK^{-1}, which is within experimental error of the observed value of −102(3) MK^{-1}. Consequently, we can be confident that the mechanism illustrated in Fig. 1(c) is responsible for area-NTE in Ag(tcm).

In order to determine whether or not Ag(tcm) exhibits the target property of NAC, we performed a series of neutron diffraction measurements across the pressure range $0 < p < 2$ GPa using the PEARL instrument at ISIS. The use of neutron radiation maximises the scattering sensitivity to C/N atoms in the presence of Ag atoms, which is all the more important for measurements performed in the high-background sample environments required for variable-pressure experiments. We found that, for powdered samples, the ambient phase is stable up to 0.615(6) GPa, but by 0.672(7) GPa it has transformed reversibly to a related phase with symmetry not higher than monoclinic. The same transformation occurs at higher pressures ($0.83 < p_c < 1.47$ GPa) in single-crystal experiments (see ESI† for further discussion); our focus here is on the pressure-dependent behaviour of the ambient phase rather than the nature of the phase transition or the high-pressure phase. Rietveld refinement against the corresponding neutron diffraction patterns revealed the anticipated increase in *a* and *c* parameters [Fig. 2(c)], with the anomalous expansion of the material in these directions being allowed by a much more rapid decrease in the interlayer spacing (given by the lattice parameter *b*). Our variable-pressure lattice parameter data can be converted into compressibilities using the relationship $K_\ell = -[\partial(\ln \ell)/\partial p]_T$, from which we obtain K_a = −3.5(6) TPa^{-1}, K_b = +66(20) TPa^{-1}, and K_c = −4.0(6) TPa^{-1}. Consequently, the compressibility is negative everywhere within the (*a*,*c*)-plane, with the magnitude

Open Access Article. Published on 09 December 2013. Downloaded on 25/08/2014 13:27:25.
This article is licensed under a Creative Commons Attribution 3.0 Unported Licence.

of NAC quantified by the corresponding area compressibility $K_{(010)} = K_a + K_c = -7.5(8)$ TPa^{-1}.

Conventional engineering materials (*e.g.* iron) have linear compressibilities $K \sim 5$ TPa^{-1} that correspond to a decrease of *ca.* 0.5% in length for each 1 GPa pressure increase;[25] consequently, the NAC behaviour of Ag(tcm) is essentially as strong as the positive area compressibility of these 'normal' phases. Moreover, despite the fact that the orthorhombic symmetry of Ag(tcm) allows for different behaviour in the *a* and *c* directions, we find that both its compressibility and its thermal expansivity are essentially isotropic within the entire (*a*,*c*) plane. Isotropy is important for NAC applications because it avoids composite warping and performance breakdown.[2]

That NAC is driven by the same layer-rippling mechanism as area-NTE is evident in the variation of the parameter θ with increasing pressure [Fig. 2(d)]. The volume reduction accommodated by rapid collapse of the interlayer spacing (note $K_b \gg 5$ TPa^{-1}) evidently couples with a reduction in the degree of layer rippling: $d\theta/dp < 0$. To substantiate further our interpretation of the NAC mechanism, we recast eqn (1) in terms of compressibilities; our refined values of θ give $K_A^{calc} = -\theta \tan(\theta/2) K_\theta = -26$ TPa^{-1}. That the measured area compressibility $K_{(010)} = -7.5(8)$ TPa^{-1} is somewhat smaller in magnitude reflects the expected $\sim$10 TPa^{-1} contribution from (positive) bond compressibilities omitted from the geometric formalism of eqn (1), as discussed elsewhere for NLC materials.[13] Indeed, that the p/T correspondence inferred in Fig. 1(c) holds qualitatively for Ag(tcm) is immediately evident in the close relationship between the temperature- and pressure-induced lattice parameter and layer rippling parameter variations documented in Fig. 2.

In conclusion, we find that silver(I) tricyanomethanide exhibits NAC over the pressure range $0 < p < 0.615$ GPa with an essentially isotropic area compressibility of similar magnitude (but opposite sign) to that of established engineering materials. From a structural viewpoint, the phenomenon can be understood in terms of pressure-driven damping of layer 'rippling', acting to increase the layer cross-sectional area at larger hydrostatic pressures. Variable-pressure spectroscopic measurements may provide valuable additional insight into the subtle variations in bonding interactions that occur throughout this process.[26] In favour of immediate application of Ag(tcm) in ultra-high-precision sensing devices are (i) the ease with which large single-crystal samples can be prepared under ambient conditions and using readily-available solvents, and (ii) its optical transparency. Moreover, the polarity of its crystal structure offers the possibility of designing multifunctional devices based on Ag(tcm) in which the interplay between responses to electric field, temperature, and pressure are exploited to produce piezoelectric and thermoelectric devices.

The authors gratefully acknowledge financial support from the E.P.S.R.C. (EP/G004528/2) and the E.R.C. (Grant Ref.: 279705), the provision of neutron beamtime on the PEARL instrument at ISIS, and the assistance of Dr Marek Jura (ISIS).

References

1 Z. G. Nicolaou and A. E. Motter, *Nat. Mater.*, 2012, **11**, 608–613.
2 R. H. Baughman, S. Stafström, C. Cui and S. O. Dantas, *Science*, 1998, **279**, 1522–1524.
3 A. E. Aliev, J. Oh, M. E. Kozlov, A. A. Kuznetsov, S. Fang, A. F. Fonseca, R. Ovalle, M. D. Lima, M. H. Haque, Y. N. Gartstein, M. Zhang, A. A. Zakhidov and R. H. Baughman, *Science*, 2009, **323**, 1575–1578.
4 R. J. Nelmes and A. Katrusiak, *J. Phys. C: Solid State Phys.*, 1986, **19**, L725–L730.
5 A. Sani, M. Hanfland and D. Levy, *J. Phys.: Condens. Matter*, 2002, **14**, 10601–10604.
6 I. Loa, K. Syassen, R. K. Kremer, U. Schwarz and M. Hanfland, *Phys. Rev. B*, 1999, **60**, R6945–R6948.
7 M. Y. Seyidov and R. A. Suleymanov, *J. Appl. Phys.*, 2010, **108**, 063540.
8 A. L. Goodwin, D. A. Keen and M. G. Tucker, *Proc. Natl. Acad. Sci. U. S. A.*, 2008, **105**, 18708–18713.
9 W. Li, M. R. Probert, M. Kosa, T. D. Bennett, A. Thirumurugan, R. P. Burwood, M. Parinello, J. A. K. Howard and A. K. Cheetham, *J. Am. Chem. Soc.*, 2012, **134**, 11940–11943.
10 H. J. Shepherd, T. Palamarciuc, P. Rosa, P. Guionneau, G. Molnár, J.-F. Létard and A. Bousseksou, *Angew. Chem., Int. Ed.*, 2012, **51**, 3910–3914.
11 A. B. Cairns, J. Catafesta, C. Levelut, J. Rouquette, A. van der Lee, L. Peters, A. L. Thompson, V. Dmitriev, J. Haines and A. L. Goodwin, *Nat. Mater.*, 2013, **12**, 212–216.
12 A. D. Fortes, E. Suard and K. S. Knight, *Science*, 2011, **331**, 742–745.
13 J. M. Ogborn, I. E. Collings, S. A. Moggach, A. L. Thompson and A. L. Goodwin, *Chem. Sci.*, 2012, **3**, 3011–3017.
14 R. W. Munn, *J. Phys. C: Solid State Phys.*, 1972, **5**, 535–542.
15 A. B. Cairns, A. L. Thompson, M. G. Tucker, J. Haines and A. L. Goodwin, *J. Am. Chem. Soc.*, 2012, **134**, 4454–4456.
16 I. M. Lifshits, *Zh. Eksp. Teor. Fiz.*, 1952, **22**, 475–486.
17 M. J. Cliffe and A. L. Goodwin, *J. Appl. Crystallogr.*, 2012, **45**, 1321–1329.
18 J. Konnert and D. Britton, *Inorg. Chem.*, 1966, **5**, 1193–1196.
19 S. R. Batten, B. F. Hoskins and R. Robson, *New J. Chem.*, 1998, **22**, 173–175.
20 A. L. Goodwin, M. Calleja, M. J. Conterio, M. T. Dove, J. S. O. Evans, D. A. Keen, L. Peters and M. G. Tucker, *Science*, 2008, **319**, 794–797.
21 R. E. Newnham, *Properties of Materials*, Oxford University Press, Oxford, 2005.
22 A. C. Bailey and B. Yates, *J. Appl. Phys.*, 1970, **41**, 5088–5091.
23 S. J. Hibble, A. M. Chippindale, A. H. Pohl and A. C. Hannon, *Angew. Chem., Int. Ed.*, 2007, **46**, 7116–7118.
24 P. Betteridge, J. Carruthers, R. Cooper, K. Prout and D. Watkin, *J. Appl. Crystallogr.*, 2003, **36**, 1487.
25 H. L. Zhang, S. Lu, M. P. J. Punkkinen, Q.-M. Hu, B. Johannson and L. Vitos, *Phys. Rev. B*, 2010, **82**, 132409.
26 K. Kamali, C. Ravi, T. R. Ravindran, R. M. Sarguna, T. N. Sairam and G. Kaur, *J. Phys. Chem. C*, 2013, **117**, 25704–25713.

 This journal is © The Royal Society of Chemistry 2014

C3 Flexibility transition and guest-driven reconstruction in a ferroelastic metal–organic framework

The final paper, Section C3 reports the synthesis of two new MOFs, copper (I) tricyanomethanide (Cu(tcm)) and its acetonitrile solvate (Cu(tcm)MeCN), and their unusual flexibility. Cu(tcm) has an unusual three-fold interpenetrated structure, each network with the (10,3)-b topology, which undergoes a ferroelastic phase transition at 240 K to a lower symmetry distorted structure. This lower symmetry structure is much more flexible, with the largest known coefficients of both negative and positive thermal expansion in a crystal ($\alpha_a = +591(28)$ MK^{-1} and $\alpha_b = -407(28)$ MK^{-1} over the range 20–240 K). Cu(tcm) can also reversibly uptake MeCN vapour, transforming to form the layered Cu(tcm)MeCN. The foundation of this paper is work carried out by a Part II student in the Goodwin Group, Sarah Hunt. My primary contribution to this work was analysing the powder diffraction data, including solving the structure of Cu(tcm).

CrystEngComm

PAPER

View Article Online
View Journal

CrossMark click for updates

Cite this: DOI: 10.1039/c4ce01572j

Flexibility transition and guest-driven reconstruction in a ferroelastic metal–organic framework†

Sarah J. Hunt, Matthew J. Cliffe, Joshua A. Hill, Andrew B. Cairns, Nicholas P. Funnell and Andrew L. Goodwin*

Received 29th July 2014,
Accepted 1st October 2014

DOI: 10.1039/c4ce01572j

www.rsc.org/crystengcomm

The metal–organic framework copper(I) tricyanomethanide, Cu(tcm), undergoes a ferroelastic transition on cooling below T_f = 240 K. Thermal expansion measurements reveal an order-of-magnitude variation in framework flexibility across T_f. The low-temperature phase α-Cu(tcm) exhibits colossal positive and negative thermal expansion that is the strongest ever reported for a framework material. On exposure to acetonitrile, Cu(tcm) undergoes a reconstructive solid-phase transition to acetonitrilocopper(I) tricyanomethanide. This transition can be reversed by heating under vacuum. Infrared spectroscopy measurements are sensitive to the phase change, suggesting that Cu(tcm) may find application in solid-phase acetonitrile sensing.

Open Access Article. Published on 02 October 2014. Downloaded on 25/11/2014 17:48:20.
This article is licensed under a Creative Commons Attribution 3.0 Unported Licence.

1. Introduction

Framework materials with the wine-rack topology have emerged as an important class of materials because their characteristic low-energy 'breathing' mode allows for extreme mechanical responses to external stimuli.[1–3] Examples include sorption- and temperature-driven breathing in the so-called MIL family of metal–organic frameworks (MOFs),[4,5] and colossal positive/negative thermal expansion (PTE/NTE) and negative linear compressibility (NLC) in the transition-metal dicyanometallates.[6–8] In all cases framework breathing couples expansion in one direction to contraction in a perpendicular direction, with the framework angle θ approaching 90° for increased framework volumes [Fig. 1]. While it is usually symmetry-allowed for these systems to adopt arbitrary geometries (*i.e.* values of θ), in some cases the θ = 90° limit actually corresponds to a higher space group symmetry.[9] For this square geometry, framework breathing is symmetry forbidden, resulting in a fundamental increase in rigidity. So the existence of a 'flexibility transition' between low- and high-symmetry geometries would allow wine-rack frameworks to be switched between compliant (low-symmetry, $\theta \neq 90°$) and rigid (high-symmetry, θ = 90°) states.

Such transitions are well established in the field of conventional ceramics, where they are usually discussed in the context of ferroelasticity.[10–13] The magnitude of symmetry-breaking strain ε [= $(b - a)/(a + b)$ for a tetragonal–orthorhombic transition] acts as an order parameter just as magnetisation does for ferromagnets and polarisation for ferroelectrics. In this way, the rigid high-symmetry 'paraelastic' state of Fig. 1 corresponds to ε = 0 and the flexible low-symmetry 'ferroelastic' state to $\varepsilon > 0$. The crucial difference between MOF-type systems and conventional ceramics is that the extreme mechanical flexibilities of the former allow, in principle, for very much larger strains to develop across a ferroelastic

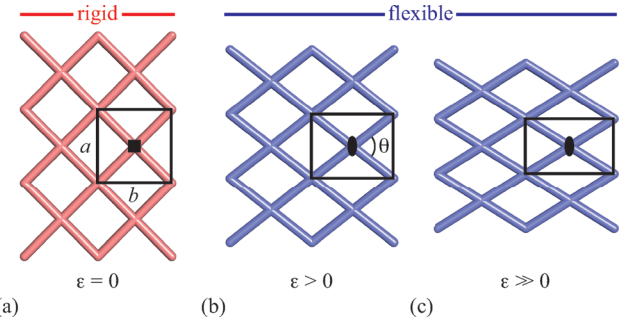

Fig. 1 The dominant low-energy deformation mode of 'wine-rack' framework materials involves 'breathing' *via* changes in the framework angle θ. For the ideal square geometry in (a) this deformation is forbidden by the presence of fourfold rotation axes. Consequently the change in angle from square (a) to rectangular (b) geometries represents a symmetry-breaking ferroelastic phase transition, for which the deviation of the angle θ from 90° is related to the order parameter $\varepsilon = (b - a)/(a + b)$. Breathing of the lower-symmetry rectangular geometry is allowed by the remaining symmetry elements (such as the diads shown here), such that the progression from geometries (b) to (c), for example, is continuous in all respects.

Department of Chemistry, University of Oxford, Inorganic Chemistry Laboratory, South Parks Road, Oxford, OX1 3QR, UK.
E-mail: andrew.goodwin@chem.ox.ac.uk

† Electronic supplementary information (ESI) available: Atomic coordinates and lattice parameter data. CCDC 1016797. For ESI and crystallographic data in CIF or other electronic format see DOI: 10.1039/c4ce01572j

Open Access Article. Published on 02 October 2014. Downloaded on 25/11/2014 17:48:20.
This article is licensed under a Creative Commons Attribution 3.0 Unported Licence.

transition. Consequently the flexibilities of paraelastic and ferroelastic states may be substantially more different for these materials than is the case for conventional inorganics. While there are a handful of very recent studies of ferroelastic transitions in MOFs,[14,15] and indeed switching between 'narrow pore' and 'large pore' states of pillared MOFs might be interpretable in terms of an improper ferroelastic response,[9] there remains a clear need to establish a model system in which ferroelasticity drives a fundamental change in framework flexibility.

Here we show that the previously-unreported framework material copper(I) tricyanomethanide, Cu(tcm), exhibits a ferroelastic transition at a critical temperature T_f = 240 K. Under ambient conditions, this system adopts a tetragonal wine-rack topology, for which breathing is symmetry forbidden. On cooling below 240 K the crystal symmetry lowers to an orthorhombic subgroup, for which breathing is symmetry allowed. Measurement of the coefficients of thermal expansion α allows quantification of the flexibility of both high- and low-temperature phases; we find that values of α within the ferroelastic phase are more than an order of magnitude larger than within the paraelastic phase. In fact the NTE effect we observe, $\alpha = -407(28)$ MK^{-1} ($20 < T < 240$ K), is many times larger than the most extreme sustained NTE behaviour ever reported: $\alpha \simeq -170$ MK^{-1} for FMOF-1,[16] $\alpha = -130$ MK^{-1} for $Ag_3[Co(CN)_6]$,[6] and $\alpha = -80(12)$ MK^{-1} for the pillared zinc/terephthalate MOF of ref. 9. Consequently, T_f signifies not only the emergence of symmetry-breaking strain, but also a fundamental shift in the degree of framework flexibility.

In an attempt to explore the extent to which a similar transition might be brought about by guest uptake, we find that Cu(tcm) is reversibly convertible into a topologically-distinct solvate [Cu(MeCN)(tcm)] upon exposure to acetonitrile. Involving reconstruction between triply-interpenetrating (10,3)-*b* and interdigitated (6,3) nets, this solid–solid transformation highlights the extreme coordinative lability of Cu^+ ions in the parent system. The two frameworks are distinguished not only by their network topology but also by their spectroscopic behaviour, suggesting that Cu(tcm) might find application as a solid-phase acetonitrile sensor.

2. Methods

All reagents were obtained from commercial suppliers and used as received.

2.1. Copper(I) tricyanomethanide

Synthesis of copper(I) tricyanomethanide followed the reduction protocol reported elsewhere for the related binuclear compound bis-(tricyanomethanido)-tetrakis-(triphenylphosphine) dicopper(I).[17] A saturated aqueous solution of copper(II) sulfate (Sigma Aldrich, 99%; 0.3991 g) was reduced by dropwise addition of a concentrated aqueous solution of excess sodium hydrogen sulfite (Sigma Aldrich, 0.3587 g). The resulting mint-green solution was stirred for 30 min, after which time an aqueous solution of a stoichiometric quantity of potassium tricyanomethanide (Alfa Aesar; 0.3229 g) was added dropwise. A fine, off-white precipitate formed immediately. After further stirring for 2 h, the precipitate was filtered, washed with H_2O, and dried under vacuum to afford a polycrystalline sample of copper(I) tricyanomethanide.

Copper(I) tricyanomethanide could also be obtained by heating the acetonitrile complex (see below) under vacuum at 473 K for 12 h.

2.2. Acetonitrilocopper(I) tricyanomethanide

Polycrystalline samples of acetontrilocopper(I) tricyanomethanide were prepared by mixing acetonitrile solutions containing stoichiometric quantities of tetrakis(acetonitrilo)-copper(I) triflate (Sigma Aldrich, 0.9421 g) and potassium tricyanomethanide (Alfa Aesar, 0.3229 g). The reaction mixture was stirred for 2 h and the off-white precipitate filtered and then dried under vacuum to afford acetonitrilocopper(I) tricyanomethanide in quantitative yield.

Single crystal samples of acetonitrilocopper(I) tricyanomethanide could be obtained using slow-diffusion techniques. To separate arms of a glass H-tube were placed chilled acetonitrile solutions of potassium tricyanomethanide (Alfa Aesar, 47.18 mg) and tetrakis(acetonitrilo)copper(I) tetrafluoroborate (Sigma Aldrich, 320.0 mg). Further chilled acetonitrile was then carefully added until the cross-bar was filled. After a period of 14 d, small colourless single crystals suitable for single-crystal X-ray diffraction measurements had formed.

Acetonitrilocopper(I) tricyanomethanide could also be made by exposing dry copper(I) tricyanomethanide to a few drops of acetonitrile and leaving for 12 h, then filtering and drying at 50 °C under vacuum.

2.3. Single-crystal X-ray diffraction

Single-crystal X-ray diffraction data were collected for acetonitrilocopper(I) tricyanomethanide using an Agilent Technologies SuperNova diffractometer (Cu Kα radiation, λ = 1.5418 Å) at 100 K using an Oxford Cryosystems cryostream,[18] scanning about the ω and ϕ circles. The data were integrated and corrected for absorption using CrysAlisPro, the structure was solved in *Pbca* using SIR92 (ref 19) and refined using CRYSTALS.[20] All non-hydrogen atoms were refined anisotropically; hydrogen atom positions were refined against the low angle data, according to the procedure described in ref. 21, and were then constrained to ride on their host atoms. A final *R*-factor of 1.99% was obtained. Crystal structure refinement details are given in Table 1.

2.4. Powder X-ray diffraction

All samples were assessed for crystallinity and purity *via* their X-ray powder diffraction patterns, measured using a Philips PW1730 diffractometer (Cu Kα radiation, λ = 1.541 Å) over the angular (2θ) range 10–70° using a step size of 0.05°. Higher-quality diffraction patterns were collected using a PANalytical X'Pert PRO diffractometer (monochromated Cu Kα_1 radiation, λ = 1.54060 Å) using the same angular range and a step size of 0.008°.

 This journal is © The Royal Society of Chemistry 2014

Open Access Article. Published on 02 October 2014. Downloaded on 25/11/2014 17:48:20.
This article is licensed under a Creative Commons Attribution 3.0 Unported Licence.

Table 1 Single-crystal X-ray diffraction data collection and refinement details for [Cu(MeCN)(tcm)] at T = 100 K

Formula	$CuC_6N_4H_3$
Crystal size (mm)	0.033 × 0.034 × 0.039
Crystal symmetry	Orthorhombic
Space group	*Pbca*
a (Å)	12.9802(3)
b (Å)	8.14490(18)
c (Å)	14.5848(3)
V (Å^3)	1541.94(5)
Z	8
No. of measured reflns.	14 516
No. of independent reflns.	1620
No. of observed rflns. [$I > 2\sigma(I)$]	1480
No. of parameters	100
R_{int}	0.025
R ($I/\sigma > 2.0$)	0.0199
wR	0.0524
$\Delta\rho_{max}$, $\Delta\rho_{min}$ (e Å^{-3})	0.26, −0.29

Variable-temperature powder X-ray diffraction patterns were measured on a Siemens D5000 X-ray diffractometer (Cu Kα radiation, λ = 1.5418 Å) fitted with an Oxford Cryosystems PheniX cryostat. For temperatures below 300 K the copper(I) tricyanomethanide sample was combined with vaseline and then loaded into the sample holder. Data collections were carried out every 10 K on heating from 20 to 290 K. Scans were ~5 h long and were carried out over the angular range $5° < 2\theta < 120°$ using a step size of 0.02°. Four minute intervals between data collections allowed for temperature equilibration of the sample.

All fits to X-ray powder diffraction data were carried out using TOPAS Academic;[22] in general a modified Thompson–Cox–Hastings pseudo-Voigt (TCHZ) peak shape with a simple axial divergence correction was used and the large anisotropic strain found in this system was accounted for by using a Stephens anisotropic peak broadening term.[23] Rietveld refinement of the room and low-temperature (20 K) structures of α- and β-Cu(tcm) were carried out. For the room temperature structure all atom positions were refined with appropriate bond distance (Cu–N, C–N and C–C) and bond angle restraints; the Cu isotropic atomic displacement parameter was refined freely and all atoms within the tcm moiety were constrained to have equal isotropic displacement parameters. A fourth-order spherical harmonic correction was used to account for preferred orientation. At low temperature, the tcm group was refined as a rigid body and all thermal parameters were fixed. Sample environment peaks were identified by their persistence across the α–β transition and were fitted using the Pawley method. Variable-temperature lattice parameters were determined by using sequential (seed-batch) Pawley fits to data in *Fdd*2 and $I4_1md$, where the starting lattice parameters for each temperature were those found for the previous temperature.

2.5. Thermogravimetric analysis

Thermogravimetric measurements were carried out using a Perkin Elmer TGA 7, with Perkin Elmer TAC 7/DX thermal analysis controller, from 30 to 600 °C at a rate of 10 °C min^{-1} under flowing nitrogen.

2.6. Infrared spectroscopy

Infrared spectra were measured using a Bruker Tensor 27 FT-IR spectrometer fitted with an attenuated total reflectance diamond. A small amount of powdered sample was pressed onto the diamond surface and spectra were measured over the range 4000–600 cm^{-1}. Background scans were recorded before each measurement. Absolute transmittance values were normalised to the tricyanomethanide C–N stretch (2200 cm^{-1}) for each measurement.

3. Results and discussion

Copper(I) tricyanomethanide structure

Having prepared a sample of Cu(tcm), its crystal structure was determined using powder X-ray diffraction methods. The ambient-temperature powder X-ray diffraction pattern—shown in Fig. 2(a)—could be indexed according to a tetragonal cell with lattice parameters a = 7.539(2) Å and c = 9.034(3) Å. A Pawley fit confirmed the space group assignment $I4_1md$. Based on the cell metric and space group symmetry, a structural model was proposed in which both Cu atoms and tcm groups were centred on the 4*a* Wyckoff positions, with z = 0

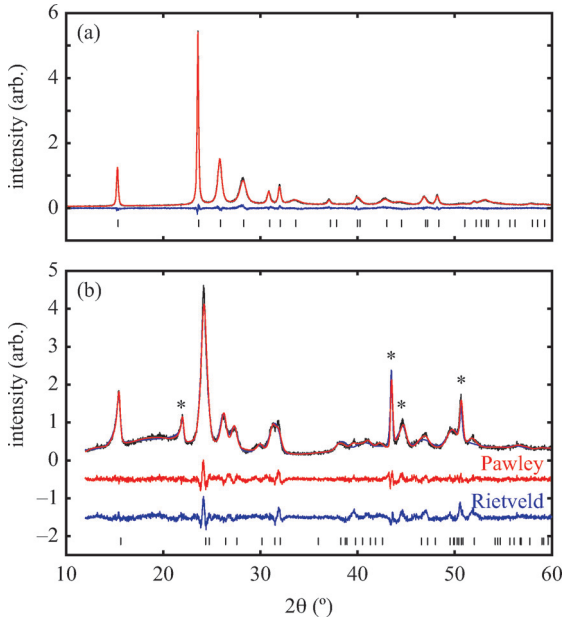

Fig. 2 Powder X-ray diffraction data measured using Cu Kα radiation (black lines), with reflection positions indicated by vertical tick marks. (a) β-Cu(tcm), measured at 298 K; Rietveld fit (red lines), and difference (data – fit, blue lines). (b) α-Cu(tcm), measured at 20 K. Impurity peaks from the low-temperature sample environment are indicated by asterisks; both Pawley (red lines) and Rietveld (blue lines) fit and difference curves are shown, with the latter shifted vertically by 0.5 and 1.5 units. Pawley fits were used to extract thermal lattice parameter variations. The quality of the Rietveld fit is low as a result of severe anisotropic peak broadening and the large number of coupled positional degrees of freedom, but is sufficient to demonstrate the displacive nature of the phase transition.

Open Access Article. Published on 02 October 2014. Downloaded on 25/11/2014 17:48:20.
This article is licensed under a Creative Commons Attribution 3.0 Unported Licence.

for the former and $z \simeq \frac{1}{2}$ for the latter. Using this initial model as a starting point, Rietveld refinement gave a satisfactory fit to data [Fig. 2(a)]. The corresponding atomic coordinates and atomic displacement parameters are given in Table 2, and the crystal structure is illustrated in Fig. 3(a–c). In this structure, both Cu^+ and tcm^- ions are three-coordinate and connect to form a three-dimensional network with the (10,3)-*b* topology (Schläfli symbol 10^3). This network is sufficiently open that three such nets interpenetrate to give a structure related to that of the MOF Δ-[Cr(Hbiim)(H_2biim$_2$)]SO_4·H_2O (biim = biimidazole).[24,25]

The established structural chemistry of copper(I) tricyanomethanides is limited to ternary and quaternary systems of the form [Cu(tcm)(N-donor)]·{guest}.[26] This is perhaps surprising, given that the analogous silver(I) complex Ag(tcm) has been known for some time.[27] The stronger preference for tetrahedral coordination over trigonal coordination for Cu^+ relative to Ag^+ may be an important factor at play in determining the different accessibilities of these two phases. It now seems that both Cu(tcm) and Ag(tcm) adopt polar crystal structures based on three-coordinate M(I)/tcm geometries, but in contrast to the three-dimensional topology of Cu(tcm) the structure of Ag(tcm) is described by stacked, pairwise-interwoven (6,3)-net layers.[27,28] Despite our reliance here on powder diffraction methods for structure solution and refinement, the relatively small number of structural parameters and the good quality of fit-to-data give us confidence in the structural model we have determined for Cu(tcm). There is no risk of confusion with the Ag(tcm) structure, which would predict a very different powder diffraction pattern to that observed in our measurements. For completeness, we note that the Cu–N bond lengths and N–Cu–N bond angles we obtain (d(Cu–N) = 2.025, 2.036 Å; ∠(N–Cu–N) = 122.8, 114.5°) are fully consistent with the values reported elsewhere for [Cu(tcm)(hmt)], [Cu(tcm)(bipy)], and [Cu(tcm)(bpe)]·0.25bpe·0.5MeCN (hmt = hexamethylenetetramine; bipy = 4,4'-bipyridine; bpe = 1,2-bis(4-pyridyl)ethene): 1.92 < d(Cu–N) <2.22 Å and 103.3< ∠N–Cu–N <129.8°.[26] Good consistency is of course expected given our use of soft Cu–N bond length restraints.

Variable-temperature behaviour

Powder X-ray diffraction patterns collected over the temperature range 20 < T < 290 K reveal a second-order phase transition near T_f = 240 K that involves splitting of a number of diffraction peaks in a manner consistent with a reduction from tetragonal to orthorhombic symmetry [Fig. 4(a)]. There are two maximal subgroups of $I4_1md$ with orthorhombic symmetry: namely, *Fdd*2 and *Imm*2. The reflection conditions differ between these two cases, and we found that our data were consistent only with the former. Making use of the appropriate cell transform

$$\begin{bmatrix}\mathbf{a}\\ \mathbf{b}\\ \mathbf{c}\end{bmatrix}_{Fdd2} = \begin{bmatrix}1 & 1 & 0\\ -1 & 1 & 0\\ 0 & 0 & 1\end{bmatrix}\begin{bmatrix}\mathbf{a}\\ \mathbf{b}\\ \mathbf{c}\end{bmatrix}_{I4_1md}, \quad (1)$$

Table 2 Structural parameters for β-Cu(tcm) as determined by Rietveld refinement against powder X-ray diffraction data collected at 298 K. Space group: $I4_1md$. Lattice parameters: a = 7.5510(4) Å, c = 9.0436(5) Å

Atom	x	y	z	B_{iso} (Å^2)
Cu	0	0	0	4.30(7)
C1	0	0	0.4873(7)	1.44(9)
C2	0	0	0.3554(7)	1.44(9)
C3	0.1560(4)	0	0.56396(25)	1.44(9)
N1	0	0	0.2267(8)	1.44(9)
N2	0.2727(6)	0	0.6277(4)	1.44(9)

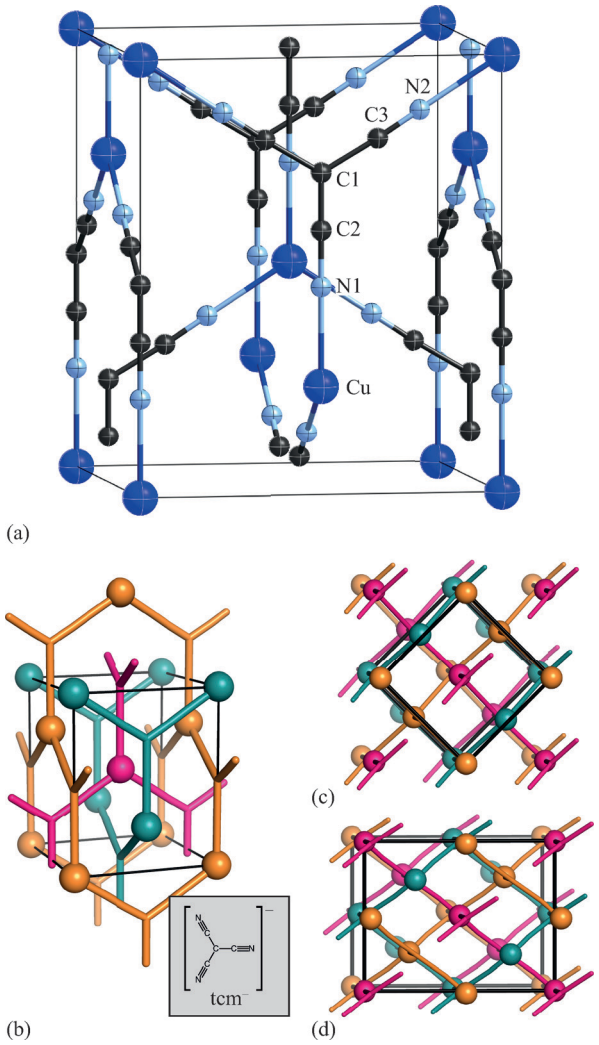

Fig. 3 (a) Representation of the crystal structure of β-Cu(tcm), viewed with the tetragonal *c* axis oriented vertically. Thermal ellipsoids are represented at 50% probability. (b) Topological representation of the same framework, where Cu atoms are shown as large spheres, tcm moieties in stick representation, and the unit cell in black. The three mutually-interpenetrating (10,3)-*b* frameworks are coloured differently. The inset shows the chemical structure of the tricyanomethanide anion. (c) The same framework, viewed slightly away from *c*, illustrating its square wine-rack geometry with θ = 90°. (d) The low-temperature α-Cu(tcm) phase—shown here in terms of the structural model determined using powder X-ray diffraction data collected at 20 K—has the same network connectivity, but the loss of tetragonal symmetry allows θ to deviate from 90°. The *Fdd*2 unit cell, shown here in black, has twice the volume of the $I4_1md$ cell of β-Cu(tcm).

This journal is © The Royal Society of Chemistry 2014

Open Access Article. Published on 02 October 2014. Downloaded on 25/11/2014 17:48:20.
This article is licensed under a Creative Commons Attribution 3.0 Unported Licence.

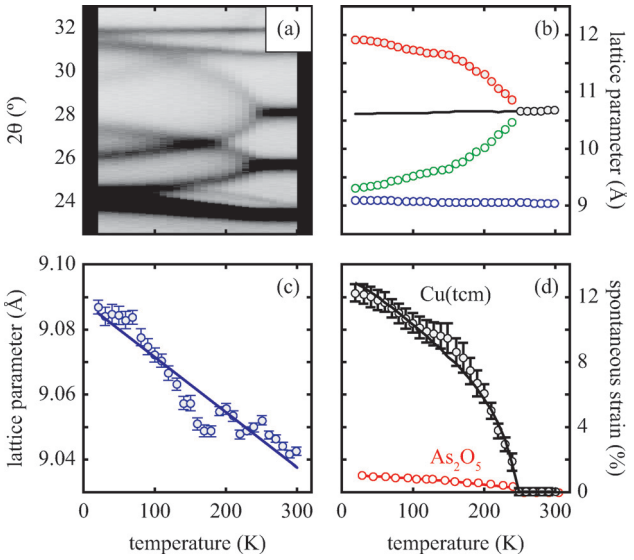

Fig. 4 (a) Thermal variation in the X-ray powder diffraction pattern of Cu(tcm), shown here over a 2θ range that illustrates the large splitting of certain peaks at T_f = 240 K. (b) The corresponding thermal variation in lattice parameters. The parameters *a* and *b* are given by green and red circles, respectively, for the orthorhombic phase and black circles for the tetragonal phase; the *c* parameter is given by blue circles for both phases. Uncertainties are smaller than the symbols. The black line represents the mean value $\frac{1}{2}(a + b)$ for α-Cu(tcm). (c) The approximately-linear thermal variation of the *c* lattice parameter, as shown in (b) but given here on an expanded scale. (d) Thermal variation of the spontaneous strain as defined in eqn (2); the corresponding fit of form $\kappa |T - T_f|^{\frac{1}{2}}$ is shown as a solid line. The strain observed for the "conventional" ferroelastic transition of As_2O_5 is shown in red, where the temperature scale has been shifted by 345 K in order to match transition temperatures.[30]

we obtained an approximate structural model for the low-temperature phase, from which Rietveld refinement was possible. The Rietveld fit obtained using data collected at 20 K is shown in Fig. 2(b). The quality of fit is satisfactory, though we note that severe anisotropic peak broadening associated with large lattice strains and also the experimental constraints of measuring diffraction data at 20 K have both degraded the fit relative to that achieved for data collected under ambient conditions. Because of the presence of anisotropic peak broadening, we have not explored the possibility of further symmetry lowering beyond *Fdd*2; nevertheless, any additional symmetry-lowering distortions—if present—must be very much weaker than the orthorhombic strain itself, which dominates the phase transition behaviour at T_f. Moreover, because the low-angle peak intensities are well accounted for by the Rietveld model, we can be confident that the transition is displacive (*i.e.*, the framework connectivity is maintained). The transition from $I4_1md$ to *Fdd*2 is a ferroelastic transition associated with softening of the Γ_3 zone-centre mode.[29] The corresponding spontaneous strain

$$\varepsilon = \frac{b - a}{a + b} \quad (2)$$

is expected on the basis of Landau theory to vary as $|T - T_f|^{\frac{1}{2}}$ near T_f (*i.e.*, the transition should be second order). Experimental values of ε determined from our lattice parameter data are shown in Fig. 4(d) and are consistent with this expected temperature dependence, indicating that this is a proper (*i.e.* strain-driven) ferroelastic transition.[13,30] A combination of spectroscopic measurements and lattice dynamical modelling would help determine the microscopic driving force for Γ_3 mode softening. Here we note only that this mode allows tilting of the tcm units about an axis parallel to *c*, which has the effect of reducing slightly the distance between tcm groups of one framework and Cu^+ centres of the other two interpenetrated frameworks. Consequently, at low temperatures there may be a small electrostatic driving force for symmetry lowering that is overcome by the increased vibrational entropy of the $I4_1md$ geometry only for temperatures above T_f.

The atomic coordinates and atomic displacement parameters determined from our Rietveld refinement for the low-temperature phase are given in Table 3, and the crystal structure itself is illustrated in Fig. 3(d). From this structural model it is clear that the framework connectivity is entirely preserved across T_f. The single most important difference between high- and low-temperature phases of Cu(tcm) is the framework angle θ: in the former it is identically equal to 90° whereas in the latter it is reduced to $\theta = 2\tan^{-1}\left(\frac{a}{b}\right) = 76°$ at 20 K. Noting the parallel to symmetry-breaking transitions in various well-known framework silicates such as cristobalite and quartz, we borrow from the terminology of that field and denote the high-temperature phase as β-Cu(tcm) and the low-temperature phase as α-Cu(tcm).

Access to variable-temperature diffraction data allows us to explore the mechanical flexibility of both α- and β-Cu(tcm) in terms of their linear coefficients of thermal expansion, and so to determine whether the intuitive picture developed in Fig. 1 does indeed hold in practice. For β-Cu(tcm) there are two independent coefficients of thermal expansion, corresponding to the behaviour parallel and perpendicular to the tetragonal *c* axis:

$$\alpha_a = \left(\frac{\mathrm{d}a}{a\,\mathrm{d}T}\right)_p \quad (3)$$

Table 3 Structural parameters for α-Cu(tcm) as determined by Rietveld refinement against powder X-ray diffraction data collected at 20 K. Space group: *Fdd*2. Lattice parameters: *a* = 9.297(5) Å, *b* = 11.891(5) Å, *c* = 9.093(5) Å. All displacement parameters were fixed at B_{iso} = 2 Å^2

Atom	*x*	*y*	*z*
Cu	0	0	0
C1	0	0	0.503(3)
C2	0	0	0.350(3)
C3	−0.075(4)	0.082(5)	0.579(3)
N1	0	0	0.229(3)
N2	−0.136(5)	0.149(6)	0.641(3)

Open Access Article. Published on 02 October 2014. Downloaded on 25/11/2014 17:48:20.
This article is licensed under a Creative Commons Attribution 3.0 Unported Licence.

$$\alpha_c = \left(\frac{\mathrm{d}c}{c\,\mathrm{d}T} \right)_p \quad (4)$$

Our data give α_a = +10.8(23) MK^{-1} and α_c =−21(4) MK^{-1},[31] which—although anomalous in sign and magnitude for conventional framework materials ($a \simeq 10$ MK^{-1})—are comparable to the values obtained for many MOFs.[32–36] In such systems the low energies of transverse vibrational modes tend to favour NTE, which then often drives anomalously large PTE in other crystal directions.[32] Within the low-temperature α-Cu(tcm) phase, the behaviour along *c* is essentially unchanged: here we find α_c = −13.6(11) MK^{-1} over the temperature range 20–240 K [Fig. 4(c)]. In contrast, the behaviour along the *a* and *b* axes is fundamentally different from that observed in β-Cu(tcm) because these are the axes affected by changes in the framework angle θ. Linear fits to our data over the same temperature range 20–240 K give α_a = +591(28) MK^{-1} and α_b = −407(28) MK^{-1}. There is clearly a drastic increase in thermal expansivity—and hence framework flexibility—on cooling below T_f, justifying our characterisation of the α/β-phase transition as a 'flexibility transition' in Cu(tcm).

The extraordinarily large coefficients of thermal expansion observed here for α-Cu(tcm) deserve further comment because they exceed even the threshold for so-called 'colossal' NTE and PTE ($|\alpha|$ = 100 MK^{-1}).[6] Examples of colossal thermal expansion remain extremely rare, even amongst MOFs. Until recently, 'FMOF-1' exhibited the strongest known thermal expansion behaviour: its coefficients of thermal expansion are α_a = +230 MK^{-1} and α_c = −170 MK^{-1}.[16] More extreme PTE has since been observed in the zinc terephthalate-based MOFs of ref. 9 for which α_b = +340(35) MK^{-1} over the temperature range 303–463 K.[31,37] Yet the response we see here for α-Cu(tcm) is larger again by some margin; in particular, the uniaxial NTE along *b* is so extreme that an aligned composite containing just 2.5% Cu(tcm) would be sufficient to counteract the PTE effect of conventional engineering materials. Moreover, the temperature range over which this NTE occurs (20–240 K)—perhaps problematic for some applications—is nonetheless relevant to industries such as aerospace.

But why is α-Cu(tcm) so very flexible? Empirically it is found that framework flexibility tends to scale inversely with metal–ligand interaction strength.[32,38,39] Here, the low charge densities of Cu$^+$ and of the terminal N atoms of the tcm$^-$ ion[40] will reduce any electrostatic contribution to the thermodynamic cost of framework flexing. Furthermore the combination of a closed-shell d^{10} configuration together with low Cu 3d–tcm π^* overlap will mean that (directional) covalent effects are also much smaller than in many other MOFs. Consequently, the mechanical properties of this system would be expected to be especially sensitive to low-energy interactions such as dispersion forces, which are well-known to drive extreme thermal expansion in other framework materials.[6] Quantum mechanical calculations would help understand more fully the origin of this extreme mechanical flexibility.[4,5,41]

Solvent-induced reorganisation

Exposure of a polycrystalline sample of Cu(tcm) to acetonitrile gave rise to a new phase with a powder diffraction profile quite distinct from that of either α- or β-Cu(tcm). TGA measurements of this phase revealed a mass loss of 19% at 400 K, which suggests the formulation [Cu(MeCN)(tcm)] (expected mass loss 21%) [Fig. 5(a)]. We found that single-crystal samples could in fact be obtained directly from acetonitrile solution, which allowed us to determine the crystal structure using single-crystal X-ray diffraction methods. Our structure solution is illustrated in Fig. 6(a), confirming the formulation [Cu(MeCN)(tcm)]; key structural parameters are given as ESI.† In this structure, the Cu$^+$ ions now have tetrahedral coordination, with one coordination site occupied by a MeCN group; the tcm$^-$ ion remains trigonal in its coordination. From a topological perspective, both Cu and tcm components are effectively three-coordinate, connecting to form (6,3) honeycomb layers (Schläfli symbol 6^3). These layers stack without interpenetration, in contrast to the related acetonitrile derivative [Ag(MeCN)(tcm)] reported elsewhere [Fig. 6(b–c)].[42]

Of greatest relevance to this study is the clear difference in connectivity between the structures of Cu(tcm) and [Cu(MeCN)(tcm)]. Generation of the latter by exposure of the former to acetonitrile must proceed by concerted cleavage and reconstruction of Cu–tcm bonds, which in itself demonstrates a remarkable coordinative flexibility of the original framework. The closed-shell d^{10} electronic configuration of Cu$^+$ facilitates bond cleavage, and allows the formation of network structures with coordination numbers between two and four.[43,44] Moreover, this interconversion process is reversible: powder samples of [Cu(MeCN)(tcm)]—themselves prepared by exposing Cu(tcm) to MeCN—revert to β-Cu(tcm) on heating at 200 °C for 3 h [Fig. 7]. This series of solid–solid transformations can be followed using infrared spectroscopy, with the acetonitrile-containing phase exhibiting an additional characteristic absorption at

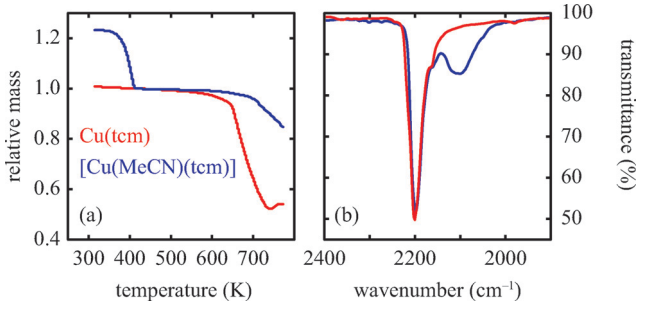

Fig. 5 (a) Thermogravimetric behaviour of Cu(tcm) and [Cu(MeCN)(tcm)]. The mass loss observed near 400 K for the latter corresponds to volatilisation of one molar equivalent of MeCN. Both TGA curves have been normalised to the mass measured at 420 K (b). High-frequency region of the infrared absorption spectra of Cu(tcm) and [Cu(MeCN)(tcm)] showing the emergence of an additional band in the latter, attributed to the nitrile C–N stretch. Colour scheme as in (a).

 This journal is © The Royal Society of Chemistry 2014

Open Access Article. Published on 02 October 2014. Downloaded on 25/11/2014 17:48:20.
This article is licensed under a Creative Commons Attribution 3.0 Unported Licence.

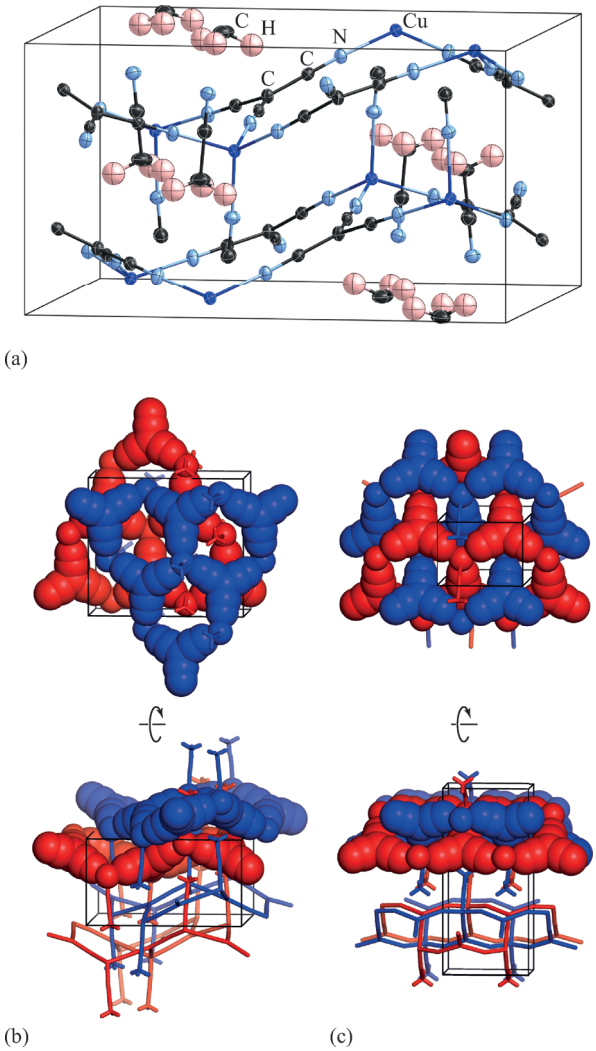

Fig. 6 (a) Representation of the crystal structure of [Cu(MeCN)(tcm)], viewed away from **a**, as determined using single-crystal X-ray diffraction measurements carried out at 100 K. Thermal ellipsoids are drawn at 50% probability level. Panels (b) and (c) show topological representations of, respectively, this same framework and that of [Ag(MeCN)(tcm)] as reported in ref. 42. Both structures are assembled from honeycomb (6,3) nets of connected Cu/Ag cations and tcm^- anions. In (b) these nets stack such that the MeCN ligands of one net interdigitate the hexagonal channels of the next. In (c) pairs of adjacent nets interweave, with the MeCN groups occupying the space between adjacent honeycomb pairs. The corresponding unit cells for both systems are shown in black; the Cu/Ag and tcm components of two adjacent honeycomb nets (but not the coordinated MeCN groups) are shown in space-filling representation.

2101 cm^{-1} associated with the nitrile C–N stretch [Fig. 5(b)]. Samples of Cu(tcm) exposed to moist air over extended periods show no structural transformation, so the binding of MeCN appears to be strongly selective even in the presence of competitive ligands such as H_2O. This observation suggests that, like the recently-reported CuCN-based systems of ref. 45, and quite separate from its extreme thermal expansion behaviour, Cu(tcm) may find application in acetonitrile sensing.

4. Conclusions

In summary, the 'wine-rack'-type framework material Cu(tcm) exhibits a ferroelastic transition at 240 K. This transition demarcates an order-of-magnitude change in elastic response, seen here most obviously in the 'colossal' PTE and NTE effects of α-Cu(tcm) that disappear in β-Cu(tcm). Indeed this anomalous thermal expansion behaviour establishes a new record within the field that means that Cu(tcm) may find application in the athermalisation of functional composites.

With respect to the ferroelastic transition itself, there are strong qualitative parallels to well-known tetragonal/orthorhombic transitions in oxide frameworks such as As_2O_5,[30] for which the elastic anomalies associated with ferroelasticity affect not only the thermal expansion, but also the lattice dynamics (*e.g.* mode softening, phonon lifetimes), microdomain formation, twin-wall motion, and susceptibility. While our study has been limited to determination of the thermal variation in lattice parameters, we anticipate that further investigation of elastic behaviour in Cu(tcm) at T_f may prove informative in establishing parallels between conventional and MOF-type framework materials.[14,46] In particular, the verification of softening of zone-centre acoustic phonons polarised along ⟨110⟩, and the use of microscopy techniques to characterise domain microstructure within the low-temperature ferroelastic phase will provide important experimental constraints on the phenomenology of what appears to be a canonical proper ferroelastic transition in a

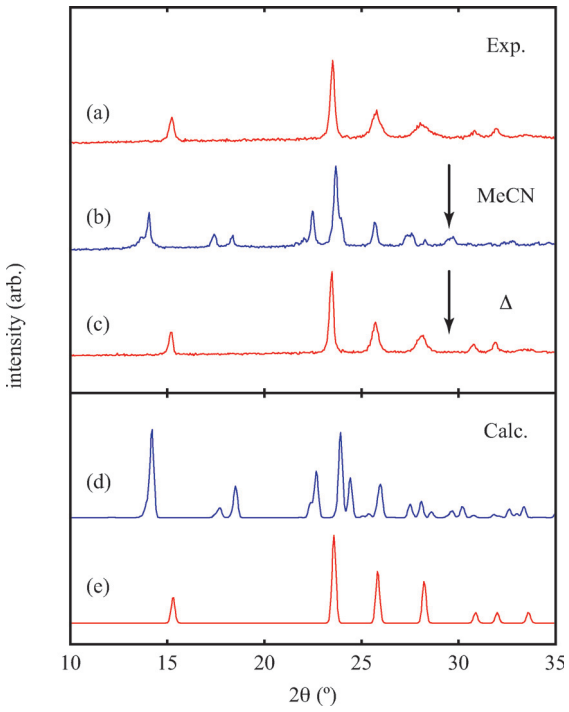

Fig. 7 (Top) Powder X-ray diffraction patterns of (a) as-prepared Cu(tcm), (b) the same sample after exposure to MeCN, and (c) after subsequent heating at 200 °C for 3 h. (Bottom) Calculated X-ray diffraction patterns of (d) [Cu(MeCN)(tcm)] and (e) Cu(tcm).

Open Access Article. Published on 02 October 2014. Downloaded on 25/11/2014 17:48:20.
This article is licensed under a Creative Commons Attribution 3.0 Unported Licence.

MOF. The most obvious difference between the ferroelastic behaviour of Cu(tcm) and that of "conventional" systems such as As_2O_5 is the very large strains realised within the ferroelastic phase [Fig. 4(d)], as implied by the colossal thermal expansion.

Finally, the coordinative flexibility of Cu(tcm) is found to affect not only elastic behaviour but also the ability of the framework to reorganise itself on exposure to a coordinating solvent. In this way, we have demonstrated proof-of-principle for application of Cu(tcm) as an acetonitrile sensor. Given the diversity of known Ag(tcm)·{guest} phases,[27,42] the possibility that Cu(tcm) may respond selectively to a variety of different solvents offers an attractive avenue for further research.

Acknowledgements

This research was supported financially by the EPSRC (grant EP/G004528/2) and the ERC (project 279705). The authors are grateful to Prof. C. J. Howard (Newcastle) for useful discussions.

References

1 S. Kitagawa and K. Uemura, *Chem. Soc. Rev.*, 2005, **34**, 109–119.
2 G. Férey and C. Serre, *Chem. Soc. Rev.*, 2009, **38**, 1380–1399.
3 C. Serre, C. Mellot-Draznieks, S. Surblé, N. Audebrand, Y. Filinchuk and G. Férey, *Science*, 2007, **315**, 1828–1831.
4 A. U. Ortiz, A. Boutin, A. H. Fuchs and F.-X. Coudert, *Phys. Rev. Lett.*, 2012, **109**, 195502.
5 A. U. Ortiz, A. Boutin, A. H. Fuchs and F.-X. Coudert, *J. Chem. Phys.*, 2013, **138**, 174703.
6 A. L. Goodwin, M. Calleja, M. J. Conterio, M. T. Dove, J. S. O. Evans, D. A. Keen, L. Peters and M. G. Tucker, *Science*, 2008, **319**, 794–797.
7 A. B. Cairns, A. L. Thompson, M. G. Tucker, J. Haines and A. L. Goodwin, *J. Am. Chem. Soc.*, 2012, **134**, 4454–4456.
8 A. B. Cairns, J. Catafesta, C. Levelut, J. Rouquette, A. van der Lee, L. Peters, A. L. Thompson, V. Dmitriev, J. Haines and A. L. Goodwin, *Nat. Mater.*, 2013, **12**, 212–216.
9 S. Henke, A. Schneemann and R. A. Fischer, *Adv. Funct. Mater.*, 2013, **23**, 5990–5996.
10 G. Thornton, B. C. Tofield and A. Hewat, *J. Solid State Chem.*, 1986, **61**, 301–307.
11 C. J. Howard, B. J. Kennedy and B. C. Chakoumakos, *J. Phys.: Condens. Matter*, 2000, **12**, 349–365.
12 J. F. Mitchell, D. N. Argyriou, C. D. Potter, D. G. Hinks, J. D. Jorgensen and S. D. Bader, *Phys. Rev. B*, 1996, **54**, 6172–6183.
13 E. K. H. Salje, *Phase Transitions in Ferroelastic and Co-elastic Crystals*, Cambridge University Press, Cambridge, 1993.
14 W. Li, Z. Zhang, E. G. Bithell, A. D. Batsanov, P. T. Barton, P. J. Saines, P. Jain, C. J. Howard, M. A. Carpenter and A. K. Cheetham, *Acta Mater.*, 2013, **61**, 4928–4938.
15 Z.-Y. Du, Y.-P. Zhao, W.-X. Zhang, H.-L. Zhou, C.-T. He, W. Xue, B.-Y. Wang and X.-M. Chen, *Chem. Commun.*, 2014, **50**, 1989–1991.
16 C. Yang, X. Wang and M. Omary, *Angew. Chem., Int. Ed.*, 2009, **48**, 1–6.
17 K. E. Bessler, L. A. d. P. Calzavara, V. M. Deflon and E. Niquet, *Acta Crystallogr., Sect. E*, 2001, **57**, m522–m533.
18 J. Cosier and A. M. Glazer, *J. Appl. Crystallogr.*, 1986, **19**, 105–107.
19 A. Altomare, G. Cascarano, C. Giacovazzo, A. Guagliardi, M. Burla, G. Polidori and M. Camalli, *J. Appl. Crystallogr.*, 1994, **27**, 435.
20 P. Betteridge, J. Carruthers, R. I. Cooper, K. Prout and D. J. Watkin, *J. Appl. Crystallogr.*, 2003, **36**, 1487.
21 R. I. Cooper, A. L. Thompson and D. J. Watkin, *J. Appl. Crystallogr.*, 2010, **43**, 1100–1107.
22 A. A. Coelho, *Coelho Software*, Brisbane.
23 P. W. Stephens, *J. Appl. Crystallogr.*, 1999, **32**, 281–289.
24 K. Larsson and L. Öhrström, *CrystEngComm.*, 2003, **5**, 222–225.
25 S. R. Batten and R. Robson, *Angew. Chem., Int. Ed.*, 1998, **37**, 1460–1494.
26 S. R. Batten, B. F. Hoskins and R. Robson, *Chem. – Eur. J.*, 2000, **6**, 150–161.
27 S. R. Batten, B. F. Hoskins and R. Robson, *New J. Chem.*, 1998, 173–175.
28 S. A. Hodgson, J. Adamson, S. J. Hunt, M. J. Cliffe, A. B. Cairns, A. L. Thompson, M. G. Tucker, N. P. Funnell and A. L. Goodwin, *Chem. Commun.*, 2014, **50**, 5264–5266.
29 H. T. Stokes and D. M. Hatch, *Isotropy subgroups of the 230 crystallographic space groups*, World Scientific, Singapore, 1988.
30 S. A. T. Redfern and E. Salje, *J. Phys. C: Solid State Phys.*, 1988, **21**, 277–285.
31 M. J. Cliffe and A. L. Goodwin, *J. Appl. Crystallogr.*, 2012, **45**, 1321–1329.
32 J. M. Ogborn, I. E. Collings, S. A. Moggach, A. L. Thompson and A. L. Goodwin, *Chem. Sci.*, 2012, **3**, 3011–3017.
33 Y. Wu, V. K. Peterson, E. Luks, T. A. Darwish and C. J. Kepert, *Angew. Chem., Int. Ed.*, 2014, **53**, 5175–5178.
34 D. Dubbeldam, K. S. Walton, D. E. Ellis and R. Q. Snurr, *Angew. Chem., Int. Ed.*, 2007, **46**, 4496–4499.
35 S. S. Han and W. A. Goddard III, *J. Phys. Chem. C*, 2007, **111**, 15185–15191.
36 W. Zhou, H. Wu, T. Yildirim, J. R. Simpson and A. R. Hight Walker, *Phys. Rev. B*, 2008, **78**, 054114.
37 These same systems undergo a first-order phase transition between 400 and 500 K, such that the authors report thermal expansion coefficients as extreme as $-380\ MK^{-1}$ and $+1161\ MK^{-1}$; however, these values hold over only very small temperature intervals immediately below the transition and so overstate the intrinsic response of the material.
38 J.-C. Tan, P. Jain and A. K. Cheetham, *Dalton Trans.*, 2012, **41**, 3949–3952.
39 S. Henke, W. Li and A. K. Cheetham, *Chem. Sci.*, 2014, **5**, 2392–2397.
40 D. A. Dixon, J. C. Calabrese and J. S. Miller, *J. Am. Chem. Soc.*, 1986, **108**, 2582–2588.

 This journal is © The Royal Society of Chemistry 2014

41 M. Calleja, A. L. Goodwin and M. T. Dove, *J. Phys.: Condens. Matter*, 2008, **20**, 255226.
42 B. F. Abrahams, S. R. Batten, B. F. Hoskins and R. Robson, *Inorg. Chem.*, 2003, **42**, 2654–2664.
43 S. J. Hibble, S. G. Eversfield, A. R. Cowley and A. M. Chippindale, *Angew. Chem., Int. Ed.*, 2004, **43**, 628–630.
44 A. M. Chippindale and S. J. Hibble, *J. Am. Chem. Soc.*, 2009, **131**, 12736–12744.
45 J.-H. Wang, M. Li and D. Li, *Chem. Sci.*, 2013, **4**, 1793–1801.
46 I. E. Collings, A. B. Cairns, A. L. Thompson, J. E. Parker, C. C. Tan, M. G. Tucker, J. Catafesta, C. Levelut, J. Haines, V. Dmitriev, P. Pattison and A. L. Goodwin, *J. Am. Chem. Soc.*, 2013, **135**, 7610–7620.

Open Access Article. Published on 02 October 2014. Downloaded on 25/11/2014 17:48:20.
This article is licensed under a Creative Commons Attribution 3.0 Unported Licence.